Fatemeh Soltanzadeh

High Performance Fiber Reinforced Concrete for the Replacement of Shear Stirrups

Fatemeh Soltanzadeh   High Performance Fiber Reinforced Concrete for the Replacement of Shear Stirrups

UMinho | 2016

Universidade do Minho
Escola de Engenharia

Fatemeh Soltanzadeh

High Performance Fiber Reinforced Concrete for the Replacement of Shear Stirrups

Tese de Doutoramento
Programa Doutoral em Engenharia Civil

Trabalho efectuado sob a orientação do
Professor Doutor Joaquim António Oliveira de Barros

janeiro de 2016

STATEMENT OF INTEGRITY

I hereby declare having conducted my thesis with integrity. I confirm that I have not used plagiarism or any form of falsification of results in the process of the thesis elaboration. I further declare that I have fully acknowledged the Code of Ethical Conduct of the University of Minho.

University of Minho, _____

Full name: Fatemeh Soltanzadeh

Signature: _____

Dedicated To:

My Beloved Parents, Mrs. Fahimeh Tabankia and Mr. Ahmad Soltanzadeh

and My Lovely Husband, Ali.

Without their help, this work would not be possible.

ACKNOWLEDEMENTS

I would like to express my heartfelt gratitude to my supervisor Professor Joaquim Barros, not only for his kind support, but also for his profuse wisdom and knowledge. Undoubtedly, his generosity in sharing his idea and time during various stages of my thesis let to progress the work easier. I am extremely grateful for his valuable guidance and patience at all stages of the development of the thesis.

My sincerely thanks also go to Doctor Eduardo Pereira, from University of Minho, for his willingness to share his thoughts and ideas.

The experimental work would not have been realized to straightforward without the enthusiastic dedication of the technicians of the laboratory of the Civil Engineering department of University of Minho: Engineers Marco Jorge, Carlos Palha, Jesus Carlos, Jose Goncalves, Fernando Pokee and most importantly, Engineer Jose Matos. I am grateful for their help during the execution of the experimental tests and helping to solve the arisen technical problems. I also would like to acknowledge the help received from Engineer Delfina Gonçalves and her colleagues in CiviTest Company, on the experimental program.

The help received from Engineer Francisco Pimenta and his colleague Engineer Claudio Ferreira, from TENSACCIAI Company, Portugal, for their effective assistance on the application of prestress reinforcements for fabricating a part of the specimens developed during my study is highly acknowledged.

I also dedicate my deeply thanks to all the secretarial staff for the completely unselfish help on the bureaucratic issues.

I own a special thanks to all my numerous friends in University of Minho for their supports, sharing thoughts and sincere friendship, which was very important to the successful realization of my thesis.

ABSTRACT

Corrosion of steel reinforcements, especially stirrups, is considered as one of the most common reasons that shorten the service life of the reinforced concrete, RC, structures. In several cases the rehabilitation of corroded RC structures is so expensive and time consuming that a decision for the demolishment of such members is currently taken, by bringing the consequent economic, social and environmental adverse impacts. Hence, in recent years there is an increasing demand for enhancing the durability and sustainability of concrete structures.

The main purpose of the present thesis is to introduce a new design framework for constructing highly durable and structurally effective prefabricated concrete beams without stirrups. These elements are produced by means of a tailor-made high performance fiber reinforced concrete (HPFRC), which is capable of suppressing the steel stirrups without occurring shear failure. A hybrid flexural reinforcement system is used for these beams, composed of glass fiber reinforced polymer (GFRP) rebars placed near to the outer surface of the tensile zone and steel reinforcements positioned with higher HPFRC cover to be protected against the corrosion, which is considered another strategy for enhancing the durability, ensuring the required ductility, and attending fire issues in terms of safety at ultimate limit states. This research combines experimental, numerical and analytical approaches to evaluate the possibilities of the proposed strategy for developing pre-fabrication beams of material and structural requisites at competitive costs. The HPFRC is developed in order to have self-compacting requisites and properties at fresh stage suitable for the type of structural application to be developed, taking also into consideration the influence of fiber distribution and orientation. The mechanical properties of this HPFRC at harden stage are deeply characterized, mainly the post-cracking behavior, due to the influence of fiber reinforcement in the fracture parameters of this cementitious material.

Considering the influence of shear span to effective depth ratio, a/d, on shear behavior of the beams, the response of both HPFRC short span ($1 < a/d \leq 2.5$) and slender beams ($a/d > 2.5$) is evaluated under shear loading configuration. During these studies, the effectiveness of fiber dosage and prestress level applied to GFRP and/or steel flexural reinforcements to improve the shear capacity and failure mode of the designed beams is

evaluated as well. By considering the obtained experimental results, the predictive performance of some analytical formulations for the shear resistance of fiber reinforced concrete beams is assessed. An analytical and a FEM-based numerical approach capable of capturing the relevant nonlinear phenomena of the intervening materials in this type of RC members are adopted to demonstrate the benefits of fiber reinforcement and prestress level on the load carrying capacity at serviceability limit state conditions and at steel yield initiation.

Based on the developed research, it is demonstrated the possibility of combining HPFRC and FRP reinforcement systems for developing innovative construction systems of high structural performance and ductility, immunes to corrosion phenomena, capable of constituting a new generation of durable and cost competitive solutions for a more sustainable built environment.

RESUMO

A corrosão das armaduras de aço, especialmente dos estribos, é considerada uma das principais causas da diminuição da vida útil das estruturas de betão armado (RC). Os custos e tempo de reabilitação de estruturas que apresentam elementos com patologias de corrosão são em diversos casos tão elevados que a opção pela demolição destas estruturas é correntemente tomada, com os consequentes impactos económicos, sociais e ambientais adversos. Assim, nos últimos anos tem existido um crescente interesse em encontrar-se estratégias para aumentar a durabilidade e a sustentabilidade das estruturas de betão armado.

O principal objetivo da presente tese é desenvolver uma metodologia de dimensionamento, do material à estrutura, que permita a produção de vigas pré-fabricadas de RC de elevada durabilidade e estruturalmente eficazes sem recorrer à utilização de estribos. Estes elementos são produzidos pelo desenvolvimento de um betão de elevado desempenho reforçado com fibras (HPFRC), com capacidade de dispensar a utilização de estribos de aço sem que ocorra rotura por corte. Nas vigas utilizou-se um sistema híbrido de reforço à flexão composto por varões de fibra de vidro (GFRP) posicionados próximo da superfície exterior da zona tracionada, e varões de aço localizados de forma a terem um maior recobrimento de HPFRC para que sejam protegidos da ocorrência de fenómenos de corrosão, o que constitui outra forma para melhorar a sua durabilidade e mitigar algumas questões relacionadas com a resistência ao fogo em termos de segurança em estados limite último. É realizada investigação experimental, numérica e analítica para se avaliar a possibilidade de utilização da metodologia proposta no desenvolvimento de vigas pré-esforçadas com requisitos materiais e estruturais a custos competitivos. O HPFRC é desenvolvido de forma a apresentar requisitos de auto-compactabilidade, com propriedades em estado fresco apropriadas para este tipo de aplicação, e considerando a influência da distribuição e orientação das fibras. As propriedades mecânicas deste HPFRC em estado endurecido são profundamente caracterizadas, principalmente as relativas ao comportamento pós-fissurado, dada a influência do reforço das fibras nos parâmetros de fratura deste material cimentício.

Considerando a influência da relação entre o vão de corte e a altura efetiva, a/d, no comportamento ao corte de vigas, são ensaiadas e estudadas vigas com $1 < a/d \le 2.5$ e

com $a/d > 2.5$ sob carregamentos de corte. Durante estes estudos também se avalia a eficiência da dosagem de fibras no HPFRC e do nível de pré-esforço aplicado aos varões de GFRP e/ou cabo de aço de reforço à flexão no melhoramento da capacidade de resistência ao corte e no modo de rotura dos elementos concebidos. Considerando os resultados experimentais obtidos, é avaliada a capacidade de previsão de algumas formulações analíticas para previsão da resistência ao corte de vigas de betão reforçado com fibras. É adotada uma abordagem analítica e numérica (esta última baseada no método dos elementos finitos), capaz de captar os fenómenos mais relevantes que governam o comportamento material e estrutural deste tipo de elementos, para demonstrar os benefícios dos mecanismos de reforço das fibras e da pré-tensão nas armaduras de flexão na capacidade de carga e ductilidade em estados limites de serviço e últimos.

Os conhecimentos resultantes dos estudos realizados foram aplicados na demonstração de ser possível combinar HPFRC e reforços em FRP no desenvolvimento de inovadores sistemas construtivos de elevado desempenho estrutural e ductilidade, imunes a fenómenos de corrosão, e capazes de constituírem uma nova geração de soluções duráveis a custo competitivo para o ambiente construído.

Palavras-chave: durabilidade; vigas sem estribos, resistência ao corte; betão de elevado desempenho reforçado com fibras; pré-esforço; análise pelo método dos elementos finitos.

Contents

LIST OF FIGURES

CAPTER 3 – HPFRC FOR THE SHEAR REINFORCEMENT: DEVELOPMENT AND CHARACTERIZATION

Chapter 4 – Shear Behavior of HPFRC

CAPTER 5 – SHEAR RESISTANCE OF HPFRC SHORT-SPAN BEAMS WITHOUT STIRRUPS

CAPTER 6 – SHEAR RESISTANCE OF HPFRC SLENDER BEAMS WITHOUT STIRRUPS

CHAPTER 7 – APPLICATION IN DEVELOPING INFRASTRUCTURES

LIST OF TABLES

Chapter 6 – Shear resistance of HPFRC slender beams without stirrups

CAPTER 7 – APPLICATION IN DEVELOPING INFRASTRUCTURES

xxx

NOTATIONS

A_{GFRP} cross sectional area of GFRP bar

$A_{F-u}^{\exp}$ area below the experimental $F-u$ curves of three point bending test

A_{F-u}^{num} area below the numerical $F-u$ curves of three point bending test

A_c cross section of beam

A_f shear plane area

A_s cross sectional area of steel bar

a shear span of the beam

b width of the specimen

b_{eff} effective width of the DSS

b_f flange width

$\underline{D}_{I,i}^{cr}$ the modulus correspondent to the fracture mode I of the ith crack

$\underline{D}_{II,i}^{cr}$ the modulus correspondent to the fracture mode II of the ith crack

$\underline{D}^{co}$ linear elastic constitutive matrix

$\underline{D}^{cr}$ crack constitutive matrix

$\underline{D}^{crco}$ cracked material constitutive matrix

D_n^{cr} stiffness modulus corresponding to the fracture mode I

D_t^{cr} stiffness modulus corresponding to the fracture mode II

d effective depth of beam

d_{GFRP} central distance of GFRP bar from top face of section

d_a	maximum size of aggregate
d_{eff}	effective depth of DSS
d_f	steel fiber diameter
d_s	central distance of steel bar from top face of section
$d_{s,eq}$	equivalent steel effective depth
E_{GFRP}	modulus of elasticity of GFRP bars
$E_{cm} = E$	modulus of elasticity of concrete
E_s	modulus of elasticity of steel bar
F_L	load at the limit of proportionality for three-point notched beams flexural tests
F_f	fiber factor
$F_{f,opt}$	optimum fiber factor
F_j	load corresponding to CMOD$_j$
f	yield function
f_{Ftuk}	characteristic value of ultimate residual tensile strength of FRC
f_{Ftum}	average value of ultimate residual tensile strength of FRC
f_{GFRP}	stress in GFRP rebars
$f_{GFRP,u}$	tensile strength of GFRP rebars
f_{Rj}	residual flexural tensile strength corresponding to $CMOD_j$ (j=1, 2, 3, 4)
f_{ck}	characteristic value of compressive strength of concrete

f_{cm}	mean value of compressive strength of concrete
f_{ct}	concrete tensile strength
f_{ctk}	characteristic tensile strength of concrete
f_{c0}	uniaxial compressive strength at plastic threshold
f_{su}	ultimate tensile strength of steel bar
f_{sy}	yielding strength of steel bar
$f_{ct,L}^{f} = f_{fct,L}$	limit of proportionality
G_c	elastic shear modulus
$G_{f,c}$	compressive fracture energy
G_f^I	mode I fracture energy
$G_{f,s} = G_f^{II}$	mode II fracture energy
h	height of beam
h_f	depth of flange
h_{sp}	distance between the tip of the notch and the top of the cross section
IP	integration point
k	size effect factor
k_f	factor for taking into account the contribution of the flange in T-sections
L	span of the specimen
l_b	crack band width
l_f	fiber length

M_{fl}	nominal flexural moment
M_u	ultimate flexural moment obtained analytically
$M_{u,\exp}$	ultimate flexural moment obtained experimentally
m_f	mass of fibers per meter cube of concrete
N_f	fiber density
N_{sd}	axial force
N_T^f	total number of fibers
P	total applied load
$P_{\max}$	average peak load supported by the HPFRC DSS
P_1	parameter that defines the amount of the decrease of β upon increasing ε_n^{cr}
s	slip value
T^{cr}	transformation matrix from crack local coordinate system to element local coordinate system
T_{50}	time to reach a spread diameter of 500 mm in the slump test
u	deflection
V_{MC2010}	estimated shear resistance according to the proposed formula by MC2010
$V_{Rd,F}$	design shear resistance attributed to the FRC
V_{RILEM}	estimated shear resistance according to the proposed formula by RILEM TC 162-TDF
$V_{Soetens2015}$	estimated shear resistance according to Soetens (2015) formula
V_{anal}	calculated shear resistance of beams

V_{cd}	design value of shear resistance attributed to plain concrete
V_{exp}	shear resistance of beams, obtained experimentally
V_f	fiber volume fraction
V_{fd}	design value of shear resistance attributed to steel fibers
V_{paste}	volume of paste
V_{total}	total volume of concrete mix
V_u	maximum shear resistance
V_{wd}	design value of shear resistance attributed to transversal reinforcement
v_u	ultimate shear strength
w	width of cracks
W_{Fs}	shear toughness
W_f	width of flange
W_w	web width
$\alpha_i \ (i=1,2,3)$	normalized stress parameter in quadrilinear diagram
α_{red}	fiber reinforcement effectiveness factor
α_0	material constant to define the beginning of the nonlinear behavior in uniaxial compressive stress-strain test
β	shear retention factor
γ_c	partial safety factor for material properties
γ_t^{cr}	crack shear strain
$\gamma_{t,\max}^{cr}$	maximum crack shear strain

$\gamma_{t,p}^{cr}$	peak crack shear strain
$\gamma_{t,u}^{cr}$	ultimate crack shear strain
$\Delta\underline{\varepsilon}$	total strain vector
$\Delta\underline{\varepsilon}^{cr}$	incremental crack strain vector
$\Delta\underline{\varepsilon}^{co}$	incremental concrete strain vector
$\Delta\underline{\varepsilon}^{e}$	incremental elastic strain vector
$\Delta\underline{\sigma}$	vectors of incremental stress components
δ	deflection at mid-span of beam
δ_L	deflection at the limit of proportionality in three-point flexural tests
$\varepsilon_{sy}, \varepsilon_{sh}, \varepsilon_{su}$	three strain points at the steel constitutive law
ε_{c1}	strain at uniaxial compression peak stress
ε_n^{cr}	crack normal strain
$\varepsilon_{n,u}^{cr}$	ultimate crack normal strain
ξ_i	normalized strain parameter in quadrilinear diagram (i =1, 2, 3)
η_f	bond efficiency factor
η_θ	fiber orientation factor
θ	inclination of the compressive strut
θ_i	out-plane angle
μ	Poisson's ratio
ρ_{eff}	effective reinforcement ratio
$\rho_{seq,GFRP}$	reinforcement ratio of longitudinal GFRP bars converted into an

	equivalent steel reinforcement ratio
ρ_s	reinforcement ratio of longitudinal steel bars
$\rho_{s,eq}$	equivalent steel reinforcement ratio
σ_f	nominal flexural stress
σ_{cp}	average stress acting on the concrete cross section
$\sigma_{sy}, \sigma_{sh}, \sigma_{su}$	three stress points at the steel constitutive law
σ_n^{cr}	normal stress in the crack coordinate system
$\underline{\sigma}$	the stress vector in damaged, respect to compression, configuration
τ_{max}	average shear strength
τ_t^{cr}	shear stress in the crack coordinate system
$\tau_{t,max}^{cr}$	maximum crack shear stress
$\tau_{t,p}^{cr}$	peak crack shear stress
ψ	a function that considers the influences of the aggregate size on flexural capacity
ω	reinforcement factor

INTRODUCTION

1.1 MOTIVATION

Nowadays there is a big demand for enhancing the sustainability and durability of concrete constructions. All the efforts that can be done for improving the durability of these structures have significant impact in terms of their sustainability due to the relatively high costs of rehabilitation or demolishment. The corrosion of steel reinforcements, especially stirrups, is one of the common causes that limits the long-term performance of reinforced concrete (RC) structures. Due to either carbonation of the RC structures or ingress of chloride into the RC elements, corrosion can affect the mechanical properties of steel reinforcements, by reducing the cross section of the reinforcements. It also influences the concrete integrity due to the expansion of the corrosion products, promoting the development of cracks through the concrete cover. The bond behavior between steel reinforcements and surrounding concrete is also detrimentally affected by the deterioration of the bond between these two materials, which consequently influences the safety and serviceability of the RC structures (Almassri et al. 2015). The high cost for rehabilitating such corroded RC elements frequently motivates the building's demolishment, which brings economic, social and environmental adverse impacts. On the other hand, the activities for producing and placing conventional shear reinforcement are very labor-intensive, and increase the production time and cost of the elements. Finding a material system that does not need conventional shear reinforcement is a relatively recent

challenge for the scientific community (Soetens 2015, Voo et al. 2010, Cucchiara et al. 2004). The attainment of this objective is not only a step forward to avoid corrosion problems in concrete structures, but also to reduce the element thickness and the structural self-weight, leading to a better production efficiency (Ferrara et al. 2007). In accordance with the literature, steel fibers can be considered as a shear reinforcement that significantly affects the ultimate shear capacity and ductility of structural elements, and may replace partially or totally the conventional shear reinforcements, depending on the concrete strength class, as well as the type and dosage of steel fibers (Barros et al. 2013, Cucchiara et al. 2004). Improving the structural behavior and durability of the members, which can be constructed in a shorter time and less labor costs, should balance at least the increase in material costs due to application of steel fibers.

The corrosion of steel flexural reinforcements is another responsible for the deterioration and damage of RC members. The use of non-corrodible fiber reinforced polymer (FRP) bars as a flexural reinforcement can be a solution for enhancing the durability and sustainability of concrete elements. Glass fiber reinforced polymer (GFRP) bars are being employed as a promising alternative for replacing steel flexural reinforcement (Aiello and Ombres 2002, Qu et al. 2009). The major driving force behind this effort is the superior performance of this type of reinforcement in corrosive environments, non-conductivity, and high strength-to-weight ratio (Sharbatdar 2008). Despite of all these advantages, the GFRP has a relatively low modulus of elasticity and brittle tensile failure. Additionally, the bond performance between FRP bars and concrete is normally lower than conventional steel bars, and strongly depends on the surface treatments of the bar (Achilides and Pilakoutas 2004, Al-Mahmoud et al. 2007, Mazaheripour et al. 2013). To improve the ductility and accomplish the serviceability limit state requirements of the GFRP reinforced concrete beams, application of steel bars as an additional reinforcement is suggested, resulting a hybrid reinforcing system (Lau and Pam 2010). This system offers lower cost constructions than when exclusively FRP reinforcements are used, and also longer service life compared to that of applying solely steel reinforcements (Qu et al. 2009).

Due to the specificities introduced by using steel fibers, the accurate evaluation of the shear capacity of steel fiber reinforced concrete (SFRC) beams is still a challenge. Hence, most of the guidelines do not support the total replacement of stirrups by steel fibers (ACI

544.1R-96, Eurocode 2), unless strain hardening cement composites are used (CEB-FIP Model Code 2010; the abbreviator MC2010 will be adopted). Even some guidelines do not have a design framework to simulate the contribution of steel fibers for the shear capacity of FRC structures (ACI 318-11). Some guidelines, such as MC2010 and RILEM TC-162-TDF, have already considered the influence of fiber contribution for predicting the shear resistance of SFRC elements. In addition to these guidelines, some alternative formulas are proposed by researchers, taking into account the effect of steel fibers (Soetens 2015, Khuntia et al. 1999, Imam et al. 1995, Ashour et al. 1992, and Narayanan and Darwish 1987). The predictive performance of these formulas need to be assessed by considering the results of experimental programs carried out on the shear strength of FRC beams with variable shear span to effective depth ratio, a/d, in order to detect the defects of the formula and assisting for improving them.

1.2 RESEARCH OBJECTIVES

By considering all the aforementioned techniques for enhancing the durability of concrete structures, the present study intends to contribute for the development of a new generation of high durable and sustainable prefabricated structural elements. This objective is pursued by combining the benefits provided by the application of steel fiber reinforced concrete, SFRC, and hybrid system of GFRP-steel reinforcements. The steel fibers assure the shear resistance of the concrete elements and reduce the necessity of using steel stirrups (its elimination will be pursued), while the hybrid reinforcements aim to decrease the susceptibility of the flexural reinforcement to corrosion (even its elimination), and assure a good balance between flexural capacity and ductility for these structural members. An extensive research on hybrid system of GFRP-steel reinforcements and the bond performance of FRC beams with such reinforcement was recently carried out (Mazaheripur 2016), but the influence of steel fibers on the shear behavior of this type of elements was not investigated. It is the objective of the present thesis to combine the knowledge from previous investigations with new experimental and theoretical findings to assess the shear resistance of high-performance fiber reinforced concrete, HPFRC, when applied to structural members without conventional steel stirrups. It is expected that the overall research work carried out in the present thesis provides an effective solution for the construction of elements of longer life cycle, with first contribute on future

professional guidelines for design purpose. The detailed objectives of this study are the following ones:

- Development and material characterization of a high strength concrete with relatively high dosage of steel fibers, herein designed as HPFRC.

  – The HPFRC should provide a shear resistance capable of suppressing the use of conventional steel stirrups in the type of developed beams (especially suitable for the prefabrication industry).

  – It should have a high compactness to improve the FRP-FRC bond performance and to increase the protection of steel bars from being attacked by corrosion agents.

  – It also should meet the requirements of self-compacting concrete, SCC, namely flowability, passing ability and filling ability in fresh stage; the mechanical performance of the HPFRC in harden stage should be suitable in order this material be applicable for developing prefabricated elements in construction industry.

- Assessment of shear behavior of the developed HPFRC, at meso-level, and the influence of fibers orientation and dispersion on this behavior.

  – The material properties and post-cracking behavior of the developed HPFRC under direct shear loading will be investigated.

  – Fiber orientation and dispersion on cracked surface of HPFRC elements under shear load will be detected by means of image analysis. This analysis better clarifies the effect of orientation and dispersion of fibers on the shear resistance of HPFRC.

- Design of hybrid GFRP-steel reinforced HFPRC beams without stirrups and investigation of the shear behavior of the developed elements experimentally and analytically.

– This type of elements should be capable of supporting prestressed slabs between 12 and 20 m span length with a live load between 4 to 6 kN/m^2.

– The influence of several factors, such as prestress level, shear span to effective depth ratio, reinforcement ratio, and most importantly the fiber dosage on shear behavior of HPFRC beams will be assessed.

– The results and knowledge obtained from the experimental studies should contribute for the development of design guidelines for the type of prefabricated HPFRC beams without stirrups to be developed.

- Exploring the applicability of the innovative methodology of developing HPFRC beams without stirrups for constructing infrastructures with higher durability.

- Deeper investigation of the shear behavior of the designed elements by means of FEM-based simulations.

1.3 OUTLINE OF THESIS

The present thesis is divided into eight chapters. The introduction represented in this chapter, Chapter 1, defines the motivation and the objectives of the present doctoral study.

Chapter 2 is dedicated to an overview of the studies on the shear behavior of FRC elements without conventional shear reinforcements, based on the scope of the present research. The main purpose of this overview is to have a comprehensive understanding about the mechanism of shear transfer in such elements and most importantly the effect of steel fibers and concrete properties on this behavior. This chapter demonstrates the drawbacks regarding the lack of information and design guidelines in connection with shear resistance of FRC structures without shear reinforcements.

Chapter 3 introduces new mix design methodology for developing HPFRC with relatively high dosage of steel fibers to be capable of suppressing the conventional shear reinforcements in RC structures. Since the steel fibers are rigid and cause a strong perturbation effect on the flowability of fresh concrete, there still remain some drawbacks

associated with the available HPFRC formulations, which are recovers in the 3rd chapter. In this chapter the mechanical properties of the developed concrete at fresh and harden stages are assessed as well.

Chapter 4 investigates the shear behavior of the HPFRC tailored in accordance with the proposed method in the former chapter, using an innovative double shear specimen, DSS. The chapter also deals with the evaluation of fiber distribution structure in the HPFRC DSS, at a meso-level, and discusses the influence of fibers density, orientation and dispersion on shear behavior of HPFRC.

An innovative design method for developing the prefabricated elements with high durability and sustainability is introduced in the next two chapters, Chapter 5 and Chapter 6. In these chapters the shear behavior of the beams developed according to the proposed method, at macro level, is studied experimentally and numerically. By analyzing these results as well as those available in the literature and investigating the effect of each parameter on shear behavior of the beams, the reliability of the current design guidelines in prediction of shear resistance of FRC beams is evaluated.

Chapter 5 evaluates the shear behavior of short-span HPFRC beams (with shear span, a, to effective depth, d, ratio of $1 < a/d \leq 2.5$) with hybrid GFRP-steel system of reinforcements. The effectiveness of varying the prestressing force applied to GFRP bars to improve the shear capacity and failure mode of the designed elements is investigated in this chapter.

Chapter 6 investigates the effect of prestressing the steel reinforcements on shear behavior of the developed HPFRC slender beams (with $a/d > 2.5$) with hybrid system of reinforcements. The shear behavior of the prestressed beams with different dosages of steel fiber is also assessed in this chapter, aiming to improve the ductility as well as load carrying capacity of the elements in the serviceability and ultimate limit state. The results of the studies in chapters 5 and 6 contribute to further enhancement of the structural behavior of the beams without stirrups, which can be applied as the alternative to the available RC elements in the corrosive areas.

The shear behavior of HFFRC shear specimens, at meso level, as well as that of the HPFRC beams without stirrups, at macro level, were also analysis numerically in chapters 4, 5 and 6.

In Chapter 7, based on the knowledge and experience acquired in the 5th and 6th chapters, the method of developing the prefabricated HPFRC beams will be extended for constructing the durable infrastructures for zones of high environmental aggressiveness. The applicability and effectiveness of the adopted strategy in developing several designed manhole covers, as an example of the infrastructures with high probability of subjecting to the corrodible environments, in terms of load carrying capacity and failure mode is evaluated experimentally and numerically.

Chapter 8 gives the conclusions of this research with general recommendations for practical applications of the developed methodology. Fig. 1.1 represents an overview over the structure of the present thesis.
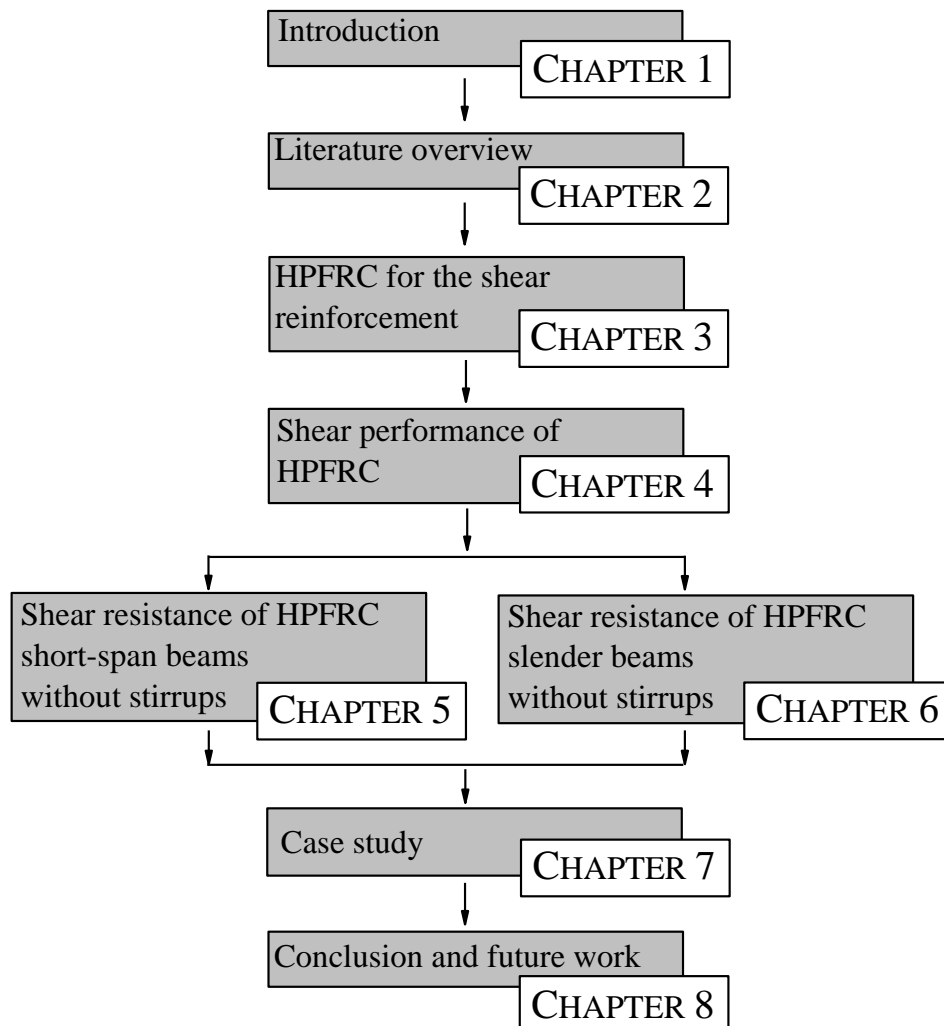
Fig. 1.1- Structure of the thesis.

CHAPTER 2

LITERATURE OVERVIEW

2.1 INTRODUCTION

Corrosion of steel reinforcements, especially stirrups, is considered as one of the most common reasons that shorten the service life of the reinforced concrete structures. To address this problem extensive researches have been performed aiming at improving the corrosion resistance of concrete elements. Hence, several strategies were proposed to reduce the corrosion problem of concrete structures, most importantly replacing stirrups with steel fibers and using non-corrodible longitudinal reinforcements.

Since fibers are closely spaced though the matrix, they can effectively bridging the cracks and improving the post-cracking ductility (Imam et al. 1997). In general, the use of steel fibers in concrete technology as a reinforcement system improves the behavior of cement-based materials, mainly in post-cracking stage (Minelli et al. 2014 and Cuenca et al. 2013b). Concrete shear behavior is reported as one of the most significant enhancements achieved by adding fibers to the concrete matrix (Cuenca et al. 2013a and Barragan et al. 2006). The steel fibers increase the bearing capacity of the concrete elements and, therefore, bring the member up to yielding of rebars (Cuenca and Serna 2013a). Anyhow, the reinforcement effectiveness of steel fibers depends on the matrix properties, fiber type and content, application technology of the fiber concrete, and geometry of the element to be produced (Laranjeira 2010 and Cucchiara et al 2004).

Application of non-corrodible fiber reinforced polymer (FRP) bars as a flexural reinforcement is also introduced as a solution for enhancing the durability and sustainability of concrete elements. However, despite all the advantages of FRP reinforcements, such as corrosion resistance, non-conductivity and high strength-to-weight ratio, their use for the reinforcement of concrete structures is still limited due to the tensile brittle nature of FRPs. In fact,, FRP-reinforced concrete (FRPRC) elements possess less ductility compared to the elements reinforced with steel bars. To improve the ductility of these members, it is proposed to include steel bars in the reinforcing system of the elements such that the brittleness of FRP rebars can be compensated by the ductile nature of the additional steel reinforcement (Lau and Pam 2010).

Although the reduction and mainly the elimination of conventional shear reinforcements in FRPRC elements enhance the durability of the concrete structures, a comprehensive understanding of the shear behavior of such elements is fundamental for their acceptance by designers and practitioners, therefore an intensive research must be executed regarding this issue. Due to the complexities of the mechanisms that govern the shear behavior of RC structures, their design, especially those made by fiber reinforced concrete (FRC) elements without stirrups, have been attracting the research efforts of a relatively large community. This chapter provides information on the mechanical behavior of fiber reinforced concrete and on the mechanisms of shear transfer in members made by this material. It also discusses the influence of steel fibers on shear resistant of the beams, and presents design approaches for predicting the shear capacity of FRC elements.

2.2 MECHANISM OF CRACK FORMATION AND PROPAGATION

Even before applying any load, a large number of micro-cracks, especially at the interface between aggregates/fibers and paste, already exist in concrete. Many of these micro-cracks are caused by segregation, shrinkage or thermal expansion of the mortar, etc. Propagation of these initial cracks can result in failure of a structure. The mechanism of crack formation and propagation or "fracture mechanism" is thereby employed to study the response and failure mechanism of structures, as a consequence of crack initiation and propagation.
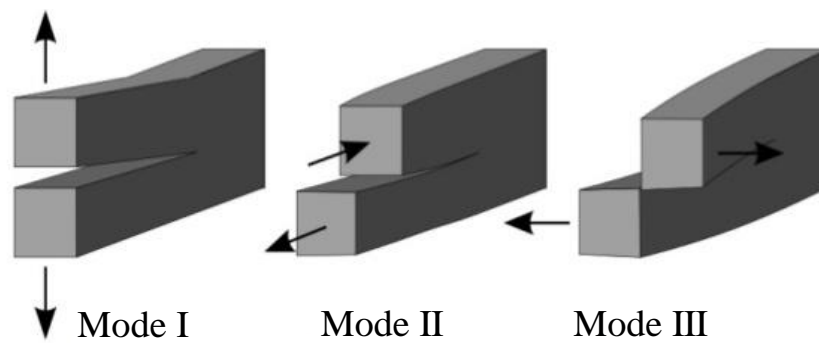
Fig. 2.1- Basic modes of crack expansion (Hasanpour and Choupani 2009).

According to the fracture mechanism, a crack in a solid can occurr in three different modes, which are called "Opening Mode" or Mode I, "Sliding Mode" or mode II, and "Tearing Mode" or Mode III, as illustrated in Fig. 2.1. Mode I is one of the most common crack propagation modes, since it occurs in uniaxial, splitting and bending tensile failure. In Mode II, which receives the special attention in the present thesis, the displacement of crack surfaces is in the plain of the crack and perpendicular to the leading edge of the crack. In most of cases, the crack sliding is accompanied by crack opening due to the friction and asperities of the crack planes, resulting a mixed failure mode (Mode I and II). The Tearing Mode or out of plain shear (Mode III) is not so common like the previous failures modes, and occur in massive structures where 3D stress field can be developed (Ayatollahi et al. 2005), or in slab or shell type structures where punching failure mode is a concern (Ventura-Gouveira et al. 2011, Teixeira et al. 2015).
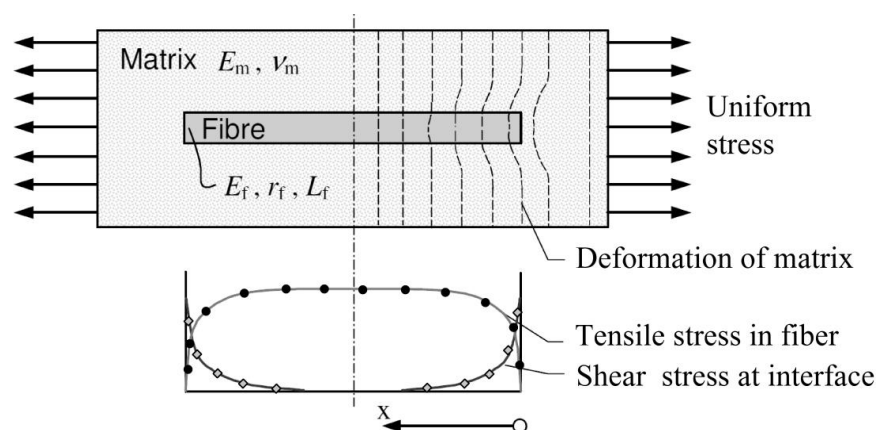
Fig. 2.2- Transferring stress from matrix to fiber by application of tensile load (löfgren 2005).

When a tensile load is applied to a fiber reinforced composite, before initiation of any new crack, the matrix transfers some of the load to the fibers. Although the applied fibers generally have a higher elastic modulus compared to the matrix itself, they do not affect the tensile stiffness and strength of the elements before crack initiation. However, the fibers affect significantly the cracking process, and the failure mode of the FRC is highly influenced by the stress transfer between the fibers and the surrounding cementitious matrix. Thus, unlike plain concrete, which exhibits a brittle manner after initiation of the first crack, the FRC presents a relatively high toughness or fracture energy, i.e. the area under the stress-crack opening curve (Fig 2.3). In plain concrete, the pullout of aggregates bridging the crack is the main mechanism that causes the dissipation of energy, and the post-cracking tensile capacity decays towards zero for crack opening of about 0.3 mm. The combined crack bridging effect of aggregate and fibers is the main responsible for controlling the crack width (Fig. 2.3), which is very beneficial to increase the stress carried across the crack. In the following sections (Sec. 2.2.1 and .2.2.2) the effect of both aggregate bridging and fiber bridging on tensile behavior of FRC is discussed.
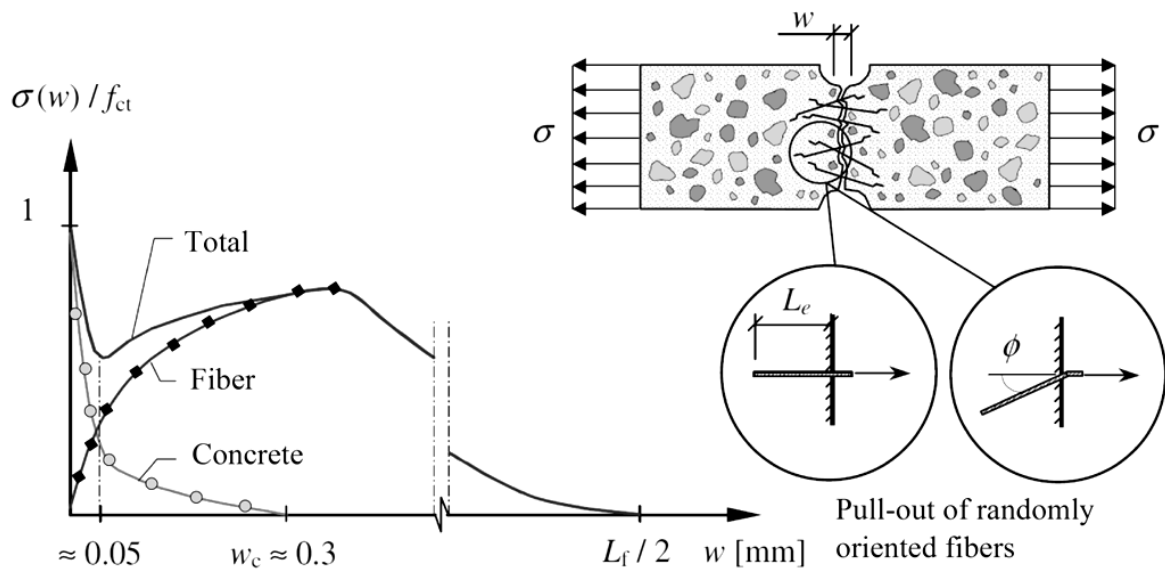
Fig. 2.3- Combined crack bridging effect of fibers and aggregate for the tensile capacity of fiber-reinforced concrete.

2.2.1   Aggregate Bridging Action

Fig. 2.4 schematically represents stress-elongation relationship of plain concrete under uniaxial load. It shows that by applying a tensile load to a concrete element, initially micro-cracks start growing at the interface between the paste and the aggregates (A), and gradually propagate into the concrete (B). The crack localization occurs by reaching to the peak stress (C). This causes the initiation and propagation of the macro-cracks through the specimen, leading to the stress-drop (D). Crack bridging and crack branching is the principal mechanism responsible for the long softening tail (D-E) observed in experiments (see Fig. 2.4). However, depending on the aggregates and their bond to the matrix, the fracture process differs for high strength and normal strength concrete. For concretes with strong aggregate-paste bonds, or with weak aggregates, e.g. lightweight aggregates, the aggregate rupture may occur, losing its bridging effect, which results in a more brittle fracture process (Löfgren 2005).
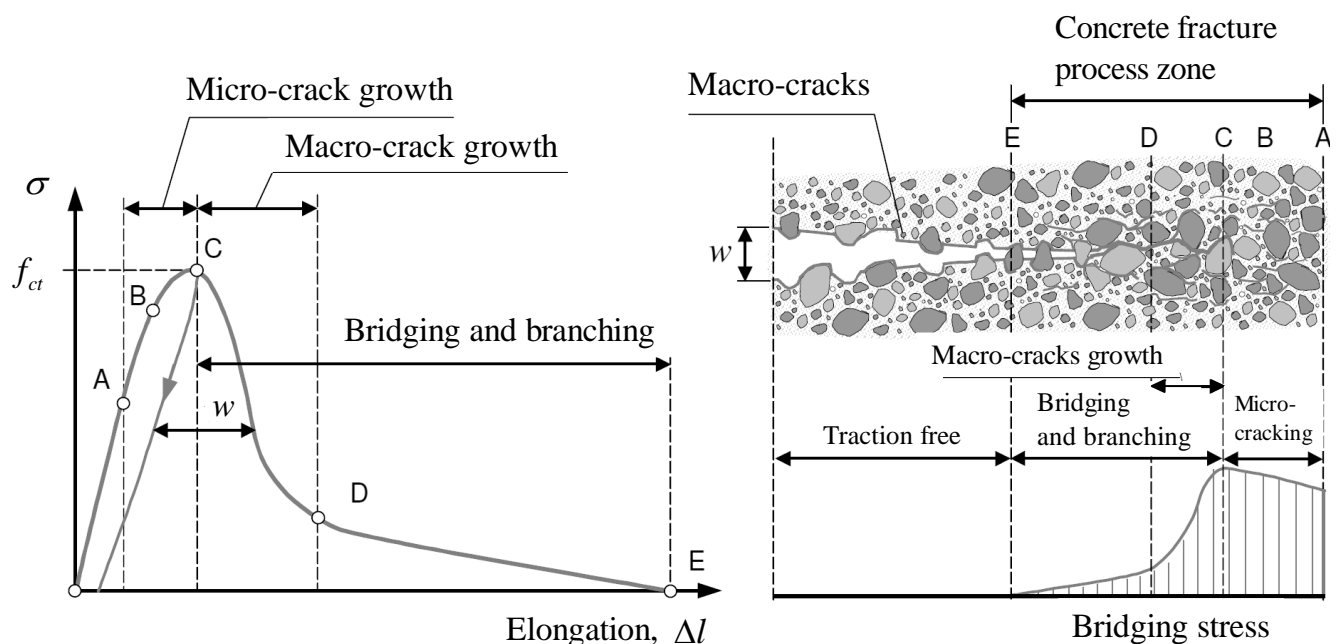
Fig. 2.4- Schematic description of fracture process in uniaxial tension and the resulting stress-crack opening relationship (Löfgren 2005).

2.2.2 Fiber Bridging Action

According to the literature, fiber pull-out behavior, i.e. load-slip relationship has a significant influence on the mechanical behavior, especially in ductility of FRC (Cunha 2010). The principal bond mechanisms that contribute to improve the ductility of the composite material during the pullout of a fiber can be classified as chemical adhesion between fiber and matrix, frictional resistance, fiber-to-fiber interlock and mechanical component, arising from particular fiber geometry, e.g. deformed, crimped, or hooked-end fibers (Naaman 2003). Among all these factors, the mechanical component has proven to be the most effective one in improving the bond between fibers and surrounding matrix (Cunha et al. 2008, Cunha et al. 2010). Thus, for the deformed fibers (e.g. crimping, indenting or hooked end) the chemical bond can be neglected in favor of the mechanical bond between the fiber and the surrounding concrete (Robins et al. 2002), while the slip of smooth fibers mostly depends on the breakdown of chemical adhesion and the friction.

(a)   (b)   (c)
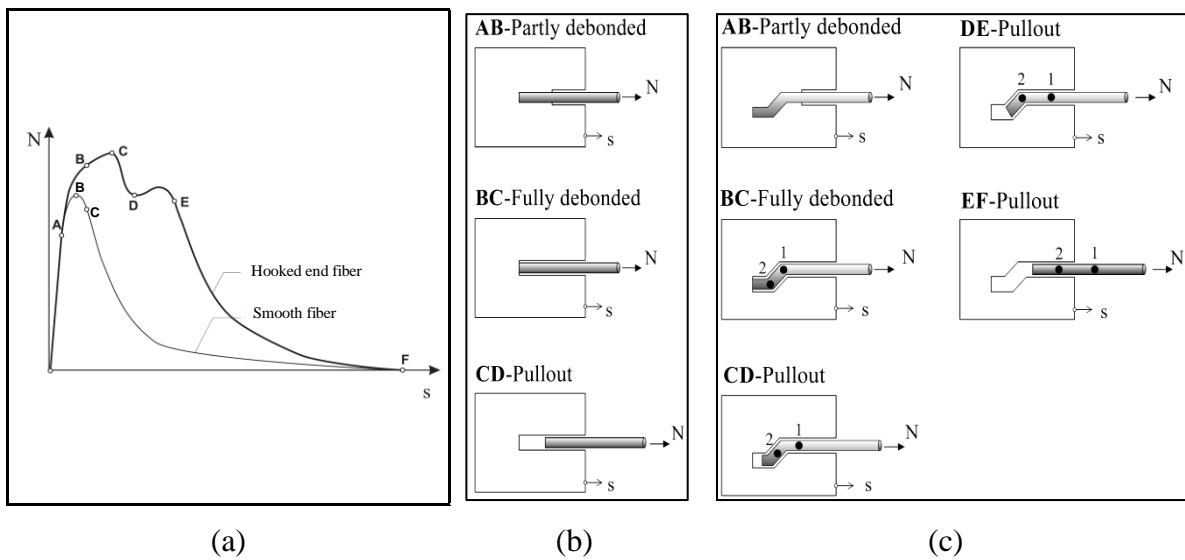
Fig. 2.5- (a) Pullout relationship between the load and the end-slip for (b) the smooth and (c) the hooked end steel fibers (Cunha 2010).

Fig. 2.5 compares the pullout behavior of the smooth and hooked end steel fibers. This figure shows two distinct phases in the pre-peak branch of load-slip relationship for the

smooth fibers (see Fig. 2.5(b)). The first phase, which is a linear ascending part (OA), is associated with the elastic bond. The second part (AB) corresponds to the initiation of the debonding process and starts with the micro-cracking of the interface transition zone between the fiber and matrix. After reaching to the maximum load, the load decreases with the increase of slip, resulting in an unstable interfacial crack growth on the post-peak behavior. Similar to the pull out behavior of smooth fibers, the pullout behavior of hooked end steel fibers consists of deboning and frictional pullout as well. However, the frictional pullout in the hooked end steel fibers is accompanied with a mechanical bond mechanism correspondent to the mechanical interlock and plastic deformation of the fiber hook (see Fig. 2.5(c)). Hence, after attaining the full debonding of the hooked end steel fibers (AB), the load still increases (BC) due to the mechanical anchorage provided by the hook of the fiber. By reaching the maximum pullout load (C), both curvatures 1 and 2 are deformed. Since the mechanical anchorage starts deforming progressively, the pullout load decreases (CD) after reaching the maximum load. However, at this stage the fiber is not fully straightened yet and, consequently another peak load is observed (DE), which coincide with the fiber (curvature 2) passing the last corner of the fiber imprint made in the matrix. After the fiber is fully straightened, likewise to the smooth fibers, the pullout action proceeds under frictional resistance (EF) (Cunha 2010). Orientation and dispersion of fibers are also factors that, together the fiber pullout mechanism, influence the mechanical behavior of FRC, as will be discussed in the following section.

2.3 FIBER ORIENTATION AND DISPERSION

Studies on the behavior of FRC have shown that the level of improvement of the concrete behavior by using fibers is sensitive to fiber dispersion and orientation. These characteristics that are dependent on the fresh properties and technology of producing FRC influence significantly its mechanical performance, and consequently the potentialities of this composite material for structural applications (Laranjeira et al. 2011). In general, factors such as the fiber length and volume fraction, wall effects due to the geometry of the formwork of the element to be cast, and the interactions between fibers and aggregates during mixing and casting, influence the orientation and dispersion of the fibers inside the matrix. The flowability of concrete has a significant impact in this

context, due to the fiber perturbation effect, especially when relatively long fibers or a high fiber volume fraction is used. Obviously, in self compacting concrete (SCC) the re-orientation of fibers due to vibration does not occur, since external compaction is not applied.

Depending on the abovementioned factors the fiber structure represents distinct distributions and orientations (Schumacher 2006). Accordingly, fibers with one dimensional, 1D, distribution are oriented in the same direction, parallel to an axis. The 1D oriented fibers then appear as circles in a section across the FRC flow direction and the value of fiber effectiveness or 1D orientation factor, η_{1D}, is equal to 1 (Cunha, 2010).

When the thickness of a structural element to be cast with FRC is less that the length of applied fibers, such as the case of thin-walled elements, e.g. flat sheets, plates, etc., the fibers are randomly oriented within a plane with two-dimensional distribution, 2D (Lofgren 2005). A 2D orientated fiber is illustrated in Fig. 2.6(a). According to this figure the fiber orientation angle, θ, which is the angle between the fiber longitudinal axis and the crack line can vary between 0 and π, while the tensile stress is applied along y-axis direction. In this situation, the fibers appear as an ellipse in a section across the flow direction of FRC during casting (Schumacher 2006). The fiber orientation factor for 2D oriented fibers is calculated using Eq. (2.1) (Abrishambaf 2015).

$$\eta_{2D} = \frac{\int_0^{\pi/2} \cos\theta . d\theta}{\int_0^{\pi/2} d\theta} = \frac{2}{\pi} \simeq 0.637 \tag{2.1}$$

When fibers can have any orientation in a three-dimensional system, the unit sphere model, depicted in Fig. 2.6(b), reflects the isotropic uniform random fiber three-dimensional distribution, 3D, in the specimen. Fig. 2.6(b) shows that the fiber orientation in 3D situation can be characterized by two angles, namely the in-plane angle "φ" and out-plane angle "θ". The in-plane angle defines the orientation of the elliptical fiber cross section major semi-axis, b, with respect to an arbitrary in-plane direction. The out-plane angle represents the fiber alignment regarding to the loading direction and can be determined by using major semi-axis, b, and minor semi-axis, a, lengths of the ellipse (see Fig.2.6(b)), using the following equation (Cunha 2010):

$$\theta = \arccos(b/a) \tag{2.2}$$

By assuming the xy-plane as the crack plane, and the z-axis as the direction of tensile stress, 3D orientation factor, η_{3D}, is given by the following equation (Cunha 2010):

$$\eta_{3D} = \frac{\int_{0}^{\pi/2} \cos\theta . \sin\theta . \, d\theta}{\int_{0}^{\pi/2} \sin\theta . \, d\theta} = \frac{1}{2} \tag{2.2}$$

The orientation of fibers toward the active crack planes significantly influences the contribution of fibers to control the cracks and, consequently affects the mechanical behavior of FRC structures (Abrishambaf et al. 2013). In the following sections the effect of fibers on mechanical behavior of FRC elements is discussed.
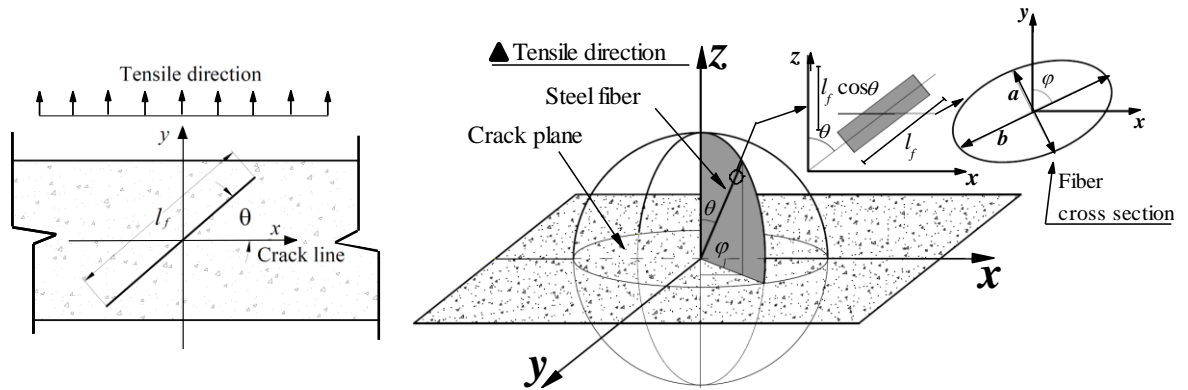
Fig. 2.6-(a) 2D fiber orientation system and (b) fiber in a 3-D space (schematically describing the in-plane angle, φ, and out-of-plane angle, θ) and an ellipse (Cunha 2010).

2.4 MECHANICAL BEHAVIOR OF FRC

When steel fibers are added to concrete mix, they distribute randomly and offer resistance to the formation and propagation of cracks. The energy required for debonding and pullout of fibers causes a substantial increase in toughness and resistance to cyclic and dynamic loads compared to that of plain concrete. Results obtained from uniaxial and flexural tensile tests, as well as compression and direct shear tests on FRC, reveal a marginal influence of steel fibers on the behavior at uncracked stage, but they show that

fibers provide a substantial increase in the post-peak energy absorption capacity (Prisco et al. 2009). The following sections describe the behavior of FRC under tensile, compressive and direct shear loads (Sec. 2.4.1 to 2.4.3).

2.4.1 Behavior of FRC in Uniaxial Tension and Bending

By considering the characteristic of fiber reinforced cement composites tested under the uniaxial and flexural loading conditions, they can be classified in two categories: strain-hardening; strain-softening FRCC (Naaman and Reinhardt 2006), as shown in Fig.2.7. This figure introduces the flexural behavior of the strain hardening materials as a deflection hardening response. According to this figure, the strain softening materials under uniaxial load can be characterized as deflection-hardening or deflection-softening materials.
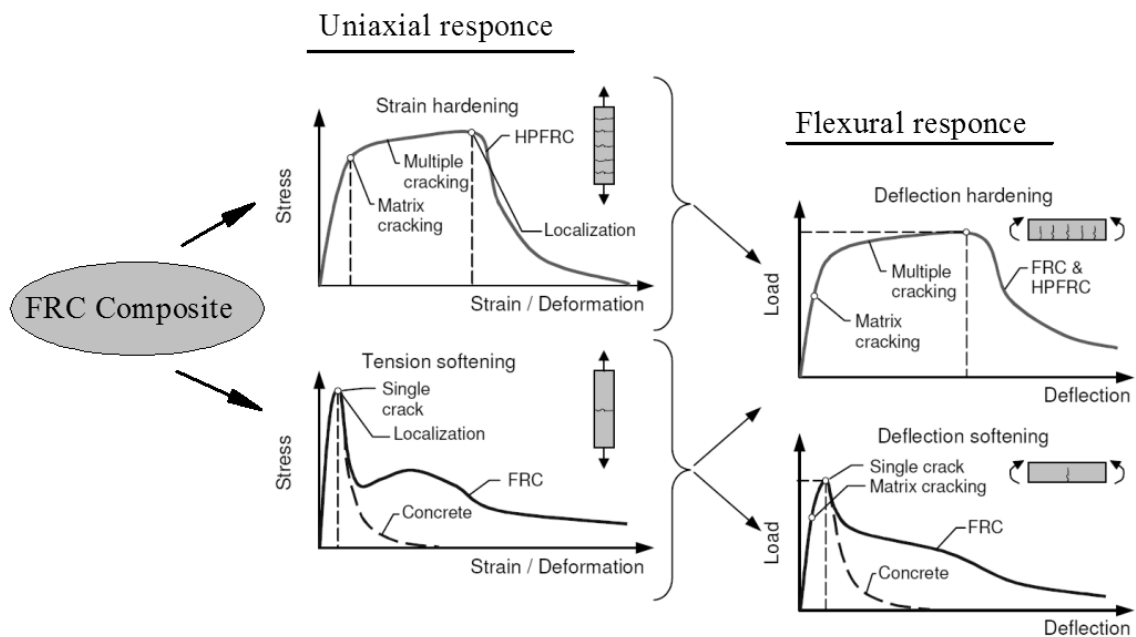
Fig. 2.7- Classification of tensile behavior of cement-based materials (Naaman and Reinhardt 2006).

Due to the difficulties in performing uniaxial tensile tests, bending test on notched beam is the best candidate to be a standard test method for the FRC classification (Prisco et al.

2009). Using force-deflection relationships, which can be obtained by three-point notched beam bending test executed in accordance with EN 14651:2005 recommendations, and using the test setup represented in Fig. 2.8(a), the parameters that define the fracture mode I parameters can be obtained by an inverse analysis (Pereira et al. 2008, Zamanzadeh et a1. 2015, Soltanzadeh et al. 2015).

Fig. 2.8(b) represents a typical relationship between the applied load and the crack mouth opening displacement (CMOD) obtained from a three-point beam-bending test (EN 14651, 2004). Using this type of relationship, the load at the limit of proportionality, F_L, defined as the highest value of the load recorded up to a deflection (or CMOD) of 0.05 mm, can be obtained. According to EN 14651:2005, the residual flexural tensile strength parameters, f_{Rj}, corresponding to four different values of the CMOD (CMOD = 0.5, 1.5, 2.5 and 3.5 mm, respectively) can be determined using the following equation:

$$f_{Rj} = \frac{3F_j . L}{2b . h_{sp}^2} \tag{2.3}$$

where b=150 mm and L=500 mm are the width and the span of the specimen; h_{sp} =125 mm is the distance between the tip of the notch and the top of the cross section.

(a)   (b)
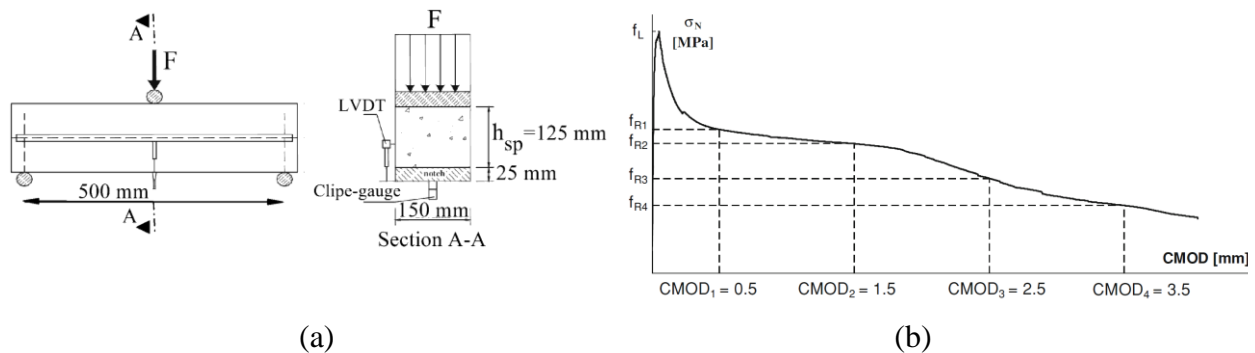
Fig. 2.8- (a) Three point beam bending test setup and (b) typical curve of the nominal stress versus CMOD for FRC (EN 14651, 2005).

The post cracking strength of strain-hardening or strain-softening FRCs can be classified using two residual values, f_{R1k} and f_{R3k}, corresponding to serviceability limit states, SLS, and ultimate limit states, ULS, respectively. In particular two parameters, a number representing the f_{R1k} class (characteristic value of f_{R1}), and a letter representing the f_{R3k}/f_{R1k} ratio (see Fig. 2.9) can be used to classify the FRC toughness. The strength classes for f_{R1k} are defined by one of the values of 1.0, 1.5, 2.0, 2.5, 3.0, 4.0, 5.0, 6.0, 7.0, (MPa) or a higher value. The f_{R3k}/f_{R1k} ratio can be represented with a letter, a, b, c or d, corresponding to the following values:

"a"   if $0.5 \leq f_{R3k}/f_{R1k} < 0.7$

"b"   if $0.7 \leq f_{R3k}/f_{R1k} < 0.9$

"c"   if $0.9 \leq f_{R3k}/f_{R1k} < 1.1$

"d"   if $1.1 \leq f_{R3k}/f_{R1k} < 1.3$

"e"   if $1.3 \leq f_{R3k}/f_{R1k}$

For instance a material with $f_{R1k} = 2.2$ MPa and $f_{R3k} = 1.8$ MPa can be classified as ''2b'' using the proposed classification.
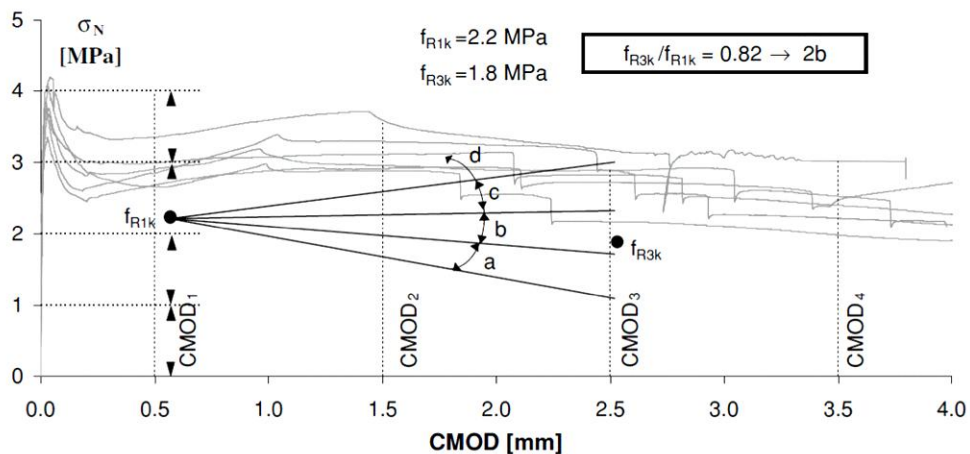
Fig. 2.9- Typical example of FRC classification (EN 14651, 2004).

2.4.2 Behavior of FRC in Compression

When concrete is loaded under uniaxial compression, tensile stresses act perpendicular to the direction of the compressive load. Hence, the failure of concrete in compression is related to failure of concrete in tension (See Fig. 2.10(a)). Although the addition of steel fibers does not provide any improvement in the compressive strength of concrete (in current fiber dosages), fiber reinforcement affects, however, the post-peak behavior of concrete in compression as shown in Fig. 2.10(b) (CEB-FIP Model Code 2010). Compared to the compressive behavior of the plain concrete, the FRC failure mode exhibits a stress - strain response of higher volumetric energy, mainly in the softening phase. This can be attributed to the energy dissipation by fracture mode I, during the opening process of the cracks propagated in the vertical direction (G_{fI}), as well as the combination of fracture modes I and II, during opening (G_{fI}) and sliding (G_{fII}) of the surfaces of the shear failure cracks (see Fig. 2.11).

(a)   (b)
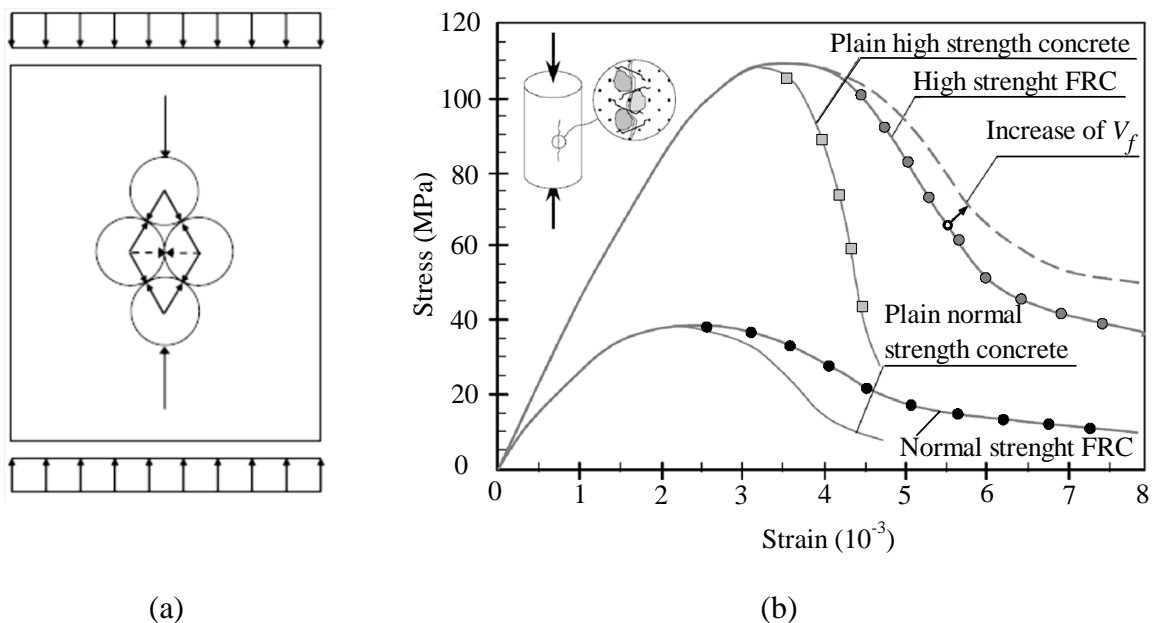
Fig. 2.10-(a) Load bearing mechanism of concrete in compression (Schumacher 2006) and (b) Plain concrete and SFRC in compression (CEB-FIP Model Code 2010).
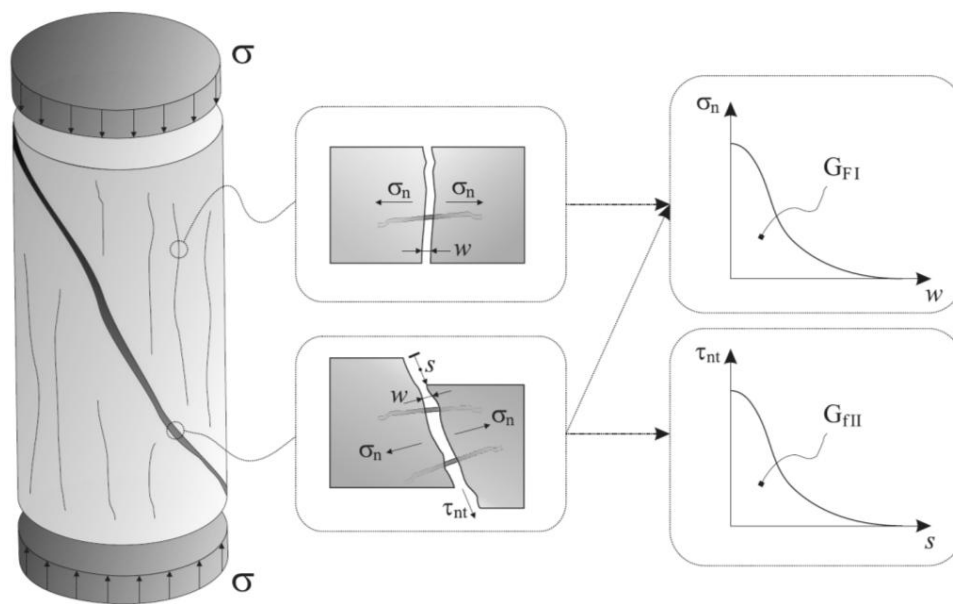
Fig. 2.11- Fiber reinforcement mechanisms of FRC in failure mode (Cunha 2010).

2.4.3 Behavior of FRC in Direct Shear

The advantages associated with the addition of steel fibers to a concrete mix can be investigated under pure shear loading at the material level, where the pure shear loading is defined in literature as a loading condition in which a specimen is subjected to equal and opposite parallel forces with negligible bending (Ayatollahi and aliha 2005). However, there is no unanimous consensus about the existence of a pure shear failure mode in concrete because the crack is assumed to be developed normal to the principal tensile stress direction and causes the damage initiation and propagation of concrete element under the fracture mode I (Arrea and Ingraffea 1982). Nevertheless, in cases where the shear stress zone is narrow enough, for instance, in the case of push-off specimens, the existence of mode II failure is evident (Barragan et al 2006).

In the past few decades, extensive efforts have been directed at modeling material properties of cement based composites loaded in direct shear. For this purpose several types of specimens have been designed and tested as shown in Fig. 2.12. Compared to the specimens with one-sided notch (e.g. specimens S2 to S5 in Fig. 2.12) the symmetrically notched specimens (e.g. specimens S1 and S6), that two cracks could propagate simultaneously along these notches, were found easier to analysis (Bazant and Pfeiffer

1986). The researchers have argued that the number and depth of the notches can be effective on the reduction of the tensile stresses at tip of the notches (Xu, et. al. 2005). A summary of the experimental methods to characterize the direct shear response of concrete and other similar engineering materials is provided by Soltanzadeh and Barros (2011), where the major part of these experimental tests were also simulated numerically.

S1   S2   S3

Petrova and Sadowski   Xu and Reinhardt   Sagaseta and Vollum
        2012   2005   2011

S4   S5   S6

Shah et al. 1995   Zhu and Tang 2002   JSCE-G 5531999
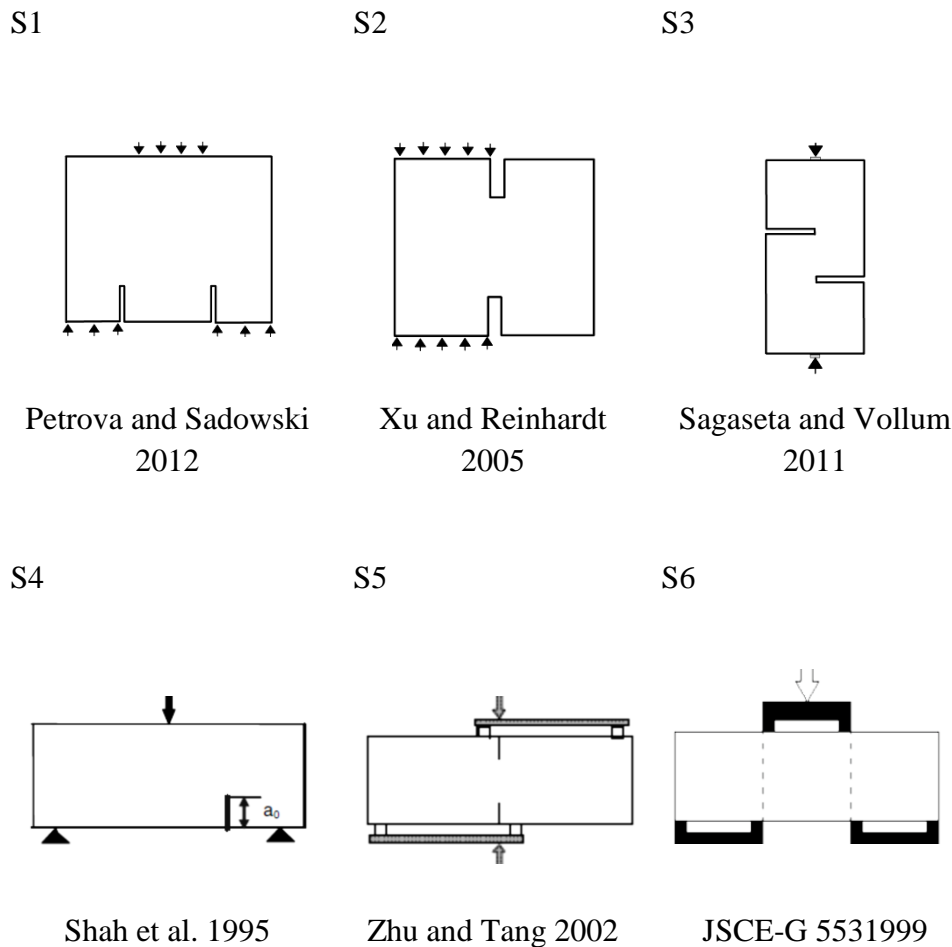
Fig. 2.12- Configuration and test setup of different shear test specimens.

Among the entire shear specimens represented in Fig. 2.12, the push-off specimens, named as "S3", proposed by Valle and Buyukozturk, 1993, and "S6", originally designed by JSCE-G 553-1999, can be introduced as the two most widely used shear specimens to study the shear behavior of concrete. Using this type of specimens to characterize the shear behavior of concrete of different strength classes and reinforced with distinct

dosages of steel fibers showed that the improvement in shear strength for high strength FRC is more pronounced compared to that obtained for the FRC with normal compressive strength. This was mainly attributed to the higher bond strength between fibers and high strength concrete matrix (Barragan et al. 2006, Mirsayah and Banthia, 2003, Higashiyama and Banthia, 2008). By investigating the shear behavior of plain concrete elements, the aggregate interlock and friction at the crack faces are known as the responsible for transferring shear stresses across a crack (Kim et al. 2010) (Fig. 2.13(a)). Although the steel fibers does not influence the cracking strength of concrete, the fibers are activated and start to be pulled out immediately after matrix cracking, increasing significantly the concrete toughness (Barragán 2006) (Fig. 2.13(b)). Due to the pullout resistance and dowel action of fibers, a relatively high residual load carrying capacity is obtained in this type of tests (Soltanzadeh et al. 2015). Similar to the dowel action of reinforcement crossing the shear plane of reinforced concrete, the dowel effect of steel fibers influence the shear friction and shear capacity of FRC. Hence, by increasing the fiber volume fraction, the dowel effect is enhanced(Barragán et al. 2006).
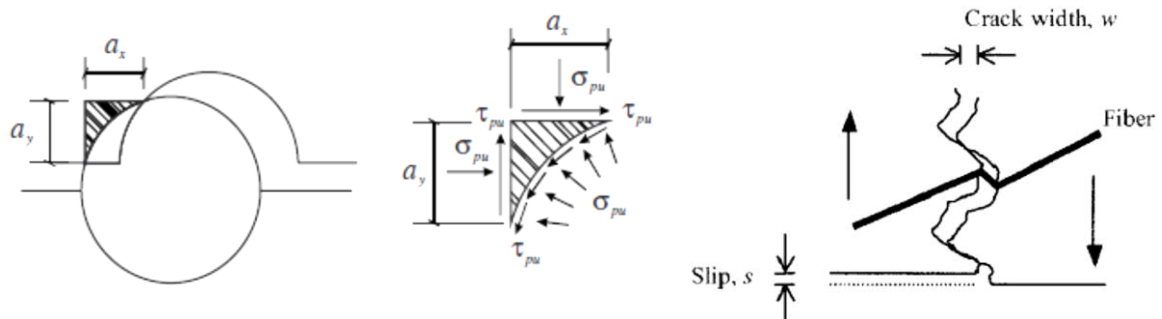
Fig. 2.13- (a) Schematic of (a) aggregate interlock (Walraven and Reinhardt 1981), and (b) fiber interlock (Barragan et al. 2006)

2.5 FAILURE MECHANISM AND SHEAR DOMAIN IN FRC BEAMS

2.5.1 Basic Theory

Fig. 2.14(a) schematically illustrates the internal forces, bending moment "M" and shearing force "V", at any section of a loaded simply supported beam. It also shows the Mohr's circle for stresses at small elements represented by a square in the tension zone (Fig. 2.14(b)). The Mohr circle gives the principal tensile and compressive stresses, f_1

and f_2 respectively, and their orientations before cracking. When f_1 attains the concrete tensile strength, a crack initiates perpendicular to the direction of the principal tensile stress.

(a)   (b)
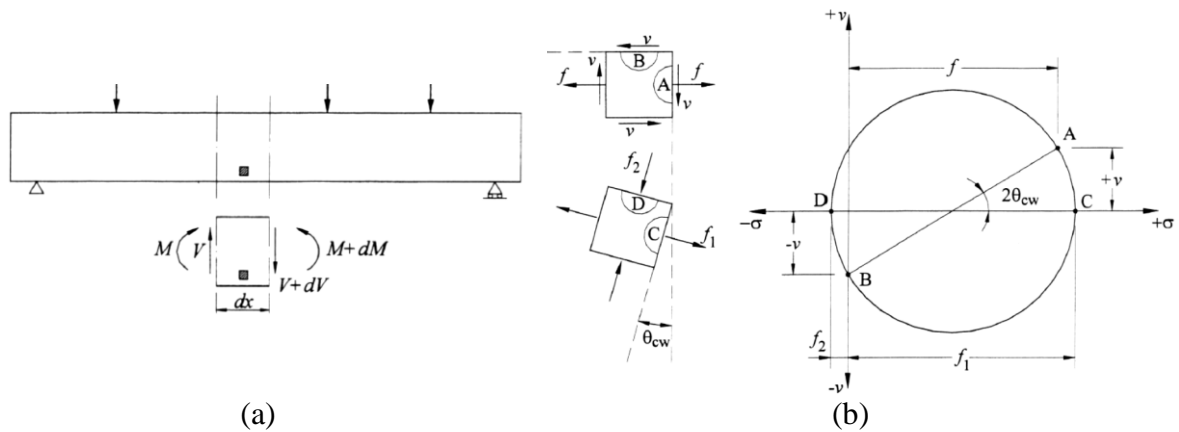
Fig. 2.14- (a) Simple beam and internal forces acting on a portion of its span, and (b) Mohr's circle of stresses.

The isostatic lines in Fig. 2.15 reflect the direction of the principal stresses to visualize the stress trajectories in the beam loaded with two points. There are two types of tensile and compressive stress trajectories, which are orthogonal to each other. Since the strength of concrete is low in tension, cracks are always normal to the tensile trajectories, i.e. the cracks follow the shape of the compressive trajectories.
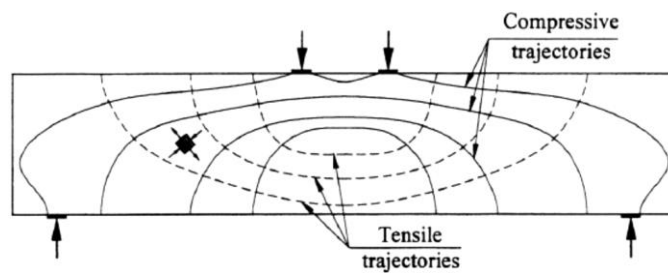
Fig. 2.15- Stress trajectories before cracking in a simply supported beam.

Fig. 2.16 represents a cracked beam and the forces acting on a concrete segment, placed between two shear cracks. From equilibrium of internal forces:

$$T = \frac{M}{jd} \tag{2.4}$$

and

$$V = \frac{dM}{dx} = \frac{d(T. \, jd)}{dx} \tag{2.5}$$

the expression of V can be expanded as:

$$V = \frac{dT}{dx} jd + \frac{d(jd)}{dx} T \tag{2.6}$$

where T is the tensile force in the longitudinal reinforcement; and jd is the flexural internal lever arm.
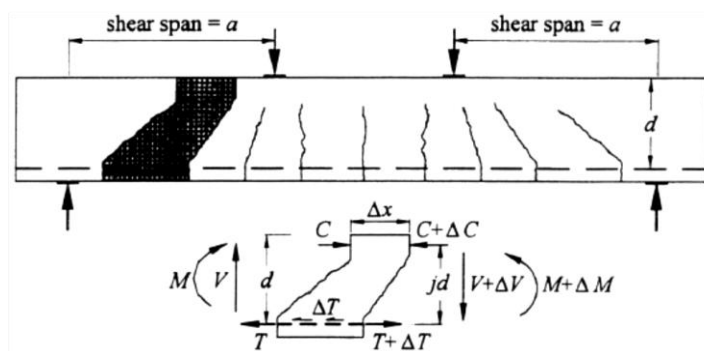
Fig. 2.16- Cracked beam and a portion between two shear cracks.

The first and second terms in Eq. (2.6) represent "beam action" and "arch action" respectively. Depending on the shear span to effective depth ratio (a/d), the mechanism of shear resistance is divided into two categories of beam action for slender beams with $(a/d) > 2.5$ and, the arch action for short-span beams with $(a/d) \leq 2.5$.

2.5.1.1 Beam action

The first term in Eq. (2.6) represents the beam action, which governs the behavior of slender beams. In 1964 Kani assumed that a slender concrete beam cracks in bending like

a concrete comb, with the compressive zone as a backbone and the concrete between flexural cracks as concrete teeth (Fig. 2.17). According to this assumption, the concrete portions between inclined shear cracks act as cantilevers, which are loaded with bond forces developing along the tensile reinforcement. Since these cantilevers support the bond forces in the longitudinal reinforcement, it is assumed that their strength governs the beam action behavior. Failure of the teeth takes place at their bases connected to the compression zone of the beam.

After failure of the concrete teeth, beams with the smaller a/d ratio transform into tied arch mechanisms, resulting further increase in the beam shear strength. In the slender beams, with $(a/d) > 2.5$, the concrete teeth capacity was found to be higher than the tied arch capacity (see Fig. 2.18). Thus, sudden failure occurs after the teeth break away.
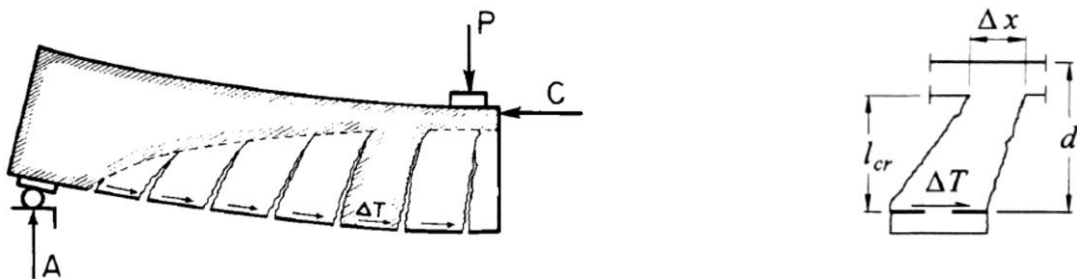
Fig. 2.17- Forces acting on a concrete portion between two shear cracks (Kani 1964).

2.5.1.2 Arch action

The second term in Eq. (2.6) represents the arch action, which governs the behavior of the short-span beams. Kani (1964) studied the capacity of the arching mechanism, and showed that the transformation from beam to arch action takes place after failure of the concrete teeth forming between the inclined shear cracks. He also showed that in beams with short shear spans the high reserve shear strength exists beyond the cracking strength due to the remaining arch capacity.

The short-span beams behave as an arch with a tie as shown in Fig. 2.18(a). The compression forces goes to the supports through inclined concrete struts, while the

longitudinal bars transmit the tensile force to the supports. The compressive force in a concrete strut changes its position along the shear span of beam from the zone beneath the loading point to the supports (see Fig. 2.18(b)). This change in the compressive force position along the shear span is expressed by the change of the internal lever arm in Eq. (2.6), ($d(dj)/dx$).
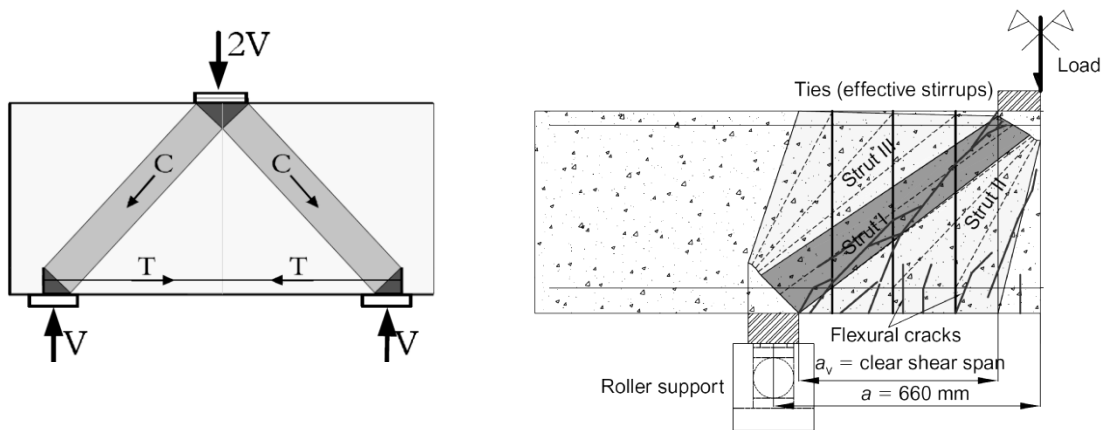
Fig. 2.18- (a) Simple strut and tie-system and (b) Typical crack pattern and load paths observed in a short span beam with $1 < (a/d) < 2$ (Sagaseta and Vollum 2010)

2.5.1.3 Effect of steel fibers on shear domain of beams without stirrups

In 1997 Imam et al. studied the mechanism of shear resistance of high strength steel fiber reinforced concert beams without stirrups. They investigated the influence of steel fiber reinforcement on relative flexural capacity (i.e. the dimensionless ratio of ultimate moment to nominal flexural moment corresponding to yield initiation of the steel reinforcements, M_u / M_{fl}) and shear resistance of these elements. An analytical model was then developed for predicting the failure mode of a FRC beam.

According to the formula proposed by these researchers, the nominal flexural moment, M_{fl}, of high strength fiber reinforced concrete beams without stirrups can be calculated as:

$$M_{fl} = \frac{1}{2}\rho_s f_{sy}bd^2(2-\Gamma) + 0.83F_f bd^2(0.75-\Gamma)(2.15+\Gamma)$$ (2.7)

where the parameter "Γ" is obtained from:

$$\Gamma = \frac{\rho_s f_{sy} + 2.32F_f}{0.85f_{cm} + 3.08F_f}$$ (2.8)

in which $F_f = (l_f/d_f)V_f.\eta_f$ is the fiber factor, $\rho_s = A_s/b.d$ is the steel flexural reinforcement ratio, l_f and d_f are, respectively, the length and diameter of the steel fibers, V_f is fiber volume fraction, η_f is the bond efficiency factor, which is assumed to be unity for the hooked ends steel fibers. In case of using deformed fibers and smooth fibers, the bond efficiency factor, η_f, is equal to 0.9 and 0.5, respectively (Imam et al. 1997). In Eq. (2.7) b and d are, respectively, the width and the effective depth of beams, f_{cm} is the concrete compressive strength, f_{sy} is the yield strength and A_s is the cross sectional area of the tension steel reinforcement.

To predict the maximum shear resistance of the beam, V_u, Imam et al. (1997) have proposed the following formula:

$$v_u = 0.6\psi\sqrt[3]{\omega}\left[f_{cm}^{0.44} + 275\sqrt{\omega/(a/d_s)^5}\right]$$ (2.9)

where ψ is size effect factor that can be calculated from the following equation:

$$\psi = \frac{1+\sqrt{5.08/d_a}}{\sqrt{1+d/(25d_a)}}$$ (2.10)

where d_a is the maximum aggregate size, and

$$\omega = \rho_s(1+4F_f)$$ (2.11)

is a reinforcement factor where the steel reinforcement ratio, ρ_s, is obtained from the following equation:

$$\rho_s = \frac{A_s}{bd_s} \tag{2.12}$$

Hence, the ultimate resisting moment at failure, M_u, which is equated to the external moment ($M_u = V_u.a$, where V_u is the maximum shear resistance of the beam) can be predicted for FRC beams using the following equation:

$$M_u = 0.6bd_{s,}^2\psi\sqrt[3]{\omega}\left[f_{cm}^{0.44}(a/d_s) + 275\sqrt{\omega/(a/d_s)^3}\right] \tag{2.13}$$
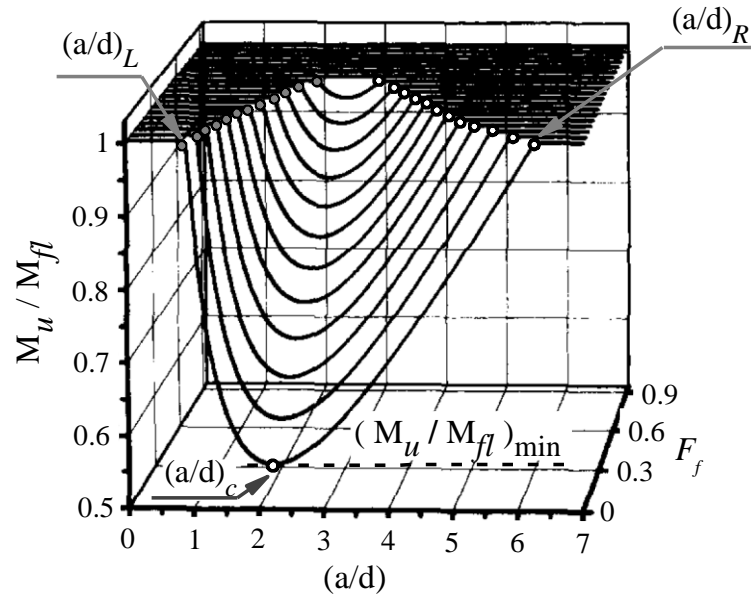
Fig. 2.19- (a) Combined effect of a/d and F_f on the relative flexural capacity (calculated for beams with f_{cm} =110MPa, f_{sy} =550MPa, ρ_s =0.0187MPa, d =300MPa, d_a =14MPa) (Imam et al. 1997).

By using these analytical formulas Imam et al. (1997) determined the domain of shear influence with respect to the fiber effect (F_f) as shown in Fig. 2.19. By means of defining such shear influence domain, it became possible to predict if a FRC beam without stirrups failed in shear. Accordingly, the relationship between M_u / M_{fl} and a/d exhibited three different important values: two limiting values, $(a/d)_L$ and $(a/d)_R$, defining an interval of a/d where the shear effect pronounced, where $M_u \cong M_{fl}$, and a third value of $(a/d)_c$ at

which the relative moment has its minimum value, $(M_u / M_{fl})_{\min}$. Henceforth, the latter value of a/d is called the critical shear span-to-depth ratio $(a/d)_c$. For beams with a/d in the interval $(a/d)_c < a/d < (a/d)_R$, the shear failure is governed by the beam action, whereas, in the interval $(a/d)_L < a/d < (a/d)_c$ the arch action is dominant.

Fig. 2.19 illustrates the influence of the combined effect of fiber factor, F_f, and a/d on the relative flexural capacity of a beam M_u / M_{fl} (the variation of F_f is only caused by the V_f). This figure shows the significant increase of M_u with the fiber factor (caused by the increase of V_f) compared to that of M_{fl}, leading to the increase of the beam's relative flexural capacity, M_u / M_{fl}. This evidences the pronounceable effect of fibers on enhancing the shear capacity of the beam, which may successfully reduce the requirement of conventional shear reinforcements for the type of beams developed in the scope of the present work.

2.5.2   Shear Transfer Components

In the 1960 and 70s the tooth model proposed by Kani was one of a few models that attempted to give a physical explanation for the interpretation of shear failure. As already mentioned in Sec. 2.5.1.1, this method was based on the assumption that the shear failure develops by breaking off a cantilever concrete tooth due to the action of bending in a beam. Kani (1964) assumed that the bending moment imposed by the force in-balance, ΔT, (see Fig. 2.17) is solely resisted by the concrete at the base of the tooth. However, some other researchers (Fenwick and Pauley 1968 and Taylor 1974) improved this hypothesis by demonstrating the existence and important influence of other mechanisms providing additional resistance. The effect of these components is briefly discussed in Sec. 2.5.2.1 to 2.5.2.5.

According to ASCE-ACI-Committee-426 (1973) shear transfer mechanisms in concrete beams are complex and difficult to clearly identify. Complex stress redistributions, affected by many factors, occur after cracking. Fig. 2.20(a) shows that the shear transfers across a concrete beam reinforced with conventional shear reinforcements is mainly assured by 4 components, namely: uncracked compression zone, V_{cc}; aggregate interlock,

V_a; dowel action of the tensile reinforcement, V_d; and tensile strength developed in the shear reinforcement, V_s. The relative contribution made by each of these components to resist the shear stress in concrete beams with stirrups is schematically represented in Fig. 2.21 (ASCE-ACI-Committee-426, 1973). This figure shows that the contribution of stirrups bridging across a crack remains constant during loading the beams. The shear stress is further resisted by the uncracked concrete compression zone and the dowel action as well as the aggregate interlock. By loading the beam the contribution of the uncracked compression zone and the dowel action increases at accelerating rate in order to resist higher shear stresses by decreasing the contribution of aggregate interlock due to widening of the cracks.

In FRC beams without conventional shear reinforcements, however, application of steel fibers increase shear resistance, V_f, by providing post-cracking diagonal tension resistance across the crack surfaces, in addition to the other three components for transferring the shear stress, V_a, V_{cc} and V_d, as shown in Fig. 2.20(b) (Kwak et al. 2002). The crack-bridging of the steel fibers reduces the width and spacing of shear cracks and, thus improve the ultimate shear capacity of the structural elements, increases deformation capacity, and can convert a brittle failure mode in a ductile one, even in FRC members without stirrups (Meda et al. 2012, Barros et al 2013, Cucchiara et al. 2004). The contribution of each component in transferring the shear stress is discussed in the following sections.
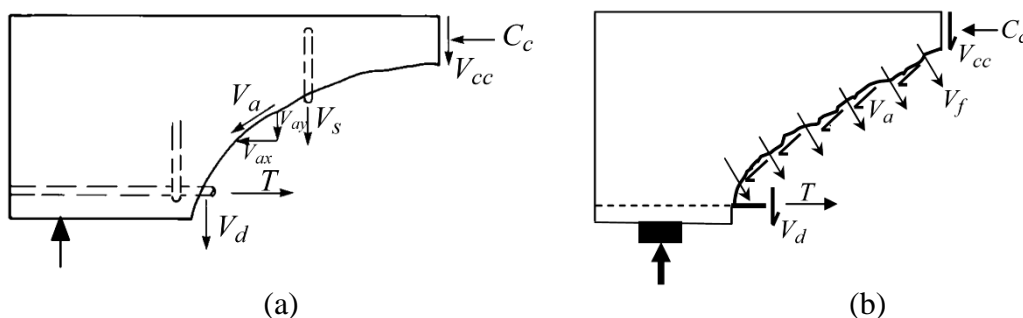
Fig. 2.20- Shear transfer components (a) in a reinforced concrete beam with stirrups and (b) in a FRC beam without stirrups.
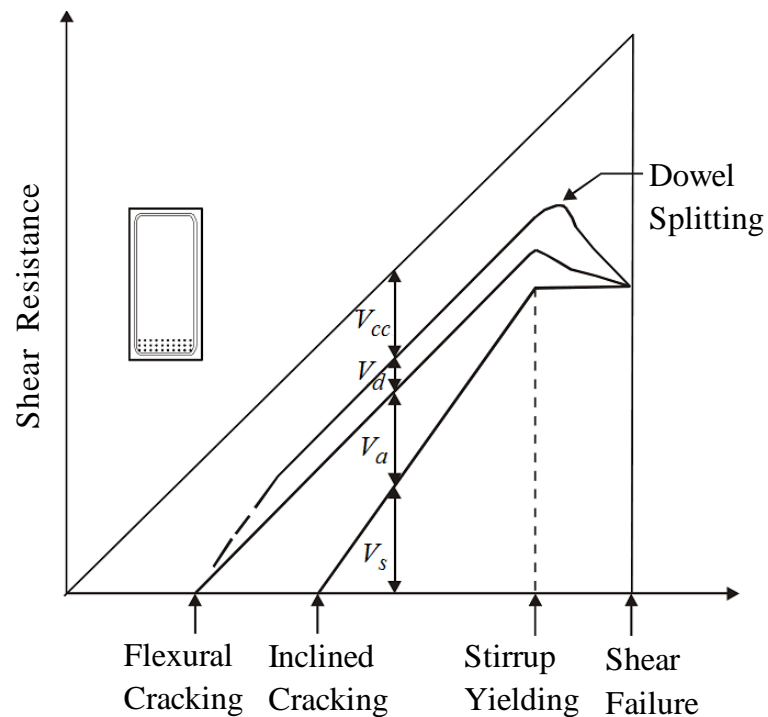
Fig. 2.21- Distribution of internal shear resistance in beams with stirrups (ASCE-ACI-Committee-426, 1973).

2.5.2.1 Shear force transferred by uncracked concrete zone

Before crack initiation, the shear stress is resisted by the inclined principal compressive and tensile stresses, referring to the stress trajectories (see Fig. 2-15). Since these trajectories exist only in the uncracked compression zone of the beam, the shear resistance decreases extensively by initiating and propagation of the cracks (ASCE-ACI-Committee-426, 1973).

2.5.2.2 Shear force transferred by aggregate interlock

The aggregate interlock component is related to the shear friction mechanisms, which provides resistance against slip, and transfers shear across the inclined cracks. In normal-strength concrete beams, the crushing strength of the aggregates is relatively higher than the concrete compressive strength. Thus, the shear cracks grow at the interface between

aggregates and paste, providing the rough crack plane which improves the interface shear transfer compared to a relatively smooth crack plane developed by shear crakes in high strength concrete (Dinh 2009, Dinh et al. 2010). The contribution of aggregate interlock to increase the shear strength is the function of several parameters, including crack width, amount of shear reinforcement as well as size and amount of aggregates in the composite. Accordingly, the aggregate contribution decreases as the amount of shear reinforcement and the size and amount of aggregates decreases and by increasing the crack width. In general, the contribution of aggregate interlock decreases near the ultimate shear load due to the excessive widening of the shear cracks.

2.5.2.3 Shear force transferred by shear reinforcement

Prior to shear cracking, strain in the shear reinforcement is equal to that of the adjacent concrete, but by formation of major inclined cracks in members with shear reinforcement, a large part of the shear stress is carried by the stirrups. The joint ASCE-ACI committee 426 in 1973 demonstrated the beneficial effect of shear reinforcement on improving both the dowel action and the aggregate interlock contributions to the shear strength, since the stirrups, respectively, prevents longitudinal splitting along the tensile bars and eliminates diagonal crack propagation. However, these criteria exist at some intermediate phase of loading while they diminish after yielding of the shear reinforcement.

2.5.2.4 Shear force transferred by dowel action

The occurrence of relative vertical displacement between the two crack faces activates the dowel action of the longitudinal bars, which provides a resisting shear force. The contribution of dowel action in shear resistance of a beam is highly influenced by the thickness of the concert cover beneath the longitudinal bars, as well as the presence of shear reinforcements, i.e. steel fiber or stirrups, to restrain the vertical displacements of the bars.

For members without any type of shear reinforcement, the dowel action is not significant, i.e. it is not higher than 25 % of the ultimate shear capacity (Fenwick and Paulay 1968 and Taylor 1974), sine the dowel action is then limited by tensile strength of the concrete

(He and Kwan 2001). Application of steel fibers improves the tensile strength of concrete in the splitting plane along the reinforcing bars, and causes the increase in the dowel resistance of longitudinal reinforcement (Cuenca and Serna 2013a).

2.5.2.5 Shear force transferred by steel fibers

Application of steel fibers as a reinforcement of cement based materials, diminishes the brittle character of these materials. The contribution of steel fibers to resist and bridging the cracks causes to reduce the crack spacing and increasing the number of cracks. Bridging the shear cracks also offers the resistance to crack opening, which causes to increase the effect of aggregate interlock and higher energy dissipation by sliding the faces of the crack. Hence, bridging the steel fiber is one of a significant source of toughness.

Since fibers can bridge the crack surfaces for relatively large opening widths, the fiber bridging zone, when compared with the aggregate interlock zone, is considerably larger. Consequently, the post-cracking behavior of FRC is mainly governed by the fiber reinforcement mechanisms, while the aggregate interlock has a relatively smaller influence.

2.6 Parameters Influencing Shear Strength of Members without Transversal Reinforcements

By considering the aforementioned mechanisms, fully or partly responsible for the transfer of shear forces prior to failure, a wide range of parameters influencing the shear strength of concrete beams can be listed. In this section is discussed the influence of the most dominant parameters on shear strength of members without transversal reinforcements, namely:

- Concrete strength, f_{cm}
- Dosage of applied steel fibers, v_f
- Longitudinal reinforcement ratio, ρ
- Level of axial force on members, σ_t

- Size effect
- Shear span to effective depth ratio, (a/d)

2.6.1 Concrete compressive strength, f_{cm}

In reinforced concrete members without steel fibers increasing the compressive strength of concrete from 25 MPa to 60 MPa results in much more brittle shear failure (Minelli et al. 2014). This can be attributed to the development of a smoother shear crack surfaces in high strength concrete members, which reduces the effectiveness of the interface shear transfer mechanism. However, increasing the compressive strength in case of FRC members with or without stirrups enhances the shear resistance of these members, since increasing the compressive strength leads to improve the bond between the steel fibers and concrete (Kwak et al. 2002). The improvement in shear resistance of the FRC members by increasing the compressive strength is more significant in the case of the elements with higher volume fraction of steel fibers. However, increasing the compressive strength above 65 MPa for the members with the same fiber volume fraction resulted in a steady rate of increase in ultimate shear strength of the members (Narayanan and Darwish 1987).

2.6.2 Dosage of applied steel fibers, V_f

Several researchers (Greenough and Nehdi 2008, Kwak et al. 2002) studied the influence of various dosage of steel fibers on cracking behavior of concrete beams, and argued that while RC members without stirrups exhibited a single diagonal crack followed by a brittle shear failure, application of v_f =0.5% ~ 1.5% steel fibers provided the development of multiple inclined cracks followed by widening of at least one dominant crack before shear failure. They reported about 38% decrease in crack spacing when v_f =0.5% ~ 0.75% steel fibers were added to RC members without stirrups (Kwak et al. 2002).
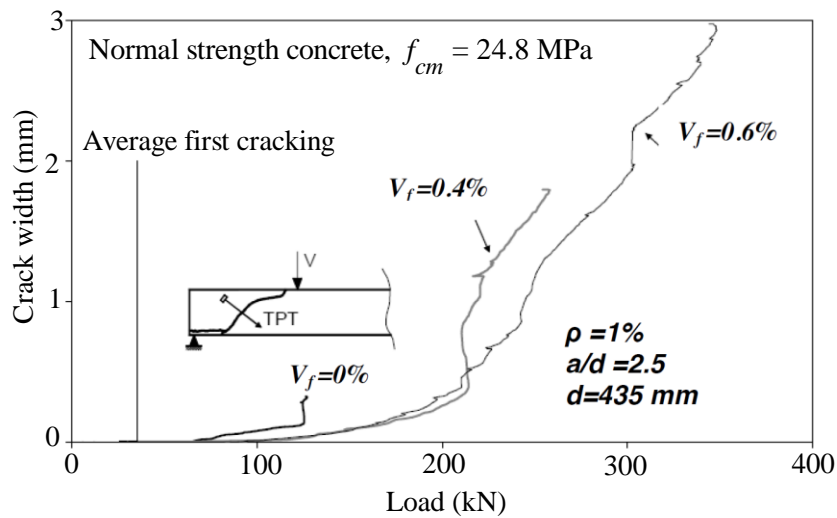
Fig. 2.22- Load *vs.* crack width relationship of FRC beams with different dosages of steel fibers (Minelli and Plizzari 2006).

Effect of fiber dosage on shear behavior of beams is more clear in Fig. 2.22, which compares the diagonal crack width *vs.* load relationship of the specimens with three different dosages of steel fibers, v_f = 0%, 0.4% and 0.6% (Minelli and Plizzari 2006). The figure shows that while the maximum crack width for the RC specimen (v_f =0%) was only about 0.3 mm, the SFRC specimens with v_f =0.4% and v_f =0.6% had maximum crack widths of respectively 2 mm and 3 mm prior to failure. This difference in maximum crack widths was attributed to the bridging action of fibers across the adjacent crack surfaces in SFRC beams, which provides a higher ductility for the members.

2.6.3   Longitudinal reinforcement ratio, ρ

By increasing the longitudinal reinforcement ratio, ρ, the effect of dowel action on increasing the shear resistance of reinforced concrete beams increases. Thus the crack width decreases and the aggregate interlock increases by the higher dowel effect of reinforcements (Ashour 2000). However, studies on the shear strength of FRC members with ρ = 1.1%, 2.2% and 3.3% demonstrated that the rate of this increase in shear strength of RC elements is relatively low for the elements with $\rho \geq 2.2\%$ (Li et al. 1993).

2.6.4 Level of prestress of members, σ_t

Application of axial compression force increases the depth of uncracked compression zone, decreases the width of shear cracks and, consequently, increases the interface shear transfer (or aggregate interlock). Hence, the presence of an axial force, which can be caused by a prestressing effect, enhances the shear capacity of RC members. However, for prestressed RC members without shear reinforcement, e.g. steel fibers or stirrups, brittle failures are common. On the contrary, by prestressing FRC beams the crack opening is delayed and, consequently, caused the fibers to be later activated, which provides a high ductility for the beams at failure moment (Soltanzadeh et al. 2014).

2.6.5 Size effect

Several researchers have compared the shear strength of geometrically similar specimens of different size, and demonstrated that there is a significant size effect on shear strength of the members without transversal reinforcement. Accordingly, the shear strength of these members appears to decrease as the effective depth, d, increases (e.g. Kani 1967, Shioya et al. 1990, Lubell et al. 2004). Fig. 2.23 represents a well-known example of the experiments on size effect of a series of RC beams, carried out by Shioya et al. (1990). According to their studies the shear stress of the largest beam at failure was only about one-third of that of smallest member, due to the propagation of wider diagonal cracks in the largest beam. By increasing the depth of the beam, the crack widths above the longitudinal reinforcement tend to increase and, consequently, the aggregate interlock across the crack decreases resulting in the reduction of shear strength.

Available studies demonstrate the influence of the effective depth on the shear strength of FRC elements. According to the research carried out by Rosenbusch and Teutsch (2002), by increasing the effective depth of the FRC beams from 260 mm to 540 mm ($1.5 \leq a/d \leq 4$), while the other parameters are kept almost the same, resulted in a decrease of 26% in the average shear strength. The size effect was not found significant in the case of FRC beams with $d \leq 300\,\text{mm}$ (Kwak et al. 2002).
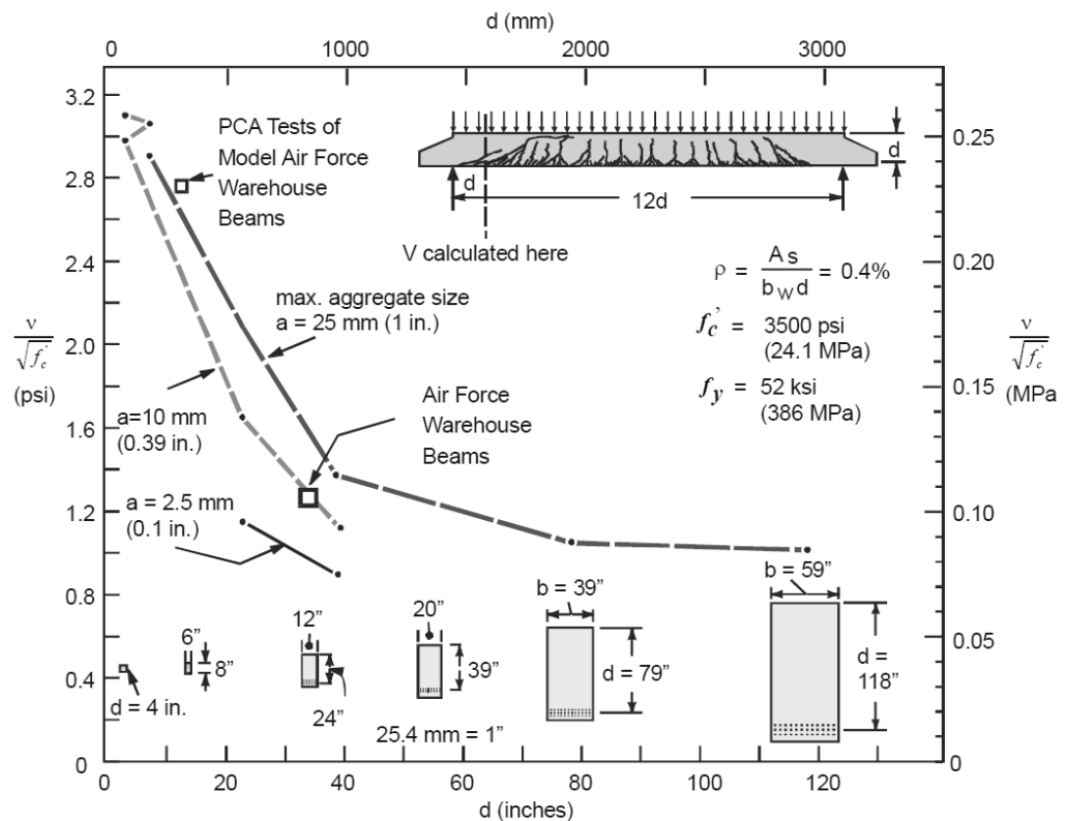
Fig. 2.23- Size effect in shear (Shioya et al. 1990).

2.6.6 Shear span to effective depth ratio, (a/d)

The influence of shear span to effective depth ratio, a/d, on shear strength of FRC members without stirrups was investigated by several researchers (e.g., Mansur et al. 1986; Ashour et al. 1992, Kwak et al. 2002). A summary of the obtained results is illustrated graphically in Fig. 2.24. According to these researches as a/d decreases the shear strength increases. The increase of shear strength in member with $a/d < 2.5$ is more significant, since a pronounceable part of shear force is transmitted directly to the support by an inclined strut (see Sec. 2.5.1.2). The key characteristic of a/d is obvious for a simple supported beam subjected to a three point bending test. Considering the term related to maximum moment and maximum shear force, $M_{max} = V_{max}a = (P/2).a$, it is clear that the beam is capable of carrying higher load, P, when the beam has a shorter shear span, a, and, consequently a lower (a/d) ratio, sin M_{max} is constant.
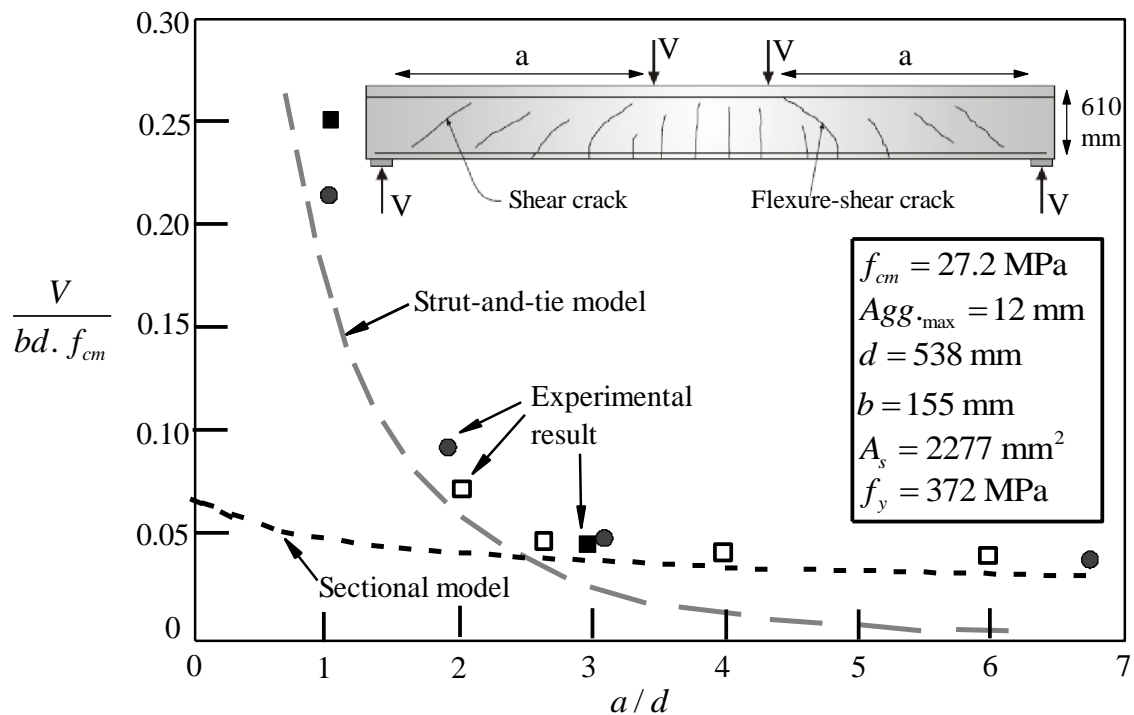
Fig. 2.24- Arch and beam action as a function of a/d ratio (Collins and Mitchell 1991).

2.7 SHEAR BEHAVIOR OF FRC ELEMENTS REINFORCED WITH FRP REBARS

Besides the application of steel fibers for suppressing partially or even completely the steel stirrups, the durability of concrete structures can be also improved by increasing the concrete quality, the cover thickness of steel reinforcements, or using non-corrodible longitudinal reinforcements, such is the case of fiber reinforced polymer (FRP) rebars. These reinforcements can be a promising alternative to steel reinforcement in concrete structures, especially in aggressive environments. However, the flexural failure mode of FRP reinforced concrete beams is brittle rather than ductile (Qu et al. 2009). Thus, FRP rebars were combined with the steel ones in order to develop a practical and effective design solution for the RC elements (Aiello and Ombres 2002). In this system of reinforcements, yielding of the steel bars provides the required ductility for the structures, while the relatively high strength of FRPs increases its ultimate capacity (Leung and Balendran 2003).

2.8 SHEAR FAILURE OF BEAMS WITHOUT STIRRUPS

Fig. 2.25 represents the variation of flexural capacity, M_u / M_{fl}, of beams without stirrups, by increasing shear span to effective depth ratio a/d. In this figure, the full flexural capacity ($M_u / M_{fl} = 1$) of beams, is shown by a horizontal line, where the beams fail in bending. The shaded area under this line represents the shear failure of the beam before reaching to the full flexural capacity. From this figure, rectangular beams can be classified in to four types, depending on a/d ratio, namely: deep ($a/d \leq 1$), short ($1 < a/d < 2.5$), slender ($2.5 < a/d < 6$) and very slender beams ($a/d \geq 6$). Consequently, four different failure modes can be introduced for the four types of beams (ASCE-ACI committee 426, 1973) as follow:

i. Very slender beams ($a/d \geq 6$): the flexural failure is the governing mode of failure, even before the formation of inclined cracks.

ii. Slender beams ($2.5 < a/d < 6$): After formation of flexural cracks, some of them degenerate in flexural-shear cracks. These diagonal cracks propagate towards the top and bottom of the beam, leading to the yielding of the steel longitudinal reinforcements, and finally to the failure of the beam. The RC beams may split in two pieces at failure. This mode of failure is called as diagonal tension failure (see Fig. 2.26a).

iii. Short-span beams ($1 < a/d < 2.5$): Shear-tension "ST" or shear-compression "SC" failure may occur in the case of the beams with $1 < a/d < 2.5$. In the shear-tension failure, several small inclined cracks form along the tension reinforcements leading to the splitting between the concrete and longitudinal bars. This mode of failure is schematically presented in Fig. 26(b). The other mode of failure, SC, may happen by the formation of diagonal shear cracks that progress towards the top of the beam leading to the concrete crushing in the compression zone (ASCE-ACI committee 426, 1973), as shown in Fig. 2.26(c).

iv. Deep beams ($a/d \leq 1$): since in this type of beams most of the shear force is transferred by arch action, according to the structural configuration represented in Fig. 2.26(d), the inclined cracks propagate along the line between load and support. Accordingly, there is the possibility of occurring several modes of failure

as follow:

1. Anchorage failure of tension steel, which may occur at the end of tension tie;

2. Bearing failure, which may occur by crushing of concrete above the support:

3. Flexural failure, may govern the failure mode by yielding of tension steel or crushing of compression zone;

4. Tension failure of the "arch-rib" may occur near to the top of an edge by means of eccentricity of the thrust of the compressive stresses in the inclined strut, and

5. Compression strut failure, which is possible to occur by crushing of the web along the line of the crack.
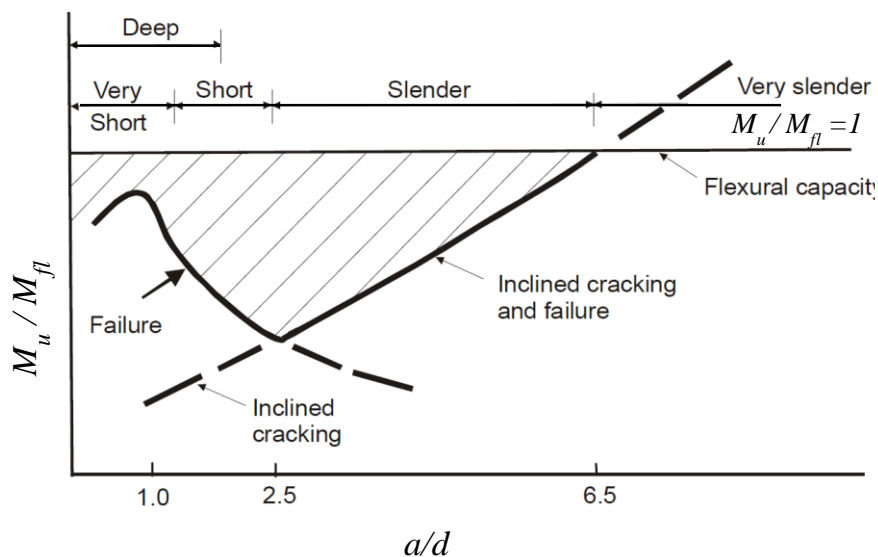
Fig. 2.25- Relative flexural capacity of beams *vs.* $a/d_{s,eq}$ (Kim and Park 1996).
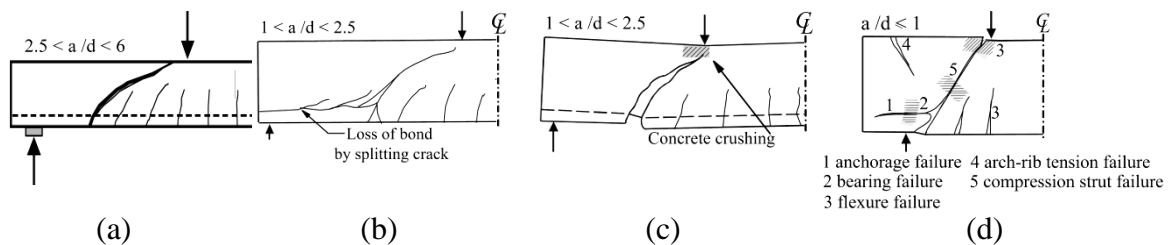
Fig. 2.26- (a) Diagonal tension failure mode in slender beams, (b) Shear-tension and (c) shear compression failure modes in short-span beams, and (d) shear failure mode in deep beams subjected to four point bending test (ASCE-ACI 426, 1973).

2.9 CONCLUSIONS

This chapter presents an overview on the material characteristic and structural behavior of RC elements developed by using steel fibers as shear reinforcement. Regarding the historical evolution toward the investigation done in the field of FRC, it can be concluded that using steel fibers gives the opportunity to improve the corrosion resistance of RC structures since fibers can replace totally or partially steel stirrups that are the reinforcement elements more susceptible to corrosion. Consequently, using fibers as the shear reinforcement, prefabricated elements of higher durability can be developed. Since the level of improvement of the concrete behavior by using fibers is sensitive to fiber dispersion and orientation, it is necessary to develop a fiber reinforced concrete that meets the requirements of SCC to be capable of providing an appropriate fiber dispersion and orientation along the casting-flow direction. Application of steel fibers with an isotropic distribution and suitable orientation to cement based materials makes them more homogeneous and, consequently transforms these materials from a brittle one to the material with high ductility. Since the fibers are closely spaced through the matrix, they are found to be more effective than the conventional shear reinforcements for bridging the cracks. The pronounceable effect of steel fibers on enhancing the shear capacity of concrete beam may successfully reduce the requirement of conventional shear reinforcements for developing these members. Application of FRP longitudinal bars or a hybrid of FRPs and steel longitudinal reinforcements (by considering a relatively thick concrete cover for steel reinforcements) can be adopted as an additional solution for increasing the service life of concrete structures, beside the enhancement of load carrying capacity of the members. Prestressing the reinforcements also can be helpful to increase the shear resistance of such elements without stirrups.

C H A P T E R 3

HPFRC FOR THE SHEAR REINFORCEMENT: DEVELOPMENT AND CHARACTERIZATION

3.1 INTRODUCTION

In late twentieth century, self-compacting concrete (SCC) capable of flowing along the framework, passing through reinforcements and filling voids and corners under its self-weight has been developed with the objective of simplifying the casting operation of large concrete elements with complex geometries and/or a high percentage of reinforcements. This technology was first developed in 1988 using a simple mixture proportioning system, and exhibited further advantages in the improvement of the precast industry, allowing to produce thinner and lighter elements in less time and costs (Okamura 1999). Since then, various investigations have been carried out to obtain a rational mix design method for tailoring SCC with better rheological and mechanical performance. Additionally, a wide range of admixtures and fillers were used with SCC, including fine particles and reducing the free water content, which has contributed to tailor the cohesion and viscosity requisites, thus improving the stability of SCC (Felekoğlu et al. 2007). By using fine fillers, such as silica fume and fly ash, the voids between cement particles are filled, resulted in a very dense and compact cement matrix. The use of superplasticizers was another alternative for providing the required flowability and self-compacting ability of the mix with relatively low water contents (Pereira et al. 2008). By combining SCC

with discrete steel fibers, the SCC post-cracking tensile strength and energy absorption capacity was increased (Jansson 2008). However, there still remain some questions about the most appropriate methodology for tailoring an optimum SCC composition when a relatively high content of fibers is used for the reinforcement of this material in order to achieve a fiber reinforced concrete with high post-cracking residual strength and flowability, herein designated as high-performance fiber-reinforced concrete, HPFRC. In the present chapter, a mix design method is proposed to develop HPFRC by means of defining the proportions of constituent materials of the binder paste, as well as a granular skeleton in an optimum manner. This concrete composition is developed in order to have aimed properties in its fresh and hardened stages, namely a suitable flowability to be poured without vibration, and attain a relatively high compressive strength at early age, in line with precast prestressed concrete element production demands. In this chapter the material properties of the developed concrete are also assessed, and the concrete structural behavior is characterized under compressive, flexural and splitting tensile loading. This study better clarifies the significant contribution of fibers for improving the mechanical properties of concrete elements.

3.2 MIX DESIGN METHOD

The methodology developed and proposed in this chapter to formulate a HPFRC mix design is based on the following three phases:

i. definition of the proportion of constituent materials for developing an optimized paste;

ii. determination of the optimum volume percentage of each type of aggregates in the granular skeleton the concrete; and

iii. assessment of an optimum correlation between the paste and the solid skeleton in order to obtain HPFRC that meets the requirements of SCC (e.g. flowability and viscosity, passing ability and filling ability, as well as blockage and segregation resistance), together with the satisfied mechanical performance in the harden stage in accordance with the structural exigencies.

The applied materials for tailoring the mix were cement, CEM I 42.5R, fly ash class F, limestone filler, superplasticizer, water, three types of aggregates (containing fine and coarse river sand, and crushed granite) and hooked end steel fibers.

In the following sections, the procedure for obtaining the optimum dosage of each material is described in detail.

3.2.1   Optimum Binder Paste Composition

In the first phase of the study, the optimum dosage of superplasticizer, fly ash, limestone filler and cement, as well as the water-to-binder ratio (w/b), were obtained executing the Marsh cone and the mini-slump tests. The optimum volume of superplasticizer to cement ratio is evaluated by measuring the flow time of several samples of pastes made of variable dosages of superplasticizer and constant volume of cement through the 8 mm obstacle of the Marsh cone, illustrated in Fig. 3.1(a). This test is also applied to determine to optimum water-to-binder ratio. The test procedure is further detailed in ASTM C939-02. The optimum volume of fillers to cement ratio is also obtained by performing the min-slump test. The total spread diameter and the time to reach the spread diameter of 115 mm are measured for paste containing distinct volumes of filler using the mini-slump apparatus, represented in Fig. 3.1(b). Method of testing the samples using the mini-slump is detailed in Pereira 2006.
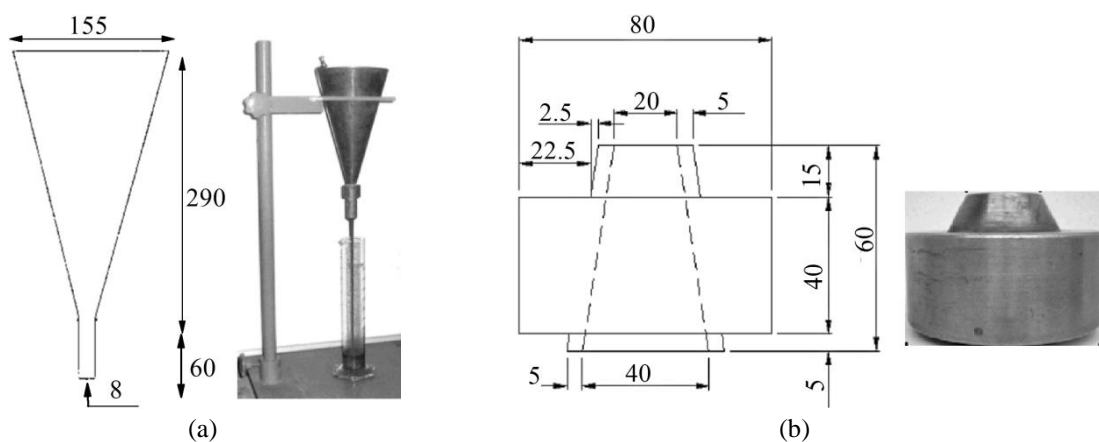
Fig. 3.1- Apparatus used to determine the optimum binder paste composition: (a) Marsh cone and (b) mini-slump (all dimensions are in mm).

Table 3.1- Physical properties of cement, fly ash and limestone filler.

Parameter	Value	Unit
CEM I 42.5R (ASTM C150/C150M-12 and BS EN 197-1)		
Specific gravity	3150	kg/m^3
Blaine fineness	387.3	m^2/kg
Setting time (initial)	116	min
Setting time (final)	147	Min
Fly Ash class F (ASTM C 618-12 and BS EN 450-1)		
Specific gravity	2360	kg/m^3
Blaine fineness	387.9	m^2/kg
Particles < 75 µm	81.15-94.40	%
Particles < 45 µm	68.45-85.90	%
Limestone Filler (ASTM C150/C150M-12 and BS EN 197-1)		
specific gravity	2700	kg/m^3
particles < 80 µm	92.0	%
particles < 2 µm	15.0	%
mean particle size	5.0	µm

Since the physical properties of cement, fly ash and limestone filler influence the
rheological behavior of fresh concrete, first of all, the properties of the adopted fine
materials were obtained, and are summarized in Table 3.1. The shape and size of cement
particles influence the rate of hydration. These characteristics of cement also affect the
packing density of the paste, and consequently increase the amount of free water
available to increase the workability of the mixture. Application of the limestone filler,
which occupies the voids between the cement particles due to the finer size compared to

the cement, improves concrete durability (Gomes 2002). Also, the spherical-shape particles of the fly ash, which act as micro-rollers, significantly decrease the friction and the flow resistance of the paste.

3.2.1.1 Selection of the suitable superplasticizer

Since the use of a suitable superplasticizer is fundamental for guaranteeing SCC requirements, a series of pastes composed of cement, water and several types and dosages of superplasticizer (Glenium from BASF: SKY 617, 77 SCC, ACE 426 and SKY 602, respectively named as SP1 to SP4 in the present research) were tested to find the most effective superplasticizer on the flowability and viscosity of the paste. The proportions of each component were defined in terms of volume. All superplasticizers were based on polycarboxylic ether (PCE) polymers with high dispersing power, workability retention and fast strength development.
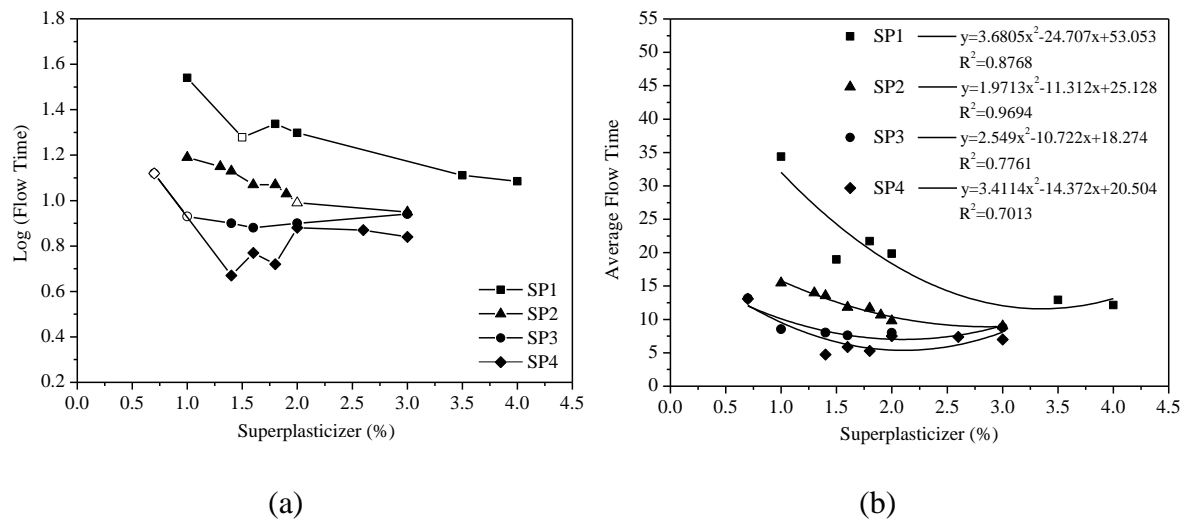
Fig. 3.2- (a) Marsh flow time at saturation point; and (b) flow time *vs.* dosage of superplasticizer

The pastes were prepared using a constant water-to-cement ratio (w/c) of 0.35 to have a good flowability without bleeding. A lower w/c ratio was not considered because the aimed pastes flowability could not be obtained using that ratio. Fig. 3.2(a) defines the

relationship between the logarithm of the marsh flow time versus the percentage of superplasticizer. By increasing the volume percentage of superplasticizer in the paste, the marsh flow time decreases up to the "saturation point", after which an increase in the dosage of the superplasticizer does not change the flow time significantly. The saturated dosage of each superplasticizer in the prepared pastes is marked as an unfilled marker in Fig. 3.2(a). Application of the superplasticizer in the saturated dosage makes the paste to have the highest fluidity without bleeding or segregation (Gomes 2002). The decrease of the mean flow time with the increase of the dosage of superplasticizers appears to be well fitted by a polynomial curve, as shown in Fig. 3.2(b).

Among all of the tested superplasticizers, two superplasticizers were selected in this study: the one that caused the highest flowability, named as SP4 in this research; and the one that promoted the highest viscosity of the pastes, SP1, at the saturation point.

3.2.1.2 Determination of the optimum dosage of fly ash

Minimizing the cement content, which is the most expensive component of the paste, is one of the goals of the mix optimization in the present study. Thus, replacing the percentage of cement volume with fly ash was the adopted strategy to optimize the paste cost. Moreover, the application of fly ash improves the packing density and, consequently, improves concrete durability. The spherical-shape particles of the fly ash act as micro-rollers and significantly decrease the friction and the flow resistance of the paste. However, to avoid the bleeding phenomenon caused by the application of a high amount of fly ash in the binder paste (Soltanzadeh et al. 2012) it is necessary to find the optimum dosage of fly ash.

A series of flow tests were carried out on binder pastes made of cement, which was replaced by various dosages of fly ash, water and a minimum dosage of the selected superplasticizers ("SP1" and "SP4"). The water content was defined as 88% of the fine materials (cement and fly ash) volume, and the fly ash dosages were varied between 0 to 55% of the cement volume. During these tests, the spread diameter of the control paste "D_{Cont}", measured in the composition without application of fly ash, was compared with the spread diameter of the testing series of pastes "D_{test}", including various dosages of fly ash, as shown in Fig. 3.3. This figure represents the influence of the cement replacement

by fly ash on the relative spread (D_{test}/D_{Cont}). It shows that the flowability can be improved rapidly by replacing up to 25% of the cement volume by fly ash. By replacing 25% to 35% of cement by fly ash the flowability in the paste containing superplasticizer SP4 has reduced, whereas an increase was registered when superplasticizer SP1 was used. Above 35% of cement replacement by fly ash has small influence on the flowability of the pastes.
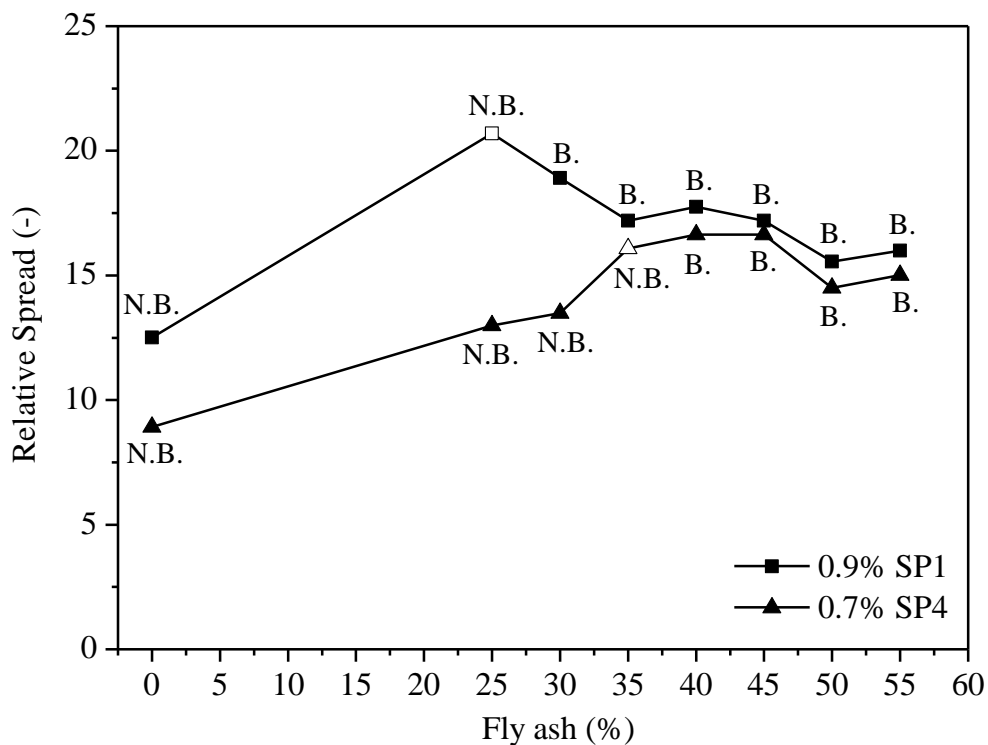
B: Bleeding is observed by adding this dosage of fly ash,
N.B: No Bleeding is found by adding this dosage of fly ash.

Fig. 3.3- Relative spread of paste by replacing cement with different dosages of fly ash.

The relative spread of the paste containing SP4 was always higher than of the paste including SP1. However, cement replacement by fly ash above 25% caused bleeding of the paste when using superplasticizer SP4, while this percentage can increase up to 35% if superplasticizer SP1 is adopted, without evidence of this phenomenon (see Fig. 3.4). The rest of the research was, consequently, carried out using superplasticizer SP1 and fly ash in contents of 30% and 35% of the cement volume.
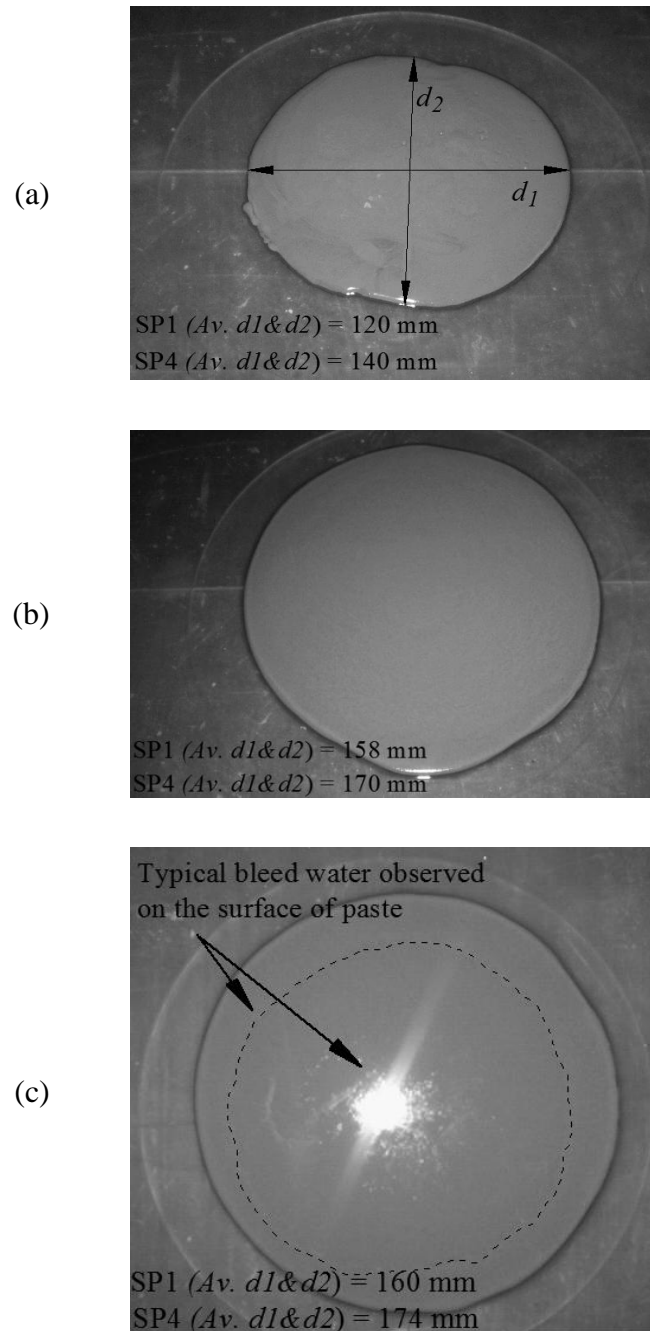
Fig. 3.4- Flow of the paste (a) without using fly ash, (b) by application 25% and 35% fly ash, and (c) using more than 25% and 35% fly ash for developing the paste contains SP1 and SP4 superplasticizer respectively.

3.2.1.3 Determination of the optimum dosage of limestone filler

The paste was optimized by taking the benefits of limestone powder with the pore filling effect in producing a more compacted concrete structure with better cohesiveness,

mechanical strength and durability (Ghrici et al. 2007 and Isaia et al. 2003). To define the optimum dosage of limestone filler, the flow test series were performed on the paste compositions made of 30% or 35% fly ash and different percentages of limestone filler relative to the cement volume. All series of the pastes were produced using a minimum dosage of superplasticizer SP1, and the content of mixing water was 88% of the total fine materials volume.

Fig. 3.5 represents the relationship between the relative spread of the paste (D_{test}/D_{Cont}) and the dosage of limestone filler. The best percentage of limestone filler, which caused the maximum spread of the paste without observation of paste bleeding, was chosen as 30%. Regardless the higher susceptibility of paste bleeding when using higher dosages of limestone filler, two additional percentages, 35% and 50%, of limestone were considered to study the effect of the filler dosage on the compressive strength of the corresponding mortar. These dosages were further selected to investigate if the bleeding of the paste also occurs when the paste is combined with aggregates for producing the corresponding mortar. The three selected limestone percentages are shown with unfilled marks in Fig. 3.5. The process for determining the optimum dosage of limestone filler and fly ash was finalized after performing compressive tests on nine $50 \times 50 \times 50 \, \text{mm}^3$ cubic mortar specimens at the age of 7 days (in accordance with ASTM C 109 / C109M - 11b and BS EN 197-1).

According to the results presented in Fig. 3.6, the decrease of activation energy when cement is replaced fly ash, mainly at early ages (Azenha 2009), justifies the higher compressive strength for the series of specimens made by lower dosage of fly ash (Felekoğlu et al. 2006 and Villain 1999). Since the strength gain of the mortar specimens at the early age is mostly resulted from hydration of the cement, application of higher replacement of cement by filers caused a reduction of compressive strength. Similar tendency was also reported by Pereira, 2006. For limestone filler in percentage between 30% and 50%, the compressive strength for the specimens was not significantly affected for the series of 35% of fly ash. However, application of limestone filler higher than 30% of cement volume caused a pronounceable bleeding in both series of the composites. Thus for producing the paste, capable of presenting a good flowability and compressive strength, 30% of the cement volume was selected as the optimum dosage of fly ash and limestone filler in the final composition.
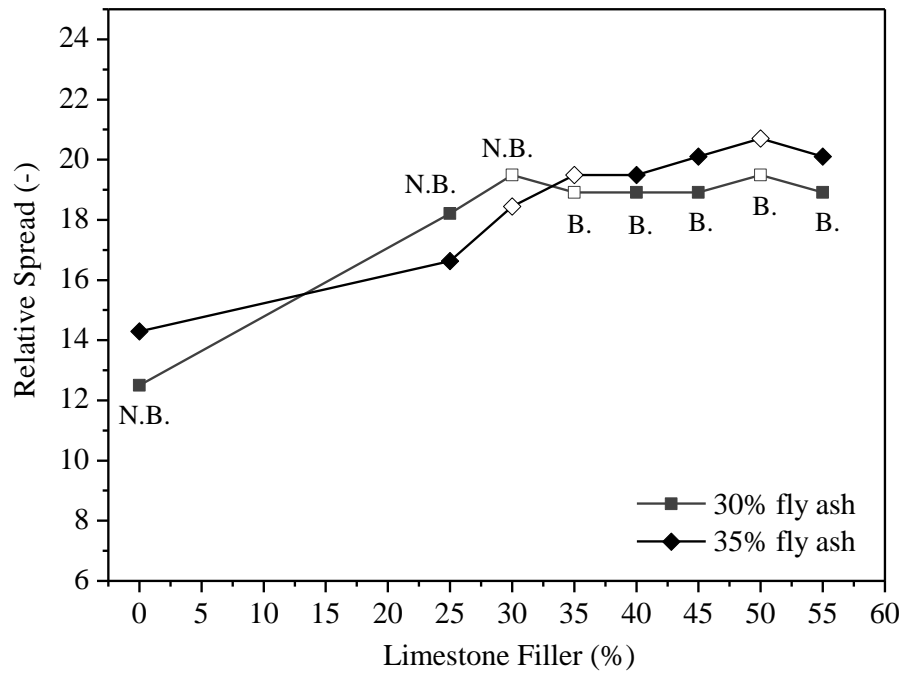
B: Bleeding is observed by adding this dosage of fly ash,
N.B: No Bleeding is found by adding this dosage of fly ash.

Fig. 3.5- Relative spread of paste made by different percentage of limestone filler
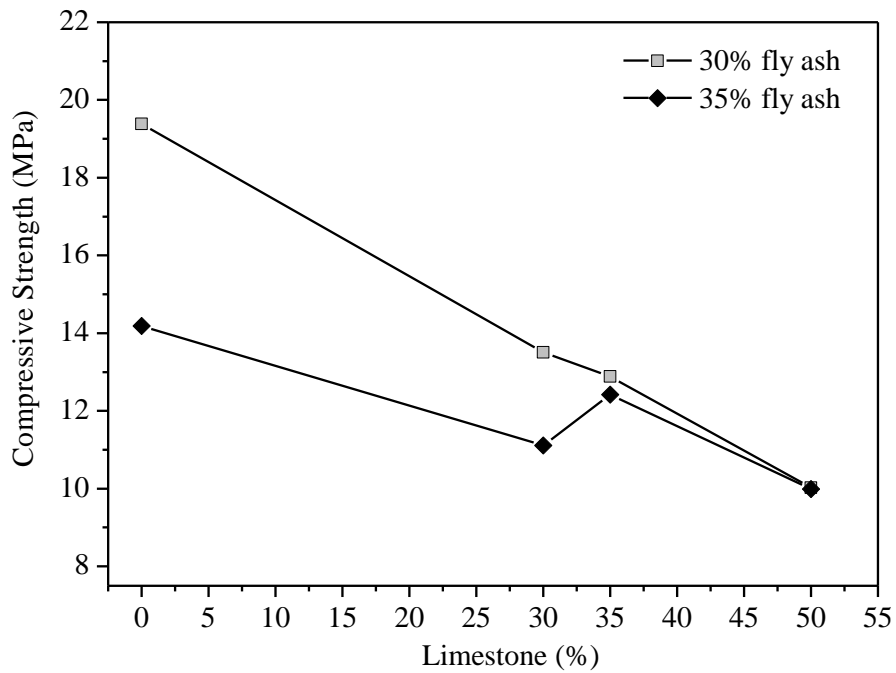
Fig. 3.6- Compressive strength of mortar made of various percentages of limestone
filler

3.2.1.4 Determination of the optimum dosage of superplasticizer

The optimum dosage of the selected superplasticizer was obtained by testing the flowability of several paste compositions. These compositions were tailored using distinct dosages of superplasticizer, constant ratio of water to cement and fly ash binder materials weight (w/b) of 0.28, and the optimum content of the fine materials: cement, fly ash and limestone filler. The superplasticizer proportions were defined in terms of the weight percentage of the fine materials. Fig. 3.7 indicates the relative spread (D_{test}/D_{Cont}) and flow time of each paste sample versus dosages of superplasticizer. The optimum percentage of superplasticizer was 1.2% of the fine materials in weight. A summary of the optimized paste composition is presented in Table 3.2.
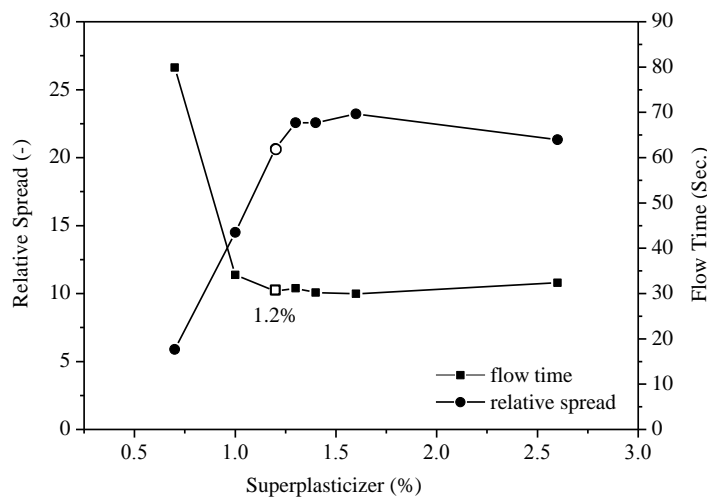
Fig. 3.7- Relative spread of the paste *vs*. the percentage of superplasticizer

Table 3.2- Optimum paste composition

Material	Volume % of Paste
Cement	36.95
Fly ash	11.09
Limestone filler	11.09
Water	40.28
Superplasticizer	0.59

3.2.2 Determination of the Optimum Aggregate Proportion

The second phase of the HPFRC mix design is composed by the evaluation of the optimum grading of the concrete solid skeleton. In this phase, the size and shape of stone particles is selected carefully in such a way that a dense and compact solid skeleton can be assured. According to the previous researches (Dewar 1999 and Kwan and Mora 2001), there is a clear relationship between shape, texture, and grading of aggregates with voids content available between aggregates in a concrete mix. In fact, flaky, elongated, angular, and unfavorably graded particles lead to higher voids content than cubic, rounded, and, well-graded particles. By comparing the shape of coarse aggregates selected for developing the mixes in the present study (Fig. 3.8(a)), with that of the aggregates introduced in the chart provided by Ahn (2000) (Fig. 3.8(b)) for the visual assessment of particle shape, the selected coarse aggregates can be categorized as cubic aggregates. For developing the optimum aggregate proportion, the well-graded fine and coarse river sand were used to fill the voids between the cubic coarse aggregates. The effects of shape and texture of these aggregates are much more important than that of coarse aggregate (Quiroga and Fowler, 2004) in terms of flowability of a concrete mix. Due to the spherical shape of the sands used in the present study, smaller quantity of paste and water is required to provide workability for the mix. These particles also help to provide a better pump ability and finish ability, as well as a higher strength and lower shrinkage for the SCC than flaky and elongated aggregates (Shilstone, 1990).

| (a) | (b) |
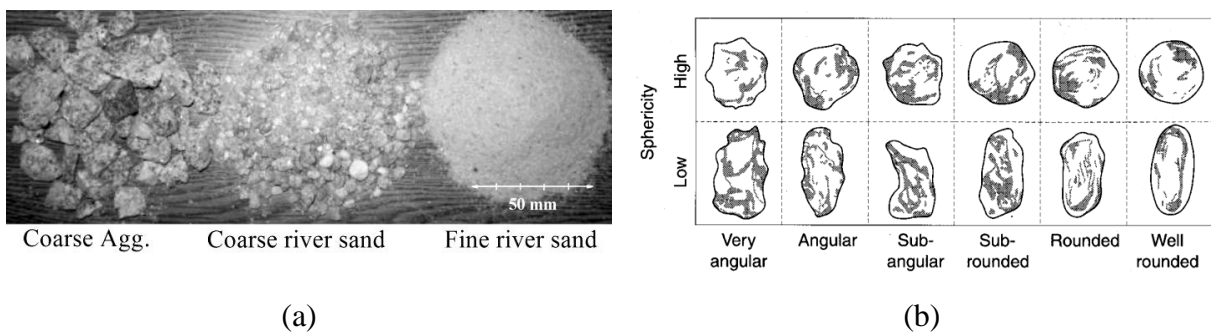
Fig. 3.8- (a) Applied aggregates in tailoring HPFRC in the present study, and (b) visual assessment of particle shape based upon morphological observations (Quiroga and Fowler, 2004).

Since the particles interact volumetrically and not by weight (Richardson 2005) the aggregate gradations were determined on the basis of the volume. In accordance with ASTM C 29 and BS EN 1097-3, the shoveling procedure was adopted to access the loose bulk density for three types of aggregates, whose properties are indicated in Table 3.3. In this phase it was assumed that 90 kg/m^3 hooked end steel fibers, with the properties introduced in Table 3.4, will be used in the HPFRC, since preliminary bibliographic research has indicated to be a suitable fiber content for constituting a cost competitive shear reinforcement system for the total replacement of conventional stirrups in flexurally RC beams (Soltanzadeh 2014).

Table 3.3- Aggregate properties

Aggregate	Specific Gravity[1] (kg/m^3)	Absorption[1] (%)	Maximum size[2] (mm)
Fine river sand	2.609	10.64	2.36
Coarse river sand	2.630	5.08	4.75
Coarse aggregate	2.613	1.58	12.5

[1] According to ASTM C 127 and BS EN 1097-6 and ASTM C 128 and BS EN 1097-6 for, respectively, the coarse and fine aggregates.
[2] According to ASTM C 136 and BS 812-103.1.

Table 3.4- Properties of steel fiber

Diameter	0.55 mm
Length	35 mm
Aspect ratio	64
Tensile strength	1100 MPa
Density	79000 kg/m^3
Profile	

To make the most compact solid skeleton, the following procedure was carried out: first of all, the coarse aggregate and fibers were used to fill the measuring cylinder. Since the

fibers were expected to settle between the stone particles, the volume of coarse aggregate was kept constant, equal to the volume of the cylinder, and the river sand was added gradually until no voids remained to be filled by river sand. In the last step, the fine sand was added to fill the smaller voids as much as possible. The test was stopped when no more fine sand was possible to add for the filling of voids, and the volume of applied fine sand was then measured. To reduce the voids in size and percentage, and therefore obtain a compact skeleton organization in each stage of this process, its filling was made in three layers by shaking the measuring cylinder after charging each layer. Fig. 3.9 represents the influence of this skeleton organization process on its relative weight, where this last concept is the ratio between the final weight of solid composition obtained in the second and third steps to the weight of coarse aggregate and steel fibers mixture that was determined in the first step of test. It is verified that the relative weight has increased with the volume percentage of fine river sand and coarse river sand on the total aggregate composition. Table 3.5 presents the percentage of total volume of fine sand, river sand and coarse aggregate in the first obtained aggregate composition, named as "S1".
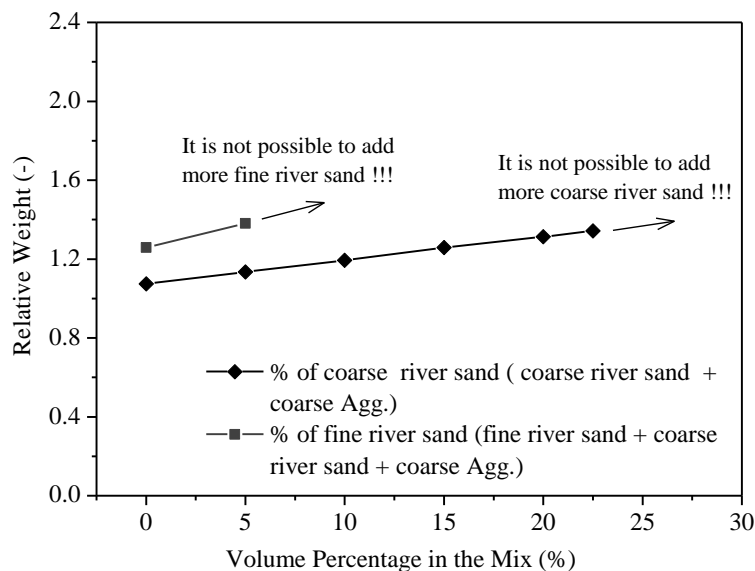
Fig. 3.9- Determination of the optimum composition of the solid skeleton
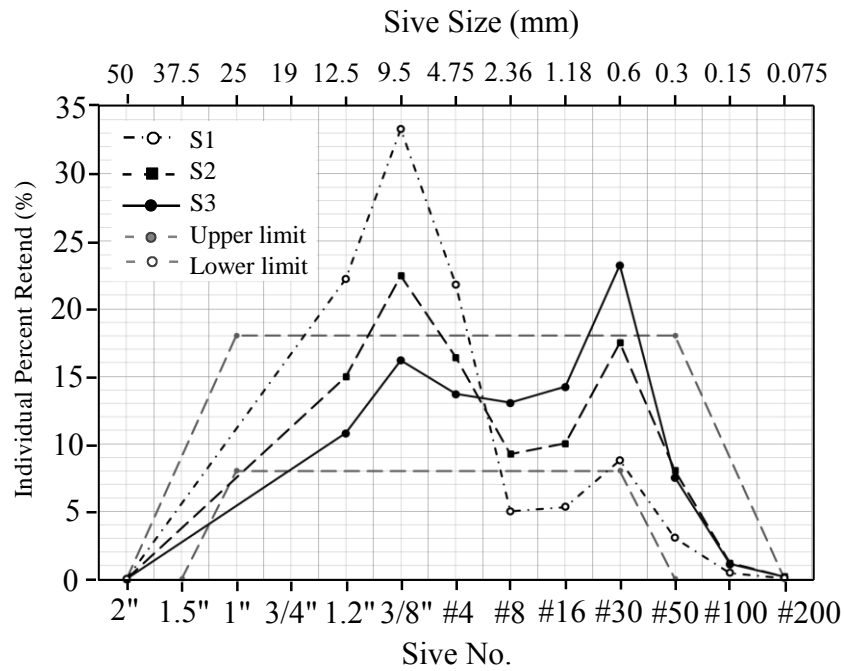
Fig. 3.10- Comparison of the results with the limitation suggested by Minnesota DOT
(Richardson 2008).

Table 3.5- Aggregate compositions and their effects on flowability of a concrete mix

Agg. Composition	Fine river sand	Coarse river sand	Coarse Agg.	Flow diameter	T_{50}	Comment
	(% of total volume of solid skeleton)			(mm)	(s)	
S1	4.85	19.10	76.05	-	-	The initial solid composition
S2	18	42	40	120	-	120mm slump loss, very harsh mix
S3	12	51	37	500	6	Good homogeneity

In order to improve S1 aggregate composition until reaching the adequate flowability for
SCC, an aggregate gradation method based on the Individual Percent Retained (IPR)
curve (which presents the percentage of the combined aggregate retained on each sieve
size), the one recommended by Minnesota DOT (Richardson 2008), was applied as the
first trial. In this method, the minimum and maximum limits for the aggregate
composition in normal concrete, which should be retained on different sieve sizes, are

recommended in a graph (Fig. 3.10). By comparing S1 with the proposed upper and lower limits of this graph, it is clear that the proportion of some intermediate particles (1.18 mm to 2.36 mm) are lower (33 to 38%) than the minimum recommended limit, while the proportion of some coarse aggregates (19 mm to 4.75 mm) exceeds the recommended upper limit (21% to 85%). In order to improve S1 aggregate composition, an attempt was made to increase the gap-graded observed in this composition by increasing the volume of intermediate particles and reducing the coarser aggregates, considering the IPR curve limit lines. Thus a series of trial concrete mixes with different aggregate gradation and constant ratio of paste volume to total volume of concrete mix ($V_{paste} / V_{total} = 0.45$) were prepared to select the best aggregate composition in this context. The flowability of the concrete mixes made by two different aggregate compositions "S2" and "S3" and a constant dosage of optimized paste were evaluated by executing slump flow tests, whose results are presented in Table 3.5. It is observed that the lower the volume percentage of the coarse aggregates is, the higher is the flowability. However, to develop a relatively high compressive strength and cost competitive HPFRC, the reduction of the coarser aggregate should be limited. Among the tested aggregate compositions (S1 to S3), the last one (S3), including 37% of coarse aggregate and 63% of river sand (12% of fine and 51% of coarse), was found to increase the viscosity properly without segregation. Fig. 3.11 compares the grading of this optimal composition (S3) with the curves corresponding to the limits recommended by ASTM C136. This figure shows that the solid skeleton of SCC includes higher percentage of finer particles compared to that of conventional concrete.
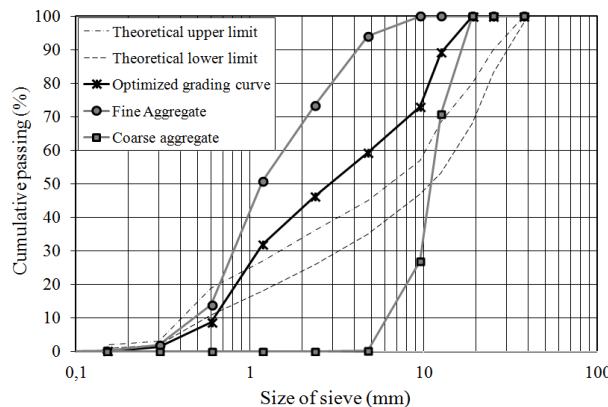
Fig. 3.11- Comparison of the results with the curves defining the upper and lower limits suggested by ASTM C136 for conventional concrete (fine aggregate includes the fine and coarse rive sand)

3.2.3 Concrete Proportioning

In the last phase of the HPFRC mix design, the content of paste in the concrete volume is evaluated. For this purposes several mixes were prepared with distinct paste/aggregate ratios to establish proper flowability in the final mix. The compositions were prepared according to the following procedure:

The saturated aggregates were mixed during 30 seconds. The fine materials (cement, fly ash and limestone filler) were added and mixed further for 1 minute. Then, 90% of the mixing water, with 10% of the amount of superplasticizer dissolved, was continuously added to the mix during approximately 30 second. One minute after, the rest of water and superplasticizer was gradually added to the composition, and the mixing process continued for one more minute. Finally, the steel fibers were added, and the mixing process was stopped two minutes later.

Fig. 3.12- HPFRC spread obtained on the slump flow test for mix B with 90 kg/m^3 steel fiber.

The flowability of each mix was evaluated by measuring the total spread diameter and the time to reach a spread diameter of 500 mm, T_{50}, in the slump test. The obtained results are presented in Table 3.6. In this study, the best paste/aggregate ratio was 0.48, which is called mix "B" in the table. No visual sign of segregation was detected in mix-B, and the mixture presented good homogeneity and cohesion during flowing through the smaller orifice of the Abrams cone (during testing the flowability of the mix, the Abrams cone was always used in the inverted position) as shown in Fig. 3.12. The mix reached the spread diameter of 500 mm in 3.5 sec, and a total spread diameter of 660 mm. Using a lower paste volume ratio was not able to assure good flowability in the mix (mix-A), while a higher paste volume (mix-C) has decreased both the compressive strength in

about 28% and the homogeneity of HPFRC, since segregation was observed. The process adopted for tailoring HPFRC is summarized in the flowchart represented in Fig. 3.13.
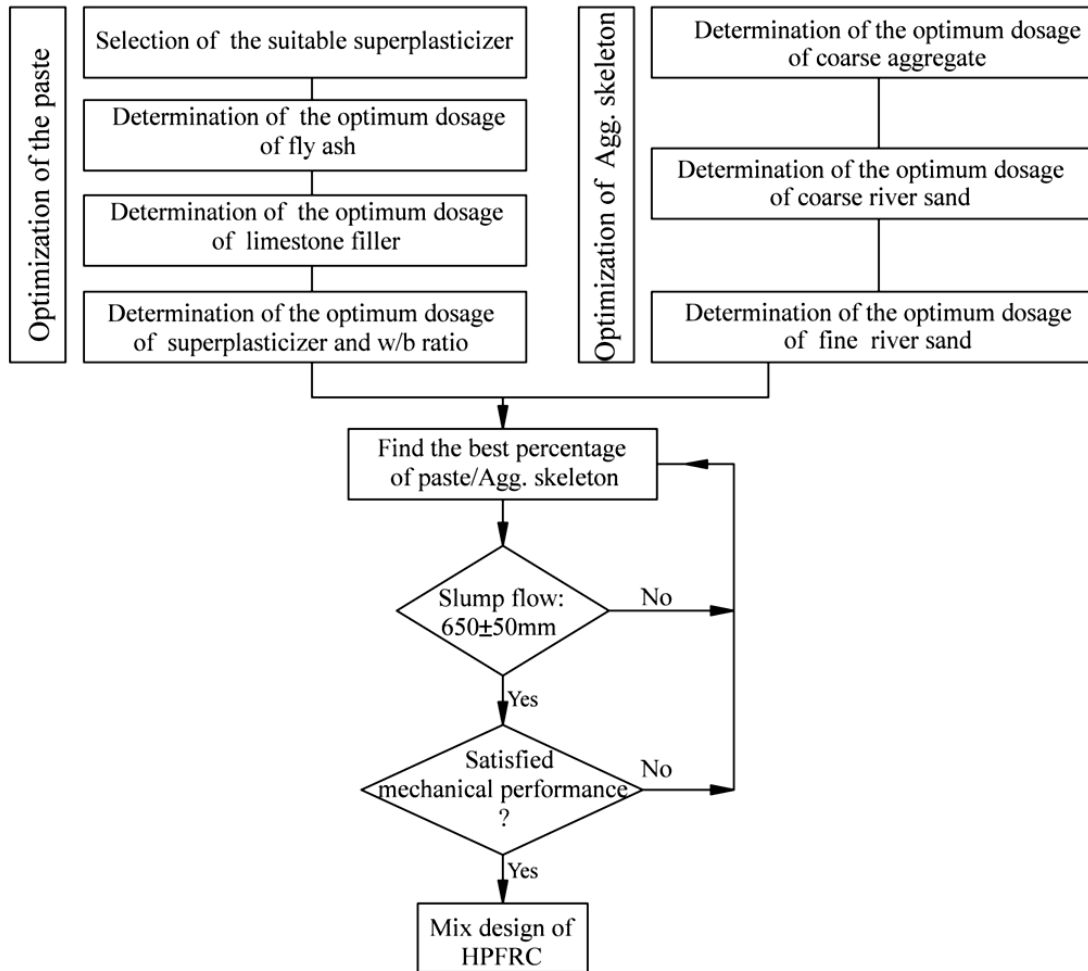
Fig. 3.13- Flowchart of HPFRC mix design.

Table 3.6- Concrete compositions executed with different paste percentages

Mix	Paste Volume (%)	C[1] kg/m^3	FA[2] kg/m^3	LF[3] kg/m^3	W[4] L/m^3	SP[5] L/m^3	FS[6] kg/m^3	RS[7] kg/m^3	CA[8] kg/m^3	SF[9] kg/m^3	w/b[10] (-)	T_{50} (Sec.)	Spread Diam. mm
A	46	443	133	133	199	15	102	724	522	90	0.35	-	490
B	48	462	138	139	208	16	99	697	503	90	0.35	3.5	660
C	50	481	144	144	216	16	95	671	483	90	0.35	2	721

[1] Cement; [2] Fly Ash; [3] Limestone Filler; [4] Mixing Water; [5] Superplasticizer; [6] Fine River Sand; [7] Coarse River Sand; [8] Coarse Agg; [9] Steel Fibers; [10]Water to Binder Ratio.

3.3 MECHANICAL CHARACTERIZATION OF THE DESIGNED HPFRC

The mechanical performance of the developed HPFRC was evaluated based on the compressive, flexural and splitting tensile behavior of hardened 28 days edge specimens, with special focus on the flexural and splitting tensile performance due to the significant impact of fiber reinforcement in these mechanical properties. Shear behavior of the HPFRC is another important characteristic of the developed concrete, which is evaluated in the next chapter.

3.3.1   Compressive behavior and elastic modulus

To characterize the compressive behavior and elastic modulus of HPFRC, nine cylindrical specimens of 150 mm in diameter and 300 mm in height were cast without applying vibration. The tests were carried out in a servo-controlled equipment of 3000 kN maximum load carrying capacity by imposing a displacement rate of $5\ \mu$m/s in the internal displacement transducer to control the test procedure.
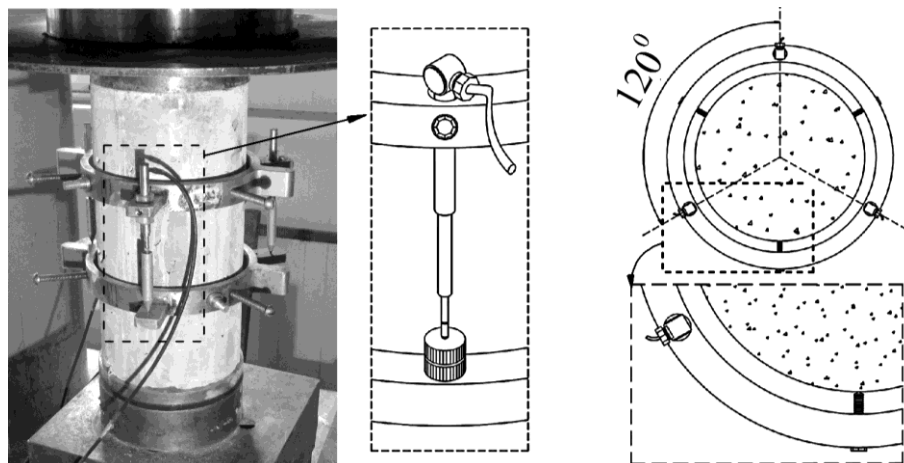
Fig. 3.14- Setup for testing modulus of elasticity.

The Young's modulus was obtained in accordance with the BS EN 12390-13 (2014) recommendation, where three loading-unloading cycles were prescribed. Using three linear voltage displacement transducers, LVDTs, disposed at 120° around the specimen

according to Fig. 3.14, the axial displacement of the specimens was monitored during the tests. The loading value was limited between an upper level of one-third of the compressive strength of the HPFRC and the lower level of 0.5 MPa. Finally the elastic modulus was computed as the ratio of the stress difference between loading and unloading cycles and the strain difference observed in the last unloading cycle. The results obtained from testing the modulus of elasticity of the developed concrete are reported in Table 3.7 for three distinct ages of 3, 7 and 28 days.

Compressive strength of the cylindrical specimens was evaluated according to ASTM C39 / C39M - 14a. The obtained results at three distinct ages of 3, 7 and 28 days are reported in Table 3.7. These results show that the strength and stiffness have increased rapidly with age, which suggests that the developed HPFRC is quite capable of being applied for constructing prefabricated elements. Taking the compressive strength value of HPFRC at 28 days as the reference, the influence of concrete age on the compressive behavior of the HPFRC was further estimated based on the modified expression recommended by Cunha et al. (2008). In accordance with this method, the compressive strength of the developed concert at the age of t days ($t = 3$ and 7 days in this study) is calculated using the following equation:

$$f_{cm}(t) = f_{cm}(28).\exp\left\{0.052\left[1-\left(\frac{28}{t}\right)^{0.89}\right]\right\}$$

(3.1)

where $f_{cm}(28)$ is the mean compressive strength value at 28 days.

Fig. 3.15(a) compares the estimated compressive strength of the HPFRC with the experimental values. It is apparent that the analytical results are in good agreement with those obtained experimentally. Similar to the experimental results, the analytical approach predicts a rapid strength gain of concrete compressive strength at early ages, which might be associated with the optimum water content used for tailoring the concrete that reduced the macroscopic entrapped voids (Cunha et al. 2008). The high dosage limestone filler has also improved the bond between the paste and the aggregates, by reducing the wall effect in the transition zone between these two phases and, consequently, has improved the microstructure of the mix (Isaia et al. 2003).

The average values of the elasticity modulus, obtained at each age (t), and the scatter of the corresponding results are illustrated in Fig. 3.15(b). These results are in agreement with those estimated by using Eq. (3.2) proposed by Cunha et al. (2008) for the elasticity modulus of SFRC at early ages.

$$E_{ci}(t) = E_{ci}(28) \cdot \left[\exp\left\{ 0.1\left[1 - \left(\frac{28}{t}\right)^{0.97} \right] \right\} \right]^{0.17}$$

(3.2)

where $E_{ci}(28)$ is the elasticity modulus at an age of 28 days.

Table 3.7- Compressive strength and Young's modulus of HPFRC

Concrete age (day)	f_{cm} [1] (MPa)	CoV [4] of f_{cm} (%)	f_{ck} [2] (MPa)	E_{cm} [3] (N/mm^2)	CoV [4] of E (%)
3	44.00	1.52	36.00	31246	1.01
7	59.24	2.76	51.24	33624	1.37
28	67.84	2.02	59.84	36056	1.26

[1] mean value of compressive strength; [2] characteristic value of compressive strength; [3] Young's modulus; [4] the CoV is related to testing of 5 specimens.
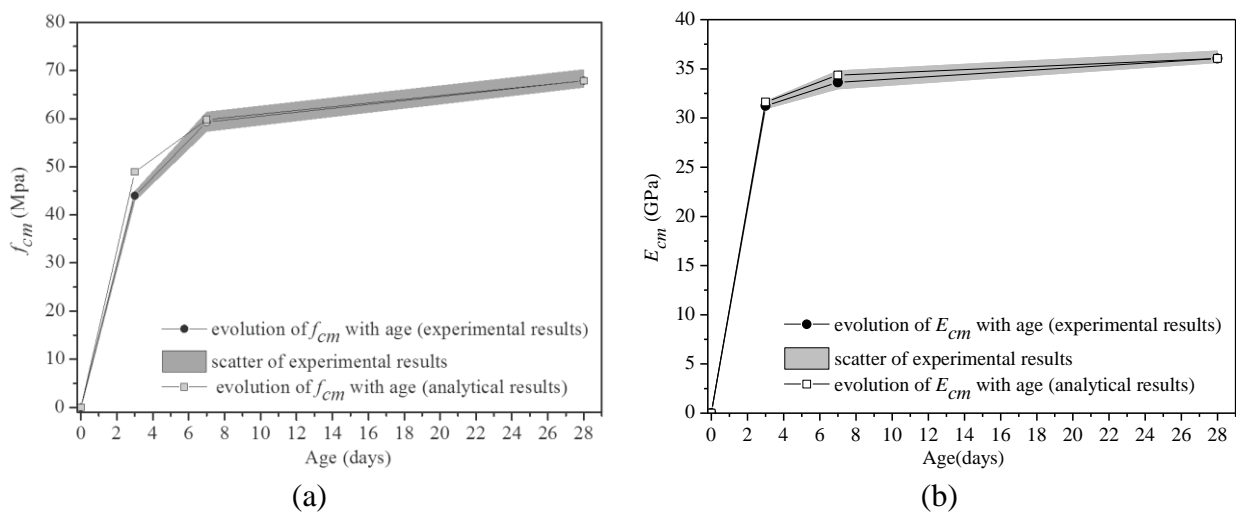
Fig. 3.15- Evolution with age of: (a) average compressive strength, and (b) average elasticity modulus.

3.3.2 Flexural Behavior

The flexural tensile behavior of the developed HPFRC was obtained by testing three simply supported notched beams with a $150 \times 150 \, \text{mm}^2$ cross section and 600 mm in length under three point loading conditions as shown in Fig. 3.16(a). The method of casting the specimens and curing procedures, position and dimensions of the notch sawn into the specimen, and specimen support conditions were those recommended by RILEM TC 162-TDF (2003), and detailed in chapter 2, Sec. 2.4.1, as well. This type of test was carried out in close-loop displacement control by a displacement transducer installed at the midspan of the prismatic specimen. To avoid instability at the first phase of the crack formation and propagation, the displacement rate at midspan of the specimen was $1 \, \mu\text{m/s}$ up to the deflection of 0.1 mm, above which this rate was $3 \, \mu\text{m/s}$. Fig. 3.16(b) shows the nominal flexural stress versus midspan deflection relationship of the specimens. From this relationship and by applying the equation proposed by RILEM TC 162 TDF (2003) for converting the midspan deflection of the beam to crack mouth opening displacements (CMOD), the values of CMOD were calculated, the stress limit of proportionality $f_{fct,L}$ (considered the flexural stress up to a deflection of 0.05 mm) and the residual flexural tensile strength parameters, $f_{R,j}$ [N/mm^2], were determined. The obtained results are indicated in Table 3.8, and it is verified that up to a crack width of about 1.5 mm the flexural strength of the developed HPFRC has exceeded 15 MPa, and at 3.5 mm this composite still presents a flexural capacity of about 12 MPa.
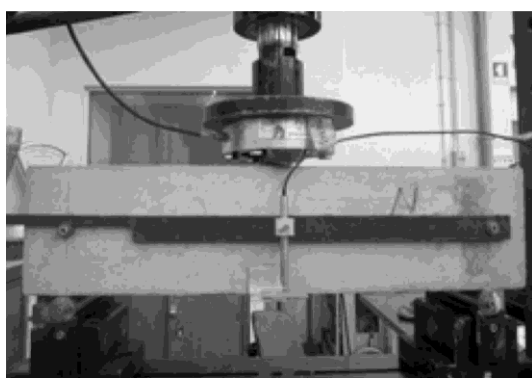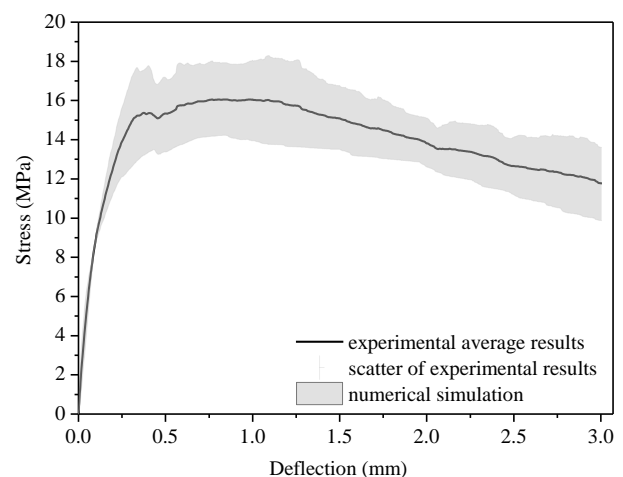
| (a) | (b) |

Fig. 3.16- (a) Adopted test setup for performing flexural tensile test, and (b) nominal flexural stress-midspan deflection relationship.

The final purpose of developing HPFRC in the present chapter is the production of prestressed prefabricated elements without stirrups (which is further discussed in chapter 5), where HPFRC is used to replace completely the conventional shear reinforcements and to improve the bond behavior of flexural reinforcements, as well as cracking process and ductility of the failure modes. Hence, the influence of the concrete age and fiber dosage on this behavior is address in section 3.3.2.1 and 3.3.2.2, respectively. This information is essential for estimating the appropriate time of releasing the prestress and demolding such precast elements, as well as selecting an adequate dosage of steel fibers to resist the shear stress in these elements without stirrups.

Table 3.8- Average limit of proportionality and residual flexural tensile strength parameters of HPFRC beams

	δ_L	$f_{fct,L}$	$f_{R,1}$	$f_{R,2}$	$f_{R,3}$	$f_{R,4}$
	(mm)	(MPa)	(MPa)	(MPa)	(MPa)	(MPa)
			$CMOD_1 = 0.5$	$CMOD_2 = 1.5$	$CMOD_3 = 2.5$	$CMOD_4 = 3.5$
Average	0.05	8.58	15.45	15.26	13.63	12.13
CoV	1.70	23.6	12.45	10.76	11.06	15.89

3.3.2.1 Influence of age on flexural behavior of HPFRC

To investigate the effect of age on the flexural behavior of HPFRC, nine HPFRC prismatic specimens were tested at distinct ages of 3, 7 and 28 days (3 specimens were tested at each age). The HPFFRC constituents applied for casting the $150 \times 150 \times 600\,\text{mm}^3$ prismatic specimens are: Portland cement CEM I 42.5R, limestone filler, fly ash class F, a second-generation of superplasticizer based on polycarboxylate ether (PCE) polymers (Glenium SKY 617), water, three types of aggregates (containing fine and coarse river sand and crushed granite with maximum size of 2.4 mm, 4.8 mm and 12.5 mm, respectively). The concrete was reinforced with a fiber volume fraction, V_f, of 1.1% of hooked end steel fibers with 33 mm length, l_f, aspect ratio (l_f/d_f) of 64, and tensile

strength of 1100 MPa (according to the supplier). The developed composition is represented in Table 3.9.

Table 3.9- HPFRC mix composition

Cement	Fly ash	Limestone filler	Water	Super plasticizer	Fine sand	Coarser sand	Coarse Agg.	Steel fiber
kg/m^3	kg/m^3	kg/m^3	Liter/m^3	Liter/m^3	kg/m^3	kg/m^3	kg/m^3	kg/m^3
462	138	139	208	16	99	697	503	90
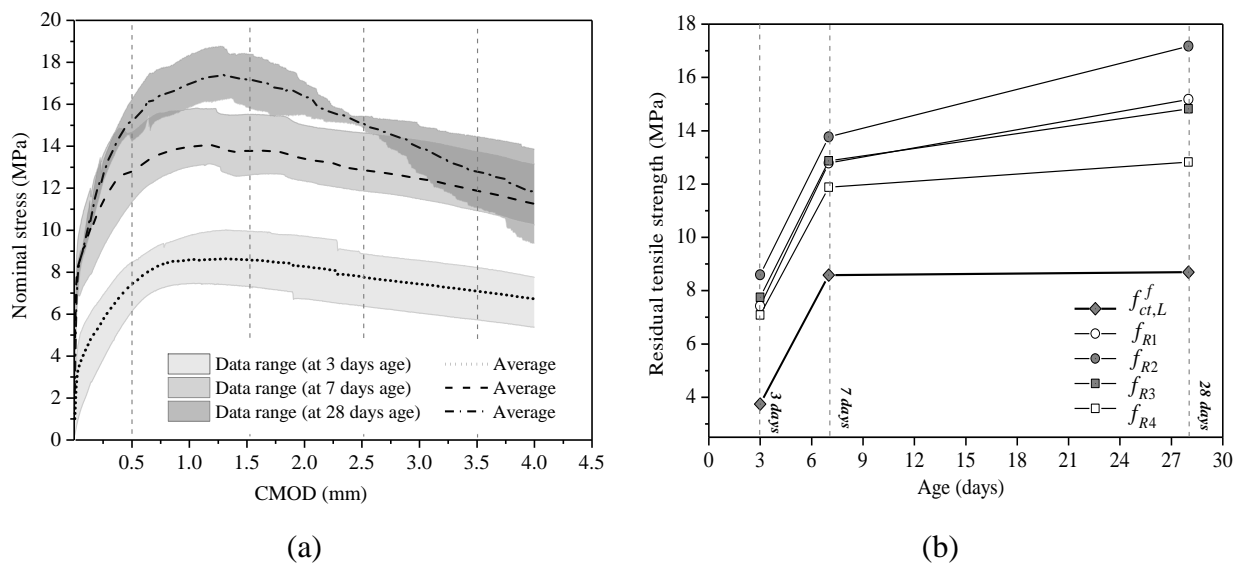
Fig. 3.17- (a) Nominal flexural stress-CMOD relationship and (b) residual tensile strength of HPFRC at distinct ages.
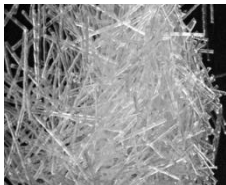
Fig. 3.17 presents the nominal flexural stress, σ_f, versus CMOD relationship of HPFRC beams ($\sigma_f = 1.5P/(b \times h_{sp}^2)$, where P is the applied load, and b and h_{sp} is the width and depth of the notched cross section of the specimens), as well as the evolution of residual tensile strength corresponding to the three testing ages. This figure shows that the flexural strength at 28 days age has exceeded 18 MPa up to the crack width of about 1.5 mm, and at 3.5 mm of crack width this composite still presents an average flexural capacity of about 13 MPa. Above a CMOD of 2.5

mm, the flexural stress has decreased faster in the case of the tested specimens at 28 days age compared to what happened in the specimens tested at the other ages. Similar tendency was also reported by Pereira et al. 2008 and Cuenca and Serna 2013. The main reason is related to the increase of concrete tensile strength during the curing age, since once the matrix cracks, the energy accumulated in the tensile deformation of the matrix is suddenly transferred to the fibers bridging the cracks, leading to occurrence of some damage on the fiber-matrix bond mechanism that causes the aforementioned decay in the flexural stress after peak load (Pereira et al. 2008).

3.3.2.2 Influence of fiber type and dosage on flexural behavior of HPFRC

The effect of fiber dosage on flexural behavior of HPFRC is assessed by developing a reference self compacting concrete without steel fibers and two HPFRC mixes with respectively 90 kg/m^3 (corresponding to the volume fraction, V_f, of 1.1%) and 120 kg/m^3 ($V_f = 1.5\%$) steel fiber, with the same properties introduced in Sec. 2.3.2.1. Additionally all the three mixed were developed using 3 kg/m^3 of synthetic macro fibers, Polyex Duro, whose properties are presented in Table 3.10. This synthetic macro fiber reduces the plastic shrinkage cracking.

Table 3.10- Properties of synthetic macro fibers.

Length	54 mm
Young's modulus	7000 MPa
Special gravity	0.91 g/cm^3
Tensile strength	450 MPa
Common dosages	3 to 12 kg/m^3
Ignition temperature	$> 400^o C$
Profile	

Excluding the cement type, the rest of HPFRC constituents used for producing the prismatic flexural tensile specimens were the same as those introduced in previous section (Sec. 3.3.2.2). The concrete compositions tailored in the present study were developed by Portland cement CEM II 52.5R. The adopted compositions for developing the three concrete mixes are introduced in Table 3.11 by a label "Mi-Fj", where "i" is the number of the mix and "j" identifies the applied fiber dosage. As it is clear in this table, the flowability is provided by means of increasing the ratio of paste to aggregate skeleton for the HPFRC mixes with high dosage of steel fibers, compared to that of the plain concrete. A nominal slump flow of about 660 mm was obtained by testing the flowability of the plain as well as both of the HPFRC mixes made by two different dosages of steel fiber, using the slump test (EN 12350-8). In order to have a reliable comparison between the mechanical properties of the concrete mixes at harden stage, all the mixes were designed to have a strength in the classes C50~C60 MPa (corresponding to the average compressive strength, f_{cm}, of 58 to 68 MPa) (MC2010).

Table 3.11- Concrete compositions executed with different dosages steel fiber.

Mix ID	C^a kg/m^3	FA^b kg/m^3	LF^c kg/m^3	W^d L/m^3	SP^e L/m^3	FS^f kg/m^3	CS^g kg/m^3	CA^h kg/m^3	SF^i kg/m^3	MF^j kg/m^3
M1-F0	462	140	140	197	15.7	126	670	512	0	3
M2-F90	472	141	142	201	16.0	123	656	503	90	3
M3-F120	551	165	165	235	18.7	125	521	425	120	3

[a] Cement, [b] Fly Ash, [c] Limestone Filler, [d] Mixing Water, [e] Superplasticizer, [f] Fine Sand, [g] Coarse Sand, [h] Coarse Agg., [i] Steel Fibers, [j] Synthetic Macro Fibers.

The nominal flexural stress, σ_f, versus CMOD relationship obtained by testing the three groups of specimens is presented in Fig. 3.18(a). The plain concrete specimens, made by M1-F0, exhibited the typical brittle behavior expected for these materials, with an abrupt decay just after initiation of the first crack. On the other hand, 90 and 120 kg/m^3 steel

fibers applied for developing the M2-F90 and M3-F120 concrete specimens significantly influenced the flexural behavior of the specimens and contributed to improve the post cracking behavior of these elements. As it is indicated in Fig. 3.18(b), the residual flexural strength of the plain concrete, $f_{ct,L}^{f}$, were respectively increased 25% and 44% by application of 90 and 120 kg/m^3 steel fibers. The improvement of residual strength in the specimens developed by M3-F120 is at least 12% compared to that of specimens developed using M2-F90 concrete.
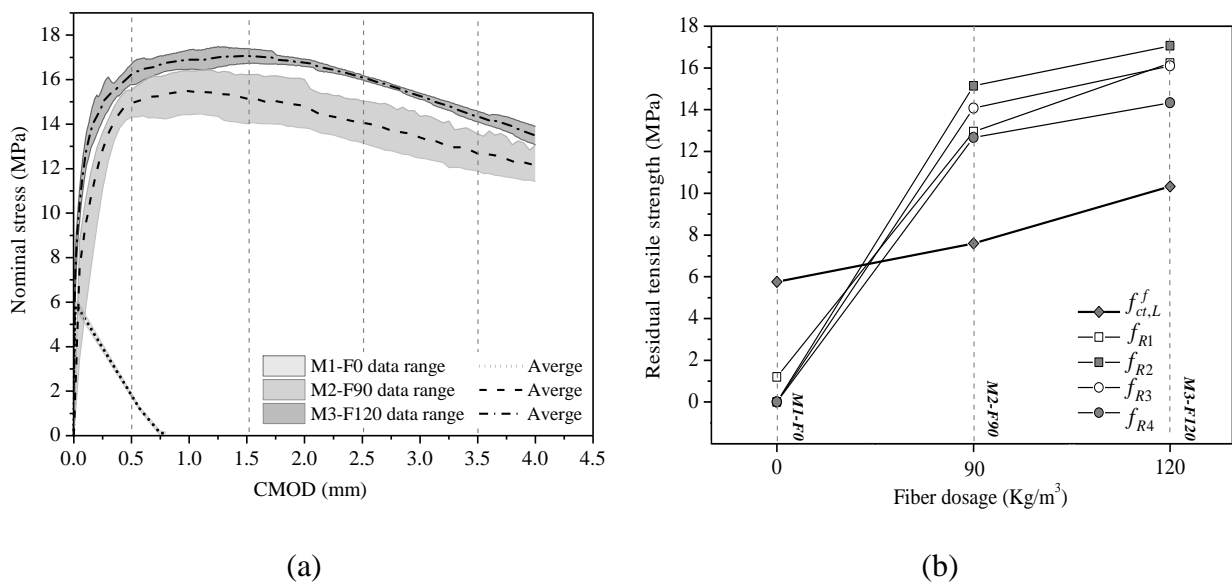
Fig. 3.18- (a) Nominal flexural stress-CMOD relationship and (b) residual tensile strength of HPFRC developed with distinct dosage of steel fibers.

3.3.3   Splitting Tensile Behavior

The splitting tensile test was carried out on six $150 \times 150 \times 150$ mm^3 cubic specimens extracted from each of the tested prismatic specimens in Sec. 3.3.2. According to the scheme represented in Fig. 3.19(a), the specimens were extracted such that the tensile planes of the splitting specimens were placed perpendicular to the concrete flow direction along the prismatic specimens. In order to localize the crack on a single fracture surface, two notches of 5 mm width and 15 mm depth were executed on both faces of the specimens.

The Brazilian splitting tensile tests (ASTM C-496) were carried out in displacement-control using a universal testing rig with a bearing capacity of 150 kN and a relatively low displacement rate of 1 $\mu m / s$ to obtain a stable response once the cracking process is initiated. An external LVDT which was positioned on the actuator to measure the vertical deformation of the specimen was used to control the test. Each specimen was placed between two rigid supports and subjected to a compressive line load applied in the plane of the notched surface of the specimen. Fig. 3.19(b) shows the test setup and loading conditions applied in all the specimens. The crack opening along the notched ligaments was measured using four LVDTs, as shown in this figure. To assess the symmetry of crack opening process in the notched plane, an LVDT was located at the back surface, while the three other LVDTs were fixed on the front surface of the specimens.

Front view   **Side view**

(a)   (b)
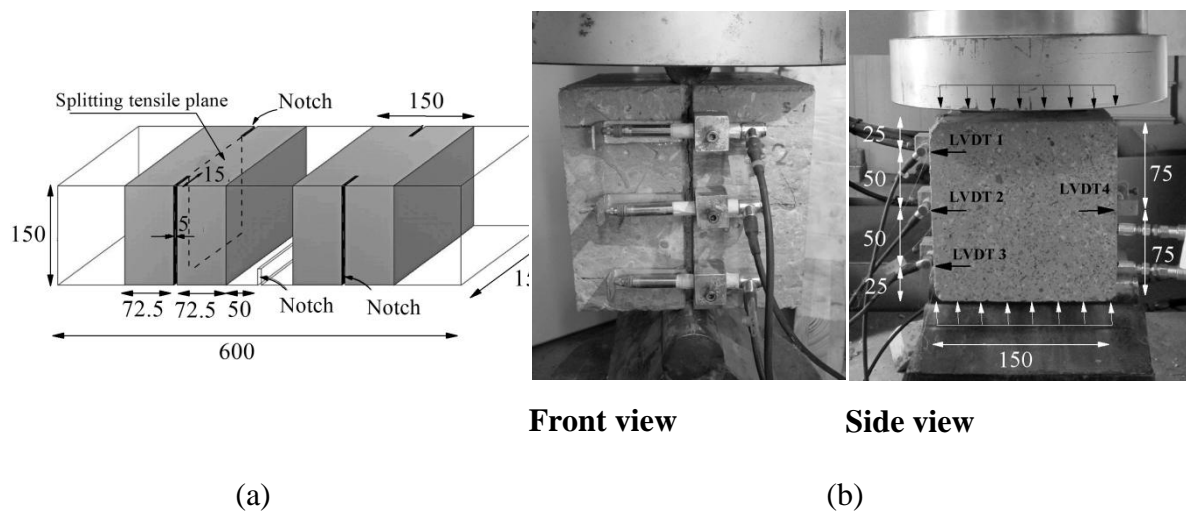
Fig. 3.19- (a) Location of the specimens along the prismatic HPFRC element and (b) geometry and loading configuration of splitting specimens.

Fig. 3.20 represents the obtained nominal stress-crack width relationship, $\sigma_{sp} - w$, of the loaded HPFRC specimens. The crack width is calculated as the average of the displacements recorded by the four LVDTs installed on the faces of the specimen, while the nominal tensile stress at the cracked surface of the specimen was obtained based on Eq. (3.3), proposed by Timoshenko 1991.

$$\sigma_{sp} = \frac{2F}{\pi A} \qquad (3.3)$$

where F is the applied load, and A is the net area of the notched plane (120×150 mm^2).

This equation is further adopted by several other researchers (Carmona and Aguado 2012, and Abrishambaf et al. 2013) to estimate the tensile stress at the cracked surface of cylindrical specimens with and without steel fibers. This formula is also applicable in the case of cubic HPFRC specimens adopted in this study (Cunha 2010).
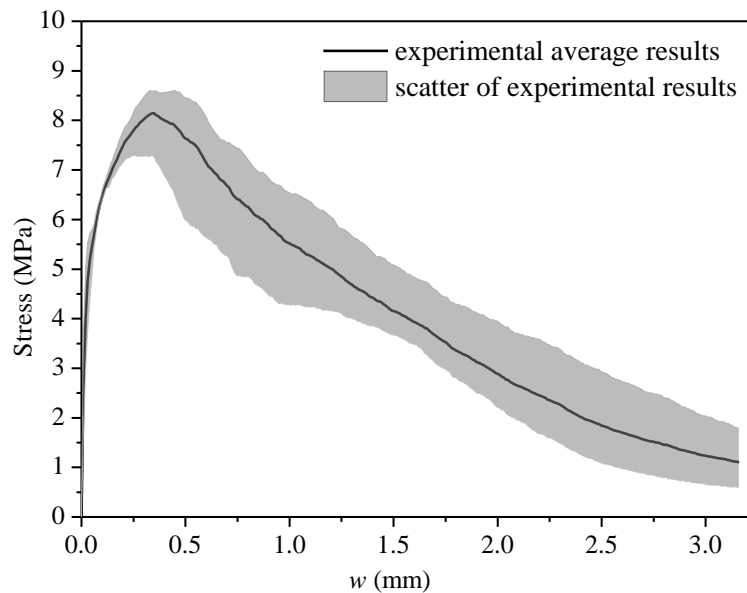
Fig. 3.20- Nominal tensile stress–crack width relationship.

The experimental results in Fig. 3.20 reveals at the nominal tensile stress corresponding to about 3 MPa ($\sigma_{sp} \approx 3$MPa), the splitting cracks were initiated (i.e. $w > 0$). After this stress level, a nonlinear $\sigma_{sp} - w$ response is observed up to attain the peak load. Once the peak load was reached, the load has decreased gradually with the crack opening (softening response). Due to the high contribution of the steel fibers bridging the splitting plane, a relatively high average tensile strength of $(\sigma_{sp})_{max} = 8$MPa was obtained. Despite the high dependency of the post-cracking behavior of FRSCC on the fiber distribution

and orientation, the scatter of results observed by testing the HPFRC specimens with a relatively high dosage of steel fibers was relatively small.

3.4 CONCLUSIONS

In the present chapter, an innovative method of designing was proposed to develop HPFRC with rheological and mechanical properties suitable for the production of precast prestressed concrete elements (self-compacting character and relatively high compressive and post-cracking residual strength). Using this method, a total spread diameter of about 660 mm was obtained for the developed HPFRC mixes composed of 90 and 120 kg/m^3 hooked end steel and 3 kg/m^3 polypropylene fibers. At 28 days the strength class of C50 ~ C60 MPa was obtained for the developed HPFRC mixes with a residual flexural tensile capacity higher than 15 MPa up to a crack width of 1.5mm.

The influence of fiber dispersion and orientation on the tensile performance of the developed concrete with 90 kg/m^3 steel fibers was characterized by performing splitting tensile tests with HPFRC specimens. Since the splitting tensile specimens were extracted from prismatic beams, the fibers had a tendency to line up perpendicularly to the flow direction and hence, contribute to improve the splitting tensile strength up to 8 MPa. The studies presented in the following chapters of this thesis provides more details about the mechanical characteristic of HPFRC developed according to the introduced mix design methodology by means of investigating the shear behavior of HPFRC at material (chapter 4) and structural level (chapter 5).

CHAPTER 4

SHEAR PERFORMANCE OF HPFRC

4.1 INTRODUCTION

Fiber reinforcement is being demonstrated especially appropriate to enhance the shear behavior of concrete elements (Cucchiara et al. 2004 and Barragan et al. 2007). Addition of steel fibers to concrete improves its ductility and therefore transforms the concrete from a brittle material to a ductile one (Minelli et al. 2014 and Cuenca et al. 2013). This is of further importance when dealing with high-strength concrete, which is as brittle as higher is its compressive strength. Hence, using steel fibers for increasing the ductility of such high strength concrete elements can make them applicable in construction elements susceptible to shear failure (Imam et al. 1997).

The advantages associated with the addition of steel fibers to a concrete mix can be investigated under pure shear loading at the material level. Pure shear loading is defined in literature as a loading condition in which a specimen is subjected to equal and opposite parallel forces with negligible bending (Ayatollahi and Aliha 2005). However, there is no unanimous idea about the existence of shear failure in concrete because the crack is assumed to be developed normal to the principal tensile stress direction and causes the damage initiation and propagation of concrete element under the fracture mode I (Arrea and Ingraffea 1982). Nevertheless, in cases where the shear stress zone is narrow enough, for instance, in the case of push off specimens, the existence of mode II failure is evident

(Barragan et al. 2007). The present chapter is dedicated to the characterization of the shear behavior of HPFRC developed in accordance with the methodology introduced in the 3rd chapter. For this purpose, an innovative specimen capable of concentrating the shear stress along its narrow shear ligaments is proposed.

The effect of fiber orientation on HPFRC fracture behavior is another aspect that this analyzed in this chapter by means of image analysis. It is observed that the level of improvement of the concrete behavior by using fibers is sensitive to fiber dispersion and orientation (Laranjeira et al. 2010). In general, factors such as the fiber length and volume fraction, wall effects generated by the geometry of the formwork of the element to be cast, and the interactions between fibers and aggregates during mixing and casting, influence the orientation and dispersion of the fibers inside the matrix. The flowability of concrete has a significant impact in this context, due to the fiber perturbation effect, especially when using relatively long fibers or a high fiber volume fraction.

After the shear behavior of HPFRC has been experimentally characterized, the applicability of a multi-directional fixed smeared crack constitutive model (Ventura-Gouveia 2011) on the simulation of the shear behavior registered in the experimental tests was appraised. To obtain the fracture mode I parameters of the developed HPFRC, an inverse analysis (Pereira et al. 2008) was carried out using the experimental results obtained from the three point bending tests on HPFRC notched beams.

4.2 EXPERIMENTAL PROGRAM

4.2.1   Material Characteristics of HPFRC

The shear behavior of the HPFRC, developed in accordance with the mix design methodology introduced in the 3rd chapter of the present thesis, is characterized in the present chapter. The values of the Young's modulus, compressive, splitting and flexural tensile strength, and the post-cracking residual flexural tensile strength parameters of the 28 days age HPFRC treated in detail in chapter 3 are indicated in Table 4.1. This HPFRC included 90 kg/m^3 of hooked end steel fibers of 35 mm length and aspect ratio of 65. All the details about the mix composition, method of mixing and casting the specimens are presented in the Section 3.2.3.

Table 4.1- Mechanical properties of HPFRC

	Average compressive strength	Young's Modulus	Flexural Properties					Splitting tensile strength
	f_{cm} (MPa)	E_{cm} (N/mm^2)	$f_{fct,L}$ (MPa)	$f_{R,1}$ (MPa)	$f_{R,2}$ (MPa)	$f_{R,3}$ (MPa)	$f_{R,4}$ (MPa)	$(\sigma_{sp})_{max}$ (MPa)
Av.	67.84	36056	8.58	15.45	15.26	13.63	12.13	8.00
CoV	2.02	1.26	23.6	12.45	10.76	11.06	15.89	10.92

4.2.2 Specimen preparation and test setup

ASTM or CSA organizations still have not proposed standard test methods to investigate the material properties of FRC under direct shear loading, such as shear strength and shear toughness (Mirsayah and Banthia 2002). In this context, some researchers have attempted to characterize the shear behavior of FRC using a push-off specimen. This specimen is made of two L-shaped blocks continuously connected by a notched surface through which the shear stress is transferred between both blocks, and the corresponding shear sliding is measured (see Fig. 2.12 in chapter 2) (Soltanzadeh and Barros 2011). Although this specimen exhibited the possibility of measuring FRC properties under a direct shear load, the failure mechanism of the specimen appeared to be governed by splitting-tension rather than shear (Barragan et al. 2007). Thus, to characterize the shear behavior of HPFRC, in the present study a new specimen is designed with some improvements over the push-off specimen. To evaluate the influence of fiber orientation and dispersion on the shear behavior of HPFRC, the specimens were extracted from different locations of prismatic elements of $150 \times 150 \times 600$ mm^3 dimensions. Since the shear specimens were extracted from different distances from the casting point adopted in the preparation of the prismatic elements, the obtained results can also give some indications on the influence of the viscosity and flowability of the HPFRC on the shear behavior of this material. The shear specimens were categorized in four groups, according to their location along the prismatic element, as shown in Fig. 4.1(a). In this figure, the

label "DSS x-y" is used to distinguish the specimens where "x" represents the number of the group and "y" identifies the row number where the DSS was located in the prism.

Top view

Front view

(a)   (b)
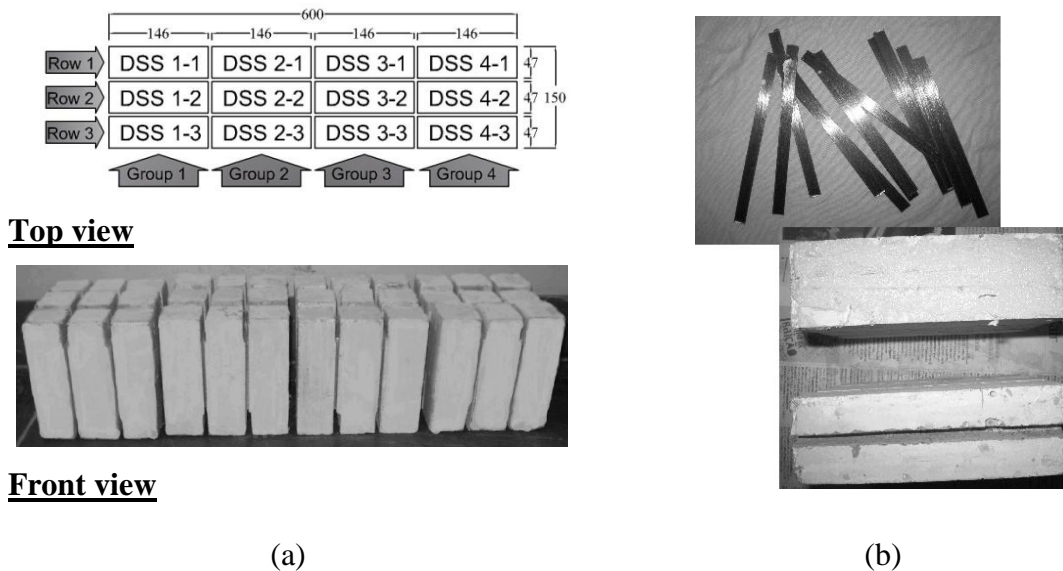
Fig. 4.1- (a) Location of the specimens along the prismatic element; and (b) Application of CFRP laminate in developing the specimens (dimensions in mm).

Fig. 4.2 illustrates a schematic representation of the adopted double shear specimen, DSS. In accordance with this configuration, a rectangular specimen of $150 \times 146 \, \text{mm}^2$ cross-section and 47 mm thick was used to determine the response of HPFRC under direct shear loading. To localize the shear crack along the pre-defined shear planes, two notches of 25 mm depth and 5 mm width were executed at the top and bottom edges of the specimens. After performing preliminary shear tests on specimens with different shear plane dimensions (Soltanzadeh and Barros 2011), a shear plane area of $20 \times 100 \, \text{mm}^2$ was found to be appropriate for designing the DSS, which was assured by executing another notch, in the front and rear faces of the specimen, with a depth and a width of 13.5 mm and 5 mm, respectively. The selection of the orientation of the notched planes in the DSS specimen (orthogonal to the axis of the prismatic element) was governed by the purpose of providing results in terms of HPFRC shear behavior representative of the shear capacity of the corresponding prismatic element. By having the double shear specimens

with shear planes at different position along the axis of the prismatic element, as well as at different distance from the lateral faces of this element, the results from the DSS tests, complemented with the image analysis to determine the fiber orientation and distribution, can constitute a relevant information to extract conclusions on the influence of the rheological properties of the developed HPFRC, casting methodology and mold geometry on the shear behavior of this material.

To avoid the formation of flexural cracks in the outer lateral faces of the DSS specimens, one carbon fiber reinforced polymer, CFRP, laminate was applied in each of these faces according to the near surface mounted technique (Barros and Fortes 2005), as represented in Fig. 4.1(b).

(a)   (b)
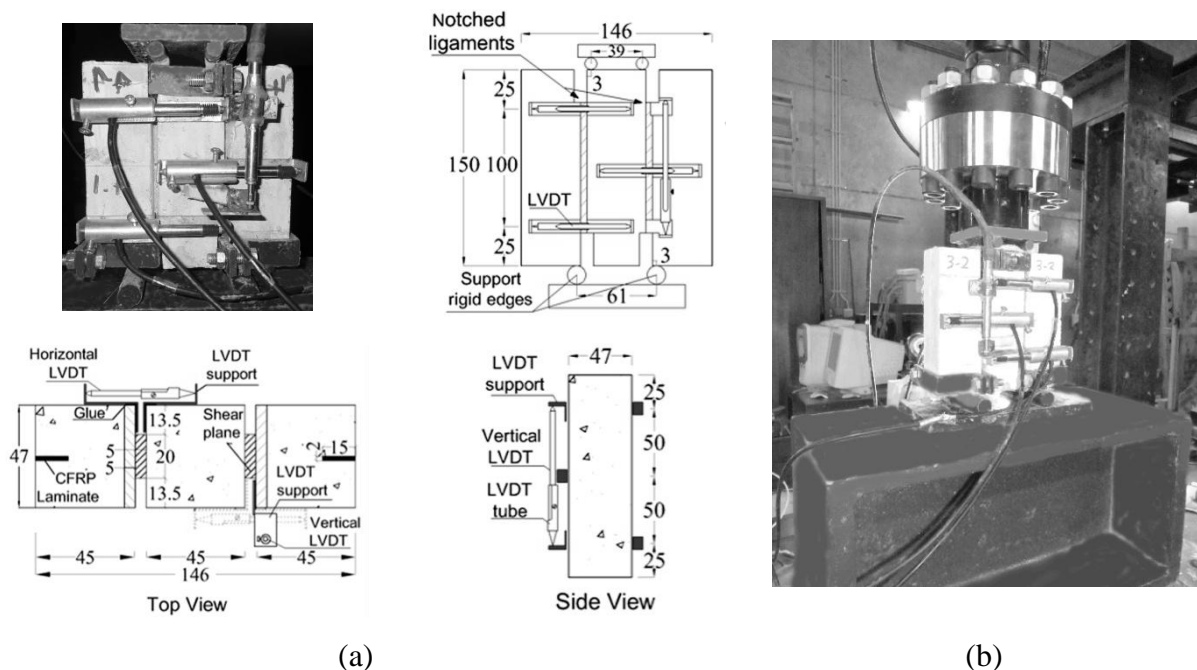
Fig. 4.2- (a) Geometry and loading configuration of DSS specimen (dimensions in mm); and (b) test setup (over view).

The shear test setup was prepared in order to provide the load versus slip relationship in the notched planes, as well as the crack width during the loading process. For this purpose, vertical and horizontal LVDTs were positioned according to the representation indicated in Fig. 4.2. The extremities of the aluminum Z shape plates supporting the

horizontal LVDTs were bonded to the lateral faces of the vertical notches in order to measure exclusively the crack width of these notches. The specimen was supported on two rigid edges, 61 mm in distance, and was loaded by means of two loading points, as depicted in Fig. 4.2. This loading condition produced a predominant shear stress zone along the ligaments of the specimen, but bending stresses are not possible to completely exclude in this zone due to the arm formed by the action and reaction loads. The tests were executed in a servo-controlled testing machine of a bearing capacity of 150 kN, conducted under displacement control at a rate of $1\,\mu$m/s by using an external displacement transducer that measured the vertical deformation of the specimen. During the tests, one LVDT recorded the vertical displacement, while three others monitored the crack openings along the ligaments on each side of the DSS (see Fig. 4.2).

4.2.3 Results and Discussion

During the loading process of the specimens, several small diagonal cracks developed along the ligaments of the DSS. These cracks joined together and formed a crack band along the shear plane, as presented in Fig. 4.3. During the formation and propagation of the smeared shear cracks, the fibers that bridge these cracks offer resistance to this cracking process due to the fiber reinforcement mechanisms detailed elsewhere (Cunha et al. 2008). Due to the beam type nature of the prismatic element, fibers have a tendency to be oriented along the axis of the prism and parallel to the main horizontal plane of the prism. Since the smeared shear cracks have an average inclination of 63 degrees (Fig. 4.3(a)), and are separated by micro-struts in compression, the fiber pullout reinforcement mechanisms of the fibers bridging these cracks (with average inclination angle of 42°) are not only benefited of the inclination of the fiber in relation to the crack shear planes (Cunha et al. 2010), but also from the lateral confinement provided by the indicated inclined concrete compressive micro-struts (represented by C-C arrows in Fig. 4.3(a)).

The results obtained in terms of the load versus slip (*P-s*) and load versus CMOD (*P-w*) are presented in Fig. 4.4. Up to crack initiation, which occurs for a load level of about 20 kN that is almost 1/3 of the average peak load, the very small values of the opening and the sliding only represent the axial and shear elastic deformation of the concrete volume

of the notch. Between cracking load and peak load the *P-s* and *P-w* have a pronounced nonlinear variation due to the post-cracking softening nature of the concrete and reinforcement mechanisms of fibers bridging the cracks. The smooth load decay after peak load is controlled by the fiber reinforcement mechanisms. In fact, the fibers offer resistance to the crack opening and sliding (micro dowel-effect), which delays the loss of shear contribution due to the aggregate interlock effect. This justifies the relatively high shear capacity of HPFRC at specimen scale, $\tau_{max} = p_{max} / (2b_{eff} . d_{eff}) = 14.5\,\text{MPa}$, where τ_{max} is the average shear strength, p_{max} is the average peak load supported by the DSS, and $b_{eff} = 20$ mm and $d_{eff} = 100$ mm are the effective width and depth of the specimen (Fig. 4.2), respectively.

(a) (b) (c)
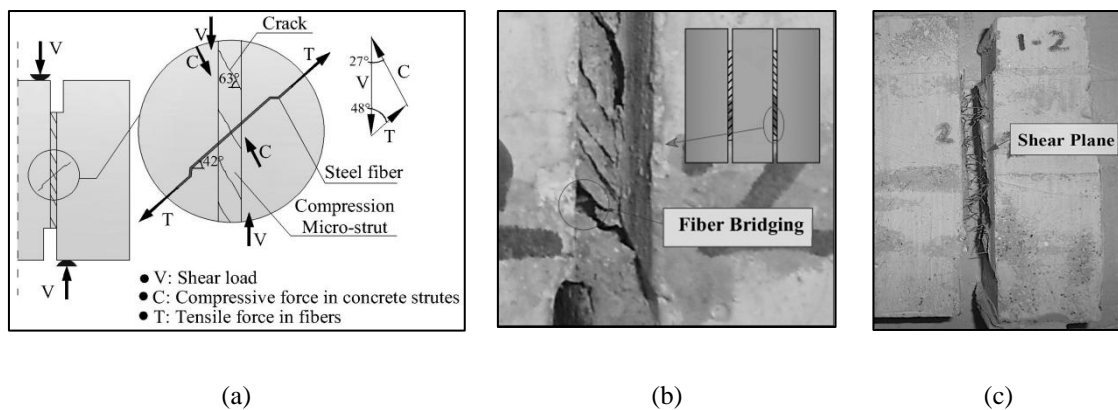
Fig. 4.3- (a) Shear transfer during the initiation of the inclined cracks (b) formation of the crack band along the shear plane; and (c) fractured plane of the specimen.

The average peak load was attained at an average slip of 0.16 mm and an average crack width of 0.12 mm. This means that the shear sliding of the notched plane has widen more than sliding, due to the favorable combined effect of micro-dowel mechanism of the fibers bridging the shear cracks and shear resistance of the micro compressive struts that restrict the shear sliding. Furthermore, the occurrence of micro-spalling of matrix around the fibers at the shear plane during the fiber pullout process, due to fiber snubbing effect, promotes the predominance of crack width over crack sliding (Foster 2009).
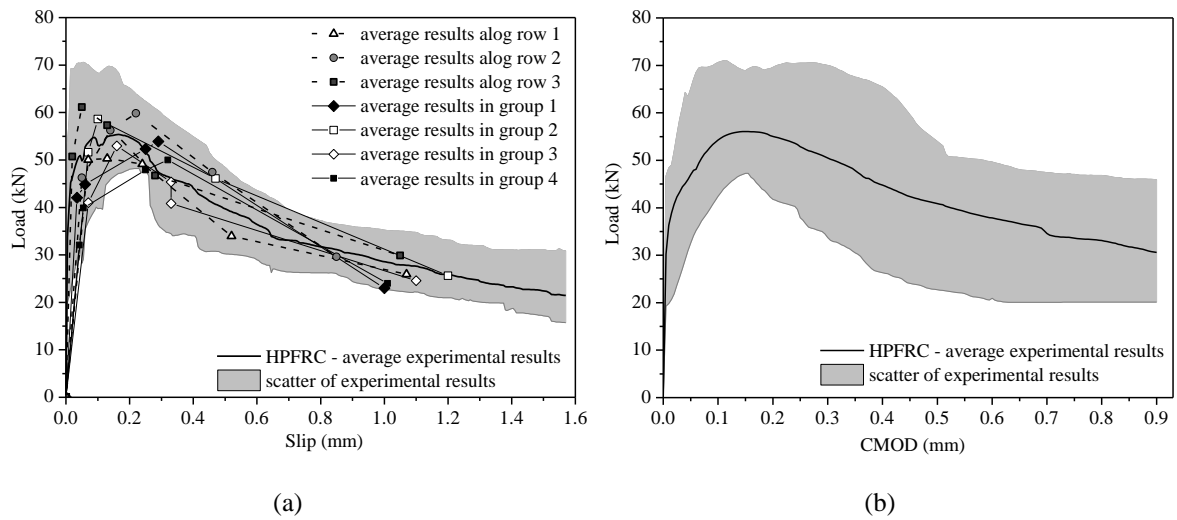
Fig. 4.4- Experimental results of (a) load-slip; and (b) load *vs.* CMOD relationship

Fig. 4.4(a) compares the relationship between the average load and slip, for the specimens located along the 3 rows and in 4 groups that were extracted from the HPFRC prism (Fig. 4.1(a)). Since the specimens from the middle row (row 2) were placed at a higher distance from the lateral walls of the mold, the fiber orientation due to wall effect is expected to be less pronounced resulting a fiber orientation closest to an isotropic nature. Due to the higher probability of having fibers better oriented in terms of being more effective for arresting the propagation and sliding of the shear cracks in these specimens (Fig. 4.3(a)), it was expected a higher shear strength and post peak residual shear resistance when compared to the results of the specimens of rows 1 and 3. However, the small differences obtained experimentally (Fig. 4.4(a)) indicate that fiber distribution and orientation was not too different among all the specimens due to the good equilibrium of flowability and viscosity of the developed HPFRC. Similarly, the comparison of the average results of load-slip relationship of the specimens of the 4 groups demonstrates the proper rheology of the HPFRC, since the small differences on the behavior of specimens located at different distance from the casting point indicate an homogeneous character of fiber distribution and orientation along the prism, a topic that will be further discussed in the following session.

4.2.4   Evaluation of the Fiber Distribution and Orientation

The mechanical properties of the HPFRC were further investigated by considering the distribution and orientation of fibers across the shear plane of the specimens. The fibers distribution and

orientation factors can be evaluated using several available methods, namely: tomography (CT-scan) (Stähli et al. 2007), image analysis (Chermant et al. 2001), X-ray method (Barnett et al 2010), electrical resistivity (Barnett et al 2010), Ultrasound and quantitative acoustic emission technique (Reinhardt et al. 2001), as well as magnetic approach (Faifer et al. 2011). In the present study the image analysis technique was adopted to evaluate these factors due to the simplicity of the image analysis method, as well as the relatively low cost of the required equipments for analyzing the images according to this technique (Reinhardt et al. 2001)

The images were captured from the shear plane of the specimens, through which the shear cracks have propagated, as shown in Fig. 4.5. For detecting the location and orientation of fibers on the shear plane of DSS in accordance with this method, the following main steps (Soltanzadeh et al. 2012 and Cunha 2008) were carried out:

1. the grinded surface of the specimens shear planes were polished and cleaned up using acetone in order to enhance the clarity properties of steel fibers,

2. a colored image was captured from these surfaces using a high resolution digital photograph camera (Canon, 12 Megapixel), and

3. using ImageJ software (Rasband 2008), the obtained images from the shear planes were processed to recognize steel fibers. For this purpose, first of all the captured colored image was converted to 8 bit gray-scale image. Afterward, a black and white image was obtained by means of defining a threshold and a mask function. In this image the circles and ellipses in white color, which represented the cross section of the fibers are distinguished from the surrounding matrix in black color. However, there still remained some areas with bright spots which are not steel fibers. These noises were eliminated by the software or manually. By comparing the obtained images and the original captured photos of the shear planes, very close fiber cross sections which looked like a single fiber cross section were detected and separated. At this stage the software allowed to calculate the number of elliptical spots corresponding to the number of fibers on the shear plane of the specimens. During this analysis some additional information that characterizes the fiber, i.e. minimum and maximum diameter and area of the fibers, can be obtained. The steps of image processing are represented in Fig. 4.6.
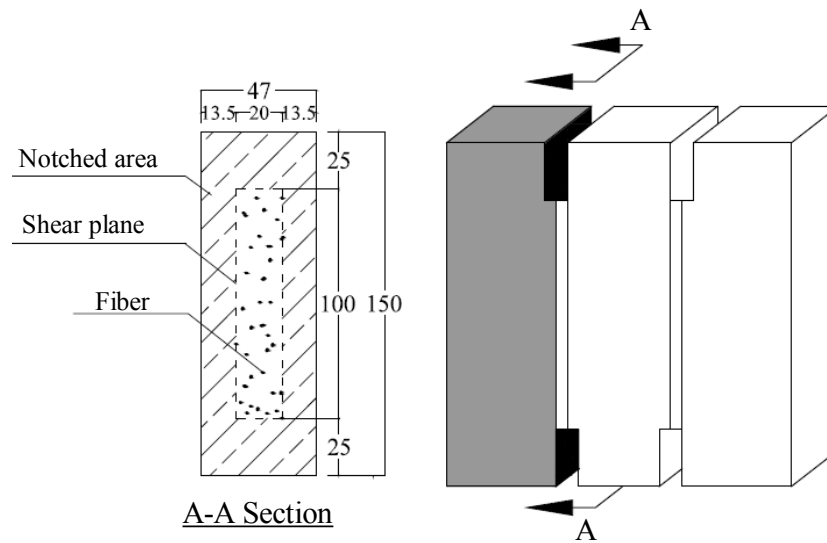
Fig. 4.5- Sawn section of DSS for image analysis (dimensions in mm)
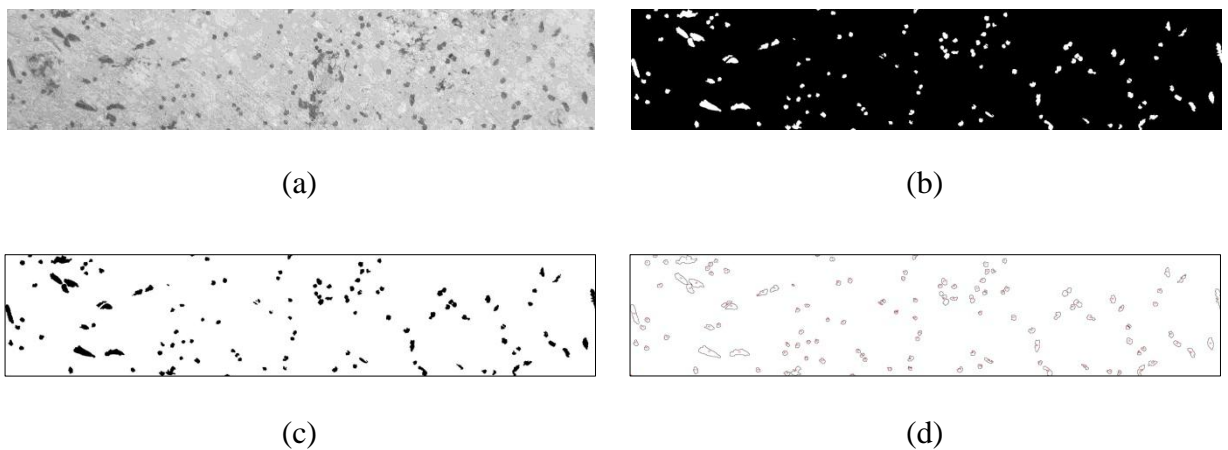
Fig. 4.6- Image processing steps: (a) converting a colored to a grayscale image (b) adjusting a threshold, (c) defining mask, noise (removal of small noises) and watershed (separated fibers that are stuck together) functions, and (d) fitting the beast ellipse to each fiber.

Using the image analyzing method, the fiber density "N_f" in the shear plane (i.e., the ratio between the total number of detected fibers "N_f^T" and the area of this plane "A_f", $N_f = N_f^T / A_f$) was calculated (See Sec. 2.3 in chapter 2). The fiber density of each specimen, as well as the average fiber density in each group of specimens is depicted in Fig. 4.7. The results evidence a marginal variation (11.5%) of fiber distribution along the

longitudinal direction of the prismatic element out of which the specimens were sawn. The figure demonstrates the proper balance of flowability and viscosity of the developed concrete that effectively caused the homogeneous distribution of fibers, as the DSS tests have already indicated.

Fig. 4.8 illustrates the relationship between the average shear toughness "W_{Fs}" per shear plane of the specimens and the average fiber density. According to Rao and Rao (2009), the W_{Fs} represents the area under the shear load–slip curve until a slip corresponding to a certain CMOD. In Fig. 4.8 the W_{Fs} per shear plane is represented for CMOD of 0.1 to 0.4 mm. The direct relation between the shear toughness of the specimens and the fiber density, which is illustrated in this figure, expresses the significant influence of the fiber reinforcement on the shear toughness of the specimens. The favorable influence of the fiber density on the shear toughness occurred for the considered levels of CMOD, and has even a tendency to increase with the CMOD since the shear resisting mechanism due to aggregate interlock decreases with the increase of crack width and, therefore, the fiber reinforcement mechanisms have a predominant effect on the shear resistance.

The fiber orientation, "η_θ", was the other property assessed from the image analysis. This factor was calculated as the average of the orientation of the fibers detected in the shear plane, and is obtained from the following equation (see also Sec.2.3 in chapter 2):

$$\eta_\theta = \frac{1}{N_f^T} . \sum_{i=1}^{N_f^T} \cos \theta_i \tag{4.1}$$

where θ_i is the angle between the longitudinal axis of the ith fiber and a vector orthogonal to the shear plane, called the "out-of-plane angle". From this equation, it can be deduced that as the out-of-plane angle tends to zero degrees, the η_θ tends to the unit value, representing the limit situation of all the fibers orthogonal the crack plane.
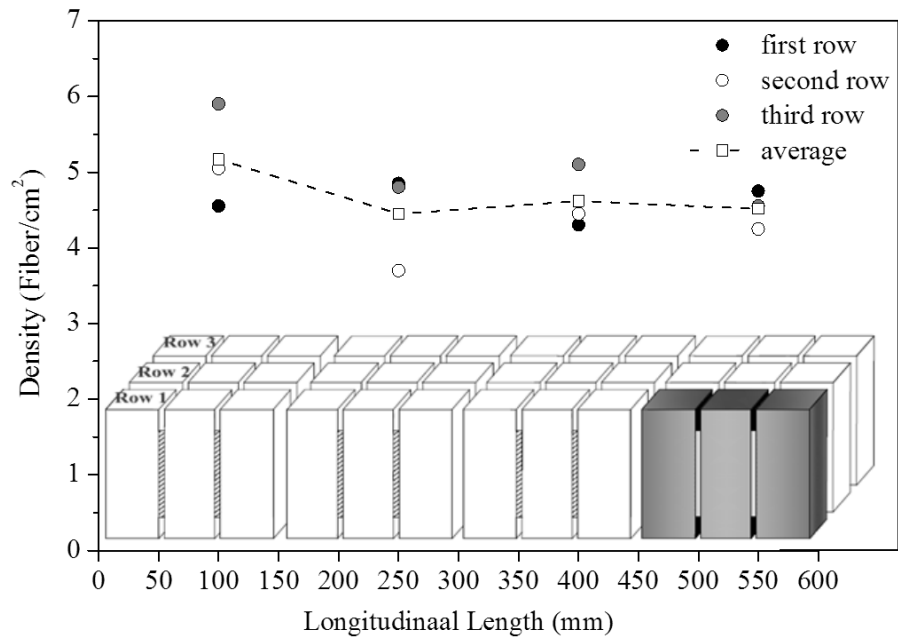
Fig. 4.7- Fiber density along the beam length.
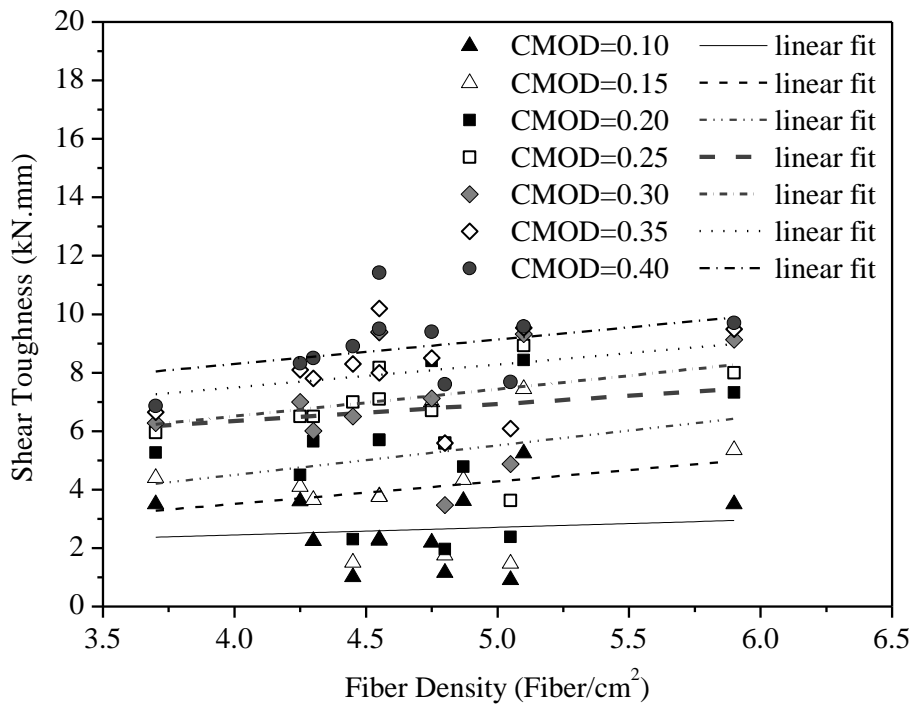
Fig. 4.8- Fiber density *vs.* shear toughness of the specimens.
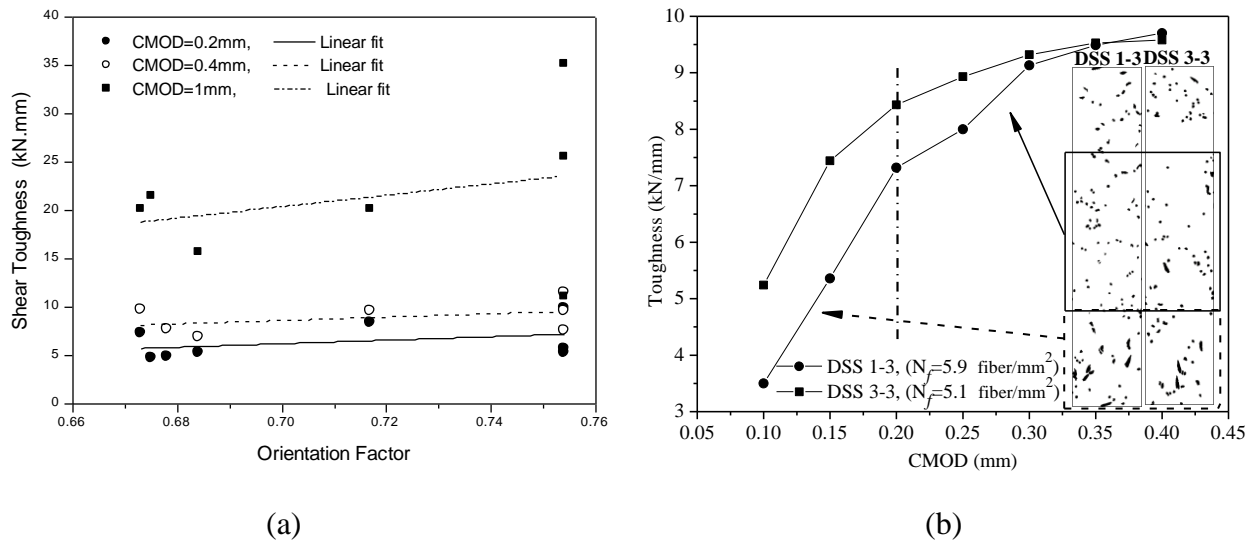
Fig. 4.9- (a) Fiber orientation factor *vs.* shear toughness of the specimens; and (b) Comparison of two shear plane.

Fig. 4.9 presents the relationship between the obtained values for the fiber orientation factor and the shear toughness of the tested specimens. In this figure it is represented the shear toughness for a CMOD of 0.2, 0.4 and 1 mm. It is verified a tendency for the increase of the shear toughness with the fiber orientation factor. The effect of fiber orientation factor seems to have an influence on the shear toughness of HPFRC similar to the fiber density. In fact, it plays the complementary role for improving the shear toughness of the specimens. For instance, the shear toughness of the specimens DSS 1-3 and DSS 3-3 (Fig. 4.1(a)), which were extracted from the same row of the prismatic element, are compared in Fig. 4.9(b). Although a higher fiber density was detected in the shear plane of DSS 1-3, it exhibited lower toughness up to a CMOD of about 0.35 mm. The activated fibers when the average CMOD was less than 0.2 mm are located in the area marked in red, where the number of fibers with elliptical cross section was higher in DSS 1-3. According to the adopted method for determining the fiber orientation (Cunha et al. 2010), as different are the axis of this ellipse (cross section shape of the cut fiber) as higher is the inclination of the fiber), which means that these fibers were not so effective as a reinforcement system for small crack widths that justifies the smaller shear toughness of DSS 1-3 during this stage of loading. However, since DSS 1-3 has higher number of

better oriented fibers in the central zone of the notched plane (signalized with green line), a higher gradient of shear toughness with CMOD was registered in this specimen, resulting similar values of this property at the final loading stage of both specimens. Therefore, the fiber reinforcement efficiency is the result of both fiber distribution and orientation in regard to the crack orientation.

4.3 FEM BASED SIMULATIONS

4.3.1   Numerical Model

This part of study introduced in this chapter, is dedicated to FEM-based simulations in order to explore the possibilities of a multidirectional fixed smeared crack model for capturing the relevant features of the HPFRC DSS tests. This model includes different approaches for modeling the cracked concrete shear behavior, and it is described in detail elsewhere (Ventura-Gouveia 2011), therefore in the present work only a short resume of this model is given.

The description of the formulation of this model is restricted to the case of cracked concrete, at the domain of an integration point (IP) of a plane stress finite element. According to the adopted mode, stress and strain are related by the following equation

$$\Delta \underline{\sigma} = \underline{D}^{crco} \Delta \underline{\varepsilon} \tag{4.2}$$

where $\Delta \underline{\sigma} = \left\{ \Delta\sigma_1, \Delta\sigma_2, \Delta\tau_{12} \right\}^T$ and $\Delta \underline{\varepsilon} = \left\{ \Delta\varepsilon_1, \Delta\varepsilon_2, \Delta\gamma_{12} \right\}^T$ are the vectors of the incremental stress and incremental strain components.

Due to the decomposition of the total strain into an elastic concrete part and a crack part, $\Delta \underline{\varepsilon} = \Delta \underline{\varepsilon}^{co} + \Delta \underline{\varepsilon}^{cr}$, in Eq. (4.2) the cracked concrete constitutive matrix, $\underline{D}^{crco}$, is obtained with the following equation (Sena-Cruz 2004):

$$\underline{D}^{crco} = \underline{D}^{co} - \underline{D}^{co} \left[\underline{T}^{cr} \right]^T \left(\underline{D}^{cr} + \underline{T}^{cr} \underline{D}^{co} \left[\underline{T}^{cr} \right]^T \right)^{-1} \underline{T}^{cr} \underline{D}^{co} \tag{4.3}$$

where $\underline{D}^{co}$ is the constitutive matrix of concrete that depends of the Young's modulus and the Poisson's ratio of concrete, $\underline{T}^{cr}$ is the matrix that transforms the stress components

from the coordinate system of the finite element to the local crack coordinate system, and $\underline{D}^{cr}$ is a matrix that includes the constitutive law of the cracks installed in the *IP*. The constitutive law of a ith crack has two components:

$$\underline{D}_i^{cr} = \begin{bmatrix} D_n^{cr} & 0 \\ 0 & D_t^{cr} \end{bmatrix}_i \tag{4.4}$$

where $D_{n,i}^{cr}$ and $D_{t,i}^{cr}$ represent, respectively, the modulus correspondent to the fracture mode I (normal) and fracture mode II (shear) of the ith crack. The crack opening propagation is simulated with the quadrilinear diagram represented in Fig. 4.10(a), which is defined by the normalized stress, α_i, and strain, ξ_i, parameters that define the transition points between the linear segments of this diagram, where G_f^I, f_{ct} are the fracture energy and the tensile strength of the concrete, while l_b is the crack band width that assures the results of the numerical simulations with a smeared crack approach are not dependent of the refinement of the finite element mesh (Pereira et al. 2008).

To simulate the fracture mode II modulus, D_t^{cr}, a shear retention factor is currently used (Sena-Cruz 2004):

$$D_t^{cr} = \frac{\beta}{1-\beta} G_c \tag{4.5}$$

where G_c is the concrete elastic shear modulus and β is the shear retention factor. The parameter β is defined as a constant value or as a function of the current crack normal strain, ε_n^{cr}, and of the ultimate crack normal strain, $\varepsilon_{n,u}^{cr}$, as follows,

$$\beta = \left(1 - \frac{\varepsilon_n^{cr}}{\varepsilon_{n,u}^{cr}}\right)^{p_1} \tag{4.6}$$

The present model also includes a softening crack shear stress *vs.* crack shear strain relationship, whose diagram is represented in Fig. 4.10(b). The crack shear stress increases linearly until the crack shear strength is reached, $\tau_{t,p}^{cr}$, followed by a decrease in

the shear residual strength (softening branch). This diagram is defined by the following equations:

$$\tau_t^{cr}\left(\gamma_t^{cr}\right)=\begin{cases} D_{t,1}\,\gamma_t^{cr} & 0<\gamma_t^{cr}\le\gamma_{t,p}^{cr} \\ \tau_{t,p}^{cr}-\dfrac{\tau_{t,p}^{cr}}{\left(\gamma_{t,u}^{cr}-\gamma_{t,p}^{cr}\right)}\left(\gamma_t^{cr}-\gamma_{t,p}^{cr}\right) & \gamma_{t,p}^{cr}<\gamma_t^{cr}\le\gamma_{t,u}^{cr} \\ 0 & \gamma_t^{cr}>\gamma_{t,u}^{cr} \end{cases} \tag{4.7}$$

The initial shear fracture modulus, $D_{t,1}^{cr}$, is defined by Eq. (4.5) by assuming for β a constant value in the range $]0,1[$. The peak crack shear strain, $\gamma_{t,p}^{cr}$, is obtained $\tau_{t,p}^{cr}$ from:

$$\gamma_{t,p}^{cr}=\frac{\tau_{t,p}^{cr}}{D_{t,1}^{cr}} \tag{4.8}$$

The ultimate crack shear strain, $\gamma_{t,u}^{cr}$, depends on the $\tau_{t,p}^{cr}$, shear fracture energy (mode II fracture energy), $G_f^{II}=G_{f,s}$, and l_b:

$$\gamma_{t,u}^{cr}=\frac{2G_{f,s}}{\tau_{t,p}^{cr}\,l_b} \tag{4.9}$$

In the present approach it is assumed that l_b is the same for both fracture mode I and mode II processes, but specific research should be done in this respect in order to assess the influence of these model parameters on the predictive performance of the behavior of elements failing in shear. In the present simulations the l_b was considered equal to the square root of the area of the IP. Five shear crack statuses are proposed and their meaning is schematically represented in Fig. 4.10(b).

The crack mode II modulus of the first linear branch of the diagram is defined by Eq. (4.5), while for the second linear softening branch it is obtained from:

$$D_{t,2}^{cr}=-\frac{\tau_{t,p}^{cr}}{\gamma_{t,u}^{cr}-\gamma_{t,p}^{cr}} \tag{4.10}$$

The crack shear modulus of the unloading and reloading branches is obtained from

$$D_{t,3-4}^{cr} = \frac{\tau_{t,max}^{cr}}{\gamma_{t,max}^{cr}} \tag{4.11}$$

being $\gamma_{t,max}^{cr}$ and $\tau_{t,max}^{cr}$ the maximum crack shear strain already attained and the corresponding crack shear stress determined from the softening linear branch. Both components are stored to define the unloading/reloading branch (see Fig. 4.10(b)).

In free-sliding status ($|\gamma_t^{cr}| > |\gamma_{t,u}^{cr}|$) the crack shear modulus, $D_{t,5}^{cr}$, is null. To avoid numerical instabilities in the calculation of the stiffness matrix and in the calculation of the internal forces, when the crack shear status is free-sliding, a residual value is assigned to this term.

A free-sliding status is assigned to the shear crack status when $\varepsilon_n^{cr} > \varepsilon_{n,u}^{cr}$. The details about how the shear crack statuses were treated can be consulted elsewhere (Ventura-Gouveia 2011).
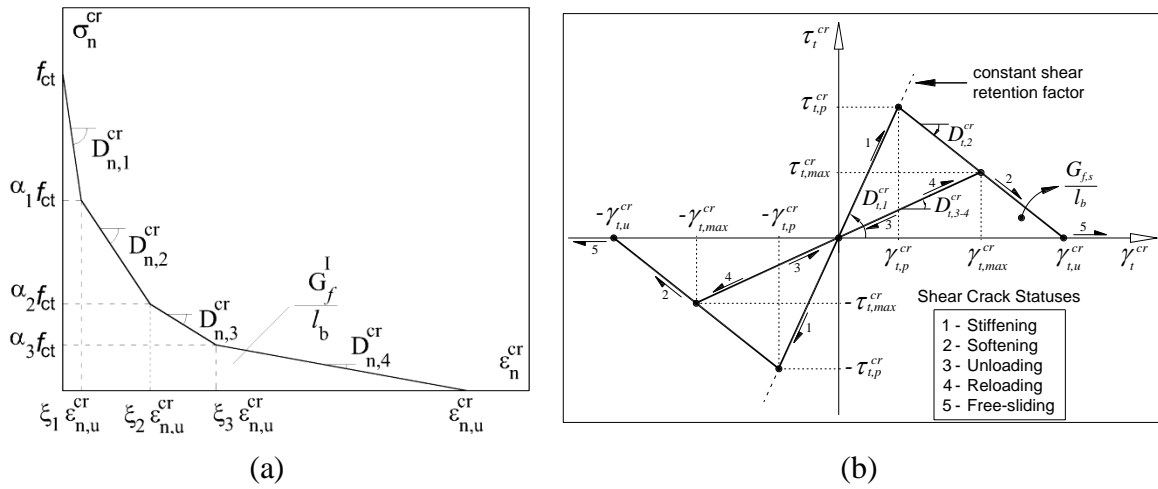
Fig. 4.10- Diagrams for modeling the (a) fracture mode I ($\sigma_{n,2}^{cr} = \alpha_1 f_{ct}$, $\sigma_{n,3}^{cr} = \alpha_2 f_{ct}$, $\sigma_{n,4}^{cr} = \alpha_3 f_{ct}$, $\varepsilon_{n,2}^{cr} = \xi_1 \varepsilon_{n,u}^{cr}$, $\varepsilon_{n,3}^{cr} = \xi_2 \varepsilon_{n,u}^{cr}$, $\varepsilon_{n,4}^{cr} = \xi_3 \varepsilon_{n,u}^{cr}$); and (b) fracture mode II at the crack coordinate system.

4.3.2 Assessment of the Mode I Crack Constitutive Law

The Mode I fracture parameters were assessed by means of an inverse analysis of the

flexural test results obtained experimentally with the three point notched HPFRC beam bending tests presented in chapter 3, Sec. 3.3.2. This method is adopted in accordance with the previous studies of Barros et al. (2005). Since the fracture mode I propagation of hardened HPFRC was simulated by the quadrilinear stress-softening diagram represented in Fig. 4.10(a), the inverse analysis procedure was followed by evaluating the parameters ξ_i, α_i (i=1 to 3), the tensile strength, f_{ct}, and the fracture energy, G_f^I, that minimize the ratio between the area underneath the experimental load-deflection curve and the numerical one.
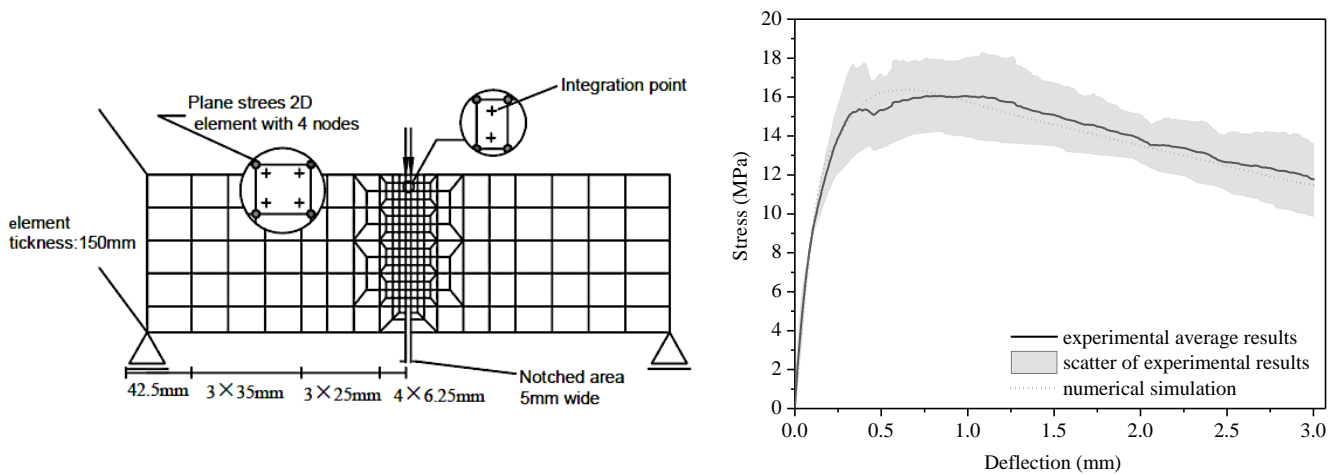
Fig. 4.11- (a) Finite element mesh relevant characteristic, load and support conditions of the type of specimen adopted in the inverse analysis, and (b) comparison between numerical and experimental results of stress *vs.* midspan deflection relationship.

The numerical curve was obtained by a FEM analysis, considering the specimen's geometry, and loading and support conditions in agreement with the experimental flexural test setup. Fig. 4.11 presents the simulated specimen, modeled by a mesh of four node plane stress finite elements with $2 \times 2\,IP$. To assure the formation of a single crack line along the specimen symmetry axis, the Gauss-Legendre integration scheme of $1 \times 2\,IP$ was adopted for the elements located in the notched area. Apart the elements located above the notch, where the elastic cracked behavior in tension was assumed, a linear elastic material behavior was assigned to the other elements. The parameters ξ_i, α_i, f_{ct},

G_f^I, E, obtained from this inverse analysis are presented in Table 4.2, and the corresponding numerical force-deflection is compared to the corresponding experimental results in Fig. 4.11(a) (see also Sec. 3.3.2 in chapter 3), where it is verified that a good agreement was obtained between the experimental and numerical load-deflection curves.

Table 4.2- Values of the fracture parameters defining the stress-strain softening laws

α_1	α_2	α_3	ξ_1	ξ_2	ξ_3	f_{ct} (MPa)	G_f^I (N/mm)	E (GPa)
0.78	0.89	0.57	0.028	0.058	0.36	7.3	7.2	40

4.3.3 Simulation of the HPFRC shear behavior

The experimental shear tests with HPFRC DSS specimens were simulated numerically by using the model briefly described in Sec. 4.3.1, and using for the fracture mode I parameters the values determined by inverse analysis, presented in Table 4.2. A FEM mesh composed of 430 plane stress elements of 4 nodes was generated in order to simulate the specimen, as shown in Fig. 4.12. A Gauss-point integration scheme of $2 \times 2\,IP$ was used in all of the elements, excluding the elements along the notched ligament, where $1 \times 2\,IP$ was used. The elastic-cracked material behavior was defined for the finite elements located along the shear ligament, while the others finite elements were assigned with an elastic type of material behavior. Due to the structural symmetry of the specimen, only half of the DSS was simulated.

Fig. 4.13 compares the load-slip and load-CMOD relationships obtained from the numerical simulations and experimental tests. When the conventional shear retention factor was used (considering any type of p parameter in Eq. (4.6)), it was verified that the model did not match the experimental results, and good agreement was found only at the initial part of the curves. By using a shear softening law, characterized by the fracture mode II parameters, the model was capable of capturing the behavior of HPFRC subjected to direct shear loading with a good estimation of the peak load as well as the structural softening behavior, mainly in terms of sliding, since the stress decay predicted

numerically in the CMOD softening stage was not so pronounced as recorded experimentally. The inverse analysis process executed with the simulations of these experimental tests has allowed the determination of the fracture mode II parameters that define the crack shear stress shear versus crack shear strain diagram adopted in the present model (Fig. 4.10(b)), and the following results were obtained: $\beta = 0.001$, $\tau_{t,p}^{cr} = 7.7$ MPa, and $G_{f,s} = 6.5$ N/mm. It is also noted that the obtained value of $\tau_{t,p}^{cr}$ represents the shear strength at the level of crack, while $\tau_{max} = 14.5$ MPa, which is registered experimentally, represents the average shear strength of the specimen.
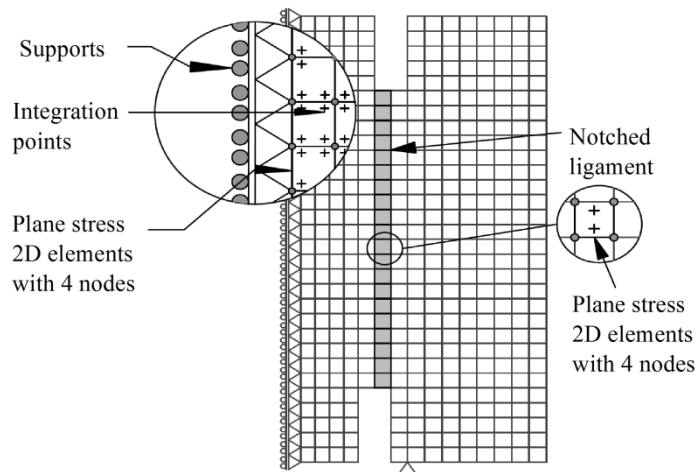
Fig. 4.12- Finite element model for simulating mixed mode fracture tests.
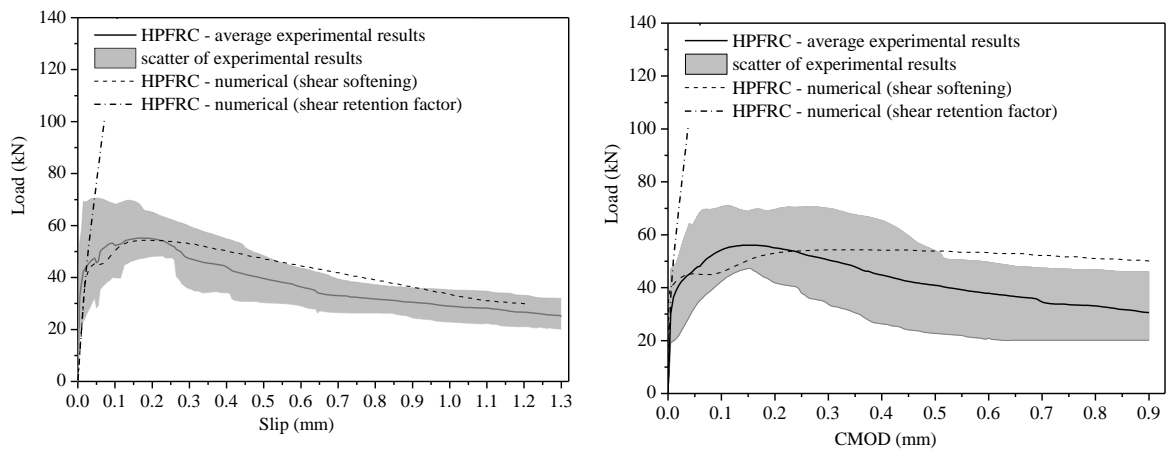
Fig. 4.13- Comparison between numerical and experimental results of (a) load *vs.* slip; and (b) load *vs.* CMOD relationships

4.4 CONCLUSIONS

In the present chapter shear behavior of the HPFRC was assessed by applying a shear loading configuration on a shear specimen designed for this purpose. The obtained results indicate that the application of steel fibers, which limits the opening of the tensile cracks, causes shear-dominated failure with considerable ductility. Due to the pullout resistance and dowel action of fibers, a relatively high residual load carrying capacity is obtained in this type of tests. From the obtained results the average shear strength of 14.5 MPa was obtained with a shear toughness of 15.3 kN.mm up to a CMOD of 0.3 mm (the maximum value allowed by CEB-FIP Model Code for accomplishing serviceability limit state conditions), revealing a high energy absorption capacity in shear loading configuration. The shear strength was attained at an average slip of 0.18 mm, when the average crack opening was 0.15 mm, indicating the high effectiveness of the developed HPFRC in terms of shear capacity and stiffness, as well as in limiting the crack width up to its maximum shear capacity, which has favorable effects in terms of durability of this composite.

To assess the influence of fiber orientation and dispersion on the shear performance of HPFRC, image analysis was executed on the notched shear plane of the tested DSS specimens. It was verified that due to the good balance in terms of flowability and viscosity for the developed HPFRC, an almost homogeneous fiber distribution and orientation was assured.

The material parameters of the fracture mode I were obtained by means of an inverse analysis applied to the force-deflection relationship recorded in the HPFRC notched beam bending tests, while the parameters of the fracture mode II were determined by executing an inverse analysis applied to the force-slip-CMOD registered in the DSS tests.

C H A P T E R 5

SHEAR RESISTANCE OF HPFRC SHORT-SPAN BEAMS WITHOUT STIRRUPS

5.1 INTRODUCTION

Corrosion of steel reinforcements embedded in concrete elements is generally known as the reason of most failures of concrete structures. To overcome this problem, the present study aims do not use steel stirrups, which are the most susceptible elements to corrosion, in the HPFRC beams investigated in the present research. The HPFRC was developed in accordance with the strategy described in the 3rd chapter of this thesis. To reduce the risk of corrosion in longitudinal reinforcements, a hybrid flexural reinforcement system was adopted for the beams. This reinforcing system, composed of glass fiber reinforced polymer (GFRP) rebars placed near to the outer surface of the tensile zone, complemented with steel reinforcements positioned with higher HPFRC cover to be protected against the corrosion, is considered another strategy for enhancing the durability and attending fire issues in terms of safety at ultimate limit states. In addition to all the adopted arrangements for improving the ductility (such as using a HPFRC of high strength and high post-cracking resistance, as well as the application of the hybrid GFRP-steel flexural reinforcements), the GFRP bars are prestressed to obviate the deficiencies created by their low modulus of elasticity. In this chapter the effectiveness of varying the prestressing force applied to GFRP bars to improve the shear capacity and failure mode

of the designed elements is evaluated. A numerical strategy is accompanied to analyze the applicability of the developed system for increasing the shear capacity of the short-span beams.

Due to the significant effect of shear span to effective depth ratio (a/d) on shear behavior of the concrete elements without stirrups, the shear behavior of the members developed by the introduced system is evaluated by means of two groups of short-span beams (with shear span to effective depth ratio of equal or less than 2.5, $a/d \leq 2.5$) and slender ones ($a/d > 2.5$). The present chapter is dedicated to the design of short-span beams and investigation of the behavior of the beams under shear load; whereas the shear behavior of slender beams is discussed in the next chapter (chapter 6). By considering the results obtained from testing the short-span beams, the predictive performance of RILEM TC 162-TDF (2003) and MC2010 (CEB-FIP Model Code 2010; the abbreviator MC2010 will be adopted), guidelines, as well as the formulation proposed by Soetens (2015) for the shear resistance of the HPFRC short-span beams is also assessed in the present chapter.

5.2 DESIGN METHOD

The present section introduces the method for determining the appropriate shear span and fiber dosage of the beams for the experimental program to be carried out in the scope of this research project. For this purpose it was considered the influence of these factors on the relative flexural capacity (i.e. the dimensionless ratio of the ultimate moment to the flexural moment, M_u / M_{fl}) and, consequently, the shear resistance of these elements. Accordingly, an optimum dosage of steel fiber was determined, and applied to increase the ultimate strength of the short-span beam without stirrups, and to attain as close as possible its full flexural capacity ($M_u / M_{fl} \approx 1$) regardless to the type of the elements, i.e. whether a beam is short span or slender one.

5.2.1   Relative Flexural Capacity and Failure Mode

In the 2nd chapter of the present thesis an analytical model (Imam et al. 1997), was introduced for predicting the relative flexural capacity (M_u / M_{fl}) of high strength fiber reinforced concrete beams without stirrups. According to this model the nominal flexural

moment, M_{fl}, can be calculated using Eqs. (2.7) and (2.8), whereas the internal ultimate resisting moment at failure, M_u, is calculated by Eq. (2.9).

In the present study Eqs. (2.7) and (2.8) are adapted to estimate the flexural moment of the HPFRC beams flexurally reinforced with the adopted hybrid system of GFRP and steel bars by introducing " $\rho_{seq,GFRP} \cdot f_{GFRP}$ " corresponding to the GFRP reinforcement in the 1st term of these equations, where " $\rho_{seq,GFRP} = A_{GFRP} \cdot E_{GFRP} / (b.d_{GFRP} E_s)$ " is the GFRP reinforcement ratio converted into an equivalent steel reinforcement ratio, "A_{GFRP}" is its cross sectional area, " E_{GFRP} " is its modulus of elasticity, and " d_{GFRP} " is the distance of the centroid of the GFRP bars to the top face of the section, while E_s is the modulus of elasticity of steel reinforcements (see Fig. 5.1). Hence, the nominal flexural strength of the beams can be predicted by:

$$M_{fl} = \frac{1}{2}(\rho_{seq,GFRP} f_{GFRP} + \rho_s f_{sy})bd_{s,eq}^2(2-\Gamma_{eq}) + 0.83F_f bd_{s,eq}^2(0.75-\Gamma_{eq})(2.15+\Gamma_{eq}) \tag{5.1}$$

In Eq.(5.1) the f_{GFRP} is the tensile strength in the GFRP bars, calculated according to the equation proposed by ACI440.IR-06:

$$f_{GFRP} = \sqrt{\frac{1}{4}(\frac{A_s f_{sy}}{A_{GFRP}} + E_{GFRP}\varepsilon_{cu})^2 + (0.85\frac{\beta_1 f_{cm}}{\rho_{seq,GFRP}} - \frac{A_s f_{sy}}{A_{GFRP}})E_{GFRP}\varepsilon_{cu}} - \frac{1}{2}(\frac{A_s f_{sy}}{A_{GFRP}} + E_{GFRP}\varepsilon_{cu}) \le f_{GFRP,u} \tag{5.2}$$

and $d_{s,eq}$ is the equivalent steel effective depth:

$$d_{s,eq} = \frac{A_s d_s + (E_{GFRP} / E_s)A_{GFRP}d_{GFRP}}{A_s + (E_{GFRP} / E_s)A_{GFRP}} \tag{5.3}$$

where d_s is the distance between the centroid of the steel bars and the top face of the section.

In Eq. (5.2) $f_{GFRP,u}$ is the ultimate tensile strength of GFRP reinforcement, ε_{cu} is the concrete compressive crushing strain, assumed equal to 0.0035 in the present study. The parameter β_1, depends of the concrete compressive strength (f_{cm}) and represents the ratio of the equivalent rectangular stress block depth to the depth of the neutral axis (for

$f_{cm} \leq 30\,\text{MPa}$, $\beta_1 = 0.85$, while for $f_{cm} > 30\,\text{MPa}$, $\beta_1 = 0.85 - (f_{cm} - 30)/7 \times 0.05$. Accordingly, the effect of the stress in tensile GFRP bars, f_{GFRP}, and the GFRP reinforcement ratio, ρ_{GFRP}, are considered in the parameter "Γ_{eq}".

$$\Gamma_{eq} = \frac{(\rho_s f_{sy} + \rho_{seq,GFRP} \cdot f_{GFRP}) + 2.32 F_f}{0.85 f_{cm} + 3.08 F_f} \tag{5.4}$$

where ρ_s is reinforce ratio of longitudinal steel reinforcements.
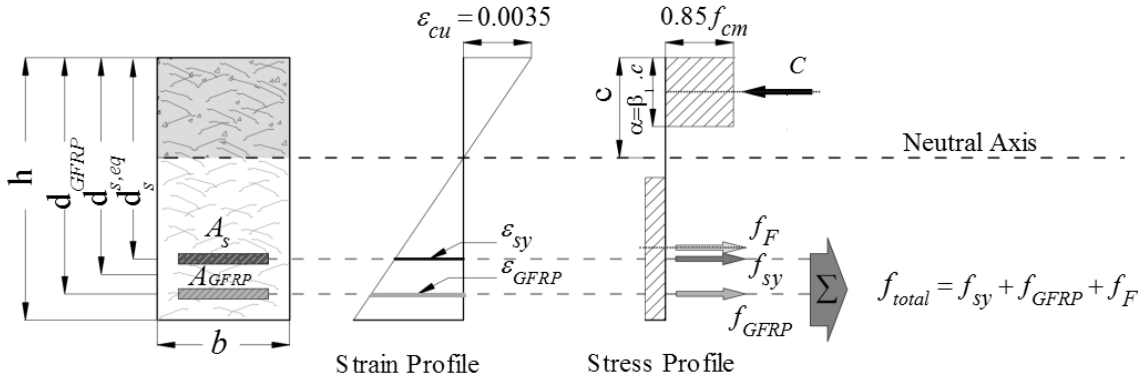
*f_F: steel fibers tensile stress,

**C:compressiv stress in concrete.

Fig. 5.1- Strain and stress distribution at ultimate condition (CEB-FIP Modal Code 2010).

In the present study, Eq. (2.9) is also improved to be applicable for fiber reinforced concrete beams flexurally reinforced with a hybrid system, using the following equation (Imam et al. 1997).

$$M_u = 0.6 b d_{s,eq}^2 \psi \sqrt[3]{\omega} \left[f_{cm}^{0.44} (a/d_{s,eq}) + 275 \sqrt{\omega/(a/d_{s,eq})^3} \right] \tag{5.5}$$

in which ψ is size effect factor that can be calculated according to the following equation:

$$\psi = \frac{1+\sqrt{5.08/d_a}}{\sqrt{1+d/(25d_a)}} \qquad (5.6)$$

where d_a is the maximum aggregate size.

and

$$\omega = \rho_{s,eq}(1+4F_f) \qquad (5.7)$$

is a reinforcement factor where the equivalent steel reinforcement ratio, $\rho_{s,eq}$, (Qu et al. 2009) is obtained from the following equation:

$$\rho_{s,eq} = \frac{A_s}{bd_s} + \frac{E_{GFRP}}{E_s}\frac{A_{GFRP}}{bd_{GFRP}} \qquad (5.8)$$

Fig. 5.2 represents the relation between the M_u/M_{fl} and $a/d_{s,eq}$ for a beam with F_f values ranging from 0 to 1, and assuming $f_{cm} = 65$ MPa, $f_{sy} = 490$ MPa, $f_{GFRP} = 897$ MPa, $d_{s,eq} = 235$ mm and $\rho_{s,eq} = 0.1\%$ (representative values of the materials available for the experimental program). Since M_{fl} is not affected by $a/d_{s,eq}$, and only M_u changes with this parameter, two different values of $a/d_{s,eq}$ can be obtained for the same M_u/M_{fl}. Considering that $M_u = V_u.a = (P/2).a$ (in the three point bending test), it is clear that the beam is capable of carrying higher load, P, when the beam has a shorter shear span and, consequently, a lower $a/d_{s,eq}$ ratio at the same level of M_u/M_{fl}. Accordingly, two different failure modes of diagonal-tension, DT, and shear-compression (or shear-tension), SC (or ST), can be addressed at two different values of $a/d_{s,eq}$ as shown in Fig. 5.2. The minimum relative flexural capacity of the beam, $(M_u/M_{fl})_{min}$, corresponding to only one critical shear span to effective depth ratio, $(a/d_{s,eq})_c$, delimits the DT from the SC (or ST) modes of failure. Fig. 5.2 also indicates two limiting values, $(a/d_{s,eq})_R$ at the right side, and $(a/d_{s,eq})_L$ at the left side, where $M_u/M_{fl} = 1$. Between these two limiting values, $(a/d_{s,eq})_L < a/d_{s,eq} < (a/d_{s,eq})_R$, the two types of shear failure govern the behavior of

the beams, depending on the $a/d_{s,eq}$ ratio. The detailed description of the failure modes is provided in Sec. 2.8 of chapter 2 of the present thesis.
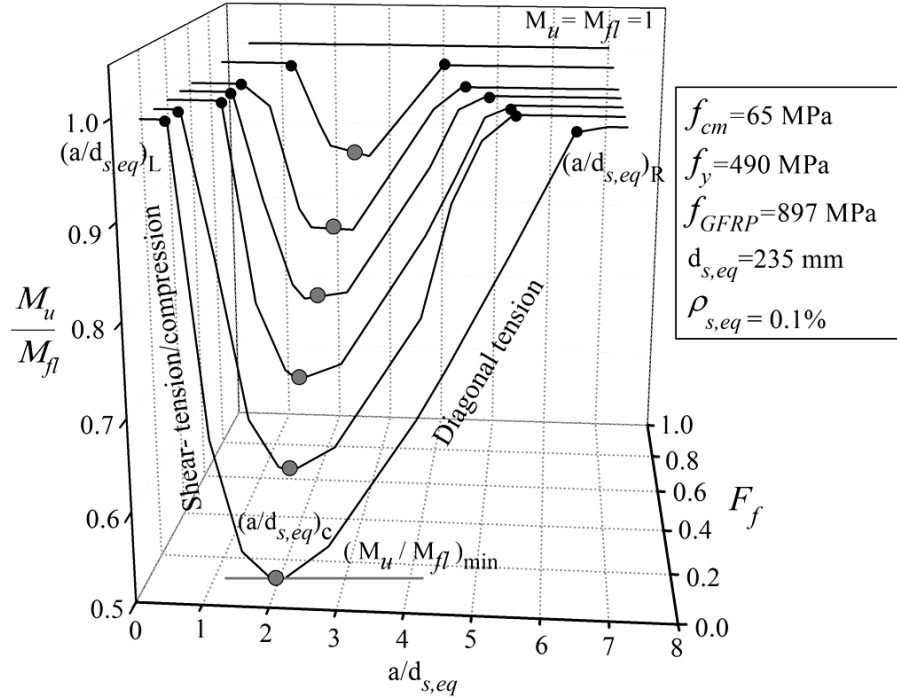
Fig. 5.2- Combined effect of $a/d_{s,eq}$ and F_f on the relative flexural capacity of a beam.

5.2.2 Dosage of Steel Fiber

In addition to the significant effect of $a/d_{s,eq}$ on the relative flexural capacity, and consequently on the shear strength of the beams (see Fig. 5.2), from the abovementioned formula it is clear that the relative flexural capacity of the beam is also affected by a large number of parameters, most importantly the volume fraction of fibers. Fig. 5.2 illustrates the influence of the combined effect of fiber factor, F_f, and $a/d_{s,eq}$ on the relative flexural capacity of a beam M_u/M_{fl} (the variation of F_f is only caused by changing V_f). The figure shows the significant increase of M_u with the fiber factor (caused by the increase of V_f) compared to that of M_{fl}, leading to the increase of the beam's relative flexural capacity, M_u/M_{fl}. This exhibits the pronounceable effect of fibers on enhancing the shear capacity of the beam, which may successfully reduce the requirement of conventional shear reinforcements for the beams to be developed in the scope of the

present work. This idea is used to attain the aimed improvements in the shear strength of the short-span beams without stirrups to be tested in this experimental program.

5.3 EXPERIMENTAL PROGRAM

5.3.1 HPFRC Mix Design and Properties

The mix design methodology proposed in the 3rd chapter of the present thesis was used for the development of the HPFRC with rheological and mechanical properties suitable for the production of precast prestressed concrete elements, such as self-compacting character (SCC) and relatively high compressive and post-cracking residual strength. The concrete was reinforced with a fiber volume fraction, V_f, of 1.1% of hooked end steel fibers with 33 mm length, l_f, aspect ratio (l_f/d_f) of 64, and tensile strength of 1100 MPa (according to the supplier). The developed composition is reported in Table 3.9 of chapter 3.

Table 5.1- Compressive strength and Youngs modulus of the developed HPFRC.

Concrete age (day)		f_{cm}[a] (MPa)	f_{ck}[b] (MPa)	E_{cm}[c] (GPa)
3	Average	34.08	26.08	24.39
	CoV[d] (%)	2.7	2.7	1.3
7	Average	52.42	44.42	31.78
	CoV (%)	2.2	2.2	1.6
28	Average	64.95	56.95	34.91
	CoV (%)	1.4	1.4	1.7

[a] Mean value of compressive strength.

[b] Characteristic value of compressive strength.

[c] Mean value of Young's modulus.

[d] Coefficient of variation (for 3 specimens).

The fresh state performance of the HPFRC mix was characterized by means of the slump-flow test. The mix reached a spread diameter of 500 mm within 3.5 sec (T_{50}), and the total spread diameter of the mix was 660 mm. The mechanical performance of the concrete at hardened state was evaluated by determining the Young's modulus (EN 12390-13, 2014), compressive strength (ASTM C39 / C39M - 14a), as well as the flexural behavior (CEB-FIP Modal Code 2010) at the ages of 3, 7 and 28 days. Table 5.1 includes the average values of the compressive strength, f_{cm}, and Young's modulus, E_{cm}, of nine HPFRC cylindrical specimens of 150 mm diameter and 300 mm height (three specimens at each age). The characteristic compressive strength, f_{ck}, is also presented in this table. The results show that the strength and stiffness have increased rapidly with age, which suggests that the developed concrete is appropriate to the requirements of the prefabrication industry in terms of fast demolding of cast RC elements.

Table 5.2- Limit of proportionality and residual flexural strength parameters of the developed HPFRC.

Concrete age (day)		$f_{ct,L}^{f}$ (MPa)	f_{R1} (MPa)	f_{R2} (MPa)	f_{R3} (MPa)	f_{R4} (MPa)	f_{R3}/f_{R1}
			CMOD$_1$= 0.5 mm	CMOD$_2$= 1.5 mm	CMOD3= 2.5 mm	CMOD$_4$= 3.5 mm	
3	Average	3.74	7.42	8.59	7.75	7.09	1.04
	CoV (%)	4.9	16	15.5	16.2	17.8	-
7	Average	8.58	12.79	13.77	12.87	11.88	1.01
	CoV (%)	18.9	13.4	11.2	11.9	13.7	-
28	Average	8.69	15.18	17.17	14.82	12.82	0.98
	CoV (%)	18.6	6.3	7.5	0.9	13.1	-

The flexural behavior of the developed concrete is assessed by determining the flexural strength and the residual flexural tensile strength parameters of the HPFRC, f_{R1} to f_{R4}, corresponding to distinct values of crack mouth opening displacement ($CMOD_j$ ($j= 1$ to 4)) according to the recommendations of MC2010. These values are indicated in Table 5.2, and a clear tendency for their increase with the age is observed, having this increase been more pronounced at the earlier ages. According to the MC2010 this HPFRC is of toughness class "13c" ($f_{R3k} / f_{R1k} = 0.9$). The nominal flexural stress, σ_f, versus CMOD relationship of HPFRC beams corresponding to the three testing ages can be found in chapter 3, Fig. 3.17.

5.3.2   Test Specimens

The experimental program is composed of six beams of a span length, L, of 1050 mm and a rectangular cross section of 150 mm wide, b, and 300 mm height, h. Two longitudinal steel bars of 12 mm diameter, $\phi12$, and one of 10 mm diameter, $\phi10$, positioned at a depth of 230 mm, d_s, and a ribbed GFRP rebar of 12 mm diameter, $\phi12$, with a depth of 270 mm, d_{GFRP}, were used for the flexural reinforcement. The general configuration of the beams and the arrangement of the reinforcements are represented in Fig. 5.3. By considering the internal arm (d_s, d_{GFRP}) and the cross sectional area (A_s, A_{GFRP}) of the steel and the GFRP bars, an equivalent internal arm, $d_{s,eq}$, of 235 mm was obtained (Eq. (5.3)). The mechanical properties of the GFRP and steel longitudinal reinforcements are reported in Tables 5.3 and 5.4, respectively.

The prestress levels of 0% (control beam), 20% and 30% of GFRP ultimate tensile strength ($f_{GFRP,u}$ =1350 MPa) were adopted for the experimental program, by respecting the recommendations of the CAN/CSA-S6-06 guideline and ISIS Educational Module. Table 5.5 presents the details of each series of fabricated beams, introduced by the label "Bi-Pj", where "i" identifies the number of the tested beams in each series (two beams were tested per each series) and "j" is the percentage of prestress applied to the GFRP bar.

Table 5.3- Mechanical properties of GFRP bars.

Diameter	Density	E_{GFRP} [a]	$f_{GFRP,u}$ [b]
mm	gr/cm^3	GPa	N/mm^2
12	2.23	56	1350

[a] E_{GFRP} Modulus of elasticity.

[b] $f_{GFRP,u}$ Ultimate tensile strength.

Table 5.4- Mechanical properties of steel bars.

Diameter	Density	f_{sy} [a]	E_s [b]	f_{su} [c]
mm	gr/cm^3	N/mm^2	GPa	N/mm^2
10	7.85	500	217	594
12	7.85	490	196	591

[a] f_{sy} Yield tensile stress.

[b] E_s Modulus of elasticity.

[c] f_{su} Ultimate tensile strength.

To determine the shear span of the beams and define the best test setup, as well as the variation of the relative flexural capacity of the beam, M_u/M_{fl}, regarding to the range of the shear span to the equivalent effective depth ratio, $a/d_{s,eq}$, the analysis shown in Fig. 5.5 were carried out. According to this figure, the critical shear span to the equivalent effective depth ratio, $(a/d_{s,eq})_c$, as well as the two limiting values of $(a/d_{s,eq})_L$ and $(a/d_{s,eq})_R$ are, respectively, 2.77, 2.23 and 3.40 for the series of beam with the introduced reinforcing ratio and fiber volume fraction. A shear span to equivalent effective depth

ratio $(a/d_{s,eq}) = 2.23$ equal to the limiting value of $(a/d_{s,eq})_L$ was selected for the test setup of the experimental program, by adopting a=525 mm. Taking into account that $a/d_{s,eq}$ ratio in the designed beams lies on the border between shear and flexural mode of failure, there is the probability of occurring the combination of shear and flexural failure, rather than pure flexural or shear failure for these beams (without prestress). In two other series of beams, with 20% and 30% of prestress, the axial compression increases the depth of the uncracked compression zone, decreases the width of the shear cracks, and thus the shear stress transference is increased. It is well known that all of these factors lead to an increase in shear capacity of the beams, but how much the shear resistance is influenced by the axial prestress load was not yet addressed, as well as its influence on the failure mode of the members.
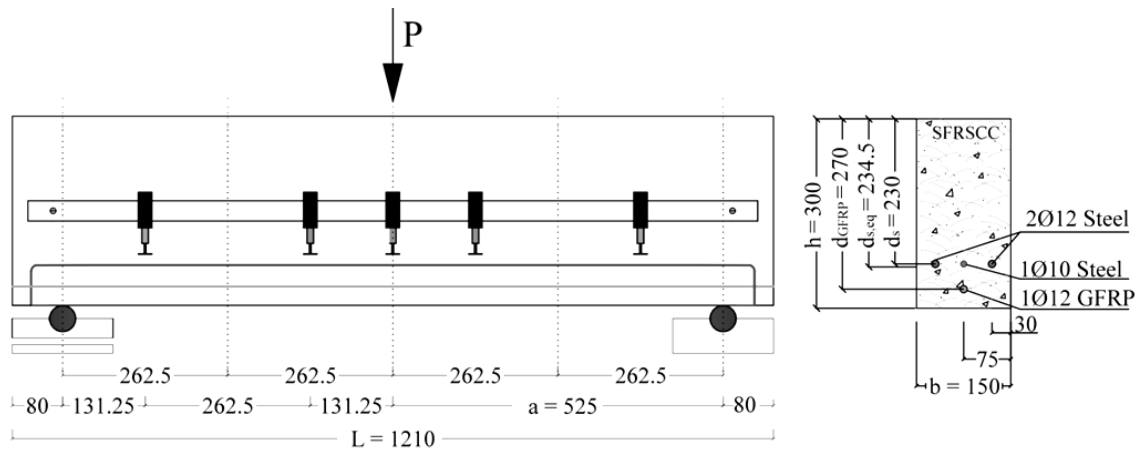
Fig. 5.3- Beam configuration and test setup (dimensions in mm).
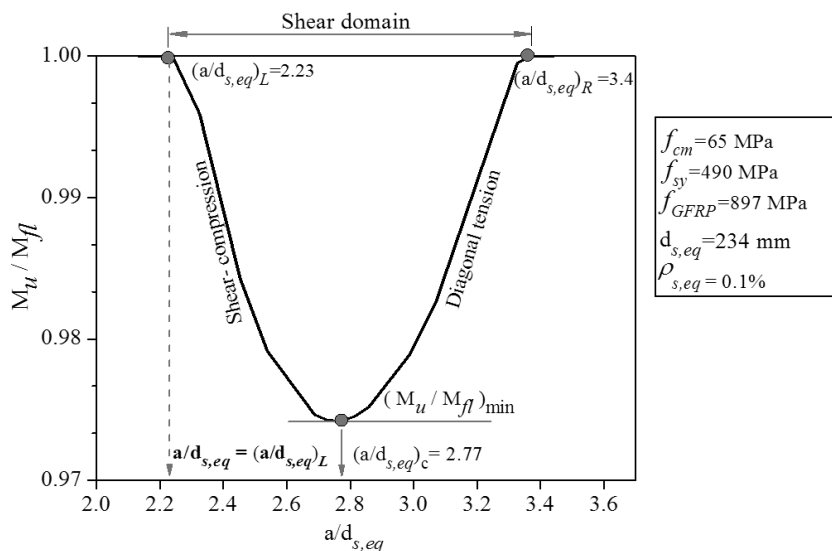
Fig. 5.4- Relative flexural capacity of beams *vs.* $a/d_{s,eq}$.

To improve the relative flexural capacity of the designed beams, M_u/M_{fl} , as a major aim of this study, the volume fraction of the fibers was designed by investigating the effect of the fiber factor, F_f , on both M_{fl} and M_u , as formulated in Eqs. (5.1) and (5.5), respectively. According to Fig. 5.5, which describes the relationship between F_f and both M_f and M_u , the improvement of M_u and, consequently, the shear resistance of the beam by increasing the fiber content is more pronounceable than that of the nominal flexural capacity M_f . The point at which $M_u = M_{fl}$ indicates the optimum fiber factor, $F_{f,opt}$ .The vertical dash line in Fig. 5.5 delimits the failure modes of the beams according to the M_u/M_{fl} ratio. In the left side of this line, where $M_u < M_{fl}$, the fibers dosage is not sufficient to avoid shear failure, while in the right side of this line, where $M_u > M_{fl}$, a flexural failure mode is expected. For the present control beams, with $a/d_{s,eq}$ =2.23, F_f is equal to 0.69, which corresponds to 90 Kg/m^3 of the adopted steel fibers. This optimum dosage of steel fibers was adopted for developing the HPFRC of the beams, since it was assumed that the favorable effect of the prestress level to be applied to the GFRP bar can contribute to assure a flexural failure mode for the B*i*-P20 and B*i*-P30 series of beams.
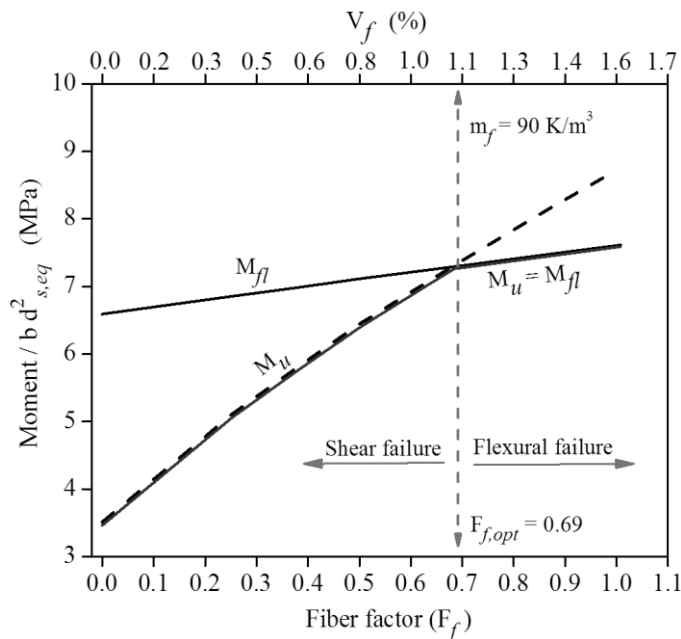
Fig. 5.5- Effect of fiber content on both nominal flexural moment, M_{fl}, and ultimate moment, M_u.

Table 5.5- Details of the short span beams.

Specimen ID	Prestress level	Prestress	Equivalent reinforcing ratio ($\rho_{s,eq}$)[a]
	(%)	(MPa)	(%)
B1-P0	Control	-	1.2
B2-P0	Control	-	1.2
B1-P20	20	270	1.2
B2-P20	20	270	1.2
B1-P30	30	405	1.2
B2-P30	30	405	1.2

[a] $\rho_{s,eq}$ Equivalent reinforcing ratio, see Eq.(5.8).

5.3.3   Prestressing System and Fabrication of the Elements

The prestress was applied at the both extremities of the GFRP bar using hollow hydraulic cylinders with maximum capacity of 200 kN. The GFRP bars were anchored in both extremities by using an active and a passive anchor. The rate of prestressing was 0.5 kN/min, and the prestressing load was monitored using a load cell placed between the bulkhead and the hydraulic cylinder. Further details of the prestressing system are depicted in Fig. 5.6.

After arranging the reinforcements and prestressing the GFRP bars, three beams were cast using the developed HPFRC of the same batch. For each batch three beams were cast: the reference beam, and two beams with a prestressed GFRP bar, one at 20% and the other at 30%. The prestressing force was released 3 days after casting the beams, adopting a

release rate of about 0.3 kN/min. Curing of the beams was carried out for 7 days at an average temperature of $23^{o}C$ and 60% humidity. The beams were tested at the age of 28 days.
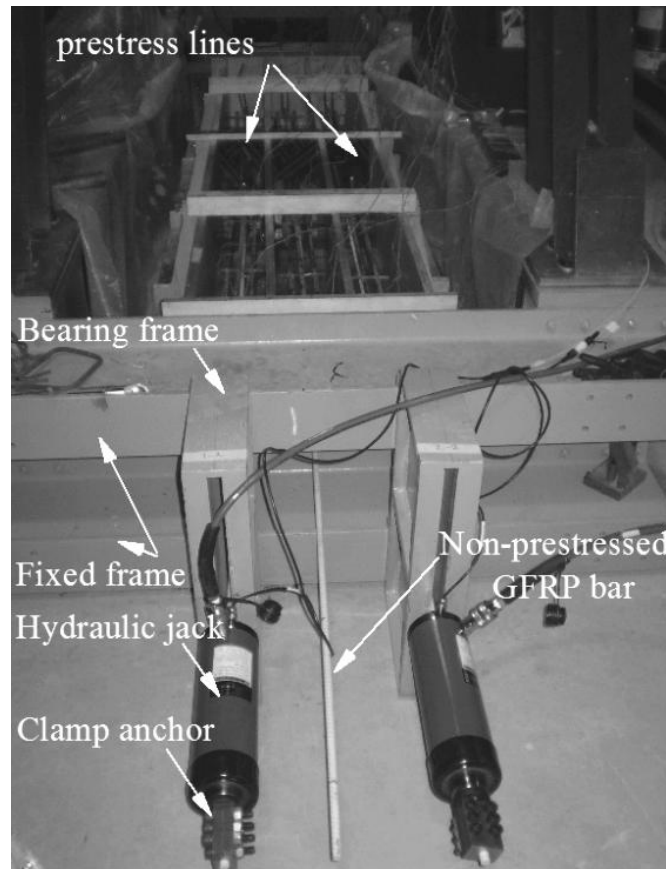
Fig. 5.6- Prestressing system.

5.3.4 Test Setup and Procedure

The tests were carried out using a three-point bending test setup adopted in the present study. The simply supported beams were subjected to a point load at the mid-span with the clear distance of 525 mm from each support, according to the adopted test setup illustrated in Fig. 5.3. All the tested beams were loaded monotonically at a displacement rate of 10 μm/s up to the failure. The applied load, P, was assured by a servo-controlled hydraulic actuator of ±700 kN with ±0.05% accuracy. To monitor the deflections at the mid-span and along the shear spans, five linear variable displacement transducers

(LVDTs) were disposed according to the arrangement indicated in Fig. 5.3.

5.3.5 Experimental Results

5.3.5.1 Load-deflection relationship

Fig. 5.7 represents the overall behavior of the beams in terms of load versus mid-span deflection, $P-\delta$, and the ultimate values of the load obtained by testing the beams are compared with the calculated ones corresponding to the full flexural capacity, $M_u = M_{fl}$, ($P_u = P_{fl}$). By testing the control beams, an average maximum load of 298 kN, corresponding to the ultimate moment of $M_{u,\exp} = 78.32$ kN.m, was obtained at an average displacement of 11.45 mm. The ratio of the ultimate moment obtained by testing the control beams, $M_{u,\exp}$, to that of calculated analytically, $M_u = 60.61$ kN.m, shows that the formulation provides safe estimates in the case of the control beams ($M_{u,\exp} / M_u = 1.3$). The application of the prestress in the other series of beams caused an increase of the beam's load carrying capacity and ductility performance. Hence, the prestress increased the bearing capacity of Bi-P20 and Bi-P30 beam series, respectively, 8.4 % ($M_{u,\exp(Bi-P0)}$ =91.6% $M_{u,\exp(Bi-P20)}$) and 15.5% ($M_{u,\exp(Bi-P0)}$ =84.5% $M_{u,\exp(Bi-P30)}$) in comparison with the control specimens. Table 5.6 summarizes the results obtained by testing the beams.
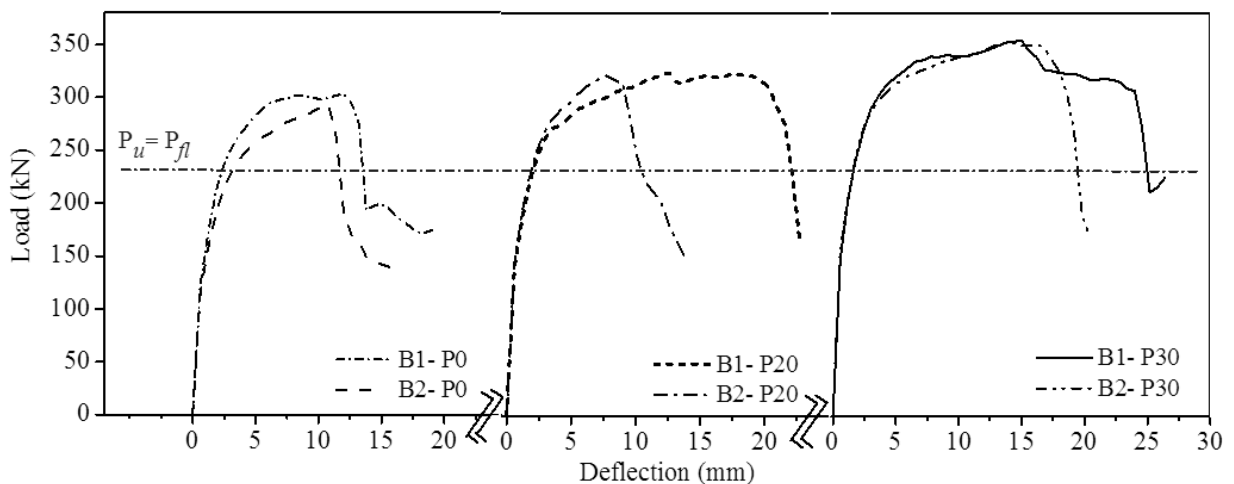
Fig. 5.7- Load-deflection relationship.

Table 5.6- Summary of the test results.

Specimen ID	P_u [a]	δ_u [b]	$M_{u,\exp}$	Mod of failure
	(kN)	(mm)	(kN.m)	
B1-P0	303.2	12.1	79.6	Shear-flexure
B2-P0	293.5	10.8	77.0	Shear-flexure
B1-P20	324.5	8.1	85.2	Flexure
B2-P20	322.8	8.1	84.7	Shear
B1-P30	356.1	14.8	93.5	Flexure
B2-P30	353.5	14.5	92.8	Flexure

[a] Maximum load,

[b] deflection corresponding to the maximum load.

5.3.5.2 Modes of failure

Fig. 5.8 shows the crack pattern of all the beams at the moment of failure. Regardless of the type of failure, the crack pattern of the beams produced by the tailor-made HPRFC with the optimum dosage of steel fibers is characterized by closely spaced cracks that appeared progressively. At the failure moment, some crushing was observed at the compression zone.

At the control beams, Bi-P0, the first flexural crack initiated at the deflection about 0.3 mm. Up to about 7.5 mm deflection the flexural cracks were highly propagated, while the shear cracks had an insignificant opening (see Fig. 5.9). By increasing the deflection, the shear cracks (the cracks in the central region of the shear span) started being progressively converted in diagonal shear ones. One of these cracks has degenerated in the shear failure crack that propagated along the longitudinal reinforcements in one extremity and towards the applied load in the other extremity. Hence, both the formed

flexural and shear cracks interacted to produce the combined shear-flexural mode of failure. The failure of the beams was followed by the occurrence of splitting cracks along the steel longitudinal reinforcements. The first member of this series, B1-P0, presented a slightly better behavior in terms of load carrying capacity and ductility (herein considered deformational capacity), which may be attributed to the better dispersion and orientation of fibers.

B1-P0

B2-P0

B1-P20

B2-P20

B1-P30

B2-P30
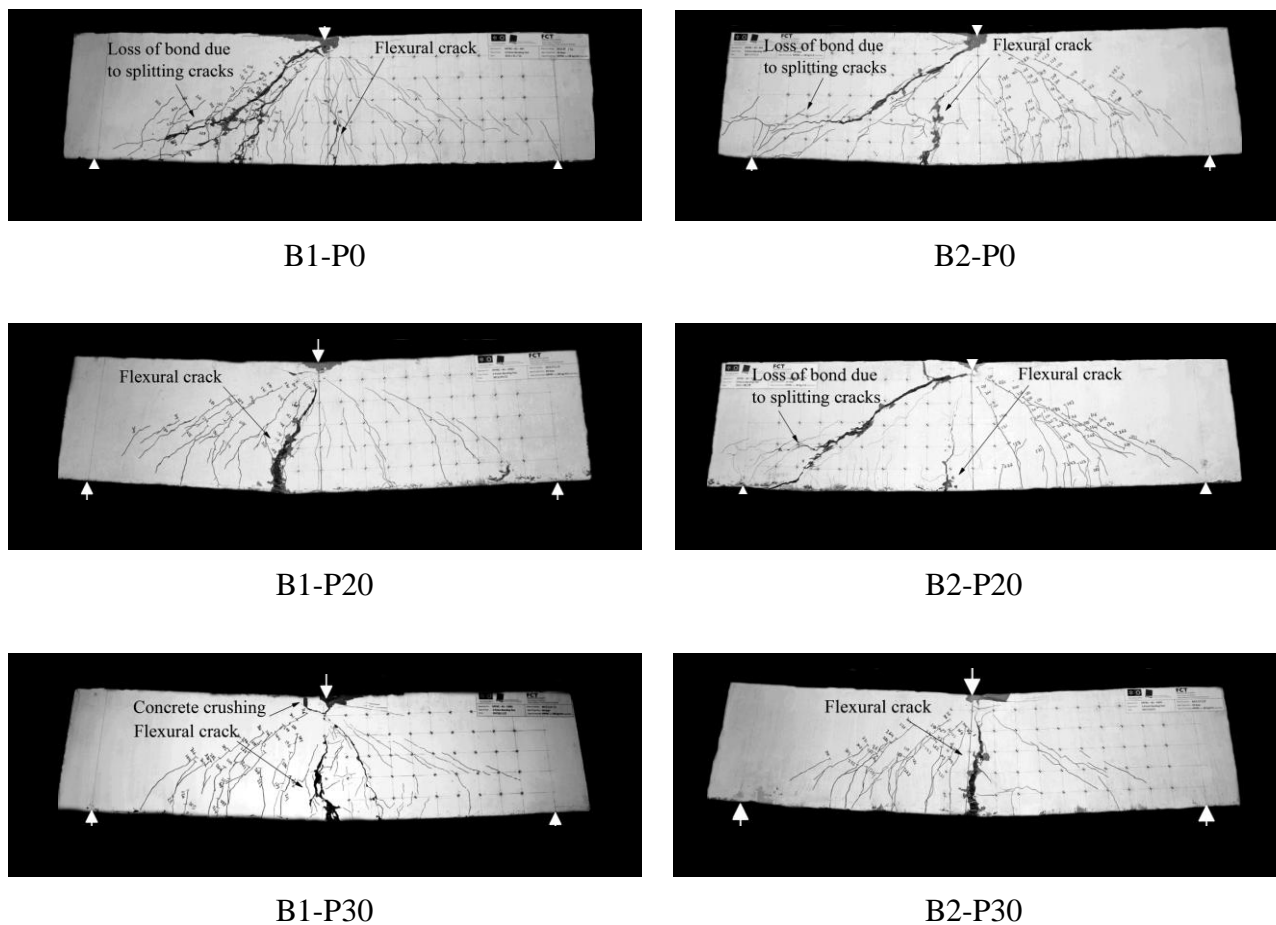
Fig. 5.8- Crack pattern of the beams at failure stage.

In general the applied prestress provided a confinement in the tested beams. This confinement delayed the crack opening and, consequently caused the fibers to be later activated. However, beside the effect of prestress on structural behavior of a beam, the number of fibers aligned across the crack and bridge the crack represent a quite important

influence on the beam behavior. In beam B2-P20, it seems that an insufficient number of fibers were properly oriented along the beam (which can be attributed to the fiber orientation) and thus, the application of prestress in combination with the fibers for bridging the crack was not effective enough to reach the flexural failure. On the other hand, the confinement provided in beam B1-P20 (with a proper fiber orientation) by application of prestress caused to increase the bridging effect of a higher number of fibers laid across the crack, leading to obtain the flexural failure. The best structural performance was observed in the beams of series B*i*-P30 that failed in bending at approximately the same load.
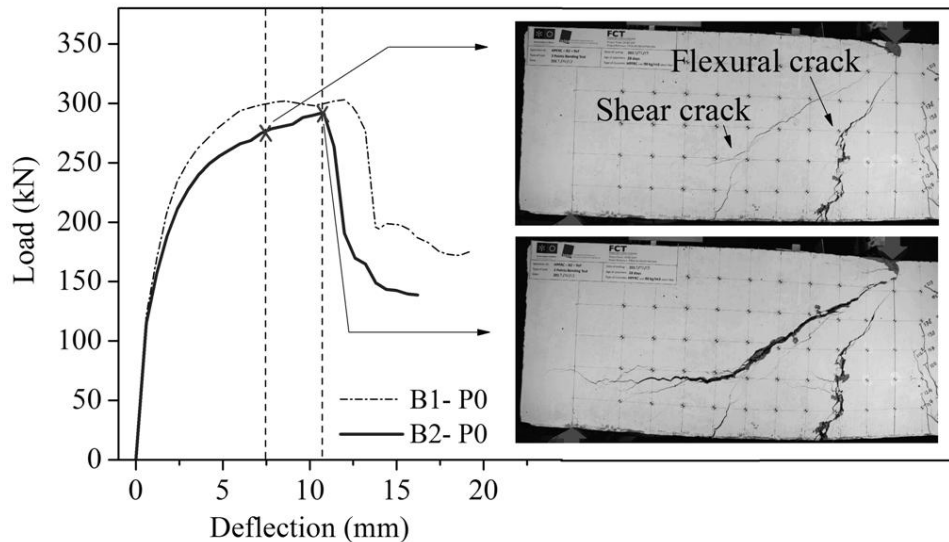
Fig. 5.9- The experimental crack pattern for the beam B2-P0 at two stages: at the deflection corresponding to 7.5 mm; at the failure stage.

5.4 FINITE ELEMENT ANALISYS

5.4.1   Model Description

Finite element simulations were performed for each series of the tested beams, with 0%, 20%, and 30% prestress applied to GFRP bar, using a plastic-damage multidirectional fixed smeared crack (PDSC) model. The PDSC model combines a multi-directional fixed smeared crack model to account for crack initiation and propagation, with a plasticity-

damage model to simulate the inelastic compressive behavior of materials between the cracks. The crack opening process is initiated based on the Rankine tensile criterion, whereas a quadrilinear softening diagram is used to simulate the crack propagation (see Fig. 4.10(a) in chapter 4). Two methods are available to simulate the crack shear stress transfer: one based on the concept of shear retention factor (the approach based on Eqs. (4.5) and (4.6) in chapter 4), and the other one based on a shear softening diagram that requires some information about fracture mode II propagation (see Eq. (4.7) and Fig. 4.10(b) in chapter 4). The plasticity part of the model accounts for the development of irreversible strains and volumetric strain in compression, whereas the strain softening and stiffness degradation of the material under compression are controlled by an isotropic strain base damage model. Combination of the plasticity and damage theories is assured by considering the plastic flow occurs in undamaged (respect to compression) material, together with the strain based damage approach assuming state of damage equally distributed in all the material directions (isotropic damage). The PDSC model is described in detail elsewhere (Edalat Behbahani et al. 2015), therefore the model formulation is not represented in this study.

5.4.2   FEM Modeling, Results and Discussions

The finite element mesh of 8-noded plain stress finite elements with 3×3 Gauss-Legendre *IP* scheme, represented in Fig. 5.10, was adopted for the beams (the differences between beams in different series are limited to the prestress load applied to the GFRP bar). The longitudinal steel and GFRP bars were modeled using 2-noded truss elements (one degree-of-freedom per each node) with two *IP*s. Perfect bond was assumed between the reinforcement bars and the surrounding concrete. For modeling the behavior of the steel bars, the stress-strain relationship represented in Fig. 5.11 was adopted. The curve (under compressive or tensile loading) is defined by the points PT1 = ($\varepsilon_{sy}, \sigma_{sy}$), PT2 = ($\varepsilon_{sh}, \sigma_{sh}$), and PT3 = ($\varepsilon_{su}, \sigma_{su}$) and a parameter P_s that governs the shape of the last branch of the curve. Unloading and reloading linear branches with slop of $E_s = \sigma_{sy}/\varepsilon_{sy}$ are assumed in the present approach (Sena-Cruz 2004). The behavior of GFRP bar was modeled using a linear-elastic stress-strain relationship defined by the values indicated in Table 5.3. The prestress load was simulated by means of temperature variation applied to the truss

elements modeling the GFRP bar. Table 5.7 represents the values of the temperature variation applied to each simulated beam. The values of parameters used to define the constitutive models of steel and concrete (HPFRC) are included in Table 5.8 and Table 5.9, respectively. To define the crack shear stress-shear strain diagram ($\tau_t^{cr} - \gamma_t^{cr}$), represented in Fig. 4.10(b), the values of the corresponding parameters, included in Table 5.9, were obtained by simulating the experimental results of the reference beams (Bi-P0) as best as possible. Then the same values of the parameters of the constitutive model were adopted for the prestressed beams (Bi-P20, and Bi-P30).
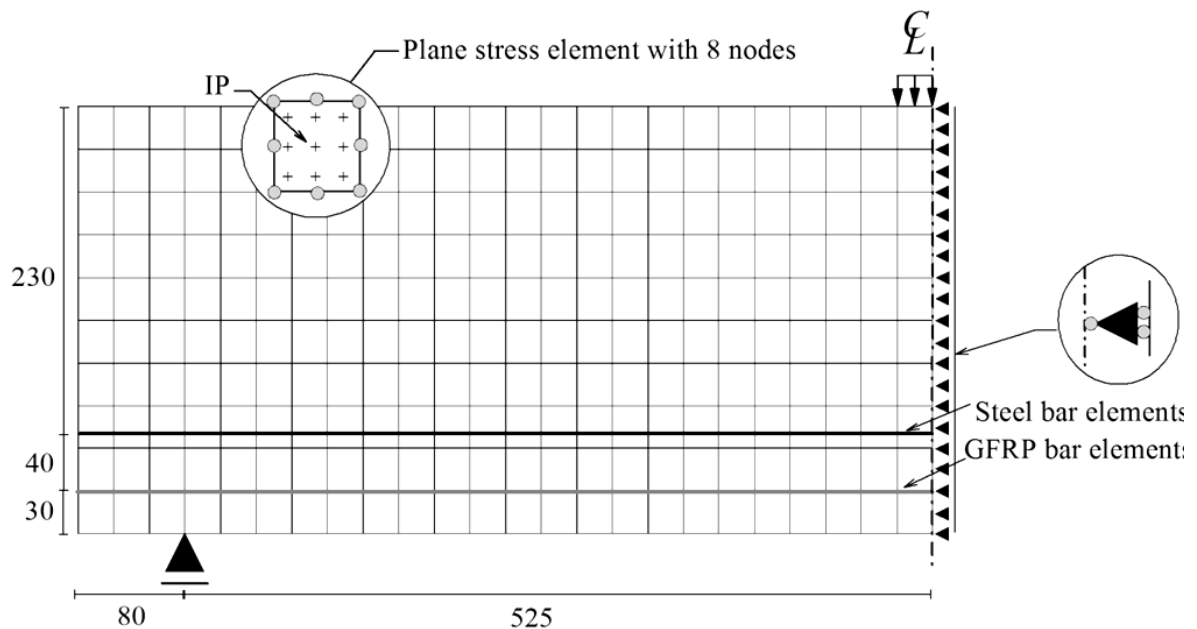
Fig. 5.10- Finite element mesh used for the simulated beams (dimensions in mm).

The experimental and the numerical relationships between the applied load and the deflection at the mid-span for all the beam series are compared in Fig. 5.12. In Fig. 5.13 the numerical crack patterns of these beam series at the end of the analysis (at the end of the last converged load increment) are compared with the obtained experimental crack patterns. This figure introduces the completely opened cracks in pink, the cracks in opening process in red, the cracks in reopening process in cyan, the cracks in closing process in green and the closed cracks in blue color. The figures 5.12 and 5.13 show that

the numerical model is able to capture with good accuracy the deformational response of the beams and captured profile of the failure crack.

The predicted strain in steel reinforcement (at the closest *IP* to the symmetric axis of the beams) versus the mid-span displacement corresponding to each simulation is represented in Fig. 5.14. These curves demonstrate that at a deflection of about 2.3 mm the longitudinal steel reinforcements of all the beam series (Bi-P0, Bi-P20, Bi-P30) started yielding, which indicates that the methodology described in section 2 to evaluate the content of steel fibers capable of assuring yield initiation of longitudinal reinforcement before the occurrence of beam's shear failure is reliable.

The numerically predicted relationship between the applied load and the deflection at the mid-span for all the beam series are gathered in Fig. 5.15. The points at crack initiation and at yield initiation of the steel reinforcement also are represented in this figure by using markers, demonstrating that by both the load at crack initiation and at yield initiation of steel reinforcements increase with the prestress level.
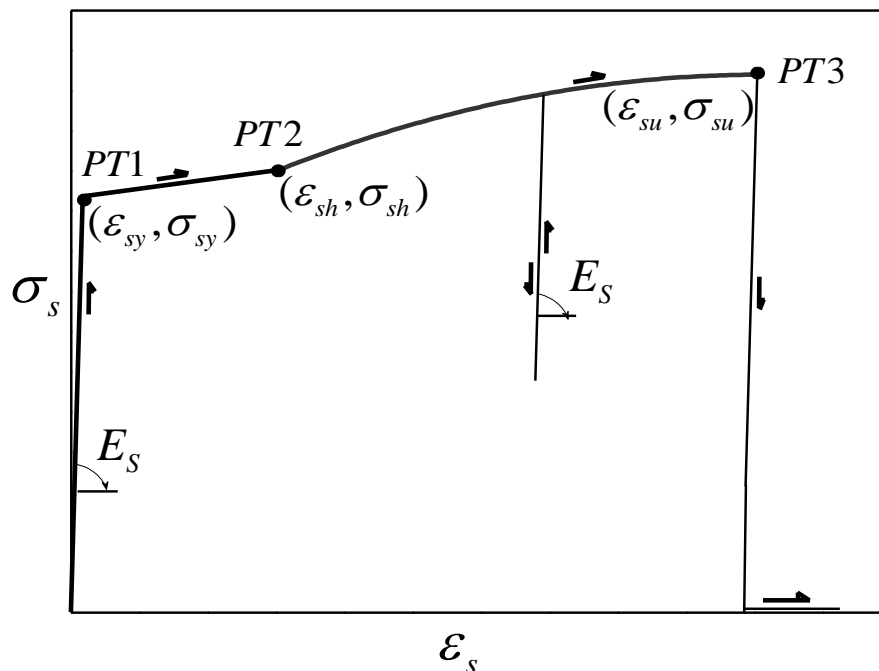
Fig. 5.11- Uniaxial constitutive model (for both tension and compression) for the steel bar (Sena-Cruz 2004).

Table 5.7- General information about the simulation of the prestress load by means of temperature variation.

	Prestress percentage	Stress applied to GFRP corresponding to prestress level σ_t [a] (MPa)	Coefficient of thermal expansion $\alpha(mm/(mm^oc))$	Temperature variation $\Delta T(^oc)$
Bi-P0 (i=1, 2)	0%	-	-	-
Bi-P20 (i=1, 2)	20%	270	1×10^{-5}	-482
Bi-P30 (i=1, 2)	30%	405	1×10^{-5}	-723

[a] σ_t = prestress percentage $\times f_{GFRP,u}$; $f_{GFRP,u} = 1350\ MPa$.

Note: the thermal strain and corresponding stress are calculated from: $\varepsilon_t = \alpha\ \Delta T$; $\sigma_t = E_{GFRP}\ \varepsilon_t$.

Table 5.8- Values of the parameters of the steel constitutive model.

Diameter (mm)	$\varepsilon_{sy}(\%)$	$\sigma_{sy}(N/mm^2)$	$\varepsilon_{sh}(\%)$	$\sigma_{sh}(N/mm^2)$	$\varepsilon_{su}(\%)$	$\sigma_{su}(N/mm^2)$	Third branch exponent
10, 12	0.28	500	0.28	500	10.0	591	1
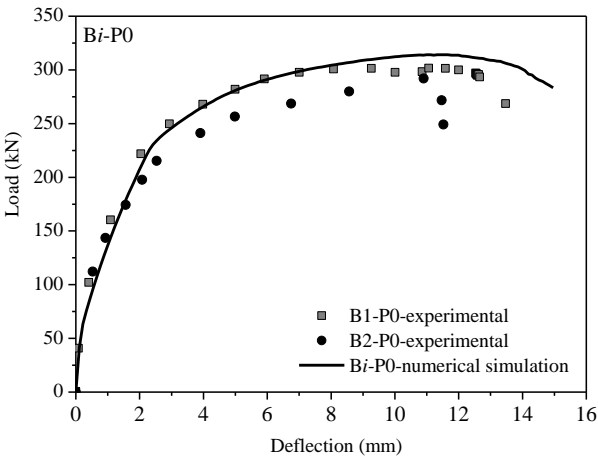
(a)
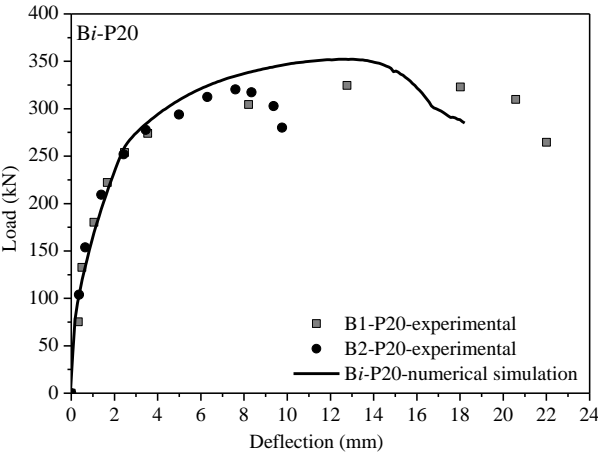
(b)
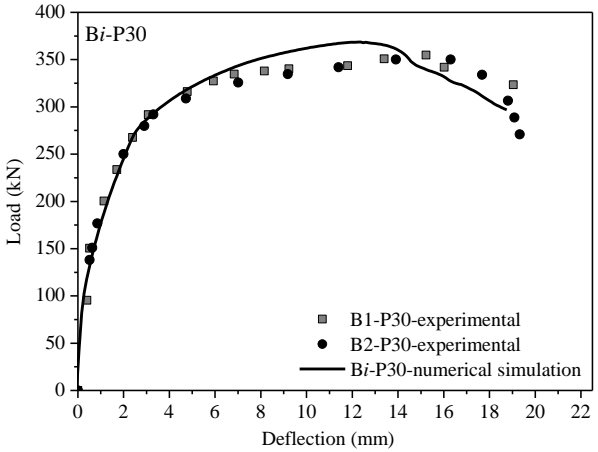
(c)

Fig. 5.12- The numerical prediction of applied load versus the mid-span deflection in compare to the corresponding experimental results of the beam series: (a) B*i*-P0; (b) B*i*-P20; (c) B*i*-P30.
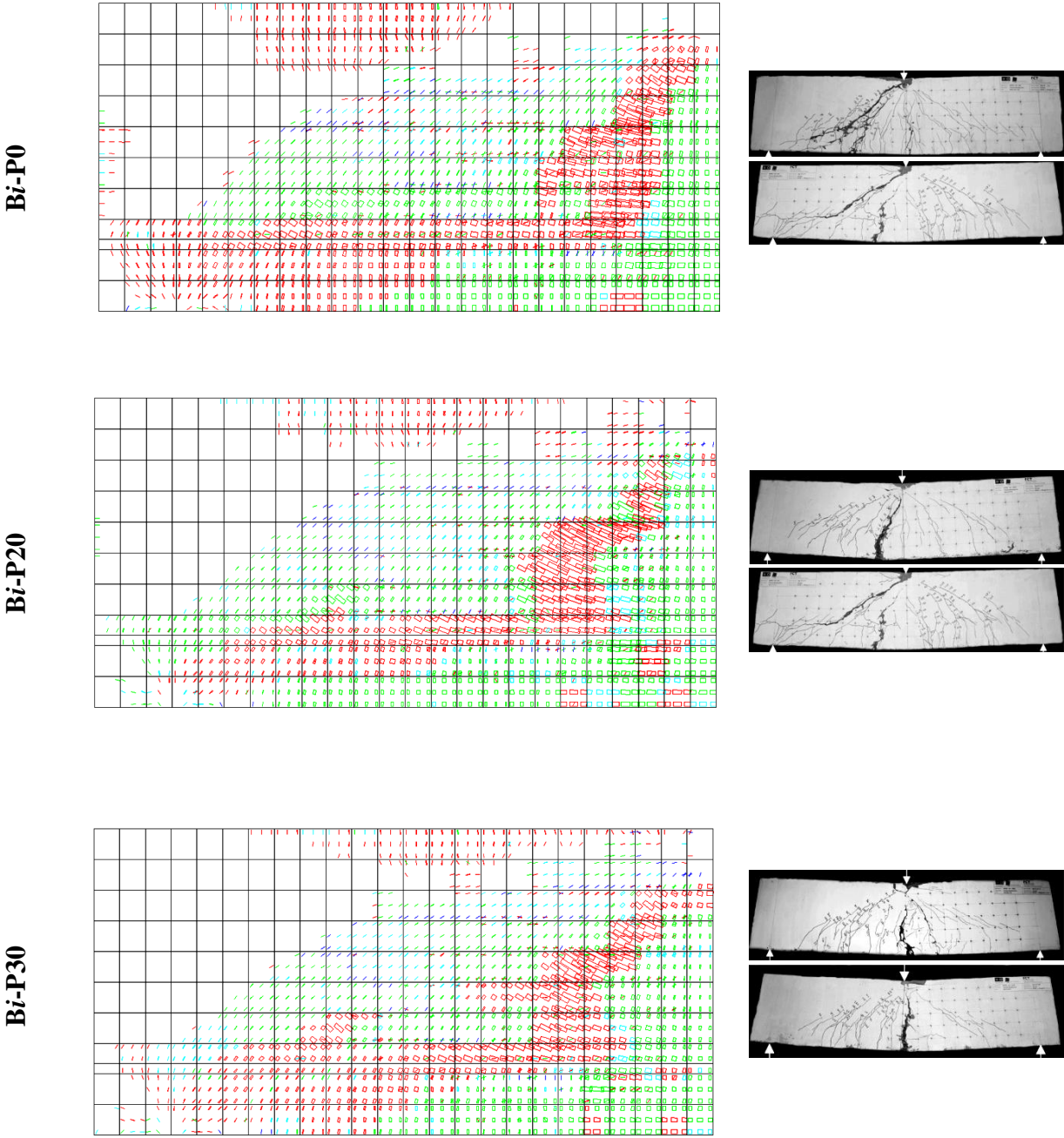
Fig. 5.13- The crack patterns predicted by the model for the beam series at the experimental: (a) B*i*-P0; (b) B*i*-P20; (c) B*i*-P30. (In pink color: crack completely open; in red color: crack in the opening process; in cyan color: crack in the reopening process; in green color: crack in the closing process; in blue color: closed crack).
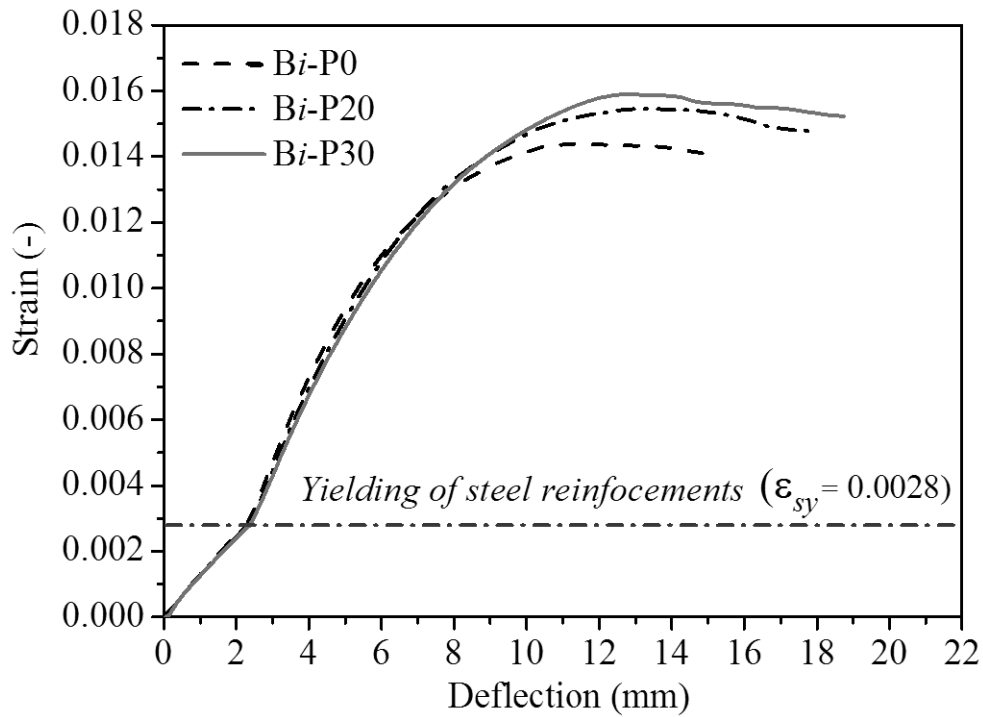
Fig. 5.14- Strain in steel reinforcement (obtained at the closest IP to the symmetric axis of the beam) versus the mid-span deflection predicted by the numerical simulations.
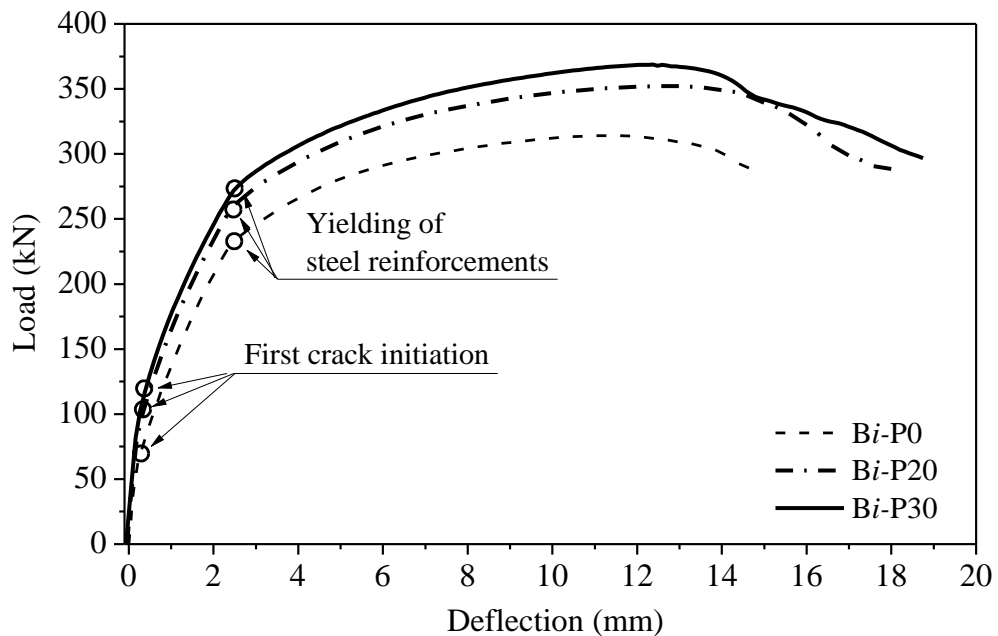
Fig. 5.15- The predicted load-deformation behavior for all the beam series.

Table 5.9- Values of the parameters of the constitutive model for concrete.

Property	Value
Poisson's ratio	$\nu = 0.2$
Young's modulus	$E_{cm} = 34000$ N/mm^2
Compressive strength	$f_{cm} = 65$ N/mm^2
Parameter defining the plastic-damage model (Edalat Bahbahani 2015)	$\alpha_0 = 0.4$; $\varepsilon_{c1} = 0.004$; $G_{f,c} = 65$ N/mm
Quadrilinear tension-softening diagram	$f_{ct} = 3.25$ N/mm^2; $G_f^I = 6.0$ N/mm; $\xi_1 = 0.0005$; $\alpha_1 = 0.75$; $\xi_2 = 0.0025$; $\alpha_2 = 1.0$; $\xi_3 = 0.1$; $\alpha_3 = 0.6$
Parameter defining the mode I fracture energy available to the new crack (Sena-Cruz 2004)	2
Parameters defining the crack shear stress-crack shear strain softening diagram	$\tau_{t,p}^{cr} = 1.75$ N/mm^2; $\beta = 0.2$; $G_{f,s} = 1.0$ N/mm
Crack bandwidth	square root of the area of Gauss integration point
Threshold angle (Sena-Cruz 2004)	30 degree
Maximum number of cracks per integration point (Sena-Cruz 2004)	2

5.5 SHEAR RESISTANCE

In the present section, the shear resistance of the tested beams is compared with the ones predicted according to the formulations presented in the MC2010, RILEM TC 162-TDF (2003) and the formula proposed by Soetens (2015). In the MC2010 and in the RILEM TC 162-TDF (2003) approaches the shear resistance of fiber reinforced concrete beams, V_{Rd}, is calculated as follow:

$$V_{Rd} = (V_{cd} + V_{fd}) + V_{wd} \tag{5.9}$$

where V_{cd}, V_{fd} and V_{wd} are the contribution of concrete, fiber reinforcement and steel stirrups, respectively. According to the RILEM TC 162-TDF (2003) approach, the shear resistance of a FRC beam without stirrups comprises the shear resistance provided by concrete, V_{cd}:

$$V_{cd} = \left[\frac{C_1}{\gamma_c} k(100\rho_s f_{ck})^{1/3} + 0.15\sigma_{cp} \right] bd \tag{5.10}$$

and the shear resistance related to the contribution of steel fiber reinforcement, V_{fd}:

$$V_{fd} = 0.7 k_f k \frac{C_1 f_{R4}}{\gamma_c} bd \tag{5.11}$$

In Eqs. (5.10) and (5.11) $C_1 = 0.18$, γ_c is the partial safety factor for the concrete without fibers, and k is a factor that takes into account the size effect:

$$k = 1 + \sqrt{200/d} \le 2.0 \text{ (d in mm)} \tag{5.12}$$

In Eq. (5.10) $\sigma_{cp} = N_{sd}/A_c < 0.2 f_{ck}/\gamma_c$ is the average stress acting on the concrete cross section, A_c, for an axial force, N_{sd}, due to loading or prestressing actions ($N_{sd} > 0$ for compression).

In Eq. (5.11) k_f is a factor for taking into account the contribution of the flanges in a T and I cross sections for the shear resistance:

$$k_f = 1 + n.(h_f/d).(h_f/d) \le 1.5 \tag{5.13a}$$

$$n = (b_f - b)/h_f \le 3 \text{ and } n \le (3b/h_f) \tag{5.13b}$$

where h_f and b_f are the height and width of the flange, respectively.

To determine the shear resistance of this type of FRC RC beams, the MC2010 merges the contribution of fiber reinforcement, V_{fd}, and concrete, V_{cd}, in an unique term, $V_{Rd,F}$, thereby Eq. (5.9) is reduced to:

$$V_{Rd} = V_{Rd,F} + V_{wd} \tag{5.14}$$

where,

$$V_{Rd,F} = \left[\frac{C_1}{\gamma_c} k (100 \rho_s C_2 f_{ck})^{1/3} + 0.15 \sigma_{cp} \right] bd \tag{5.15}$$

$$C_2 = 1 + 7.5 \frac{f_{Ftuk}}{f_{ctk}} \tag{5.16}$$

being f_{Ftuk} the characteristic value of the ultimate residual tensile strength of FRC.

The $V_{Rd,F}$ is assumed to be not smaller than the value provided by:

$$V_{Rd,F\min} = \left[0.035 k^{3/2} f_{ck}^{1/2} + 0.15 \sigma_{cp} \right] b.d \tag{5.17}$$

Both guidelines address the contribution of the transversal reinforcement, V_{wd}, by means of Eq. (5.18). Since no stirrups were used in the tested beams, this term, V_{wd}, is considered to be null in the calculations.

$$V_{wd} = \frac{A_{sw}}{s} 0.9d \, f_{ywd} (1 + \cot \alpha) \sin \alpha \tag{5.18}$$

where A_{sw} is the cross section area of a shear reinforcement, s is spacing between the stirrups measured along the longitudinal axis, f_{ywd} is design yield strength if the stirrups and α introduces the angle of each stirrup with the longitudinal axis.

The approach proposed by Soetens (2015) can be written in the following general form:

$$V_{Soetens2015} = (A\sqrt{f_{cm}} + Bf_{Ftmu}) b_w z \tag{5.19}$$

where the first term represents the concrete contribution for the shear resistance of the FRC beams. The factor " A " in this term is a function of the parameters assumed as having the highest influence for the reinforced concrete shear resistance, namely the effective depth of the beams, d, the longitudinal reinforcement ratio, ρ_s, the shear span to effective depth ratio, a/d, and the compressive stress due to the application of prestress, σ_{cp}. The second term of Eq. (5.19) considers the contribution of the fiber reinforcement

for the shear resistance of a FRC beam. The factor "B" in this term is a function of the inclination of the compressive strut "θ" and of the fiber reinforcement effectiveness factor, represented by the parameter "α_{red}". In this term, "f_{Ftum}" is the average ultimate post-cracking tensile strength of FRC, calculated according to the following equation:

$$f_{Ftu}^* = \min \begin{cases} f_{Ftum} \\ f_{ctm}(1-2\sigma_{cp}/f_{cm}) \end{cases} \tag{5.20}$$

where f_{Ftum} is the average ultimate post cracking tensile strength of FRC. The final configuration of Eq. (5.19) is the following one:

$$V_{Soetens2015} = \left[0.388\sqrt{1+\frac{\sigma_{cp}}{f_{ck}}}k(3\frac{d}{a}\rho_s)^{1/3}\sqrt{f_{cm}} + f_{Ftu}^*(1+4\frac{\sigma_{cp}}{f_{ck}}) \right]b_w z \tag{5.21}$$

Table 5.10 includes the shear resistance of the tested beams, $V_{\exp}$, and corresponding shear strength, $v_u = V_{\exp}/(bd_{s,eq})$, as well as the estimated values of shear resistance according to MC2010, V_{MC2010}, and RILEM TC 162-TDF (2003), V_{RILEM}, and Soetens approach, $V_{Soetens2010}$. For the calculations of V_{MC2010}, V_{RILEM} and $V_{Soetens2010}$ average values were considered for the material properties, and $\gamma_c = 1$ was adopted. For the beams reinforced with hybrid GFRP-steel bars, d is substituted by the equivalent steel depth, $d_{s,eq}$, presented in Eq. (5.3), and ρ_s is replaced by the equivalent steel reinforcement ratio, $\rho_{s,eq}$, determined according to Eq. (5.8). The ratios of the shear resistance obtained experimentally to the estimated ones, $V_{\exp}/V_{RILEM}$, are also compared in this table. The $V_{\exp}/V_{RILEM}$ ratio, which was very close to the unit value, suggests that RILEM TC 162-TDF (2003) approach estimates more accurately the shear resistance of HPFRC short-span beams than the other approaches. The shear resistance calculated using the formula proposed by Soetens (2015), however, is only 17% higher than the values obtained experimentally. On the other hand the MC2010 provides quite conservative estimations, with an average $V_{\exp}/V_{MC2010}$ of 1.66. The calculated values according to this approach are, in average terms, leastwise 39% lower than the ones calculated by RILEM TC 162-TDF (2003) provisions, and 47% lower than Soetens (2015) formula.

The effect of prestress on the shear resistance of the beams is one of the factors

considered by these formulations. In both MC2010 and RILEM TC 162-TDF (2003) approaches the shear resistance provided by prestressing the beams is evaluated by the same term "$0.15\sigma_{cp}bd$", while in Soetens (2015) formula the term "$\sqrt{1+(\sigma_{cp}/f_{ctk})}$" has this purpose. The effect of the inclination of the shear crack "$\cot\theta$" is indirectly considered in the second term of the formula, "$1+4(\sigma_{cp}/f_{ck})$". The influence of the prestress level on the shear resistance predicted by the three considered approaches is compared in Fig. 5.16(a), by also indicating the results obtained experimentally. Although in the experimental tests the shear resistance of the beams was improved 15.6% by the application of 30% prestress ($\sigma_{cp}=1$ MPa), only 3.3%, 5.4% and 6.2% is the predicted increase provided by RILEM TC 162-TDF (2003), MC2010 and Soetens (2015) approaches, respectively.

Additionally, since for the beams of series Bi-P30 failed in bending the shear capacity was not fully mobilized, the V_{exp}/V_{anal} value was expected to be less than unit, which did not, however, occur in the predictions of MC2010 and RILEM TC 162-TDF (2003) approaches. Based on the obtained experimental results, it seems that the estimation of prestressing effect on the shear resistance of FRC elements requires specific research in this subject for assuring more reliable predictions.

Comparison of Eq. (5.10), proposed by RILEM TC 162-TDF (2003), with Eq. (5.15) recommended by MC2010, shows that the effect of fibers in Eq. (5.15) is only reflected on parameter "$C2$". In Eq. (5.15) is assumed to model the shear contribution of fibers by modifying the longitudinal reinforcement ratio (Minelli et al. 2013) through the factor $C2$ that includes a parameter representative the post-cracking performance of FRC at ultimate crack width of 1.5 mm, f_{Ftuk}. In order to estimate how the fiber effects are taken into account according to MC2010 approach, the shear resistance of plain concrete was calculated, keeping $C2=1$ (which means $f_{Ftuk}=0$). By subtracting the obtained value from the estimated shear resistance of FRC, the fiber contribution was evaluated. Fig. 5.16(b) compares the average shear resistance provided by fiber reinforcement, V_{fd}, in accordance with MC2010, RILEM TC 162-TDF (2003) and Soetens (2015) approaches. It is verified that the contribution of steel fibers for the shear capacity of the beams is estimated 59% lower by MC2010 approach compared to the one calculated according to the RILEM TC 162-TDF (2003) formulation. This figure evidences that MC2010

underestimates significantly the contribution of fiber reinforcement for the shear resistance, regardless the prestress levels considered.

In the Eqs. (5.19) to (5.21) of the Soetens (2015) approach the concrete, V_{cd}, and fiber contribution, V_{fd}, for the shear resistance of the FRC beams are estimated by the functions A and B, respectively, and the obtained values are compared in Fig. 5.16(b) to those determined from the RILEM TC 162-TDF (2003) and MC2010 approaches. This comparison shows that the Soetens (2015) approach predicts the highest contribution of the fiber effects, respectively, 67% and 19% higher than the calculated ones by MC2010 and RILEM TC 162-TDF (2003) approaches, when estimating the shear resistance of FRC beams.
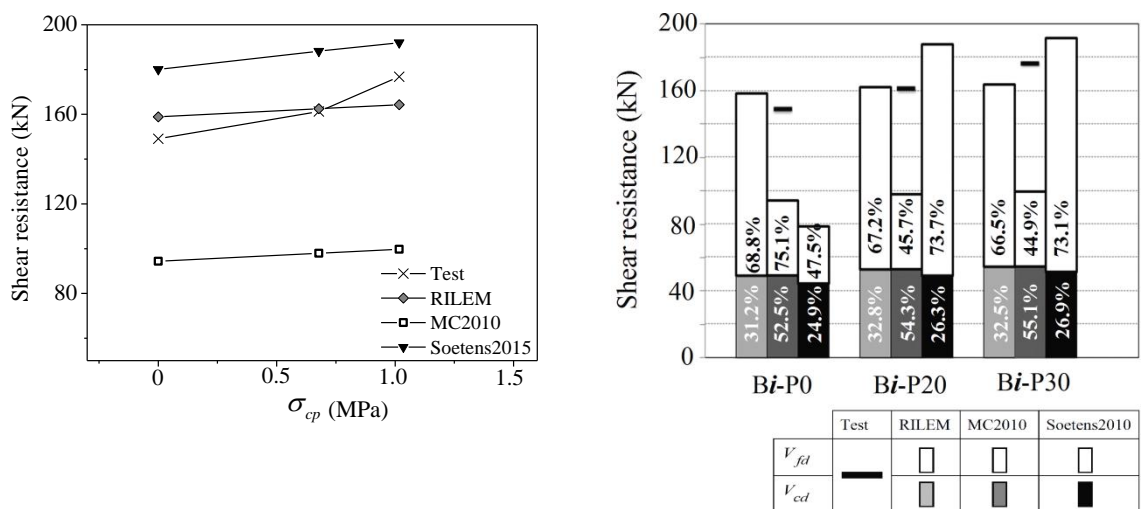
Fig. 5.16- (a) Shear capacity *vs.* σ_{cp} (b) Comparison of the effect of V_{fd} and V_{cd}.

Fig. 5.16(b) evidences that the significant difference on the estimation of shear resistance of the beams is related to distinct calculation of V_{fd}. Since all the tested beams were reinforced with the same content of steel fibers, the accuracy of the estimation of fiber contribution for the shear resistance of the beams cannot be evaluated using exclusively the present experimental results. To have a better assessment of the predictive performance of the three approaches, and a deeper analysis of the influence of fibers on the shear resistance of the beams, the experimental results of 9 additional developed

beams as well as that of fifteen beams without stirrups, collected from literature, are considered. The results of this analysis are discussed in Chapter 6.

Table 5.10- Shear resistance calculated analytically in comparison with the experimental results.

Specimen ID	V_{exp} (kN)	v_u (MPa)	V_{MC2010} (kN)	$\dfrac{V_{exp}}{V_{MC2010}}$	V_{RILEM} (kN)	$\dfrac{V_{exp}}{V_{RILEM}}$	$V_{Soetens2015}$ (kN)	$\dfrac{V_{exp}}{V_{Soetens}}$
B1-P0	152.34	4.3	94.39	1.61	158.88	0.96	180.02	0.84
B2-P0	146.73	4.2	94.39	1.55	158.88	0.92	180.02	0.81
B1-P20	162.24	4.6	97.97	1.65	162.47	1.00	188.15	0.86
B2-P20	161.41	4.6	97.97	1.64	162.47	0.99	188.15	0.85
B1-P30	178.05	5.6	99.75	1.78	164.26	1.08	191.96	0.93
B2-P30	176.74	5.0	99.75	1.76	164.26	1.07	191.96	0.92
Average				1.66		1.00		0.87
CoV (%)				5.33		6.20		5.42

5.6 CONCLUSIONS

Three series of short-span beams with hybrid GFRP-steel flexural reinforcement and including a relatively high dosage of steel fibers (high performance fiber reinforced concrete - HPFRC), capable of assuring the yield initiation of the steel bars, were designed and tested. To assess the effectiveness of prestress for the increase of the shear resistance and the ductility level of the failure modes of these members, the behavior of these beams were studied experimentally and numerically. A summary of remarks can be drawn as follow:

– Application of prestress in HPFRC beams without stirrups provides significant increase in their shear resistance and tends to increase the ultimate flexural capacity, M_u, up to 16% of that in the control beams. Hence, the mode of failure was enhanced and changed from a flexure/shear failure mode (yield initiation followed by the

formation of a critical diagonal crack) in the control beams to the flexural failure mode in the case of the beams with 30% prestress.

– A numerical approach capable of capturing the deformation response as well as the crack pattern developed in this type of RC members was adopted to demonstrate the benefits of fiber reinforcement and prestress level on the load carrying capacity at serviceability limit state conditions and at steel yield initiation. These numerical studies also demonstrated the applicability of the analytical approach developed for estimating the fiber reinforcement content capable of assuring ductile failure modes for this type of beams.

– By comparing the shear resistance estimated by RILEM TC 162-TDF (2003), MC2010 and Soetens (2015) approaches, it was verified that all the formulations demonstrated acceptable accuracy for design of the beams without prestress. In the case of the prestressed beams RILEM TC 162-TDF (2003) approach provided more accurate predictions. The shear capacity of the prestressed beams obtained by MC2010 was found quite low compared to that of calculated experimentally, which should be received more attention according to the economical point of view.

– For the development of a design approach of higher predictive performance than the ones analyzed in the present work, the effects that influence the shear capacity of RC beams should be comprehensibly evaluated, which requires the collection of a relatively large data base and its analysis with sophisticated algorithms, like data mining, as well as the execution of parametric studies with advanced FEM-based constitutive models capable of simulating the relevant phenomena involved.

CHAPTER 6

SHEAR RESISTANCE OF HPFRC SLENDER BEAMS WITHOUT STIRRUPS

6.1 INTRODUCTION

Although concrete is a structural material capable of withstanding aggressive environmental conditions, there is still a large number of failure of RC structures as a result of the premature corrosion of the reinforcements embedded in concrete (Böhni 2005). A design methodology to contribute for the development of beams with higher durability and sustainably is the main objective guiding the research activities described in the previous chapters of the present thesis. The method for developing such elements is described in the 5th chapter, and its effectiveness when applied to beams requiring high shear capacity is assessed testing several short-span beams. In accordance with this method, the beams are fabricated by a HPFRC with a relatively high dosage of steel fibers aiming to suppress the stirrups. They are flexurally reinforced with hybrid GFRP-steel longitudinal reinforcements. The effect of prestressing the GFRP bars on increasing the shear capacity of such beams was assessed in the 5th chapter. The results demonstrated that prestressing the GFRP bars contributes to obviate the deficiencies created by using GFRP bars of relatively low modulus of elasticity. It also aids to control the crack width and increase the shear capacity of the members. In the present chapter, a step forward is proposed for improving the structural behavior of the HPFRC beams by

investigating the influence of the prestress level applied on the steel reinforcements, as well as by using distinct dosages of steel fibers on the shear behavior of 9 almost full-scale slender beams.

6.2 EXPERIMENTAL PROGRAM

6.2.1   HPFRC Mix Design and Properties

Based on the mix design methodology proposed in the 3rd chapter, a reference self compacting concrete, SCC, without steel fibers, and two HPFRC mixes with, respectively, 90 kg/m^3 (corresponding to the volume fraction, V$_f$, of 1.1%) and 120 kg/m^3 (V$_f$ = 1.5%) steel fibers of 33 mm length, were developed. In these three concrete compositions, 3 kg/m^3 synthetic fibers of 54 mm length were applied. The adopted compositions are introduced in Table 3.11, in chapter 3, using a label "Mi-Fj", where "i" is the number dedicated to, respectively, SCC, HPFRC with 90 kg/m^3 steel fiber, and HPFRC with 120 kg/m^3 steel fiber, while "j" identifies the applied fiber dosage.

Table 6.1 Average compressive strength and Young's modulus of the developed concrete mixes.

Mix ID	f_{cm} [a] (MPa)	CoV[d] of f_{cm} (%)	f_{ck} [b] (MPa)	E_{cm} [c] (GPa)	CoV[d] of E_{cm} (%)
M1-F0	66.45	1.29	58.45	32.10	2.07
M2-F90	67.05	1.31	59.05	33.23	1.15
M3-F120	60.03	1.94	52.03	30.58	1.58

[a] Mean value of compressive strength.
[b] Characteristic value of compressive strength.
[c] Mean value of Young's modulus.
[d] Coefficient of variation (for 3 specimens).

The average values of the Young's modulus, E_{cm}, as well as the average and characteristic compressive strength, respectively, f_{cm} and f_{ck} , are indicated in Table 6.1. According to

the obtained results all the concrete mixes are categorized as the strength class of "C50". However, the table demonstrates a higher compressive strength for the developed SCC (M1-F0) compared to that of HPFRC compositions, specially the one developed by 120 Kg/m^3 steel fibers (M3-F120). It can be attributed to 17% reduction of the coarse aggregate volume and 14% increasing the past volume in tailoring M3-F120 mix compared to that of the mix M1-F0 in order to ensure a proper flowability and avoiding the perturbation effect of 120 Kg/m^3 steel fiber used for tailoring this concrete.

In accordance with CEB-FIP Modal Code 2010, the flexural tensile behavior of all the three developed compositions at 28 days age was obtained. From these tests, the stress at the limit of proportionality, $f_{ct,L}^f$, (related to the maximum load reached up to CMOD of 0.05 mm) and the residual flexural tensile strength parameters, f_{R1} to f_{R4}, were obtained for all the compositions, and their values are indicated in Table 6.2. Further details regarding to the nominal flexural stress versus CMOD relationship of the developed mixes can be found in Fig. 3.13 in chapter 3.

Table 6.2- Limit of proportionality and residual flexural strength parameters of the developed concrete mixes.

Mix ID		$f_{ct,L}^f$ (MPa)	f_{R1} (MPa)	f_{R2} (MPa)	f_{R3} (MPa)	f_{R4} (MPa)
			CMOD$_1$= 0.5 mm	CMOD$_2$= 1.5 mm	CMOD3= 2.5 mm	CMOD$_4$= 3.5 mm
M1-F0	Average	5.72	1.2	-	-	-
	CoV (%)	4.4	7.7	-	-	-
M2-F90	Average	7.6	14.95	15.14	14.08	12.67
	CoV (%)	18.6	6.3	7.5	0.9	13.1
M3-F120	Average	10.32	16.23	17.06	16.1	14.33
	CoV (%)	10.52	4.1	2.7	1.0	2.3

6.2.2 Test Specimens

A total number of 9 full-scale I cross section beams of 4000 mm overall length, L, and 500 mm high, h, were designed, fabricated and studied in terms of shear resistance and load carrying capacity in two groups with four and five members, respectively. Fig. 6.1 shows the cross section and the arrangement of the reinforcements of the beams in both the first and second group. The members of both groups shared the same configuration and geometry, but featured different level of prestress (in the first group of beams) and fiber volume fraction (in the second group of beams). Two different shear span length of 1475 mm and 1650 mm were also considered respectively for the members of the first and second group. The influence of prestress level of the steel longitudinal reinforcements on the shear behavior of the beams was assessed by testing the members of the first group, while the beams of second group were tested to investigate the effectiveness of fiber dosage on improving the shear resistance of the developed members.

All the beams were longitudinally reinforced with one steel strand (15.2 mm diameter with a nominal cross section of 140 mm^2) of seven wires (of 5 mm diameter each, $\phi 5$), and different number of GFRP rebars of 8 or 12 mm diameter. From the tensile tests executed according to the standard ASTM D7205/D7205M-06, an average value of 56 GPa was obtained for the GFRP bars (Mazaheripour et al. 2013). In contrast with the behavior of the high tensile strength steel strand, the GFRP bar behaves elastically and linearly up to failure. The yielding and ultimate tensile stress of steel tendon was, respectively, 1740 and 1917 MPa, while the ultimate tensile strength of GFRP bars of 8 and 12 mm diameter was, respectively, 1500 and 1350 MPa. The mechanical properties of the GFRP and steel longitudinal reinforcements are reported in Tables 6.3 and 6.4, respectively. For each member of the two groups, an equivalent internal arm, $d_{s,eq}$, is calculated according to the following equation, considering the internal arm (d_s, d_{GFRP}) and the cross sectional area (A_s, A_{GFRP}) of the steel and the GFRP reinforcements:

$$d_{s,eq} = \frac{A_s d_s + (E_{GFRP}/E_s)A_{GFRP}d_{GFRP}}{A_s + (E_{GFRP}/E_s)A_{GFRP}} \qquad (6.1)$$

where E_{GFRP} and E_s are, respectively, the modulus of elasticity of GFRP bar and steel

strand.
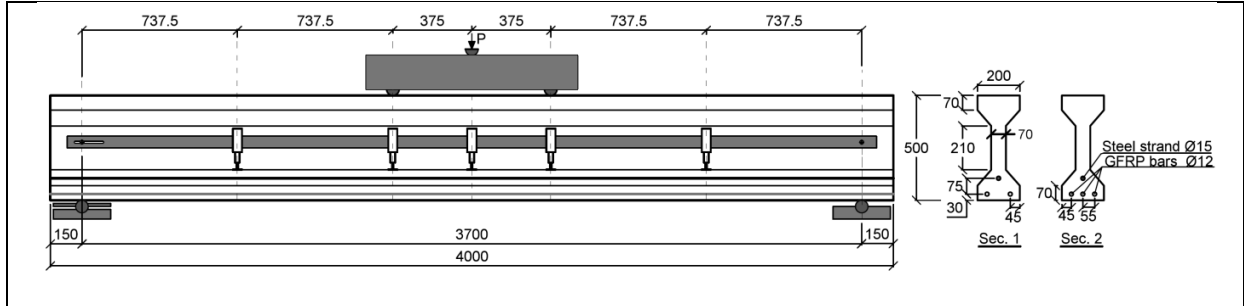
(a)
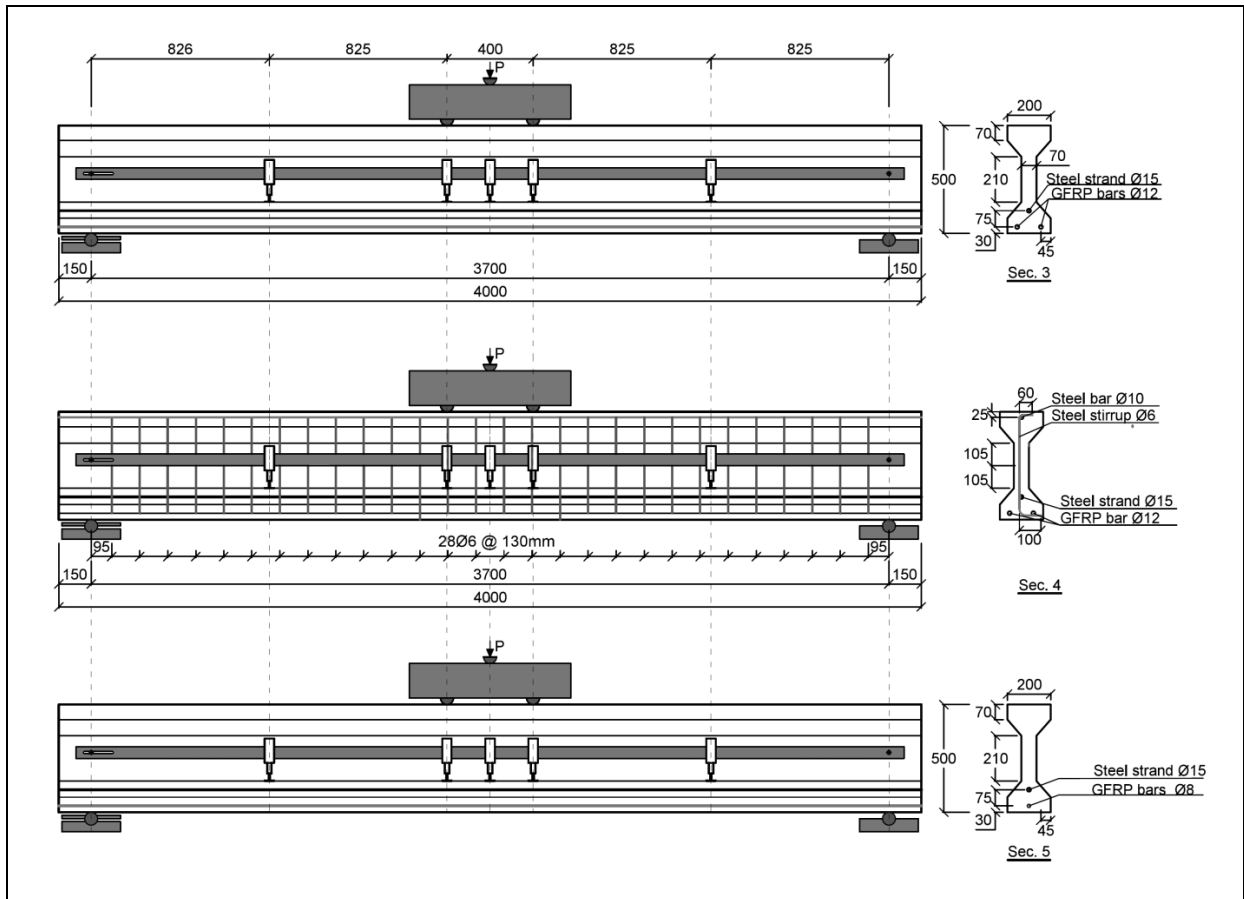
(b)

Fig. 6.1- Configuration and test setup of the beams in (a) the first and (b) second group of the beams (dimensions in mm).

Of the four beams in the first group, three beams were reinforced with a steel strand and 2 GFRP rebars of 12 mm diameter (see Sec.1 in Fig.6.1(a)). In order to assess the effect of higher reinforcing ratio on load carrying capacity, the last beam of this group was reinforced with one more GFRP bar with the same diameter (see Sec.2 in Fig.6.1(a)). In the previous chapter, the effect of prestressing the GFRP bars on shear resistance of the HPFRC beams without stirrups was assessed. Thus, in the present research, the level of prestress, solely applied to the steel strand, is the main variable investigated by testing the beams of the first group. All the beams of the first group, which were developed without stirrups, resist the shear stress using 90 kg/m^3 steel fibers (equal to 1.1% of the concrete volume), since they were casted by M2-F90 concrete composition. Table 6.5 presents the relevant characteristics of the beams in the first group, using the following designation: Si-nG, where "i" is the prestress level applied to the steel strand (as a percentage of the nominal yield strength of the strand f_{sy}=1740 MPa) and "n" is the number of GFRP bars applied without prestressing. For instance "S46-3G" refers to the HPFRC beam reinforced with a steel strand prestressed with 46% of its nominal tensile strength and 3 passive GFRP rebars.

After evaluating the effect of prestress on shear behavior of the beams in the first group, three members of the second group were developed with constant level of prestress and distinct dosage of steel fibers, respectively, 0%, 1.1% and 1.5% of the concrete volume (see Sec.3 in Fig.6.1(b)). In order to compare the effectiveness of steel fibers with that of stirrups for improving the shear resistance of the beams, the other beam of this group was fabricated with SCC and shear reinforced with conventional steel stirrups, as shown in Fig.6.1, Sec.4. This beam with steel stirrups was reinforced with vertically aligned C-shaped steel stirrup of 6 mm diameter, $\phi6$, with spacing of s=130 mm. The shear reinforcement ratio of this beam ($\rho_{sw} = A_{sw} / b_w.s = 0.31\%$, where A_{sw} is cross sectional area of a steel stirrup) and the spacing were designed in accordance with EUROCODE 2. The vertical tendon of the stirrups resist the opening forces across the shear cracks, while the bended ends of the stirrups keep it anchored in the concrete. To facilitate the installation of the stirrups and to assure their proper arrangements, a longitudinal bar of 10mm diameter, $\phi10$, were placed at the compressive region of this beam.

The four introduced beams of the second group were reinforced with one steel strand similar to the one applied for reinforcing the beams in the first group, and 2 GFRP bars of 12 mm diameter. The last member of this group, illustrated in Fig. 6.1, Sec 5, was reinforced with a lower reinforce ratio, by means of adopting a GFRP rebar of 8 mm diameter, and the same steel strand, applied for fabricating the rest of the beams.

All the beams of the second group are introduced by a label "Fj-NW-nGi" in Table 6.5, where "j" is replaced by the volume fraction of steel fibers used for fabrication of the beams, "n" and "i" are respectively the number and diameter of applied GFRP longitudinal rebars, and "NW" shows that the beam has no steel stirrups. In the case of the beam developed with conventional steel stirrups, the letter "N" drops from the label, and the beam is introduced by the designation of "Fj-W-nGi". For instance, the HPFRC beam with fiber volume fraction of 1.5%, flexurally reinforced with 2 GFRP bars of 12 mm diameter, and without stirrups, is identified as "F1.5-NW-2G12" in Table 6.5.

Table 6.3- Mechanical properties of GFRP rebars.

Diameter	Density	E_{GFRP} [a]	$f_{GFRP,u}$ [b]	$\varepsilon_{GFRP,u}$ [c]
(mm)	(gr/cm^3)	(GPa)	(N/mm^2)	(‰)
12	2.23	56	1350	240
8	2.23	56	1500	270

[a] E_{GFRP} Modulus of elasticity.

[b] $f_{GFRP,u}$ Ultimate tensile strength.

[c] $\varepsilon_{GFRP,u}$ Ultimate tensile strain.

The prestress levels of GFRP rebars and steel strand in the case of the second group of beams were selected by considering the results obtained in the beams tested in chapter 5, as well as the results obtained from testing the beams of the primary group in the present chapter. According to the obtained results in the previous chapter regarding to the prestress level of GFRP bars and by respecting the recommendations of the Canadian Standard Association, CSA, (2006) and ISIS Educational Module (2007), the prestress

level of GFRP bars was adopted as the maximum one that can be applied to these rebars (30% of the tensile strength of GFRP bars). Since the final purpose of the present study is the development of prefabricated HPFRC beams without conventional steel stirrups, a higher level of prestress was applied in the steel strand of the second group of beams in order to ensure the adequate shear resistance for these beams. Hence, a prestress percentage of 56% for the steel strand and 30% for the GFRP bars, equal to a total prestressing force of 238 kN, were adopted in the 4 beams of this group with the same flexural reinforcement ratio, namely: F0-NW-2G12, F0-W-2G12, F1.1-NW-2G12 and F1.5-NW-2G12. The last beam of the second group, F1.1-NW-1G8, were prestressed by applying 80% prestress to steel strand and 30% to GFRP reinforcements, providing a total prestressing force of 218 kN.

Table 6.4- Mechanical properties of steel reinforcements.

Diameter	Cross section area	f_{sy} [a]	ε_{sy} [b]	E_s [c]	f_{su} [d]
(mm)	(mm^2)	(N/mm^2)	(‰)	(GPa)	(N/mm^2)
6	28.26	613	2.81	218	696
10	78.50	585	2.81	208	656
15.20	140.05	1740	9.35	200	1917

[a] f_{sy} Yield tensile stress.

[b] ε_{sy} Yield tensile strain.

[c] E_s Modulus of elasticity.

[d] f_{su} Ultimate tensile strength.

[e] ε_{su} Ultimate tensile strain.

The flexural reinforcement ratio of the beams in both the first and second group is calculated by Eq. (6.2) for the hybrid GFRP-steel longitudinal reinforcement, as the equivalent steel reinforcement ratio, $\rho_{s,eq}$, (Qu et al. 2009):

$$\rho_{s,eq} = \frac{A_f}{b_w d_s} + \frac{E_{GFRP}}{E_s} \frac{A_{GFRP}}{b_w d_{GFRP}}$$

(6.2)

In this equation b_w is the web width of the beam's cross section. In order to explore the potentialities of the HPFRC in terms of shear resistance, all the beams were over reinforced by adopting a high equivalent steel reinforcement ratio, $\rho_{s,eq}$ for all the members, except the beam F1.1-NW-1G8, by potentiating shear as the governing failure mode for these beams.

Table 6.5- Details of the slender beams.

Group No.	Specimen ID	GFRP bars	Prestress level		V_f (%)	$d_{s,eq}$ (mm)	$\rho_{s,eq}$ (%)
			Strand (% of f_{sy})	GFRP (% of $f_{GFRP,u}$)			
Group 1	S0-2G	$2\phi12$	0	0	1.1	418.4	0.71
	S23-2G	$2\phi12$	23	0	1.1	418.4	0.71
	S46-2G	$2\phi12$	46	0	1.1	418.4	0.71
	S46-3G	$3\phi12$	46	0	1.1	425.3	0.81
Group 2	F0-NW-2G12	$2\phi12$	56	30	0	418.4	0.71
	F0-W-2G12	$2\phi12$	56	30	0	418.4	0.71
	F1.1-NW-2G12	$2\phi12$	56	30	1.1	418.4	0.71
	F1.5-NW-2G12	$2\phi12$	56	30	1.5	418.4	0.71
	F1.1-NW-1G8	$1\phi12$	80	30	1.1	401.8	0.55

6.2.3 Prestressing System and Fabrication of the Elements

The system applied for prestressing the beams is shown in Fig. 6.2. After arranging the reinforcements, the steel strand and GFRP bars were prestressed in accordance with Table

6.5. For prestressing the steel strands of the beams in both of the groups, the force was applied to one extremity of the tendon, while the other extremity remained fixed using a steel anchor. The GFRP bars of the second group of beams were pretensioned according to the prestressing method introduced in Sec. 5.3.3 of chapter 5. By completing the prestressing procedure, the beams were cast and the prestressing force was released 4 days after casting the beams, by adopting a release rate of about 0.3 kN/min. Curing of the beams was carried out for 7 days, and the beams were tested at the age of 28 days.
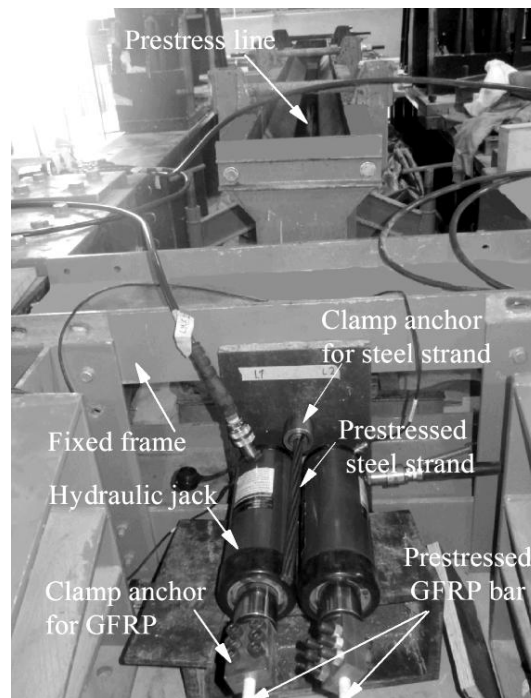
Fig. 6.2- Prestressing system.

6.2.4   Test Setup and Measurements

Fig. 6.1 represents the test setups adopted for testing the beams of both groups. All the beams were simply supported and tested up to the ultimate failure under a four-point loading configuration. Two rollers attached to a steel bearing plate were placed on top of the elements in order to apply two point loads on the beams. The load, P, applied to the mid-span of this steel spreader, was assured by a servo-controlled hydraulic actuator of ±700 kN with $\pm0.05\%$ accuracy. The supports were located at a distance of 150 mm from

the ends of the beams. The first group of the beams were tested by adopting the shear span to effective depth ratio, $a/d_{s,eq}$, of 3.5, while the second group of the beams were tested with $a/d_{s,eq}$=3.9, by considering the shear span of 1475 mm and 1650 mm, respectively, for the beams of the first and second groups.

The tests were displacement-controlled by imposing a speed of 0.01 mm/sec to the piston of the actuator. Five LVDTs were installed along the span length of the beam, according to the schematic representation in Fig. 6.1.

6.2.5 Experimental Results and Discussion
6.2.5.1 Load-deflection relationship

Fig. 6.3 represents the load versus mid-span deflection, $P-\delta$, of the both groups of the tested beams. As it was expected, all the beams, apart beam F1.1-NW-1G8, failed in shear due to the relatively high flexural capacity. The failure of the first group of beams has occurred with a considerable deflection level, much higher than the one corresponding to the serviceability limit state condition by deflection, SLS (L/250=16mm), δ_{SLS}. Comparing to the reference beam of the first group, S0-2G, with passive longitudinal reinforcements, it can be concluded that by increasing the prestress level of the steel strand the load carrying capacity at SLS, F_{SLS}, exhibited an increase of 6% and 15% for S23-2G and S46-2G beam, respectively. However, the ultimate load carrying capacity was almost the same, since it is limited by the shear resistance of the beams. By comparing the behavior of the beam S46-3G reinforced by 3 GFRP bars with that of its similar prestressed case, beam S46-2G with 2 GRFP bars, it is observed that the higher flexural reinforcement ratio has assured a larger post-cracking stiffness, with higher load carrying capacity for the deflection at SLS. However, the deflection at ultimate load has decreased because the load carrying capacity of the elements was limited by its shear resistance that is common for both of the beams.

Similar to the deflection behavior of the first group of the beams, all the beams in the second group presented a relatively high deflection at failure, which was more than twice the deflection of these beams at SLS. The control beam, F0-NW-2G12, presented abrupt

load decay just after the peak load. An almost similar F_{SLS} was obtained by testing the beam "F0-W-2G12" with conventional shear reinforcement (compared to in the reference beam, F0-NW-2G12, with neither stirrups nor steel fibers) since the stirrups, does not affect the load carrying capacity of the beam, up to 37.7 mm deflection corresponding to the formation of a critical shear crack. The stirrups made the beam to be capable of continuing supporting load and deflection higher than those values registered at critical shear crack formation. However, it still exhibited a brittle failure that occurred due to the rupture of stirrups. Application of 90 and 120 kg/m^3 steel fibers for developing, respectively, the beams F1.1-NW-2G12 and F1.5-NW-2G12 has increase the F_{SLS} in 16% and 18% compared to the control one. The F_{SLS} of 223 kN and 230 kN obtained in the case of beam F1.1-NW and F1.5-NW, respectively, indicates that this type of beams, with convenient geometric adjustements, can be adopted in pre-fabrication for constituting structural systems of buildings of industrial or commercial activities. F1.1-NW beam, with 90 kg/m^3 steel fibers, for instance, can constitute the support of pre-stressed slabs of a span length between 12 to 20 m for a live load in the range of 4 to 6 kN/m^2, which is one of the objectives of the present research project. In spite of having higher $a/d_{s,eq}$ ratio, and therefore the comparison cannot be a straightforward process between these beams (with $a/d_{s,eq}$=3.9, belonged to the second group) and the ones in the first group (with $a/d_{s,eq}$=3.5), the $P-\delta$ clearly supports the benefits of increasing, as much as possible, the prestress level in both flexural reinforcements.
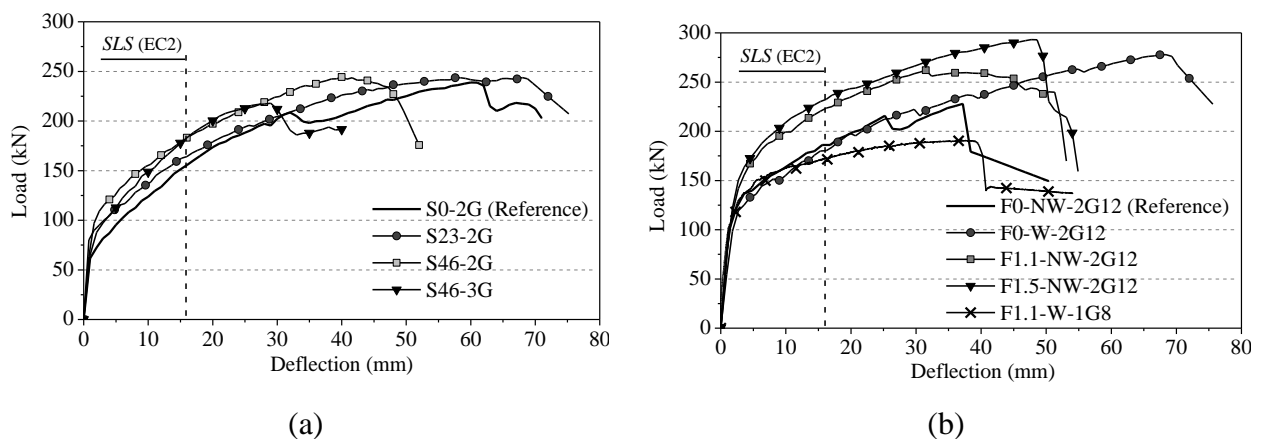
Fig. 6.3- Load *vs.* mid-span deflection relationship of (a) the first and (b) second groups

of the beams.

Although an almost similar F_{SLS} was obtained by testing the beams F1.1-NW-2G12 and F1.5-NW-2G12, application of higher dosage of steel fibers in the HPFRC of the F1.5-NW beam caused an increase of 10% in the load carrying capacity at ultimate limit state, F_{ULS}. However, both beams failed at almost similar deflection by reaching their ultimate shear capacity. In comparison with the control beam, the F1.1-NW-2G12 and F1.5-NW-2G12 beam presented an increase in the F_{ULS} of, respectively, 13% and 22%. The increase of F_{ULS} was 17% in the case of the beam reinforced with stirrups, F0-W-2G12, when compared to the control beam. The F1.1-NW-2G12 and F1.5-NW-2G12 beams presented an increase of 20% and 22% in the F_{SLS}, respectively, when compared to that of F0-W-2G12 beam. The results also show a negligible difference in F_{ULS} obtained by testing the beam F1.1-NW-2G12 (which its shear resistance was provided by application of 90kg/m^3 steel fiber), and the beam F0-W-2G12 (with conventional stirrups).

As it was expected, the F1.1-NW-1G8 beam presented a flexural failure mode. At serviceability limit state, the beam F1.1-NW-1G8 presents a relatively high load carrying capacity, which was close to the corresponding one of F0-W-2G12 beam with steel stirrup, as well as S46-2G beams of the first group. Since the beam has failed in flexure, it presented a lower ultimate load carrying capacity compared to the rest of the beams. Table 6.6 resumes the relevant results obtained in both groups of the tested beams.

In order to compare the shear strength between members of the first and second group with different $a/d_{s,eq}$ ratio, the shear strength of the beams were normalized using " $V_{nz} = V/(b_w d_{s,eq}\sqrt{f_{cm}})$ " formula, in accordance with American Concrete Institute (ACI) 440.IR-06, and the results are depicted in Fig. 6.4. The value corresponding to the F1.1-NW-1G8 beam is not presented, since this beam failed in bending before reaching its ultimate shear strength. By comparing the normalized shear strength, V_{nz}, of the beams S0-2G (V_{nz}=0.503), S23-2G (V_{nz}=0.513) and S46-2G (V_{nz}=0.514) of the first group, in Fig. 6.4, with that of the F1.1-NW (V_{nz}=0.550) beam of the second group of beams, all of them with the same dosage of steel fibers, a significant effect of the prestress level on the increase of the shear strength is verified. Hence, by applying 1.6 MPa, 3.2 MPa and 6.8

MPa of prestress in the beams S23-2G and S46-2G (by prestressing the strand) and F1.1-NW-2G12 (by means of prestressing both the steel strand and GFRP bars) the normalized shear strength has increased 9.3%, 7.2% and 7% compared to the control beam with no prestress, S0-2G. On the other hand, the figure demonstrates the lowest V_{nz} for the beam F0-NW-2G12 without steel fiber, although this beam was prestressed with the highest level of prestress. Comparing the normalized shear strength of the beam F0-NW-2G12 (V_{nz} =0.490) with that of obtained for the HPFRC beams of the first group (with lower level of prestress), represents a pronounceable influence of the steel fibers on increasing the shear capacity of the beams. Finally, the close value of the V_{nz} computed for the beam F0-W-2G12, with steel stirrups, and F1.1-NW-2G12 and F1.5-NW-2G12, reinforced with steel fibers, indicates the possibility of developing a beam without conventional stirrups by adopting an adequate dosage of steel fiber together with an appropriate level of prestress, depending on $a/d_{s,eq}$ ratio (Soltanzadeh et al. 2015), reinforcement ratio and concrete compressive strength (Qu et al. 2009).
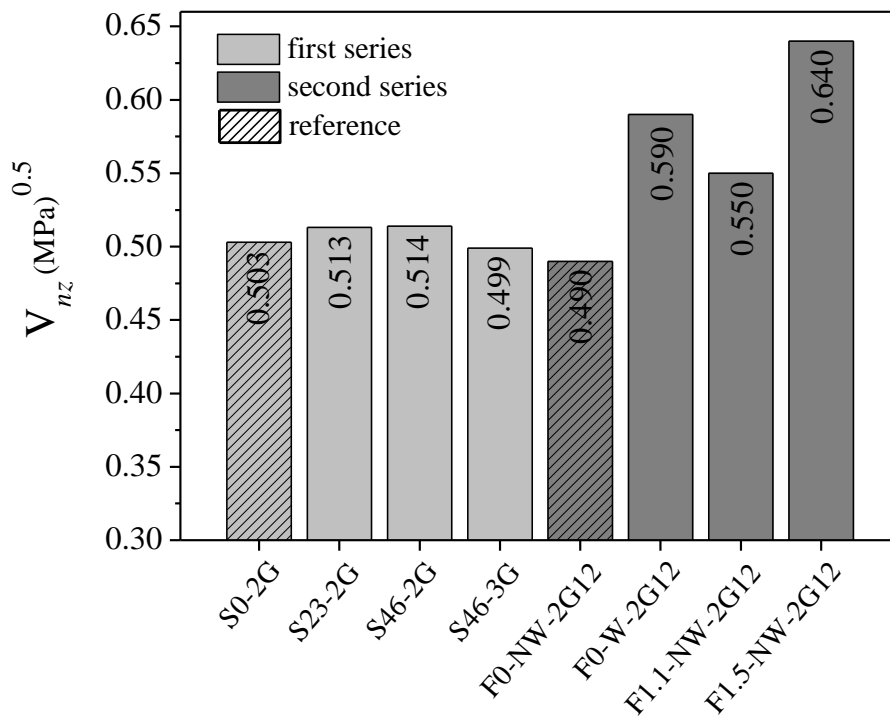
Fig.6.4- Effect of prestress and fiber dosage on the normalized shear strength of the

beams.

Table 6.6- Main results.

Group No.	Specimen ID	F_{SLS} [a] (KN)	Improvement of F_{SLS} [b] (%)	F_{ULS} [c] (KN)	δ_u [d] (mm)	V [e] (KN)
	S0-2G (Reference)	151.42	-	240.12	60.71	120.06
Group 1	S23-2G	161.98	6.5	244.80	67.68	122.40
	S46-2G	178.14	15.0	245.60	40.21	122.80
	S46-3G	198.84	23.8	242.48	27.91	121.24
	F0-NW-2G12 (Reference)	187.83	-	229.52	37.14	114.76
Group 2	F0-W-2G12	179.27	-	277.98	68.35	138.99
	F1.1-NW-2G12	222.93	15.7	263.00	32,70	131.10
	F1.5-NW-2G12	229.84	18.3	293.75	47.39	146.88
	F1.1-NW-1G8	171.96	-	192.08	36.88	96.04

[a] F_{SLS} Load at serviceability limit state.

[b] Increase of F_{SLS} for the beams of each group compared to the reference beam of the same group.

[c] F_{ULS} Ultimate load.

[d] δ_u Deflection corresponding to F_{ULS}.

[e] V Shear load.

6.2.5.2 Mode of failure

During testing the beams the crack patterns were carefully mapped simultaneously by capturing the photos each 20 second of both the shear span zones of the beams. Fig. 6.5

shows the crack patterns registered at the failure of all the tested beams of the first and second group. By loading the beams, the flexural cracks appeared at the midspan and gradually spread out to the shear span by increasing the load.

The diagonal tension failure was the predominant mode of failure in the first group of the beams where the prestress level was the main considered variable. The confinement provided by the applied normal stress on the cross section of the beams delayed the cracking initiation. When compared to the control beam without prestress, S0-2G0, in the other beams of this group a higher number of cracks was detected, with the tendency to increase with the prestress level applied to the beam. These multiple cracks developed gradually in a stable manner, leading to the increase of the post cracking stiffness of the beams, depending on the level of prestress. Similar to the beams of the first group, the beams F0-NW-2G12, F0-W-2G12, F1.1-NW-2G12 and F1.5-NW-2G12 of the second group failed by the diagonal tension mode of failure. By loading the reference beam, F0-NW-2G12, initially the flexural and diagonal cracks developed, but the diagonal cracks propagated and grown more rapidly due to the beam weakness in resisting the shear cracks, followed by a sudden and abrupt load decay, typical of a shear failure. The cracking behavior of the beam F0-W-2G12 with the conventional shear reinforcement was characterized by the development of some critical inclined cracks, which caused the yielding of the stirrups. The beam exhibited a significant deflection by yielding of the stirrups, but the failure was violent, due to the rupture of steel stirrups.

Unlike the beams F0-NW-2G12 and F0-W-2G12, which were produced without steel fibers, the HPFRC beams F1.1-NW-2G12 and F1.5-NW-2G12 developed multiple flexural and diagonal cracks before occurrence of the failure. The formation of a much diffuse crack pattern in beam F1.1-NW-2G12, with several potential shear failure cracks, is responsible for the pseudo-plastic plateau in the $P-\delta$ response above a deflection of about 30 mm, which is quite evident in Fig.6.5. After initiation and propagation of the diagonal cracks, the F1.5-NW-2G12 beam continued to resist higher shear load and developing more cracks without exhibiting any reduction in load carrying capacity up to reaching the ultimate shear capacity of the beam. Comparing the F0-W-2G12 beam reinforced with conventional stirrups, with those made by HPFRC it is verified that in the former beam a smaller number of cracks with larger distance were formed, while in the

second type of beams the reinforcement provided by steel fibers resulted in the development of multiple thinner cracks with smaller spacing, leading to a higher energy dissipated in the fracture process, and ductility.

Group 1

S0-2G (Reference)

S23-2G

S46-2G

S46-3G

Group 2

F0-NW-2G12 (Reference)

F0-W-2G12

F1.1.NW-2G12

| F1.5-NW-2G12 | F1.1-NW-1G8 |
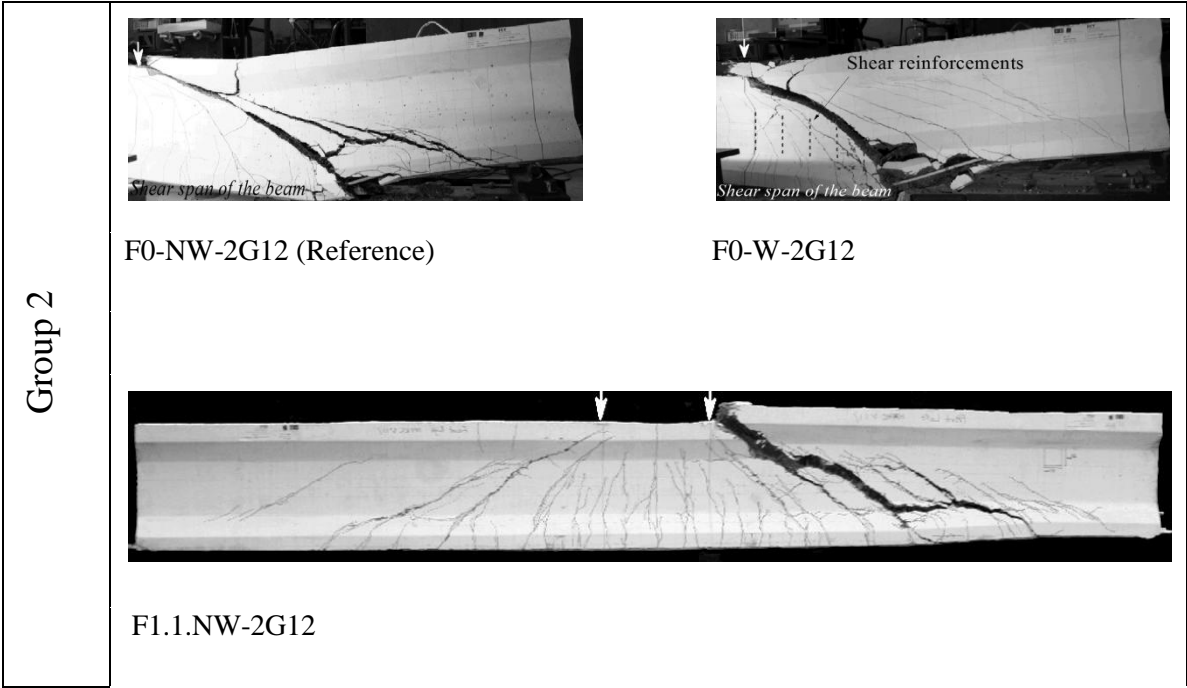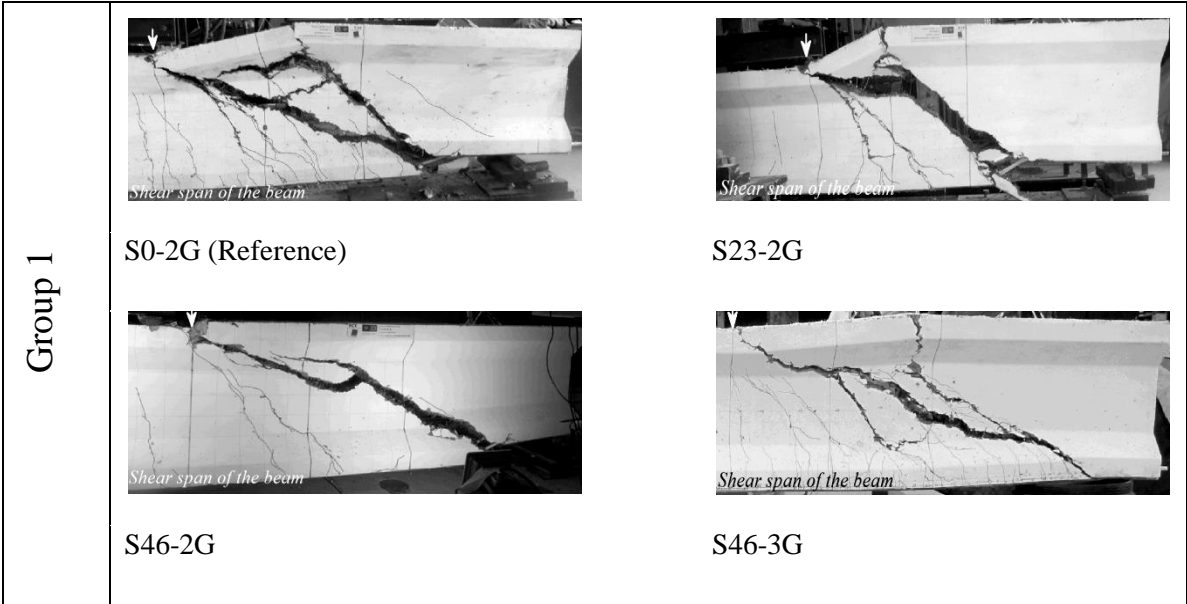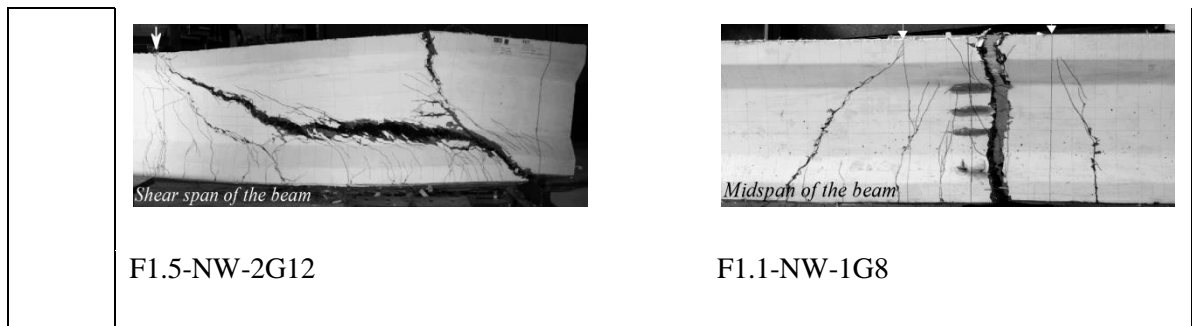
Fig. 6.5- Crack pattern of the beams at failure stage.

6.3 SHEAR RESISTANCE

In chapter 5 of the present thesis, the formulations presented in MC2010 and RILEM TC 162-TDF (2003), as well as the one proposed by Soetens (20015) for predicting the shear resistance of beams were introduced, and the accuracy of these approaches in case of short-span beams was evaluated. In the present chapter the predictive performance of these formulations in case of slender beams is assessed using the results obtained in the HPFRC beams considered in the present chapter. The formulations were already introduced through the equations 5.9, 5.14 and 5.19 in chapter 5, respectively, in accordance with RILEM TC 162-TDF (2003), MC2010 and Soetens (20015) approaches. For the calculations of V_{MC2010}, V_{RILEM} and $V_{Soetens2010}$ average values were considered for the material properties, and $\gamma_c = 1$ was adopted. Table 6.7 compares the shear resistance of the tested beams in the present chapter, V_{exp}, with those estimated analytically, V_{MC2010}, V_{RILEM} and $V_{Soetens2010}$, according to MC2010, RILEM TC 162-TDF (2003) and Soetens (20015) formulas. The corresponding shear strength of the beams, $v_u = V_{exp} / (bd_{s,eq})$, is also indicated in Table 6.7, where the ratio of shear resistance of the beams obtained experimentally to the estimated ones, V_{exp} / V_{anal}, is considered for evaluating the accuracy of the formulas. In this evaluation, the shear resistance of F0-W-2G12 beam is not estimated by Soetens (20015) formulas, since this formulation is valid only in case of beams without stirrups.

The V_{exp} / V_{anal} ratio evidences that the RILEM TC 162-TDF (2003) and Soetens (2015) formulas predict with higher accuracy the shear resistance of the HPFRC slender beams than the MC2010 formula. A quite conservative estimation is obtained using MC2010 formula, with an average V_{exp} / V_{MC2010} of 1.6. The obtained by MC2010 formula are, in average terms, about 40% lower than the ones calculated by RILEM TC 162-TDF (2003) provisions, and 38% lower than Soetens (2015) formula. Considering the average V_{exp} / V_{anal} ratio obtained using all the three introduced

approaches for estimation of shear resistance of the slender beams in the present chapter, with that of the short-span beams studied in chapter 5, suggests that RILEM TC 162-TDF (2003) approach estimates more accurately the shear resistance of both HPFRC short-span and slender beams than the other approaches. The shear resistance calculated using the formula proposed by Soetens (2015) provided higher accuracy in case of slender beams than in short-span beams, but the dispersion of the V_{exp}/V_{anal} was the highest amongst the three approaches. MC2010 provided the highest conservative estimations for both types of the beams.

Table 6.7- Shear resistance calculated analytically in comparison with the experimental results.

	Specimen ID	V_{exp} (kN)	v_u (MPa)	V_{MC2010} (kN)	$\dfrac{V_{exp}}{V_{MC2010}}$	V_{RILEM} (kN)	$\dfrac{V_{exp}}{V_{RILEM}}$	$V_{Soetens\,2015}$ (kN)	$\dfrac{V_{exp}}{V_{Soetens}}$
Group 1	S0-2G	120.1	4.1	60.9	1.97	135.9	0.88	139.1	0.86
	S23-2G	122.4	4.2	67.9	1.80	143.0	0.86	151.4	0.81
	S46-2G	122.8	4.2	75.0	1.63	150.0	0.82	161.5	0.76
	S46-3G	121.2	4.1	78.8	1.54	153.1	0.79	165.9	0.73
Group 2	F0-NW-2G12	114.8	3.9	62.0	1.85	62.0	1.85	44.16	2.6
	F0-W-2G12	139.0	4.7	112.6	1.23	112.6	1.23	-	-
	F1.1-NW-2G12	131.1	4.5	90.7	1.45	165.8	0.79	176.23	0.74
	F1.5-NW-2G12	146.9	5	89.3	1.65	178.2	0.82	172.83	0.85
	F1.1-NW-1G8	96.04	3.4	80.4	1.19	156.3	0.61	163.78	0.59
	Av.				1.60		0.96		0.99
	CoV				16.8		38.6		66.0

In Fig. 6.6(a), the effect of prestress level on the shear resistance predicted according to

all the three approaches is compared with that obtained by testing the members of the first group: S0-2G, S23-2G and S46-2G, with the same reinforcement ratio and different level of prestress. Although the experimental results demonstrate an increase of 2.2% in shear resistance of these beams by application of 46% prestress (σ_{cp} =3.2 MPa), this increase is predicted as 9.4%, 18.8% and 13.9% when using, respectively, the RILEM TC 162-TDF (2003), MC2010 and Soetens (2015) approaches. It demonstrates the requirements of further research in case of prestressing influences on the shear resistance of FRC elements in order to improve the reliability of the predictions.

The influence of the shear reinforcements, i.e. steel fibers and stirrups, on shear resistance of the slander beam is another factor, which is considered for evaluation of the formulas. Fig. 6.6(b) represents this effect on the shear resistance of the second group of beams with exception of the beam F1.1-NW-1G8 that was failed in bending. Since both RILEM TC 162-TDF (2003) and MC2010 guidelines address the contribution of plain concrete and stirrups in a same way, they represent the same predictions for the shear resistance of the beams F0-NW-2G12 and F0-W-2G12. The contribution of stirrups for the increase of the shear resistance of the beams is considered as 44.9% by these equations, while this contribution was obtained only 17.4% experimentally.
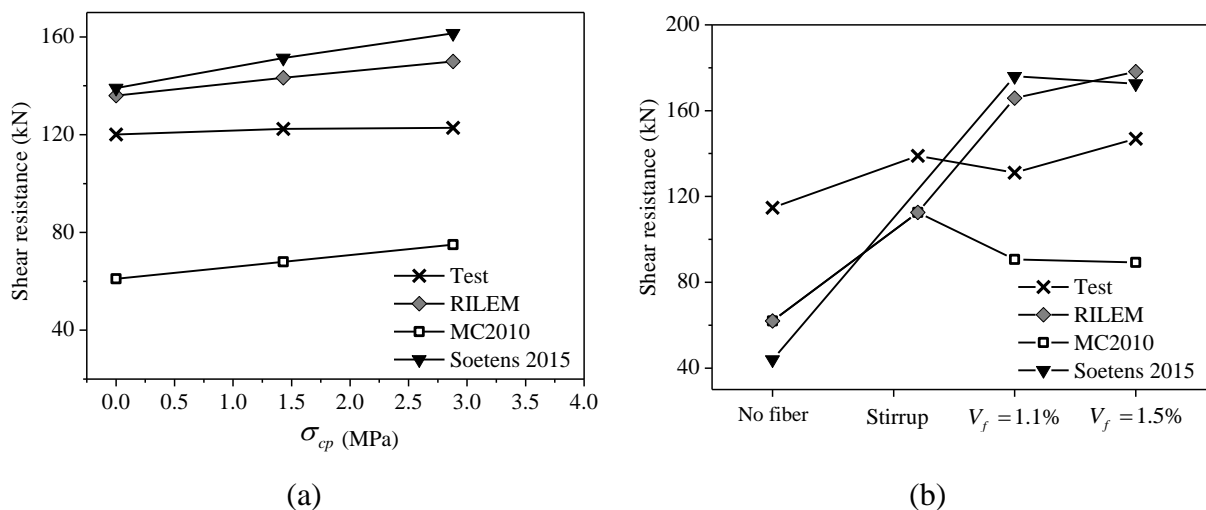
Fig. 6.6- (a) Shear capacity *vs.* σ_{cp} in first group, and (b) Shear capacity *vs.* V_f in the second group of beams.

Fig. 6.6(b) also shows that RILEM TC 162-TDF (2003) and Soetens (2015) formulas provided better estimations of the shear resistance in case of the beams with 90 kg/m^3 and 120 kg/m^3 steel fibers, when compared to the results obtained by MC2010 guideline. This conclusion also can be drawn by comparing the average V_{exp}/V_{anal} ratio obtained using the three formulas in case of the beam F1.1-NW-1G8. Since this beam failed in bending before reaching its full shear capacity, it was expected to obtain a higher estimation compared to that of obtained experimentally ($V_{exp}/V_{anal} < 1$). However, it just found in the predictions of RILEM (2003) and Soetens (2015) approaches. The lower estimated shear resistance of F1.1-NW-1G8 beam by MC2010 formula, compared to the experimental results, can be attributed to the conservative estimation of prestressing effect contributed to the shear resistance of the beam. The shear contribution, as a percentage attributable to concrete and shear reinforcement, is reported in Table 6.8.

In the present chapter the accuracy of estimating the fiber contribution in the shear resistance of the beams, mainly for a larger range of fibers volume fraction, was assessed by considering the experimental results obtained in the present chapter accompanied with those corresponding to fifteen other beams collected from literature. This database includes regular and high strength concrete reinforced with different content of hooked end steel fibers of aspect ratio (l_f/d_f) in the interval 62 to 65. The ranges of other considered parameters are as follow:

– Height of the beam's cross section: $300\,\text{mm} \leq h \leq 1500\,\text{mm}$;

– Cylindrical average concrete compressive strength: $32\,\text{MPa} \leq f_{cm} \leq 67\,\text{MPa}$;

– Fiber volume fraction: $0\% \leq V_f \leq 1.5\%$;

– Longitudinal tensile reinforcement ratio: $0.7\% \leq \rho_{eff} \leq 1.83\%$, and

– Shear span to effective depth ratio: $2.23 \leq a/d \leq 3.9$.

All the beams selected from the literature are introduced in Table 6.9. The beams were labeled as Chi-Fj-P/x, where: "C" can be replaced by the type of the beam's cross section, indicating if the beam has a rectangular (R) or T-shape (T) cross section; "i" represents the height of the beam's cross section in mm, and "j" is the applied dosage of steel fiber (kg/m^3). When a beam is not prestressed "P" is dropped from its designation. Finally, a number (x) is assigned to each beam in order to distinguish the specimens with the similar

depth, fiber dosage and prestressing condition. For instance, "Th750-F60-P/1" refers to a prestressed beam number 1 of T-shape cross section with 750 mm height, reinforced with 60 kg/m^3 of steel fibers. Additional information about the beams can be found in Table 6.10.

The analytical shear values corresponding to the contribution of concrete and fibers for the shear resistance of the selected beams, according to the three considered approaches, are indicated in Fig. 6.7. In this figure the calculated values for the two groups of beams, with and without prestress, are sorted in ascending order regarded to the dosage of steel fiber, and are compared to the reported results obtained experimentally. Regarding the values given in Table 6.9 and represented in Fig.6.7, it can be found that RILEM TC 162-TDF (2003) formula yields more accurate predictions for the presented sample of test data in comparison with the two other shear models, in terms of the predicted load and coefficient of variation. Hence, it can be concluded that RILEM TC 162-TDF (2003) formula gives more accurate predictions of fiber contribution compared to MC2010 formula, since the contribution of concrete is estimated similarly according to both these guidelines.

Table 6.8- Shear contribution of concrete and fibers according to the current design codes.

	Beam ID	V_{MC2010}		$\dfrac{V_{exp}}{V_{MC2010}}$	V_{RILEM}		$\dfrac{V_{exp}}{V_{RILEM}}$	$V_{Soetens2015}$		$\dfrac{V_{exp}}{V_{Soetens}}$
		V_{cd}	V_{fd}		V_{cd}	V_{fd}		V_{cd}	V_{fd}	
		(%)	(%)		(%)	(%)		(%)	(%)	
Group 1	S0-2G	53	47	1.97	24	76	0.88	19	81	0.86
	S23-2G	58	42	1.80	27	73	0.86	21	79	0.81
	S46-2G	62	38	1.63	31	69	0.82	23	77	0.76
	S46-3G	62	38	1.53	32	68	0.79	24	76	0.73
ou	F0-NW-2G12	100	0	1.85	100	0	1.85	100	0	2.6

F0-W-2G12	55	45[*]	1.23	55	45[*]	1.23	-	-	-
F1.1-NW-2G12	68	32	1.44	37	63	0.79	25	75	0.74
F1.5-NW-2G12	68	32	1.65	34	66	0.82	25	75	0.85
F1.1-NW-1G8	68	32	1.19	35	65	0.61	23	77	0.89

*Related to the contribution of stirrups.

Fig 6.8 represents the V_{exp}/V_{anal} obtained with the three approaches for the data base organized in two groups: non-prestressed beams; prestressed beams. For each of these two groups, the results are organized according to the content of fibers, and each group of beams of equal fiber content is composed of beam's of different cross section height. The results show that for the non-prestressed beam, by increasing the depth of the beam's cross section, the V_{exp}/V_{anal} has a tendency to decrease, which means that shear resistance is overestimated. For instance, while the obtained shear value for Rh500-F50/5 beam is suitably close to the experimental value and is quite safe, it becomes rather unsafe by increasing the depth of the beam's cross section (e.g. compare the predicted shear resistance values of the beam Rh500-F50/5 with that of Rh1000-F50/8 and Rh1500-F50/11 respectively). This confirms the requirement of improving size effect factor, k, to boost the reliability of the predictions. In the case of prestressed beams, conservative values were generally obtained by using MC2010 formula ($V_{exp}/V_{anal} > 1$). The experimental results were predicted adequately by using the RILEM TC 162-TDF (2003) approach, while mostly were found to be marginally overestimated by Soetens (2015) formula. The decrease of V_{exp}/V_{anal} with the increase of the depth of the beam's cross section seems to be well fitted by a polynomial curve, is shown clearly in Fig. 6.9.

For the flanged beams, the RILEM TC 162-TDF (2003) approach estimates the contribution of the flange for the shear resistance by introducing the k_f factor in its formula. For the beams with rectangular cross section, the k_f is assumed to have unit value, while this value increases for the flanged beams, according to the equations (5.13a) and (5.13b) presented in chapter 5. The variation of the safety margin obtained for the

flanged beams with and without considering the k_f factor is compared in Fig. 6.10. This figure shows that, using the k_f factor equal to one results in a better estimation of shear resistance (compared to that of estimated by accounting $k_f = 1.31$ in accordance with RILEM TC 162-TDF (2003) provision) for the HPFRC beams developed in the present study with flange to web width ratio, W_f / W_w, of 2.85. In case of the other beams, with larger W_f / W_w ratio, namely 4 and 6, with $k_f = 1.5$, the estimation is more accurate by using the k_f value, proposed by RILEM TC 162-TDF (2003) approach.

Table 6.9- Shear contribution of concrete and fibers according to the current design codes.

Reference	Beam ID	V_{MC2010}		$\dfrac{V_{exp}}{V_{MC2010}}$	V_{RILEM}		$\dfrac{V_{exp}}{V_{RILEM}}$	$V_{Soetens2015}$		$\dfrac{V_{exp}}{V_{Soetens}}$
		V_{cd}	V_{fd}		V_{cd}	V_{fd}		V_{cd}	V_{fd}	
		(%)	(%)		(%)	(%)		(%)	(%)	
Cuenca and Serna (2013)	Th750-F60-P/1	72	28	1.58	61	39	1.34	41	59	1.12
	Th750-F60-P/2	72	28	1.40	61	39	1.19	44	56	1.06
	Th800-F60-P/3	72	28	1.62	61	39	1.36	42	58	1.15
Minelli et al. (2013)	Rh500-F0/4	100	-	1.00	100	-	1.00	100	0	1.30
	Rh500-F50/5	54	46	1.19	51	49	1.12	33	67	0.97
	Rh500-F75/6	52	48	1.11	46	54	0.99	29	71	0.84
	Rh1000-F0/7	100	-	0.88	100	-	0.88	100	0	1.14
	Rh1000-F50/8	54	46	0.74	51	49	0.69	30	70	0.54
	Rh500-F75/9	52	48	0.90	46	54	0.80	26	74	0.61
	Rh1500-F0/10	100	-	0.70	100	-	0.70	100	0	0.91
	Rh1500-F50/11	54	46	0.93	50	50	0.86	28	72	0.64

	Rh1500-F75/12	52	48	1.01	46	54	0.88	25	75	0.64
Soltanzadeh et al. (2013)	Rh300-F90/13	53	47	1.40	32	68	0.85	27	73	0.74
	Rh300-F90-P/14	54	46	1.60	33	67	0.99	28	72	0.84
	Rh300-F90-P/15	55	45	1.66	34	66	1.05	29	71	0.87
Average				1.31			0.94			0.87
CoV (%)				28.6			20.1			23.6
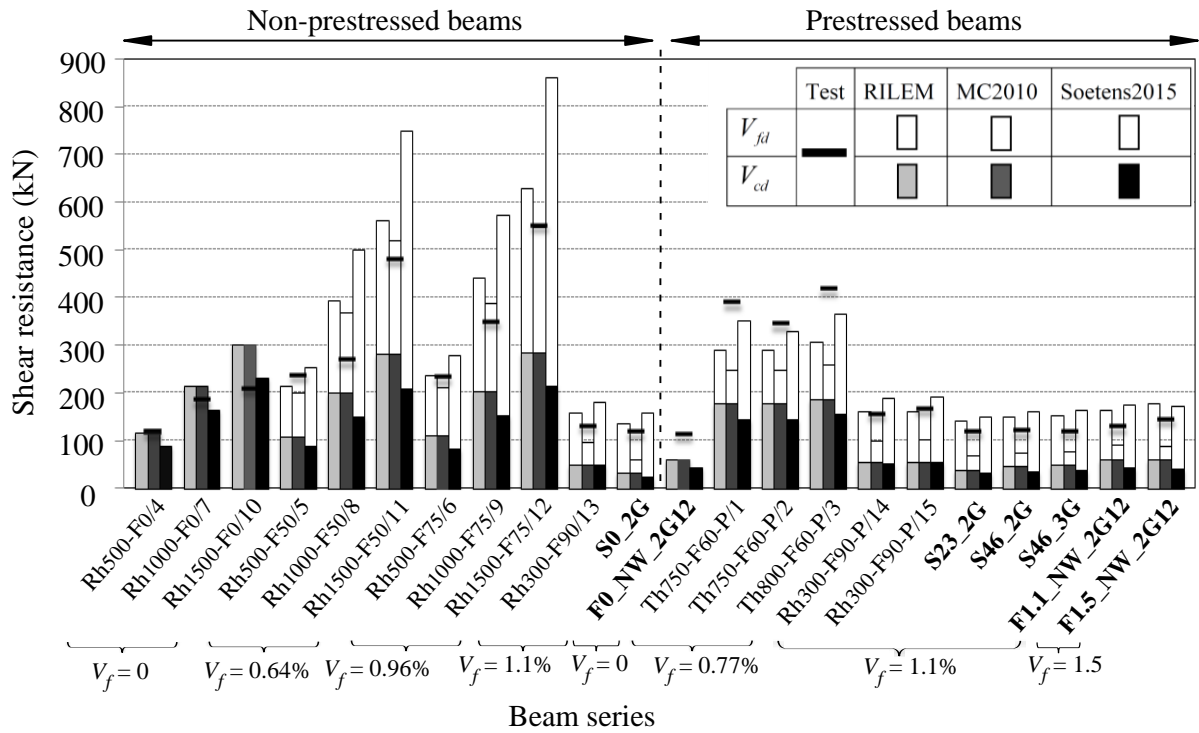
Fig. 6.7- Contribution of concrete and fiber reinforcement to the calculated ultimate shear capacity of the beams.
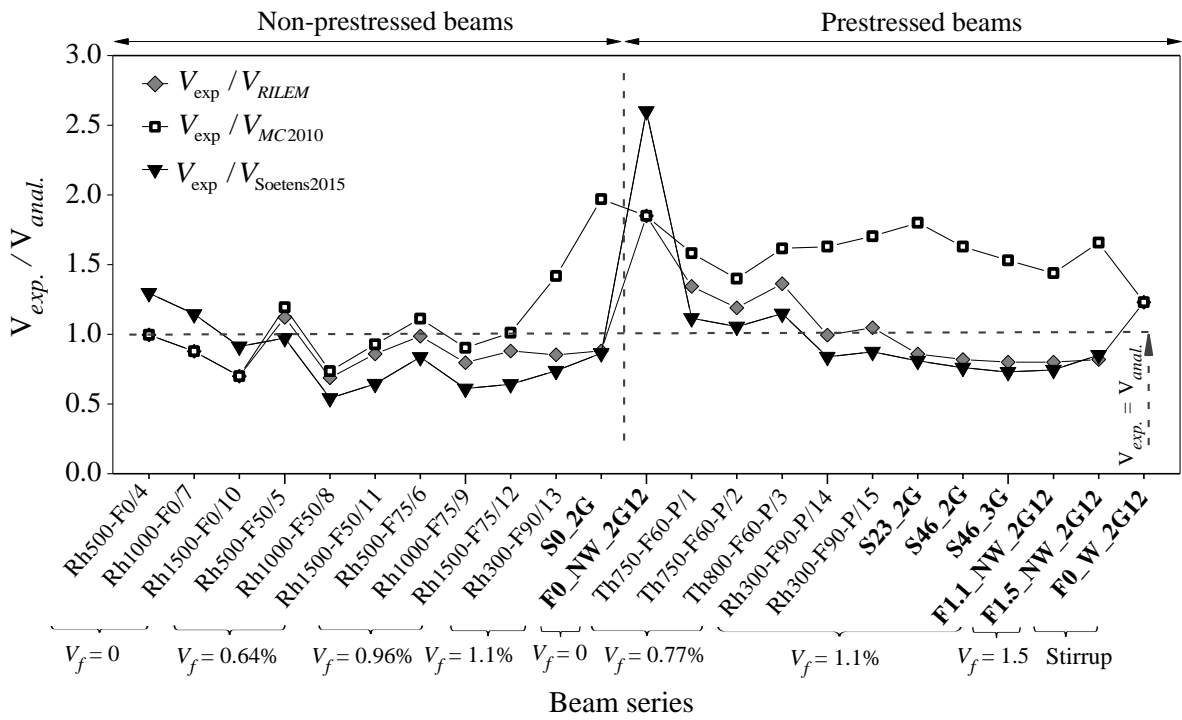
Fig. 6.8- $V_{\exp} / V_{anal}$ versus fiber volume fraction for groups of prestressed and non-prestressed RC beams of different beam's cross section.
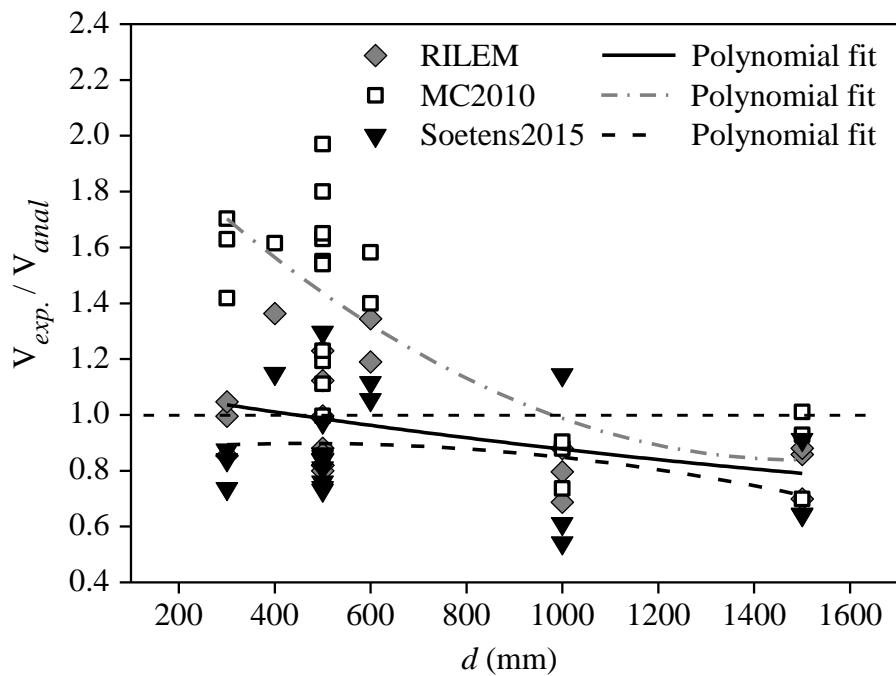
Fig. 6.9- The influence of the beam's cross section depth, d, on the $V_{\exp} / V_{anal}$.
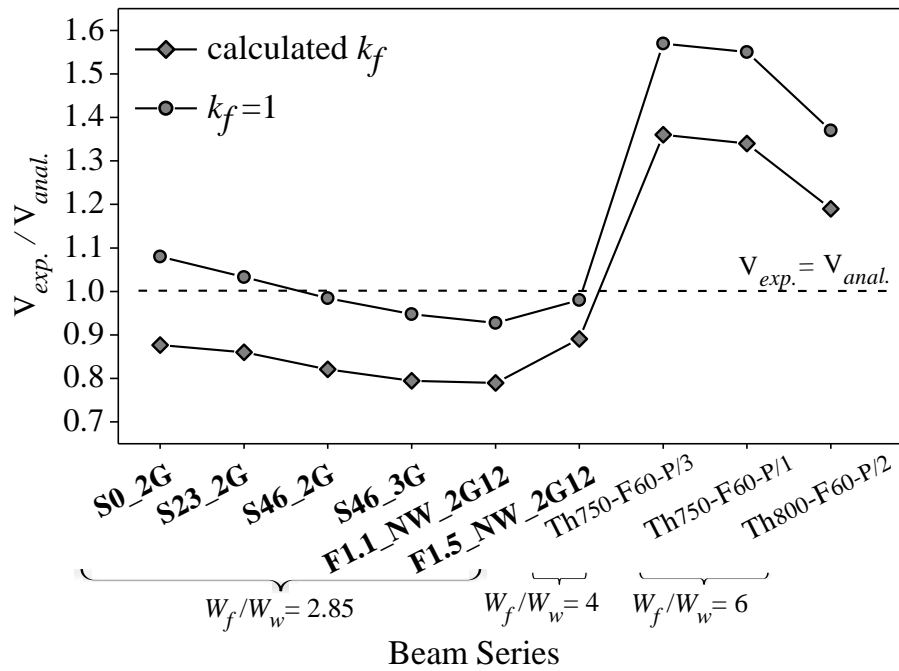
Fig. 6.10- Effect of flange factor on safety margin.

Table 6.10- Data base corresponding to the main characteristics of the beams collected from literature.

Reference	Beam ID	Cross section	b	d	L	a/d	ρ	f_{cm}	l_f/d_f	m_f	σ_{cp}	V_{exp}
			(mm)	(mm)	(mm)		(%)	(MPa)		(kg/m³)	(MP)	(kN)
Cuenca and Serna (2013)	Th750-F60-P/1	T[a]	100	689	5100	3	1.83	60	65	60	8.23	392
	Th750-F60-P/2	T	100	689	5100	3	1.83	60	65	60	8.23	347
	Th800-F60-P/3	T	100	739	5100	2.8	1.71	60	65	60	8.23	420
Minelli et al. (2013)	Rh500-F0/4	R	250	440	3000	3	1.12	38.7	62.5	0	0	116
	Rh500-F50/5	R	250	440	5900	3	1.12	32.1	62.5	50	0	240
	Rh500-F75/6	R	250	440	9000	3	1.12	33.1	62.5	75	0	235
	Rh1000-F0/7	R	250	940	3000	3	1.07	38.7	62.5	0	0	188
	Rh1000-F50/8	R	250	940	5900	3	1.07	32.1	62.5	50	0	272
	Rh1000-F75/9	R	250	940	9000	3	1.07	33.1	62.5	75	0	351

	Rh1000-F0/10	R	250	1440	3000	3	1.01	38.7	62.5	0	0	211
	Rh1000-F50/11	R	250	1440	5900	3	1.01	32.1	62.5	50	0	484
	Rh1000-F75/12	R	250	1440	9000	3	1.01	33.1	62.5	75	0	554
	Rh300-F90/13	R^c	150	228.9	1210	2.2	1	64.9	65	90	0	134
Soltanz adeh et al. (2013)	Rh300-F90-P/14	R	150	228.9	1210	2.2	1	64.9	65	90	0.68	159
	Rh300-F90-P/15	R	150	228.9	1210	2.2	1	64.9	65	90	1.00	169

^{a} T-shape cross section.

^{b} Hooked end steel fiber.

^{c} Rectangular cross section.

^{d} I-shape cross section.

A similar observation was reported by Cuenca and Serna (2013) when estimating the shear resistance of nine beams with T-shape cross section and W_f / W_w of 2.6, 4 and 6 by adopting $k_f = 1$, as well as the calculated k_f factor by Eq. (5.13a) in chapter 5. These researchers have verified that the application of the calculated k_f factor by Eq. (5.13a) for predicting the shear resistance of the beams, with $W_f / W_w \geq 4$, increases the accuracy of the estimations (V_{exp} / V_{anal} has varied from 1.3 to 1.5 in the present research), while adopting $k_f = 1$ resulted in a better estimation of the shear resistance of the beams with $W_f / W_w < 4$. The results presented in Fig. 6.10, as well as those reported by Cuenca and Serna (2013) demonstrate the requirement of modifying the equations (5.13a) and (5.13b) in order to consider the W_f / W_w ratio in calculating the k_f factor. Fig. 6.10 also demonstrates an abrupt increasing of V_{exp} / V_{anal} from beam F1.5-NW-2G12 to beam Th750-F60-P/3. This jump is not only due to the increase of the W_f / W_w ratio, but would be also caused by a combination of the size effect and prestress level.

6.4 CONCLUSIONS

In the present chapter an experimental program composed of 9 I-shape slender HPFRC beams flexurally reinforced with a hybrid system of a steel strand and several GFRP rebars was executed for assessing the possibilities of these new types of materials for the development of an innovative structural system almost immune to corrosion. The beams were fabricated with different dosages of steel fibers and various levels of prestress to assess the effectiveness of the fiber dosage and prestress level on the increase of shear resistance and ductility of these beams. The obtained results have evidenced that using the HPFRC containing 90 Kg/m^3 of steel fibers, and adopting a prestress level of 60% for steel strand and 30% for GFRP bars, a quite high load carrying capacity can be achieved, with a very ductile response, since deflection at failure was about 3 times higher than the deflection at serviceability limit state.

Based on the results obtained in the present study, and considering those derived from the analysis of beams tested by other researchers, collected in a data base, the reliability of existing analytical approaches for estimating the shear resistance of the beams was investigated. A summary of remarks can be drawn as follow:

– By comparing the shear resistance estimated by RILEM TC 162-TDF (2003), MC2010 and Soetens (2015) approaches, it was verified that all the formulations demonstrated acceptable accuracy for design of the beams without prestress. In the case of the prestressed beams, RILEM TC 162-TDF (2003) approach provided more accurate predictions. The shear capacity of the prestressed beams obtained by MC2010 was found quite low compared to that of calculated experimentally, which should be received more attention according to the economical point of view.

– Comparing the estimated shear resistance of the beams fabricated with a same dosage of fibers and equal ratio between shear span and cross section effective depth, a/d, a reduction on the safety margin was obtained with the increase of the depth of the beams ($V_{\exp}/V_{anal}$ has decreased). This demonstrates the requirement for improving the size effect factor "k" in order to assure safer predictions of the shear capacity of deeper beams.

– For the development of a design approach of higher predictive performance than the ones analyzed in the present work, the effects that influence the shear capacity of RC beams should be comprehensibly evaluated, which requires the collection of a

relatively large data base and its analysis with sophisticated algorithms, like data mining, as well as the execution of parametric studies with advanced FEM-based constitutive models capable of simulating the relevant phenomena involved.

EXPLORING THE POTENTIALITIES OF HPFRC AND GFRP REINFORCEMENT SYSTEMS IN INFRASTRUCTURES – A CASE STUDY

7.1 INTRODUCTION

Nowadays, the rise in urbanization and the growth of the traffic density, which is placing greater strain on the road network, emphasizes the importance of long-term service life of infrastructures. The premature failure of conventional steel and iron-based manhole covers and chambers top illustrations, mainly due to corrosion and traffic loads (Fig. 7.1), has been shown to be a major contributory factor to the annual maintenance budget of the roads (HA 104/09, 2009). The present study introduces the corrosion-free prefabricated manhole covers for application in aggressive environments, i.e. wastewater collector system, sewer system, stormwater systems, etc., by extending the concepts of the proposed system for developing precast beams with higher durability introduced in chapter 5 and 6, namely exploring the potentialities of the strength and ductility performance of HPFRC and the tensile capacity and corrosion immunity of GFRP reinforcement systems. The purpose of this study is to evaluate the effectiveness of this strategy in producing the prefabricated infrastructural elements, such as manhole covers,

by means of giving more insight into the influence of steel fibers on shear capacity and ductility of these members.

(a)   (b)   (c)
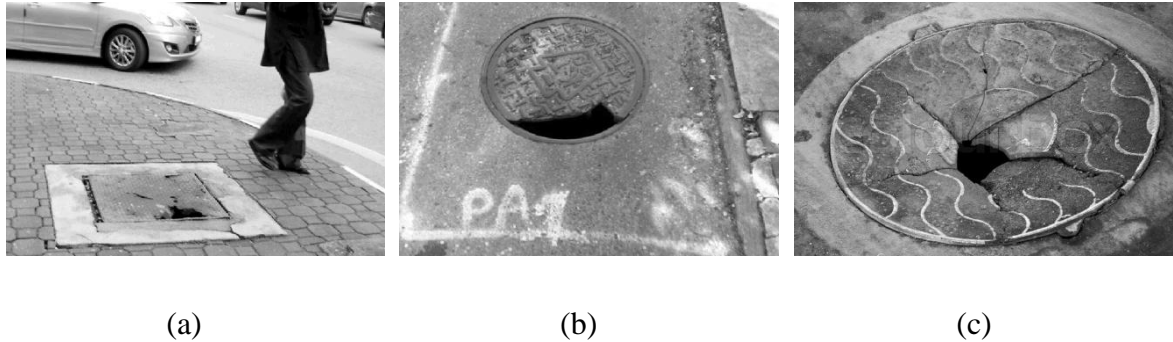
Fig. 7.1- Corroded iron manhole cover installed in footway area, and (b) broken cover in a parking area, and (c) hard shoulder of a road.

In accordance with BS EN 124:1994, the manhole covers are classified in 6 groups according to the load carrying capacity demands required, which is dependent of the place where they will be installed, as indicated in Table 7.1. The first four classes of manhole covers are related to the urban roads and highway, which starts from the 1st class of manhole covers, A15, that are used in areas where only pedestrians have access, though to the 4th class of these elements, D400, which are applicable where the cars and lorries have access. Fig. 7.2 shows the location of these four groups in a highway environment. In the present study the HPFRC was designed to be applicable for producing prefabricated manhole covers of these four classes. The behavior of the HPFRC manhole covers developed according to the strategy introduced earlier, in chapters 5 and 6, is discussed in the following sections.

For developing such elements, the HPFRC were applied to provide a high compressive strength, shear resistance and structural durability for the manhole covers. Application of GFRP reinforcements is adopted as the further enhancements for increasing the load carrying capacity of these elements without concerning about the corrosion. This study also introduces the relevant features of a developed HPFRC manhole cover captured by a FEM-based analysis.

[1] Manhole covers with loading strength > 15 kN (Footways),
[2] Manhole covers with loading strength > 125 kN (Footways, pedestrian areas, parking area),
[3] Manhole covers with loading strength > 250 kN (kerbside channels of roads),
[4] Manhole covers with loading strength > 400 kN (Carriagways, hard shoulders and parking areas).
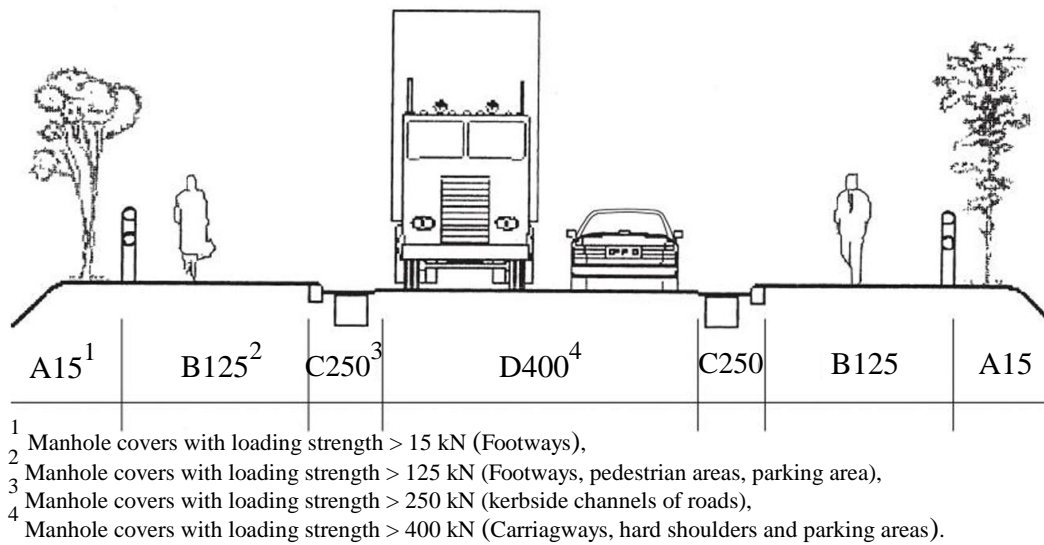
Fig. 7.2- Typical highway cross-section showing the location of the different illustration groups.

Table 7.1- Classification of manhole covers.

Classifications	Test load	Place of application
A15	15	For use in areas where only pedestrians have access.
B125	125	For use in care parks and pedestrian areas where only occasional vehicular access is likely.
C250	250	For use in car parks, forecourts, industrial sites and areas with slow moving traffic, also in highway locations up to 500 mm from the kerb and up to 200 mm into verge, excluding motorways.
D400	400	For use in areas where cars and lorries have access, including carriageways, hard shoulders and pedestrian areas.
E600	600	For use in areas where particularly high wheel load are imposed such as aircraft pavements.
F900	900	For use in are where particularly high wheel loads are imposed such as aircraft pavements.

7.2 EXPERIMENTAL PROGRAM

7.2.1 HPFRC Mix Design and Properties

A HPFRC with strength class of C50 was adopted for producing the manhole covers. Excluding the cement type, which was Portland cement CEM I 42.5R, the rest of HPFRC constituents were the same as those introduced in chapter 3 of the present thesis (Sec. 3.3.2.2). The adopted HPFRC compositions for producing the specimens and the properties of the 28 days age tailored concrete are respectively represented in Table 7.2 and Table 7.3.

Table 7.2- Concrete compositions.

C^a	FA^b	LF^c	W^d	SP^e	FS^f	CS^g	CA^h	SF^i	MF^j
kg/m^3	kg/m^3	kg/m^3	L/m^3	L/m^3	kg/m^3	kg/m^3	kg/m^3	kg/m^3	kg/m^3
462	139	139	197	15.7	126	670	512	90	3

[a] Cement, [b] Fly Ash, [c] Limestone Filler, [d] Mixing Water, [e] Superplasticizer, [f] Fine Sand, [g] Coarse Sand, [h] Coarse Agg., [I] Steel Fibers, [j] Synthetic Macro Fibers..

Table 7.3- HPFRC properties at the age of 28 days.

	E	f_{cm}	f_{R1} MPa	f_{R2} MPa	f_{R3} MPa	f_{R4} MPa	$f_{ct,L}^{f}$
	N/mm^2	MPa	CMOD1= 0.5 mm	CMOD2= 1.5 mm	CMOD3= 2.5 mm	CMOD4= 3.5 mm	MPa
Av.	35583	58.12	13.23	13.09	11.73	10.22	13.63
CoV (%)	2.2	3.5	12.45	10.76	11.06	15.89	23.6

7.2.2   Reinforcement Properties

Two GFRP grids with different dimensions of $615 \times 615 \times 35 \, \text{mm}^2$ (having the element cross section of $7 \times 35 \, \text{mm}^2$) and $565 \times 565 \times 50 \, \text{mm}^2$ (with the element cross section of $6.3 \times 50 \, \text{mm}^2$) were applied for reinforcing the manhole covers, in order to investigate the influence of size of the reinforcing mesh on the behavior of these elements. The Young's modules of these elements are reported as 14 GPa by the manufacturing company. Fig. 7.3 represents schematically the two types of 3D GFRP grids adopted for producing the manhole covers.

Prior to testing the manhole covers reinforced with the introduced GFRP grids, the Young's modulus and flexural strength of the reinforcements were assessed using a similar test setup and loading rate applied for testing the covers, which meets the specification defined by BS EN 124:1994. From each type of GFRP grid, 2 samples were tested using the test setup depicted in Fig. 7.4(a). A HPFRC frame with clear opening (CO) of 600 mm was produced and used for supporting both the GFRP grids and the concrete specimens during the test. This support consists of four additional openings near to its base for providing access to the interior of the support in order to be possible the installation of LVDTs for measuring the deflection of the specimens. A steel layer of 5 mm thickness was applied to cover the top surface of the support, as shown in Fig. 7.4(b). This steel layer avoid the direct contact of the specimens and the supporting concrete block and prevents any possible deterioration in the referred surface due to abrasion/friction effect in the test.

Each test was carried out using a servocontrolled testing machine, with a load carrying capacity of 500 kN. An internal LVDT, installed inside the loading equipment, was used to control the axial displacements during the test. The test procedure consisted of applying a constant displacement rate of 0.02 mm/s at the center of the GFRP grid by means of loading a circular steel plate of 250 mm diameter and 100 mm thickness. A LVDT was used to measure the vertical deflection beneath the loading point, at the center of the GFRP, and another one was placed within 170 mm distance from the center point of the mesh. The obtained load-deflection relationship for each sample is depicted in Fig. 7.5. In this figure each sample is identified with a label of "HiGFRPj", where "i"

represents the height of the GFRP mesh and "*j*" is the number of the tested samples. The results evidence that the GFRP grid with 50 mm height developed a higher flexural load carrying capacity compared to the other GFRP grid with 35 mm height. According to the obtained results, H35GFRP*j* and H50GFRP*j* (j=1 and 2) samples supported an average maximum load of 79 kN and 99 kN, respectively.
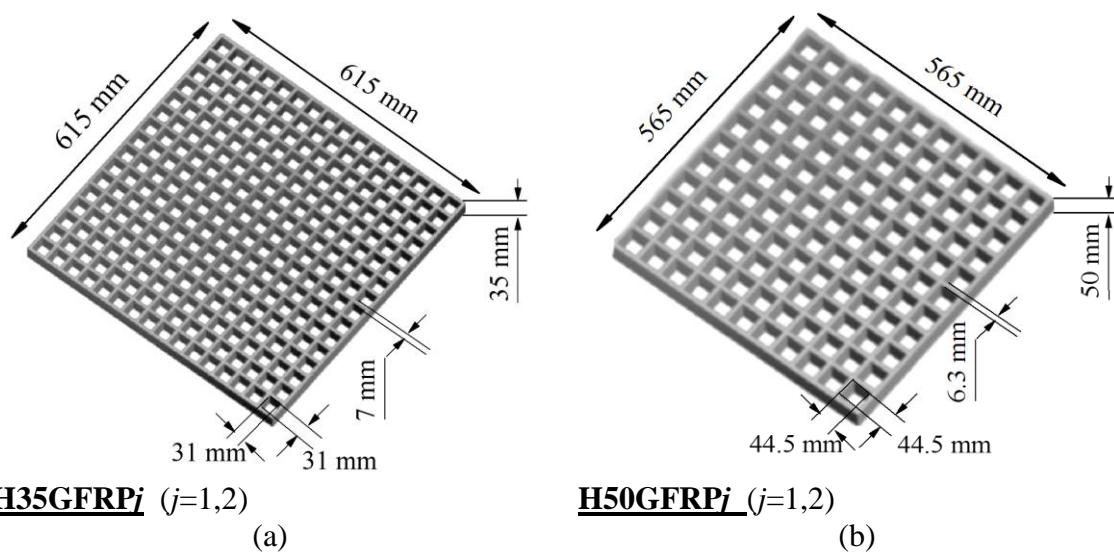
Fig. 7.3- GFRP reinforcement with (a) smaller and (b) larger size 3D GFRP grids.
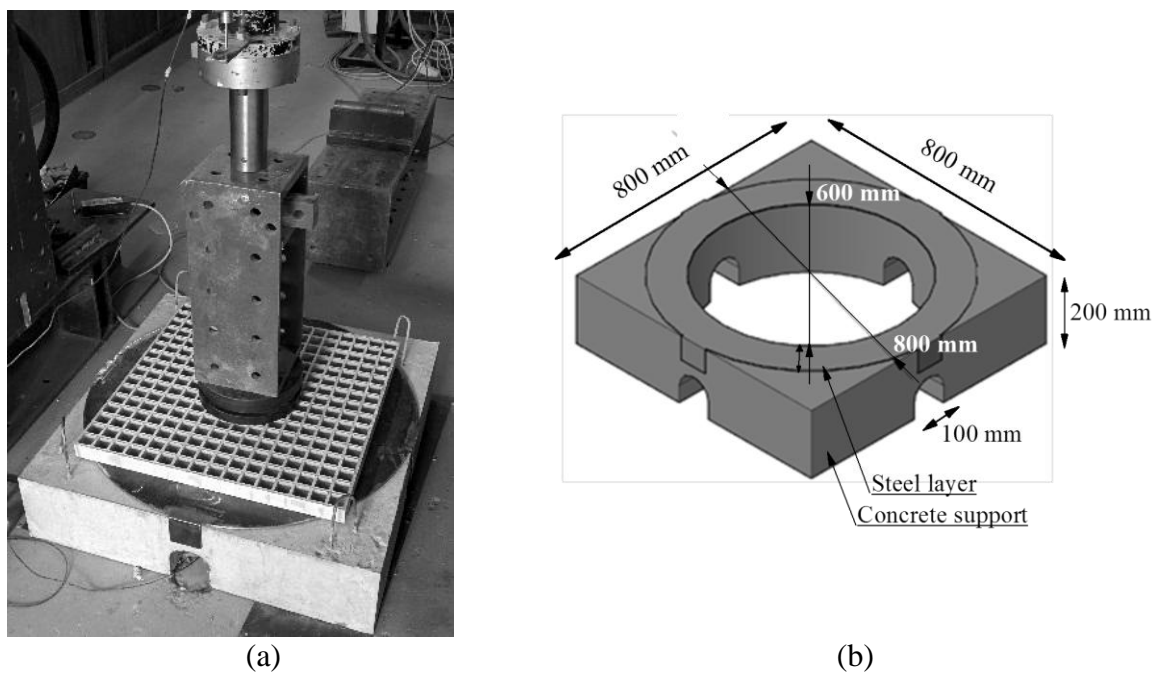
Fig. 7.4- (a) Test setup adopted for testing the tensile strength of the GFRP mesh and (b) HPFRC support.
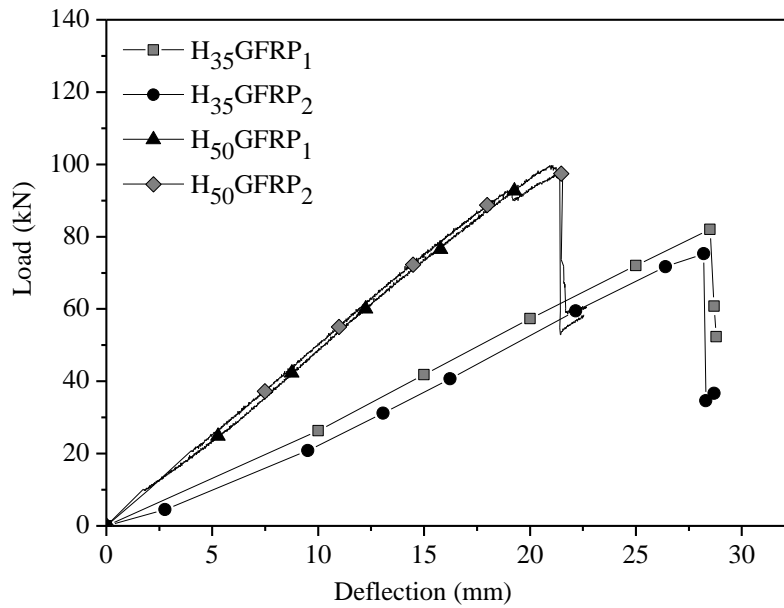
Fig. 7.5- Load-deflection relationship obtained by testing two GFRP reinforcements with different height of 35 mm and 50 mm.

7.2.3 Fabrication of Test Specimens

A total number of 6 square manhole covers with two different dimensions, $645 \times 645 \, \text{mm}^2$ and $600 \times 600 \, \text{mm}^2$, were developed using HPFRC and the two types of GFRP grids. The specimens were produced with various HPFRC cover thickness in order to define the most appropriate configuration capable of resisting the traffic demands for class D400 of manhole covers. Fig. 7.6 represents the adopted specimen configurations, labeled as "H*x*C*i*GFRP*j*", where "*x*" is replaced by the total height of the manhole cover in mm and "*i*" represents the top HPFRC cover of the specimens in mm. The letter "*j*", which is the grid height in this designation, identifiers whether the GFRP grid of 35 mm height is used for producing the elements or the other one with 50 mm height is applied. For instance, the HPFRC manhole cover of 100 mm total height and 35 mm top HPFRC cover reinforced by a GFRP grid of 35 mm height, is identified as "H100C35GFRP35" in Fig. 7.6.
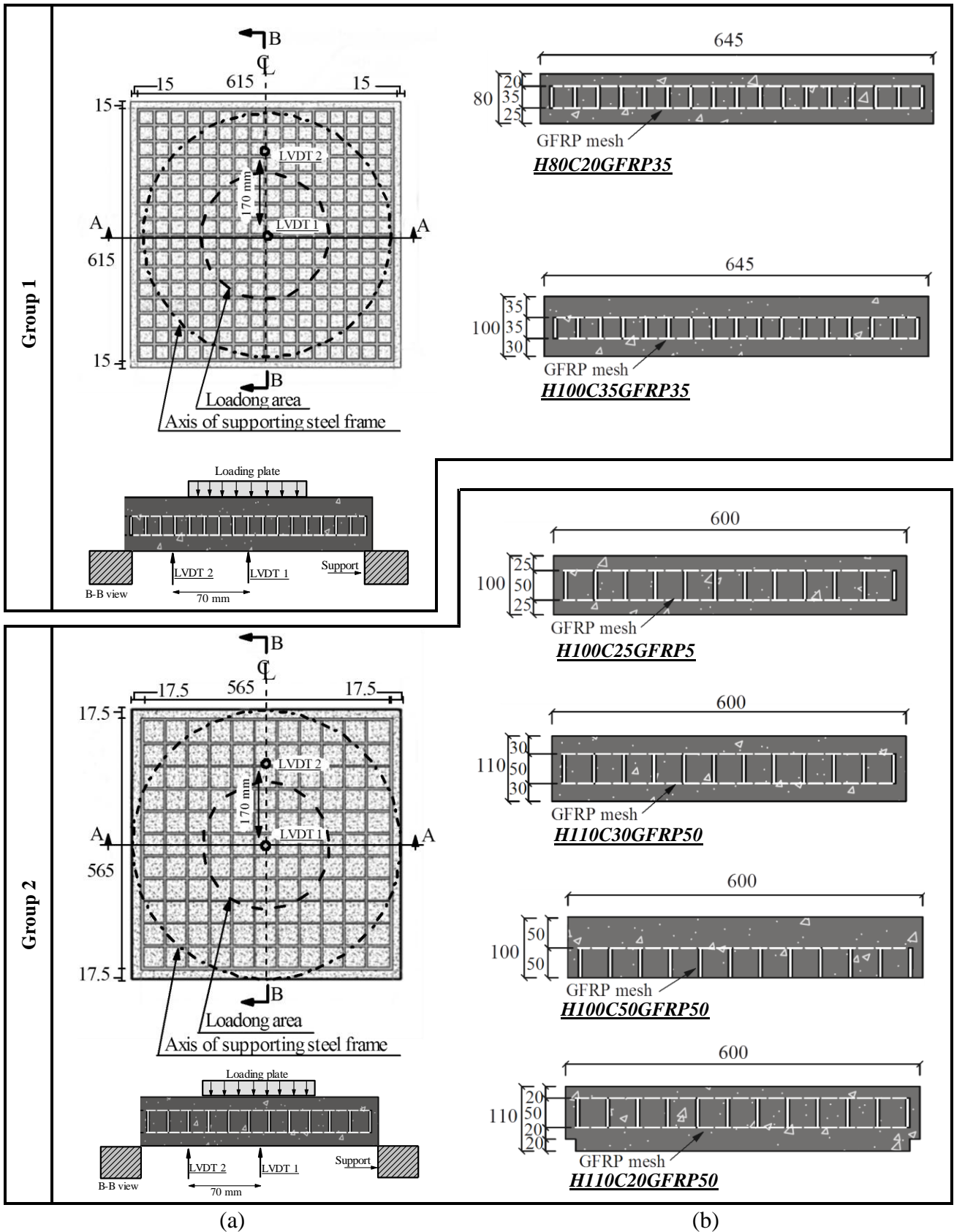
Fig. 7.6- (a) HPFRC manhole covers configuration and test arrangements; and (b) specimens layout and reinforcement arrangement (A-A view).

As it is presented in Fig. 7.6, two manhole covers were produced using the GFRP grid of 35 mm height and the rest of specimens were developed by the GFRP grid of 50 mm height. In the first group of the specimens with 35 mm high GFRP grids, the effect of cover thickness at compressive zone (top part of the members) and tensile zone, as well as the effect of reinforcements, in increasing the load carrying capacity, are evaluated. A similar investigation was carried out in the case of the two specimens "H100C25GFRP50" and "H110C30GFRP50" in the second group, with 50 mm high GFRP grid. By considering the obtained results of testing these 4 specimens, the last two HPFRC members, H100C50GFRP50 and H110C20GFRP50, were designed in order to reach the target load carrying capacity of D400 class manhole covers. In producing the H100C50GFRP50 specimen, no HPFRC cover was considered at tensile zone, and the element was designed to have a HPFRC cover of 50 mm only at compressive zone. The tensile strength of this member was mainly provided using a GFRP grid of 50 mm height placed at the bottom of the specimen. The H110C20GFRP50 specimen was designed with circular concrete layer of 200 mm thick and 600 mm diameter at the bottom side, which were placed inside the support during testing the specimen (see Fig. 7.7(b)). Hence, the support provides some confinement for the bottom layer of H110C20GFRP50 manhole cover. The loading area, location of the illustrated LVDTs and the supporting condition during testing the specimens is shown in Fig. 7.6.

7.2.4 Test Setup and Procedure

Fig 7.7 represents the test setup applied for testing all the manhole covers. The specimens were tested using a similar test setup and supporting condition introduced for testing the GFRP grids. The deflection of the members was measured using 2 LVDTs. One was placed beneath the center point of each manhole cover, aligned with its geometric center, and the other LVDT was installed at 170 mm from the center of the elements (see Fig. 7.6(a)). All the specimens were tested by the same loading rate and loading conditions applied for testing the GFRP grids, with exception of the manhole cover H110C30GFRP50. By obtaining this information, the type of each designed manhole cover was verified regarding to the classification suggested by BS EN 124:1994 (see Fig

7.2) in order to define the beast strategy for developing the manhole covers of class D400 to be installed in areas subjected to high vehicular traffic.
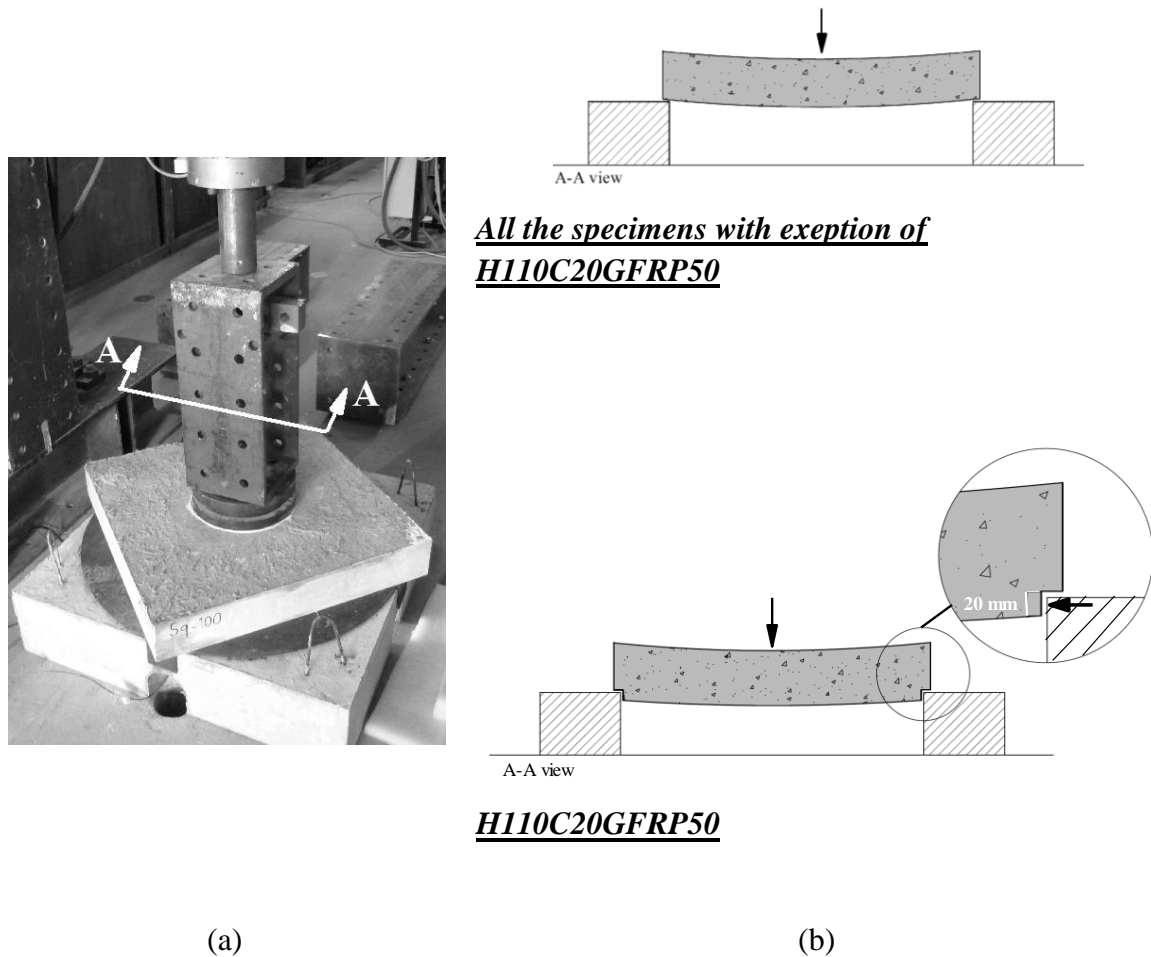
Fig. 7.7- (a) Test setup and (b) position of manhole covers on the supporting frame (A-A view).

The H110C30GFRP50 specimen was selected for being submitted to a set of loading/unloading cycles in order to assess the behavior of this material/structural system when submitted to loading conditions representative of real traffic. Since this element was reinforced by a GFRP grid similar to that of used for fabrication of the H100C25GFRP50 manhole cover and were produced by the same configuration and almost similar concrete cover thickness it was assumed that the load carrying capacity will be obtained by testing H110C30GFRP50 manhole cover is close to that of H100C25GFRP50 specimen. In

accordance with BS EN 124:1994 guideline, H110C30GFRP50 specimen was loaded up to 2/3 of the test load. The specimen was then unloaded after reaching the target level of load (2/3 of the test load). After application of 5 cycles of loading and unloading, the target load was maintained constant for 30 Sec. In accordance with BS EN 124:1994 the specimen should pass this step without any loss of bond performance between the concrete and reinforcement. Loading of the specimen was then continued up to failure of the specimen.

7.2.5 Experimental Results
7.2.5.1 Load-deflection relationship

All the tested specimens were failed in punching shear as shown in Fig. 7.8. The main cracks always started developing from the top surface of the elements and gradually propagated trough the inferior layers. The results obtained in terms of load-deflection curve are represented in Fig. 7.9. Comparing these results, it is verified that increasing the thickness of concrete layer placed above the GFRP grid increases both the load carrying capacity and the stiffness of the initial elastic part of the force-deflection response of the specimens. Hence, the specimen H100C35GFRP35 with 35 mm cover thickness at its upper layer has reached to a maximum load of 349.3 kN at a deflection of almost 10 mm, while the specimen H80C20GFRP35, with less cover thickness, has reached a maximum load of 208.2 kN at 33 mm deflection. A similar behavior can be found by comparing the load-deflection relationship obtained for the two manhole covers H100C50GFRP50 and H110C20GFRP50. Although the specimen H110C20GFRP50 was developed by a higher total thickness and a relatively thick HPFRC cover at the tensile zone of the specimen, compared to H100C50GFRP50, but H100C50GFRP50 manhole cover represents 11.33% higher peak load.

The contribution of concrete layers in flexural behavior of the elements is more pronounceable after reaching the peak load. The steel fibers in this layer contribute significantly to prevent the abrupt decay of the peak load by resisting to the propagation and opening of the tensile and shear cracks at the lower layer of the manhole covers. The effective collaboration of the fibers with the GFRP reinforcement caused a ductile

behavior in all the developed elements after the peak load. It is observed that the load carrying capacity has decreased smoothly after the peak load in the case of the specimens with thicker concrete layer at the bottom surface compared to thickness of their concrete layer above the GFRP grid, likewise the case of manhole covers H80C20GFRP35, H100C25GFRP50 and H110C20GFRP50. The post peak phase of H100C35GFRP35 and H100C50GFRP50 manhole covers, on the other hand, has started with an initial abrupt decay of the maximum load, respectively equal to 38% and 48% of the maximum load, which later became stabilized and maintained constant up to the end of the test.
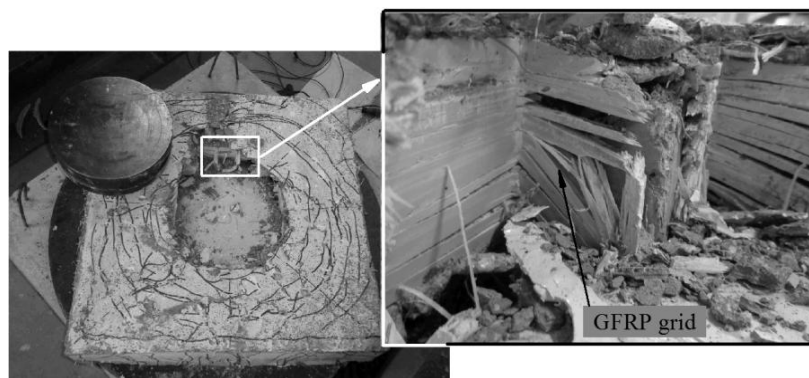
Fig. 7.8- Typical crack propagation at the upper surface of the manhole covers.

Comparison of the flexural behavior of H100C50GFRP50 manhole cover with H110C20GFRP50 one shows that, as much as the GFRP grid can be placed lower in developing the manhole covers, the more protected for the punching failure and, consequently, the load capacity of the members is increased. This concrete cover can also contribute to increase the durability of the manhole covers by protecting the GFRP grid in chemical and high temperature environments.

The response of H110C30GFRP50 element, which was tested according to BS EN 124:1994 guideline, with that of H100C25GFRP50 manhole cover is compared in Fig. 7.9. This comparison demonstrates the high potentiality of the applied strategy for developing the manhole covers, since after application of several cycles of loading and unloading to H110C30GFRP50 specimen, it was still capable of representing the similar

load carrying capacity and post peak behavior to that of obtained by testing H100C25GFRP50 specimen.

Table 7.4- Summary of the test results and the corresponding class of utilization.

Specimen ID	Maximum load	Deflection	Classification
H80C20GFRP35	208.2	33.05	B125
H100C35GFRP35	349.3	9.82	C250
H100C25GFRP50	311.7	18.21	C250
H110C30GFRP50	290.1	22.19	C250
H100C50GFRP50	478.08	9.84	D400
H110C20GFRP50	423.87	16.07	D400
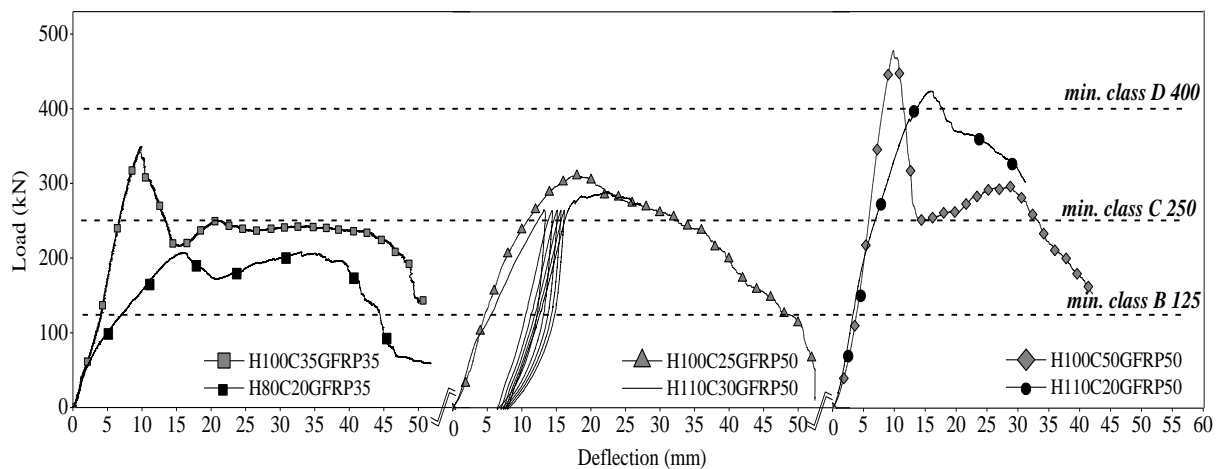
Fig. 7.9- Load-deflection response of the HPFRC manhole covers.

The maximum load carrying capacity and the corresponding deflection for each manhole cover are presented in Table 7.4. According to the obtained results, the H80GRFP35 manhole cover can be placed in B125 classification, introduced by BS EN 124:1994, and can be installed in the footways, as well as in pedestrian and parking areas. The manhole covers H100C35GFRP35, H100C25GFRP50 and H110C30GFRP50 are categorized as class C250, which are applicable in the kerbside channels of roads. The two last manhole covers, H100C50GFRP50 and H110C20GFRP50, are classified as D400, and accordingly are applicable in carriageway roads, hard shoulders and parking areas for all types of road vehicles.

7.2.5.2 Crack pattern

The punching-shear crack patterns obtained typically for all the tested manhole covers are illustrated in Fig. 7.10. Since the specimens were developed using a relatively high dosage of steel and macro synthetic fibres, the multiple cracks of small widths were distributed uniformly all over the bottom surface of the specimens, with exception of H100C50GFRP50 manhole cover with GFPR grid at the bottom layer. This demonstrates the ductile behaviour of the tested elements. The filling ability of the developed HPFRC for producing the precast manhole covers was also verified by removing the bottom concrete cover of H100C35GFRP35 specimen reinforced with the smaller GFRP grids of 35 mm height. As it is shown in Fig. 7.11 the HPFRC has properly filled up all the GFRP grid spaces, representing the proper flowability of the developed concrete.

In the next section of the present chapter the behaviour of H100C35GFRP35 manhole cover is also studied numerically in order to explore the possibilities of a smeared crack model for capturing the relevant features of the tested HPFRC manhole cover.
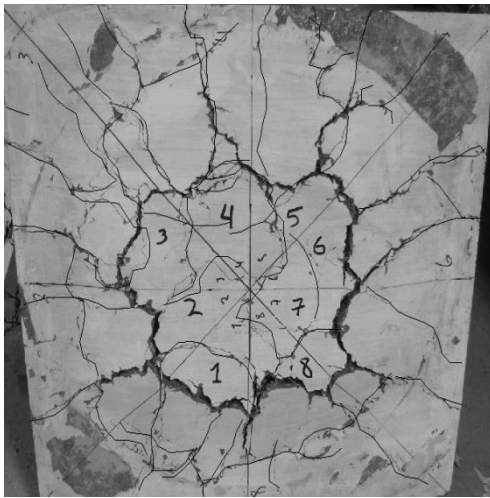
H80C20GFRP35
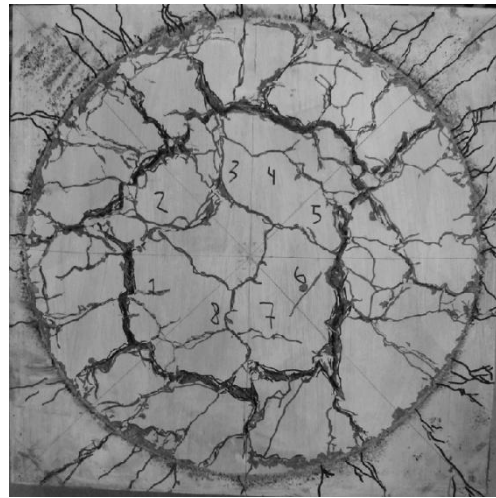
H100C35GFRP35
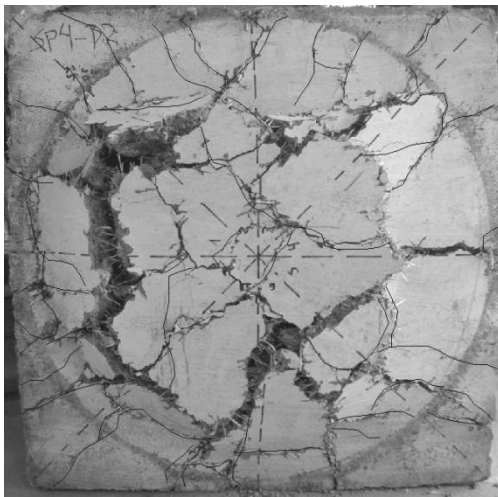
H100C25GFRP50
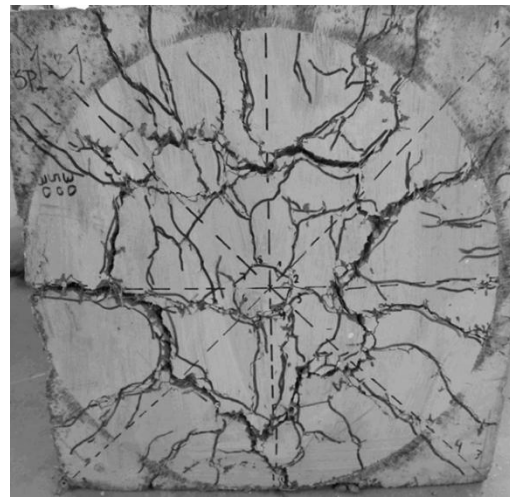
H110C30GFRP50
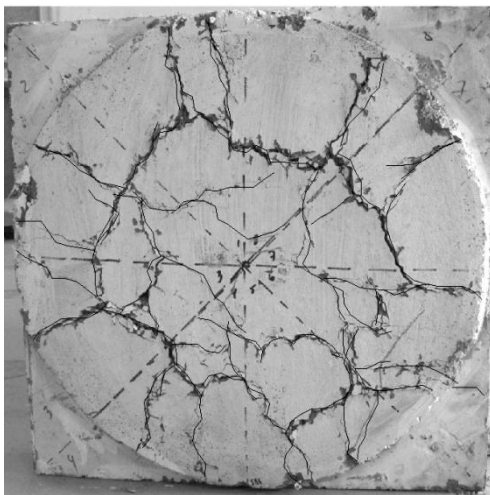
H110C20GFRP50
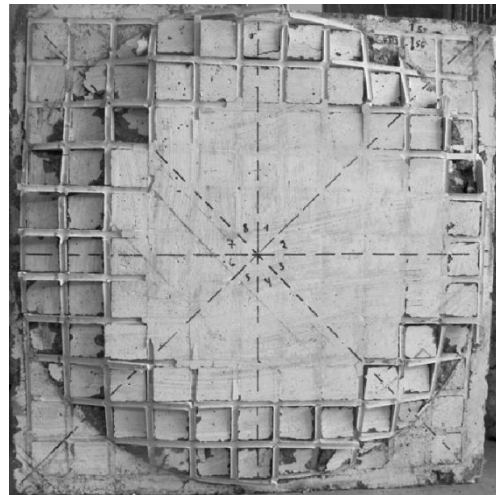
H100C50GFRP50

Fig. 7.10- Crack pattern of tested manhole covers (bottom view).
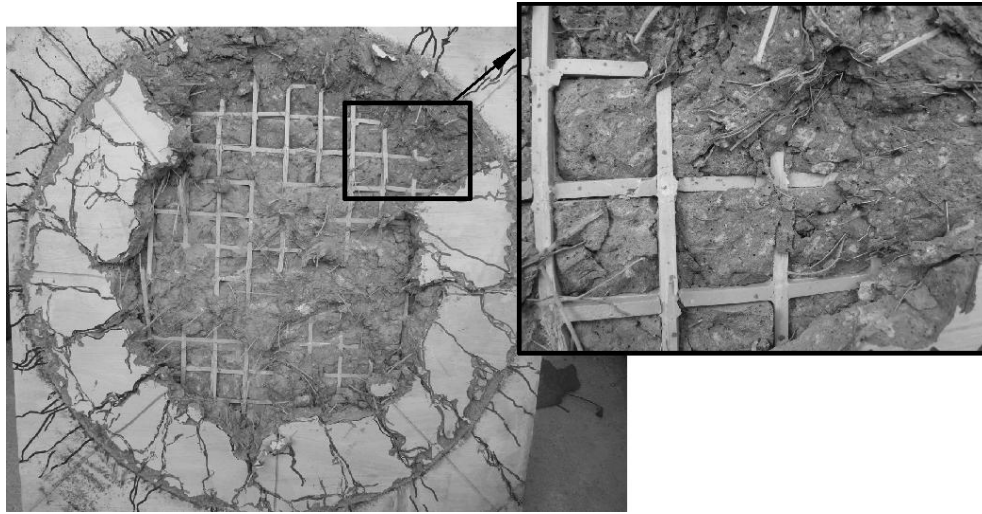
Fig. 7.11- Evaluation of filling ability of the HPFRC by removing the bottom cover of H100C35GFRP35 specimen.

7.3 FEM BASED SIMULATIONS

7.3.1   Numerical Model

A multi-fixed smeared three-dimensional, 3D, crack model is applied to simulate the behavior of the developed HPFRC manhole covers failing in shear-punching. Since fiber reinforcement can assure the formation of diffuse crack patterns, a smeared crack model (Sena-Cruz 2004) is conceptually more appropriate, and more effective from the computational point-of-view, for the simulation of the behavior of fiber reinforced concrete structures. Hence, the fracture mode I is simulated using a tri-linear softening diagram introduced in the 4th chapter of the present study (see Fig. 4-10(a)) (Ventura-Gouveia 2011). For simulating the structural softening with high accuracy a softening shear stress-strain diagram is adopted, which is also introduced in chapter 4 (see Fig. 4-10(b)). Since the applied multi-fixed smeared 3D crack model for simulating the behaviour of H100C35GFRP35 manhole cover is the generalized of the multi-fixed smeared 2D crack model, previously introduced in the 4th chapter of the preset thesis the formulation of the model is not represented in this chapter. The detailed description of the model formulation is addressed in Ventura-Gouveia (2011).

7.3.2 Numerical Simulation

A 3D numerical simulation was carried out using the introduced numerical model for capturing the relevant features of the specimen H100C35GFRP35, which corresponds to manhole covers of class C250according to the BS EN 124:1994. The numerical model where the specimen, the loading, and the support conditions were simulated in agreement with the experimental test setup is shown Fig. 7.12. Due to symmetry around the center of the specimen, only a quarter of the specimen was considered. The domain is discretized with 8-noded hexahedral finite elements with an integration scheme of $2\times2\times2$ points. The displacement of the nodes along the side boundaries parallel to X_1-coordinate and X_2-coordinate are respectively fixed in the u_2 and u_1-direction, while the displacement of those nodes along the bottom boundary is fixed in the u_3-direction.

(a)   (b)
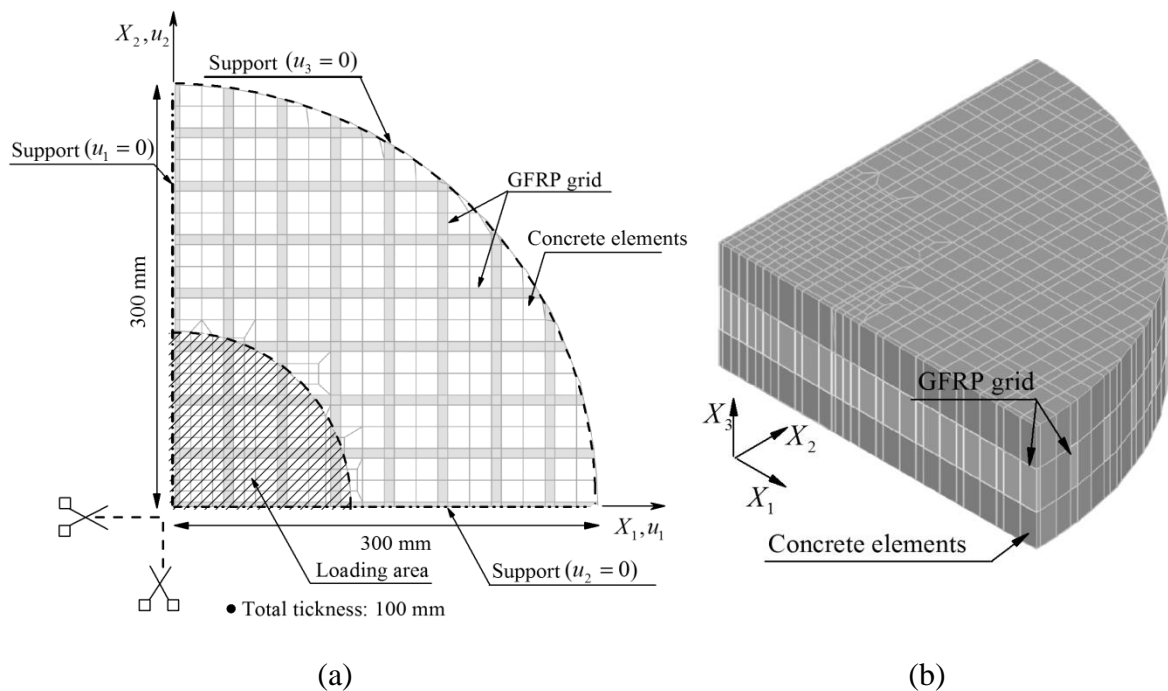
Fig.7.12- (a) Geometry, load and support conditions (top view), and (b) three-dimensional finite element mesh used for simulating the behaviour of the manhole cover H100C35GFRP35.

The values of the parameters of the constitutive model for HPFRC are summarized in Table 7-5. Since the small size of the edge of the GFRP grid caused to place less steel fibers in these locations, the elements modelling these zones were considered constituted by the plain concrete element. The values of the parameters for the constitutive model for this plain concrete are indicated in Table 7.5.

(a)   (b)
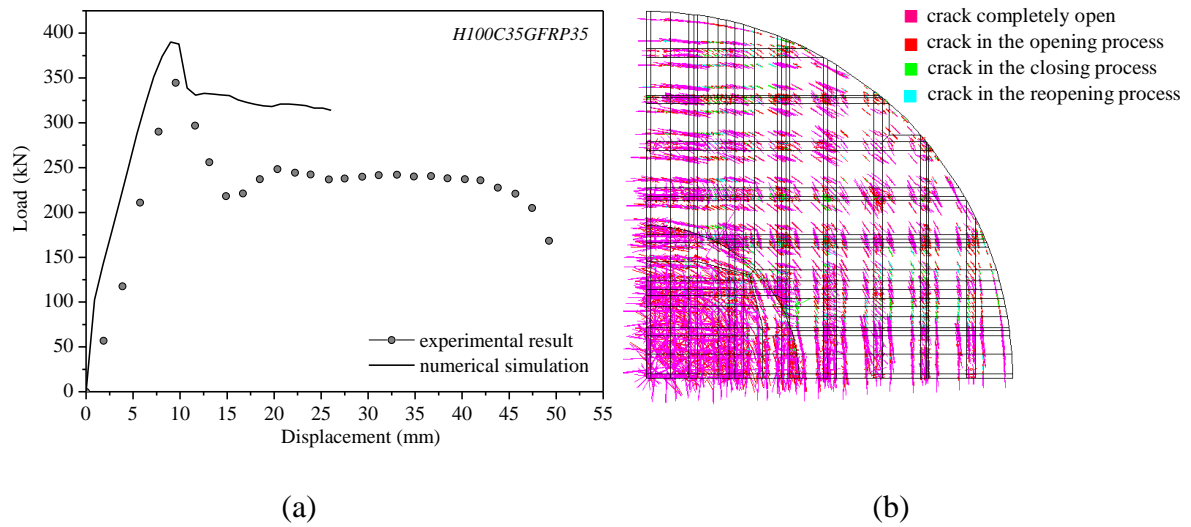
Fig. 7.13- (a) Load-deflection, experimental and numerical results and (b) upper face crack pattern predicted by the numerical model

Table 7.5- Values of the parameters of concrete constitutive model for manhole cover test

Property	HPFRC	Plain Concrete
Poisson's ratio (ν)	0.2	0.15
Young's modulus (E)	32000 N/mm^2	27000 N/mm^2
Compressive strength (f_c)	60.0 N/mm^2	60 N/mm^2
Trilinear tension-softening diagram	$f_{ct} = 2.8\,N/mm^2$ $G_f^I = 3\,N/mm$ $\xi_1 = 0.005; \alpha_1 = 0.78$ $\xi_2 = 0.058; \alpha_2 = 0.89$ $\xi_3 = 0.36; \alpha_3 = 0.57$	$f_{ct} = 1.7\,N/mm^2$ $G_f^I = 0.07\,N/mm$ $\xi_1 = 0.005; \alpha_1 = 0.3$ $\xi_2 = 0.3; \alpha_2 = 0.2$
Crack shear stress-crack shear strain softening diagram	$\tau_{t,p}^{cr} = 1.5\,N/mm^2; \beta = 0.2$ $G_{f,s} = 1\,N/mm;$	-
Threshold angle	30°	30°
Maximum number of cracks per integration point	2	2

Table 7-6- Values of the parameters of GFRP constitutive model for manhole cover test

Property	Value
Poisson's ratio (ν)	0.15
Young's modulus (E)	$14000 \, N/mm^2$
Compressive strength (f_c)	$30 \, N/mm^2$
Trilinear tension-softening diagram	$f_{ct} = 170 \, N/mm^2$
	$G_f^1 = 1000 \, N/mm$
	$\xi_1 = 0.005; \alpha_1 = 0.3$
	$\xi_2 = 0.3; \alpha_2 = 0.2$
Type of shear retention factor law	$P_1 = 2$
Threshold angle	30°
Maximum number of cracks per integration point	2

The GFRP mesh was modeled using hexahedral finite elements and 2×2×2 integration points. These elements were assumed to have a perfect bond with concrete elements. The experimental observation demonstrated that the GFRP material exhibits an almost linear behavior up to its tensile strength, followed by an abrupt rupture. So, to capture this sudden drop, a multi-directional fixed smeared crack model was assigned to these elements (the parameters of the constitutive model were defined to capture this sudden drop as much as possible). The parameters of the constitutive model for GFRP material are presented in Table 7.6. Fig. 7.13(a) compares the load-deflection relationship obtained from the numerical simulations with the experimental results. It demonstrates that this modelling strategy was capable to capture with reasonable accuracy the flexural response of this type of specimens. However there is a tendency for predicting a higher stiffness, peak load and post-peak load carrying capacity, which indicates that assuming some debonding between GFRP grid and surrounding HPFRC seems relevant for assuring higher accuracy on the modelling performance. The final crack pattern estimated by the numerical model at the bottom face of the manhole cover is represented in Fig. 7.13(b). Comparing this pattern with the one obtained by testing the manhole cover

H100C35GFRP35 represented in Fig. 7.10, an overall good agreement can be observed between the model behaviour and the experimental results. The major flexural cracks are predicted by the model and the accuracy reached by the model is acceptable.

7.4 CONCLUSION

In this chapter the proposed strategy for developing the HPFRC beams of high durability was extended and applied for developing the durable prefabricated infrastructures. A HPFRC were evaluated along with a GFRP grid reinforcement system in order to constitute an alternative solution for manhole covers currently made of steel or steel reinforced concrete. In this program, six specimens with different configurations and reinforcing arrangements were designed and submitted to a compressive point load in order to assess their load carrying capacity. The obtained results were compared with the values defined by the BS EN 124:1994, in order to establish an appropriate class of utilization for the production of precast manhole covers, and most importantly introducing the best prototype for developing a durable D400 class of manhole cover applicable for the carriageways.

A high increase in the load carrying capacity has been observed in the case of the specimens with higher thickness in the upper concrete layer (above the GFRP reinforcement). The specimens produced with a higher concrete cover thickness at their bottom layer compared to the thickness of their top concrete cover, have shown a better elastic and post peak ductile behavior.

The appropriate interaction between the concrete–GFRP reinforcement has been observed in the HPFRC specimens, along with a perfect filling of the concrete mix in the spaces between the GFRP grids. This suggested that the developed HPFRC is applicable to ease the manufacturing process for the massive production of precast elements, such as manhole covers in the industry.

Numerical simulation of H100C35GFRP35 specimen with C250 classification has been carried on. The model was capable to capture with relative accuracy the flexural response of this specimen. The minor deviation of results suggests that debonding between concrete and the FRP system should be considered.

CHAPTER 8

CONCLUSIONS AND FUTURE PERSPECTIVES

8.1 CONCLUSIONS

The present work aimed to develop a high performance fiber reinforced concrete (HPFRC) of properties capable of eliminating the use of steel stirrups (the most susceptible to corrosion) for the shear reinforcement in a new type of pre-fabricated beams flexurally reinforced with a hybrid system formed by steel and glass fiber reinforced polymer (GFRP) bars applied with a certain prestress level, in order to constitute a new generation of structural elements of enhanced durability. To attain this objective, the first research activity dealt with the development of a method for preparing high strength concrete reinforced with relatively high dosage of steel fibers and presenting self-compacting requisites (SCC). Although there exist several available methods for developing steel fiber reinforced concrete (SFRC), tailoring a SCC with a relatively high dosage of steel fibers, and assuring appropriate fiber orientation and dispersion was an objective that was successfully attained. Application of relatively high dosages of steel fibers, in general, causes a significant decrease of concrete flowability due to the fiber perturbation effect. Hence, in the present study a new methodology to formulate a HPFRC with suitable rheological and mechanical properties for production of precast prestressed FRC elements were developed. The mechanical properties of several different mixes tailored with 0, 90 and 120 kg/m^3 of steel fibers, together with 3 kg/m^3 of macro synthetic polymer fibers, were assessed at fresh stage, as well as different ages in hardened stage. The shear behavior of the developed HPFRC at meso level was evaluated by means of double shear specimens, DSS, designed in this study. Results obtained by testing the HPFRC DSS demonstrated the high effectiveness of the developed concrete in terms

of shear capacity and stiffness. The image analyzing performed on the shear plane of the tested HPFRC shear specimens showed the appropriate fiber distribution and orientation. This analysis demonstrated the capability of the developed method of tailoring HPFRC for providing a good balance in terms of flowability and viscosity of the mix.

The shear behavior of the tailored HPFRC was then investigated at structural level by developing short-span and slender beams without stirrups. A hybrid flexural reinforcement system was used for all these beams, composed of GFRP rebars placed near to the outer surface of the tensile zone, and steel reinforcements positioned with higher concrete cover to be protected against the corrosion, which is considered another strategy for enhancing the durability and fire protection in terms of safety at ultimate limit states. Using these specimens, the effect of several aspects such as fiber dosage, as well as level of prestress of GFRP and steel longitudinal reinforcements for enhancing the shear behavior of the elements were investigated.

Through the study of short span beams, it was observed that by 30% (of GFRP nominal ultimate strength) prestressing of the GFRP bar, ultimate flexural capacity (M_u) of the beam was increased significantly (as 16% of that of control beams without prestress). Thus, the mode of failure was changed from a flexural/shear failure mode (yield initiation followed by the formation of a critical diagonal crack) in the control beams (without prestress) to the flexural failure mode in the case of beams with 30% prestress.

By using HPFRC containing 90 Kg/m^3 of steel fibers, and adopting a prestress level of 56% (of steel nominal yield strength) for steel strand and 30% (of GFRP nominal ultimate tensile strength) for GFRP bars in the developed slender beams, a quite high load carrying capacity was achieved (more than 24% compared to the concrete beam with conventional stirrups) at serviceability limit state, with a very ductile response, since deflection at failure was about 3 times higher than the deflection at serviceability limit state.

Based on the experimental results obtained in the present study, and considering those derived from the analysis of beams tested by other researchers, collected in a database, the reliability of existing analytical approaches namely: RILEM TC 162-TDF (2003), MC2010 and Soetens (2015), for estimating the shear resistance of RC beams was investigated. By comparing the shear resistance estimated by these three approaches with the experimental results, it was verified that all the formulations demonstrated acceptable accuracy for designing the beams without prestress. In the case of the prestressed beams, RILEM TC 162-TDF (2003) approach provided more accurate predictions. The shear capacity of the prestressed beams according to the MC2010 approach was found quite low when compared to that registered experimentally, which indicate

the necessity of further research for improving the predictive performance of this formulation regarding economic considerations for the designed solutions.

Comparing the estimated shear resistance of the beams fabricated with a same dosage of fibers and equal ratio between shear span and cross section effective depth, a/d, a reduction on the safety margin was obtained with the increase of the depth of the beams ($V_{\exp}/V_{anal}$ has decreased with the increase of a/d). This demonstrates the requirement for improving the size effect factor "k" in order to assure safer predictions of the shear capacity of deeper beams.

After a comprehensive investigation on the shear behavior of the developed HPFRC at both meso (using double shear specimens) and structural levels (using short-span and slender beams), application of the proposed strategy to enhance the durability of structures (i.e. replacement of stirrups by means of a tailor made HPFRC together with application of none corrodible tensile reinforcements) were further extended for designing prefabricated infrastructures to be applied in aggressive environments. For this purpose several manhole cover specimens having different geometries and reinforcement arrangements were developed and tested according to the provisions of BS EN 124:1994 design code. The results demonstrate the applicability of the proposed method for developing innovative manhole covers for all types of urban roads and highways (corresponding to class A15, B125, C250 and D400).

8.2 RECOMMENDATIONS FOR FUTURE WORK

In the present thesis a methodology for developing HPFRC elements without conventional shear reinforcement (stirrups) was proposed to overcome the durability problems that come with application of conventional RC members. This study provided a comprehensive understanding about the behaviour of such elements under monotonic load. However, to apply the proposed methodology as a standard solution for civil engineering practice, it is necessary further explore the behaviour of this type of elements under fatigue, dynamic, creep, fire, and blast loading conditions, as well.

The present thesis proposed a new solution for enhancing the durability of the structures by replacing the stirrups using a tailor made HPFRC, as well as the application of hybrid GFRP-steel system of flexural reinforcements for developing high performance structural elements. Hence, a comprehensive life-cycle analysis integrating the direct and indirect costs related to the durability should be executed in the future to assess the competitiveness of the developed solutions for fabricating reinforced concrete elements.

Regarding to the analytical studies carried out in the present thesis it should be pointed out that for the development of a design approach of higher predictive performance than the ones analyzed in the present work, the effects that influence the shear capacity of RC beams should be comprehensibly evaluated, which requires the collection of a relatively large database and its analysis with sophisticated algorithms, like data-mining, as well as the execution of parametric studies with advanced FEM-based constitutive models capable of simulating the relevant phenomena involved.

The proposed method of developing HPFRC mix is flexible to adopt any type of discrete fibers, likewise those with the low heat conductivity, such as polypropylene fibers. However, in order to use the HPFRC with polypropylene fibers for fabrication of constructions which are under thermal degradation, it seems very interesting to study the behavior of this concrete at temperature range between 25°C to 800°C.

REFERENCES

Abrishambaf A, Barros JAO, Cunha VMCF. Relation between fibre distribution and post-cracking behaviour in steel fibre reinforced self-compacting concrete panels. Cem Conc Res 2013; 51:57-66

Abrishambaf A. Creep behaviour of cracked steel fibre reinforced self-compacting concrete laminar structures [Doctoral thesis]. Portugal: University of Minho; 2015.

Achilides Z, Pilakoutas K. Bond behavior of fiber reinforced polymer bars under direct pullout condition. J Compos Constr 2004; 8(2):173-181.

ACI440.IR-06. Guide for the design and construction of structural concrete reinforced with FRP Bars. ACI committee report, 2006. p. 44.

ACI Committee 318-11. Building code requirements for structural concrete and commentary. Farmington Hills (MI): American Concrete Institute, 2006. 44 pp.

ACI Committee 544.1R-96. State-of-the-Art Report on Fiber Reinforced Concrete. ACI committee report, 1996. p. 66.

Ahn N. An experimental study on the guidelines for using higher contents of aggregate micro fines in Portland cement concrete [Doctoral thesis]. Austin, USA: University of Texas;. 2000.

Aiello MA, and Ombres L. Structural performance of concrete beams with hybrid (fiber-reinforced polymer-steel) reinforcements. J Compos Constr 2002; 6(2):133-140.

Al-Mahmoud F, Castel A, Francois R, Tourneur C. Effect of surface pre-conditioning on bond of carbon fiber reinforced polymer rods to concrete. Cem Concr Compos J 2007; 29 (9):677-689.

Almassri B, Krit A, Al-Mahmoud F, Francois R. Behavior of corroded shear-critical reinforced concrete beams repaired with NSM CFRP rods. J Compos Struct 2015; 123:204-215.

Arrea M, Ingraffea AR. Mixed in mode crack propagation mortar and concrete, Technical report, Ithaka: Cornell University, 81-13; 1982.

Ashour SA. Effect of compressive strength and tensile reinforcement ratio on flexural behavior of high-strength concrete beams. Eng Struct 2000; 22:413-423.

Ashour SA, Hasanain GS, Wafa FF. Shear behavior of high- strength fiber reinforced concrete beams. ACI Struct J 1992; 89(2):176-184.

ASTM C29 / C29M – 09. Standard test method for bulk density ("unit weight") and voids in aggregate, Annual Book of ASTM Standards, American Society of Testing Materials, 2009.

ASTM C39/C39M-14a. Standard test method for compressive strength of cylindrical concrete specimens, Annual Book of ASTM Standard, American Society of Testing Materials, 2014. DOI: 10.1520/C0039M-14A.

ASTM C109 / C109M - 11b. Standard test method for compressive strength of hydraulic cement mortars (using 2-in. or [50-mm] cube specimens), Annual Book of ASTM Standards, American Society of Testing Materials, 2011.

ASTM C127 - 12. Standard test method for density, relative density (specific gravity), and absorption of coarse aggregate, Annual Book of ASTM Standards, American Society of Testing Materials, 2012.

ASTM C128 - 12. Standard test method for density, relative density (specific gravity), and absorption of fine aggregate, Annual Book of ASTM Standard, American Society of Testing Materials, 2012.

ASCE-ACI-Committee-426. The shear strength of reinforced concrete members. J struct Div 1973; 99(6): 1091-1187.

ASTM C136 - 06. Standard test method for sieve analysis of fine and coarse aggregates, Annual Book of ASTM Standards, American Society of Testing Materials, 2006.

ASTM C150 / C150M – 12, Standard specification for Portland cement, Annual Book of ASTM Standards, American Society of Testing Materials, 2012.

ASTM C496, Standard test method for splitting tensile strength of cylindrical concrete specimens, Annual Book of ASTM Standards, American Society of Testing Materials, 2004.

ASTM C618 − 12, Standard specification for coal fly ash and raw or Calcined natural Pozzolan for use in concrete, Annual Book of ASTM Standards, American Society of Testing Materials, 2012.

ASTM C939- 02. Standard test method for flow of grout for preplaced-aggregate concrete (flow cone method), Annual Book of ASTM Standards, American Society of Testing Materials, 2002.

ASTM D7205/D7205M-06. Standard test method for tensile properties of fiber reinforced polymer matrix composite bars. ASTM International. 2006. United state.

Ayatollahi MR, Aliha MRM. Cracked Brazilian disc specimen subjected to mode II deformation. Eng Fracture Mech 2005; 72:493-503.

Azenha MAD. Numerical simulation of the structural behaviour of concrete since its early ages [Doctoral thesis]. Portugal: University of Porto, 2009.

Barnett SJ, Lataste JF, Parry T, Millard SG, Soutsos MN. Assessment of fiber orientation in ultra high performance fibre reinforced concrete and its effects on flexural strength. Mater Struct 2010; 43:1009-1023.

Barragan B, Gettu R, Agullo L, Zerbino R. Shear failure of steel fiber-reinforced concrete based on push-off tests. ACI Mater J 2006; 103(4):251-257.

Barros JAO, Cunha VMCF, Ribeiro AF, Antunes JAB. Post-cracking behaviour of steel fibre reinforced concrete. Mater Struct 2005; 38:47-56.

Barros JAO, Fortes AS. Flexural strengthening of concrete beams with CFRP laminates bonded into slits. Cem Conc Compos 2005; 27:471-480.

Barros JAO, Lourenço LAP, Soltanzadeh F, Taheri M. Steel-fiber reinforced concrete for elements failing in bending and in shear. Eur J Environ and Civil Eng 2013; 18(1):33-65.

Bazant ZP, Pfeiffer PA. Shear fracture tests of concrete. Mater Struct 1986; 19(110):111-121.

Böhni, H. Corrosion in reinforced concrete structures, 2005. Woodhead, Cambrigd, U.K.

BS EN 197-1. Cement - Part 1: Composition, specifications and conformity criteria for common cements, BSI, London, UK, 2000.

BS EN 124:1994. Gully tops and manhole tops for vehicular and pedestrian areas-design requirements, type testing, marking, quality control, 1994.

BS EN 812-103.1. Testing aggregates. Method for determination of particle size distribution. Sieve tests, 1985.

BS EN 1097-3. Tests for mechanical and physical properties of aggregates. Determination of loose bulk density and voids, British Standards Institution, 1998.

BS EN 12390-13. Testing hardened concrete-Part 13: determination of secant modulus of elasticity in compression, 2014.

Campione G. Simplified flexural response of steel fiber-reinforced concrete beams. Mater Civil Eng 2008; 20(4):283-293.

CAN/CSA-S06-06. The Canadian Highway Bridge code (CHBDC), Canadian Standards Association, Ottawa, Ontario, Canada, 2006.

Carmona S, Aguado A. New model for the indirect determination of the tensile stress-strain curve of concrete by means of the Brazilian test. Mater Struct 2012; 1-13.

CEB-FIP Model Code 2010 - Final draft, 2011.

Chermant JL, Chermant L, Coster M, Dequiedt AS, Redon C. Some field of applications of automatic image analysis in civil engineering, Cement and Concrete Composites 2001; 23:157-169.

Collins MP, Mitchell D. Prestressed concrete structures. Englewood Cliffs, New Jersey: Prentice-Hall 1991; 766 pp.

Cucchiara C, Mendola LL, Papia M. Effectiveness of stirrups and steel fibers as shear reinforcement. J Cem Con Compos 2004; 26(7):777–786.

Cuenca E, Serna P. Shear behavior of self-compacting concrete and fiber concrete push-off specimens (2013b). In: Khayat KH, Feys D, editors. Design production and placement of self-consolidating concrete, Proc. of SCC2010, vol. 1. Montreal, Canada: RILEM Book Series; 2010. p. 429–66.

Cuenca E, Serna P. Failure modes and shear design of prestressed hollow core slabs made of fiber-reinforced concrete. Comps Part B: Eng J 2013a; 45(1):952-964.

Cuenca E, Serna P. Shear behavior of prestressed concrete beams made of self-compacting fiber reinforced concrete. J Constr Build Mater 2013; 45:145-56.

Cunha VMCF. Steel fibre reinforced self-compacting concrete [Doctoral thesis]. Portugal: University of Minho; 2010.

Cunha VMCF, Barros JAO, Sena-Cruz JM. Modelling the influence of age of steel fibre reinforced self-compacting concrete on its compressive behavior. Mater Struct 2008; 41:465-478.

Cunha VMCF, Barros JAO, Sena-Cruz JM. Bond-slip mechanisms of hooked-end steel fibers in self-compacting concrete. Mater Sci Forum 2008; 587-588:877-881.

Cunha VMCF, Barros JAO, Sena-Cruz JM. Pullout behavior of steel fibers in self-compacting concrete, Mater Civil Eng 2010; 22(1):1-9.

Dewar JD. Computer modeling of concrete mixture, E&F Spon, London.

Dinh HH. Shear behavior of steel fiber reinforced concrete beams without stirrup reinforcement [Doctoral thesis]. Michigan , United States: University of Michigan; 2009.

Dinh HH, Parra-Montesinos GJ, Wight JK. Shear behavior of steel fiber-reinforced concrete beams without stirrup reinforcement. ACI Struct J 2010; 107(5):597-606.

Edalat Bahbahani A, Barros JAO, and Ventura-Gouveia A. Plastic-damage smeared crack model to simulate the behaviour of structures made by cement based materials. J Solid

Struct 2015; 73-74:20-40.

EN 14651. Test method for metallic fibre concrete-measuring the flexural tensile strength (limit of propor- tionality, residual) Varenna, Italy; 2004.

EUROCODE 2. Design of concrete structures –Part 1-1: General rules and rules for buildings. UNI-ENV 1992-1-2, 2004.

Faifer M, Ottoboni R, Toscani S, Ferrara L. Nondestructive testing of steel-fiber reinforced concrete using a magnetic approach, IEEE Trans. Instrument Measur   J   2011;   60: 1709-1717.

Felekoğlu B, Tosun K, Baradan B, Altun A, Uyulgan B. The effect of fly ash and limestone fillers on the viscosity and compressive strength of self-compacting repair mortars, Cem Conc Res 2006; 36:1719-1726.

Felekoğlu B, Türkel S, Baradan B. Effect of water/cement ratio on the fresh and hardened properties of self-compacting concrete. Build Environ 2007; 42:1795-1802.

Fenwick RC, Paulay T. Mechanisms of shear resistance of concrete beams. J Struct Div 1968; 94(10):2325-2350.

Ferrar L, Park Y, Shah SP. A method for mix-design of fiber-reinforced self-compacting concrete. J Cem Conc Res 2007; 37(6):957–971.

Foster SJ. The application of steel-fibres as concrete reinforcement in Australia: from material to structure. Mater Struct 2009. 42: 1209-1220. DOI 10.1617/s11527-009-9542-7

Greenough T. Nehdi M. Shear behavior of fiber-reinforced self-compacting concrete slender beams. ACI Mater J 2008; 105(5):468-477.

Ghrici M, Kenai S, Said-Mansour M. Mechanical properties and durability of mortar and concrete containing natural pozzolana and limestone blended cements. Cem Conc Compos 2007; 29: 542-549.

Gomes PCC. Optimization and characterization of high-strength self-compacting concrete [Doctoral thesis]. Spain: Polytechnic University of Catalonia, 2002.

HA 104/09. Chamber tops and gully tops for road drainage and services: installation and maintenance, Part 5. 2009; 4(2). pp 11.

Hasanpour R, Choupani N. Rock fracture characterization using the modified arcan test specimen. Rock Mech Mining Sci 2009; 46:346-354.

He XG, Kwan AKH, Modeling dowel action of reinforcement bars for finite element analysis of concrete structures. Comput struct J 2001; 79:595-604.

Higashiyama H, Banthia N. Correlating flexural and shear toughness of lightweight fiber-reinforced concrete. ACI Mater J 2008; 105(3):251-257.

Imam M, Vandewalle L, and Mortelmans F. Shear-moment analysis of reinforced high strength concrete beams containing steel fibers. Can J Civil Eng 1995; 22(2):462-470.

Imam M, Vandewalle L, Mortelmans F, and Van GD. Shear domain of fiber-reinforced high-strength concrete beam. J Eng struct 1997; 19(9):738-747.

Isaia GC, Gastaldini ALG, Moraes R. Physical and pozzolanic action of mineral additions on the mechanical strength of high-performance concrete. Cem Conc Compos 2003; 25:69-76.

ISIS Canada. A Canadian Network of Centres of Excellence. ISIS Educational Module 9: Prestressing Concrete Structures with Fibre Reinforced Polymers 2007; 10:2(139).

Jansson A. Fibres in reinforced concrete structures analysis, experiments and design [Doctoral thesis]. Sweden: Chalmers University of Technology, 2008.

JSCE-G 553-1999. Test method for shear strength of steel fiber reinforced concrete, Standard specification for concrete structures, Test method and specification. JSCE, 2005.

Kani G. The riddle of shear failure and its solution. ACI J, Proc. 1964; 61(4): 441-467.

Khuntia M, Stojadinovic B, Goel S. Shear strength of normal and high-strength fiber reinforced concrete beams without stirrups. ACI Struct J 1999; 96(2):282-289.

Kim JK, Park YD. Prediction of shear strength of reinforced concrete beams without web reinforcement. ACI Mater J 1996; 93(3):213-222.

Kim YH, Hueste MBD, Trejo D, Cline DBH. Shear characteristics and design for high-strength self-consolidating concrete. Struct Eng 2010; 136(8):989-1000.

Kwak YK, Eberhard MO, Kim WS, Kim J. Shear strength of steel fiber-reinforced concrete beams without stirrups. ACI Struct J 2002; 99(4):530-538.

Kwan AKH, Mora CF. Effect of various shape parameters on packing of aggregate particles. Mag Conc Res 2001; 53(2):91-100.

Laranjeira F. Design-oriented constitutive model for steel fiber reinforced concrete [Doctoral thesis]. Spain: Polytechnic University of Catalonia; 2010.

Laranjeira F, Grünewald S, Walraven J, Blom C, Molins C, Aguado A. Characterization of the orientation profile of steel fiber reinforced concrete. Mater Struct J 2011; 44:1093-111.

Lau D. and Pam HJ. Experimental study of hybrid FRP reinforced concrete beams. J Eng Struct 2010; 32(12):3857-3865.

Leung HY, Balendran RV. Flexural behavior of concrete beams internally reinforced with GFRP reds and steel rebars. Struct Survey J 2003; 21(4):146-157.

Li VC, Ward R, Hamza A. Steel and synthetic fiber as shear reinforcement. ACI Mater J 1993; 89(2):499-508.

Löfgren I. Fibre-reinforced concrete for industrial construction [Doctoral thesis]. Sweden: Chalmers University of Technology; 2005.

Lubell A, Sherwood T, Bentz E, Collins M, Safe shear design of large wide beams. Conc Inter 2004; 26(1):66-78.

Mansur MA, Ong KCG, Paramasivam P. Shear Strength of fibrous concrete beams without stirrups. Struct Eng 1986; 112(9):2066-2079.

Mazaheripour H. Hybrid steel and fiber-reinforced polymenr (FRP) pre-stressed bars as a new reinforcing system for pre-fabricated concrete structures [Doctoral thesis]. Portugal: University of Minho; 2016.

Mazaheripour H, Barros JAO, Sena-Cruz JM, Soltanzadeh F. Analytical bond model for GFRP bars to steel fiber reinforced self-compacting concrete. J Compos Constr 2013; 17(6).

Mazaheripour H, Barros JAO, Soltanzadeh F, Sena Cruz J. Deflection and cracking behavior of HPFRC beams reinforced with hybrid pre-stressed GFRP and steel reinforcements. 2016; Under preparation.

Meda A, Minelli F, Plizzari GA. Flexural behavior of RC beams in fiber reinforced concrete. Compos: Part B 2012; 43:2930-2937.

Minelli F, Conforti A, Cuenca E, Plizzari GA. Are steel fibres able to mitigate or eliminate size effect in shear? J Mater Struct 2014; 47(3):459-473.

Minelli F, Plizzari GA. Steel fibers as shear reinforcement for beams. Proc. 2nd International *fib* congress, Naples, Italy; 2006.

Mirsayah AA, Banthia N. Shear strength of steel fiber-reinforced concrete. ACI Mater J 2003; 99(5):473-479.

Naaman AE. Engineered steel fibers with optimal properties for reinforcement of cement composites. Adv Conc Tech 2003; 1(3):241-252.

Naaman AE, Reinhardt HW. Proposed classification of HPFRC composites based on their tensile response. Mater Struct 2006; 39:547-555.

Narayanan R, Darwish I. Use of steel fiber as shear reinforcement. ACI Struct J 1987; 84(3):216-227.

Okamura H, Ouchi M. Self-compacting concrete development, present use and future.

Proc. of the 1st International RILEM Symposium on Self-Compacting Concrete, Stockholm, Sweden: RILEM Publications S.A.R.L.; 1999.

Ona M, Soltanzadeh F, De Sousa C, Barros JAO. Exploring the use of HPFRC and GFRP grids for the production of manhole covers. Proc. of the 8th International Conference on Fiber Concrete (FC2015), Prague, Czech Republic, 10-11 September 2015. DOI: 10.13140/RG.2.1.2778.6962.

Petrova VE, and Sadowski T. Theoritical analysis of Mode II cracks in a compact shear specimen, Componential Mater Sci, 64:248-252.

Pereira ENB. Steel fibre reinforced self-compacting concrete: from material to mechanical behavior [Master thesis]. Portugal: University of Minho, 2006.

Pereira ENB, Barros JAO, Camões A. Steel fiber reinforced self-compacting concrete: experimental research and numerical simulation. Struct Eng 2008; 134:1310-1321.

Prisco M, Plizzari G, Vandewalle L. Fibre reinforced concrete: new design perspectives. Mater Struct 2009; 42:1261-1281.

Qu W, Zhang X, Huang H., Flexural behavior of concrete beams reinforced with hybrid (GFRP and steel) bars. J Compos Constr 2009; 13(5):350-359.

Rao GA, Rao AS. Toughness indices of steel fiber reinforced concrete under mode II loading. Mater Struct 2009; 42:1173-1184.

Rasband W. *ImageJ*. USA: National Institutes of Health; 2008.

Reinhardt HW, Grosse CU, Weiler B. Material Characterization of Steel Fibre Reinforced Concrete Using Neutron CT, Ultrasound and Quantitative Acoustic Emission Techniques, 6. NDT International 2001; No.5.

Richardson DN. Aggregate gradation optimization- literature search. Technical report, University of Missouri- Rolla, Missouri , RDT 05-001; 2005.

RILEM TC162-TDF. Test and design methods for steel fiber reinforced concrete, $\sigma - \varepsilon$ design method. Final Recommendation. Mater Struct 2003; 35:560-567.

Robins P, Austin S, Jones P. Pull-out behavior of hooked steel fibers. Mater Structr 2002; 35:434-442.

Rosenbusch J, Teutsch M. Trial beams in shear. Final Report, Brite/Euram Project 97-4163, Sub Task 4.2. Germany: Technical University of Braunschweig; 2002.

Sagaseta J, Vollum RL. Shear design of short-span beams. Magaz Conc Res 2011; 62(4):267-282.

Schumacher P. Rotation capacity of self-compacting steel fiber reinforced concrete [Doctoral thesis]. Duitsland: Darmstadt University of Technology; 2006.

Sena-Cruz JM. Strengthening of concrete structures with near-surface modeling CFRP laminate stirrups [Doctoral thesis]. Portugal: University of Minho, Portugal, 2004.

Shah SP, Swartz SE, Ouyang C. Fracture mechanics of concrete: applications of fracture mechanics to concrete, rock and other quasi-brittle materials. A WILEY-INTER SCIENCE PUBLICATION, United State of America, 1995.

Sharbatdar MK. Monotonic and cyclic loading of new FRP reinforced concrete cantilever beams. Inter J Civil Eng 2008; 6(1):58-71.

Shilstone JM. Concrete Mixture Optimization, Concrete International: Design and Constr J 1990; 12(6):33-39.

Shioya T, Iguro M, Nojiri Y, Akiayma H, Okada T. Shear strength of large reinforced concrete beams, Fructure Mechanics: Application to Concrete. SP-118, ACI, Detroit, 1990:259-276.

Soetens T. Design models for the shear strength of prestressed precast steel fiber reinforced concrete girders [Doctoral thesis]. Belgium: Ghent University; 2015.

Soltanzadeh F, Edalat Behbahani A, Mazaheripour H, Barros JAO. Shear resistance of HPFRC short-span beams without transversal reinforcements, Compos Struct 2016; 139:42-61.

Soltanzadeh F, Barros JAO. Test setup for the characterization of shear behavior of cement based materials, Technical Report 11/DEC/E-23, Guimaraes, Portugal: University of Minho; 2011.

Soltanzadeh F, Barros JAO, Santos RFC. Study of the fracture behavior of fiber reinforced concrete under direct shear loading, Technical report 12-DEC/E-18, Guimarães, Portugal: University of Minho; 2012.

Soltanzadeh F, Barros JAO, Santos RFC. Steel fiber reinforced self-compacting concrete: from material to mechanical behavior. Technical report, University of Minho, Guimarães, Portugal, 12-DEC/E-19; 2012.

Soltanzadeh F, Barros JAO, Santos RFC. High performance fiber reinforced concrete for the shear reinforcement: experimental and numerical research. Constr Build Mater 2015; 77:94-109.

Soltanzadeh F, Mazaheripour H, Barros JAO, and Sena-Cruz J. Shear capacity of HPFRC beams flexurally reinforced with steel and prestressed GFRP bars. Proc. of the 11th international symposium on fiber reinforced polymers for reinforced concrete structure (FRPRCS-11), Guimaraes, Portugal, 25-28 June 2013.

Soltanzadeh F, Mazaheri H, Barros JAO, Taheri M, Sena-Cruz JM. Experimental study on shear behavior of HPFRC beams reinforced by hybrid pre-stressed GFRP and steel bars. Proc. 7th International Conference on FPR Composites in Civil Engineering, Vancouver, Canada; 2014.

Stähli P, Custer R, van Mier JGM. On flow properties, fibre distribution, fibre orientation and flexural behaviour of FRC. Mater Struct J 2007; 41:189-196.

Standard test method for density, relative density (specific gravity), and absorption of fine aggregate. Annual Book of ASTM Standards, American Society of Testing Materials, 2012.

Teixeira MDE, Barros JAO, Cunha VMCF, Moraes-Neto BN, Ventura-Gouveia A. Numerical simulation of the punching shear behaviour of self-compacting fibre reinforced flat slabs. Constr Build Mater 2015; 74:25-36.

Timoshenko SP, Goodier JN. Theory of Elasticity, McGraw-Hill, New York, 1991.

Taylor HPJ. The fundamental behavior of reinforced concrete beams in bending and shear. ACI SP-42: Shear in Reinforced Concrete 1974; Detroit pp. 43-77.

Valle M, and Buyukozturk O, Behavior of fiber reinforced high-strength concrete under direct shear. ACI Mater J 1993; 90(2):122-133.

Vandewalle L. RILEM TC 162-TDF, Test and design methods for steel fibre reinforced concrete σ-ε design method - Final Recommendation. Mater Struct 2003; (36):560-567.

Ventura-Gouveia A. Constitutive models for the material nonlinear analysis of concrete structures including time dependent effects [Doctoral thesis]. Guimarães, Portugal: University of Minho, 2011.

Ventura-Gouveia A, Barros JAO, Azevedo AFM. Crack constitutive model for the prediction of punching failure modes of fiber reinforced concrete laminar structures. Comput Conc 2011; 8(6):735-755.

Villain G, Barigel-Bouny V, Kounkou C. Compressive study on the induced hydration, drying and deformations of self-compacting and ordinary mortars. Proc. of the 11th international symposium on fiber reinforced polymers for reinforced concrete str 1st International RILEM Symposium, 1999 131–142.

Villain G, Barogel-Bouny V, Kounkou C. Comparative study on the induced Quiroga PN, and Fowler DW. The effects of aggregates characteristics on the performance of Portland cement concrete, Technical report, Austin, United State: University of Texas; 2004.

Voo Y, Poon W, and Foster S. Shear Strength of Steel Fiber-Reinforced Ultrahigh-Performance Concrete Beams without Stirrups. J Struct Eng 2010; 136(11):1393-1400.

Walraven JC, Reinhardt HW. Theory and experiments on the mechanical behavior of crack in plain and reinforced concrete subjected to shear load. HERON 1981; 26 (1A):68 pp.

Xu S, Reinhardt HW. Shear fracture on the basis of fracture mechanics. Otto-Graf J 2005; 16:21-78.

Zamanzadeh Z, Lourenço L, Barros JAO. Recycled steel fibre reinforced concrete failing in bending and in shear. Const Build Mater 2015; 85:195–207

Zhu WC, Tang CA. Numerical simulation on shear fracture process of concrete using mesoscopic mechanical model. Const Build Mater 2002; 16:453-463.